Study of Doping Phenomena in Functional Materials

This thesis is submitted in partial fulfilment of the requirements for the Degree of
Doctor of Philosophy (Chemistry)

Shiny Mathew

UCL

2019

I, Shiny Mathew, confirm that the work presented in this thesis is my own. Where information has been derived from other sources, I confirm that this has been indicated in the thesis.

I would like to dedicate this thesis to my loving and supportive family,

without whom nothing would have been possible.

Abstract

The disruptive technologies that are currently emerging across the semi-conductor and electronics industries demand the need for a continual focus on decreasing the size of integrated circuits and renewable energy technology devices. To support this demand requires comprehensive research into understanding the functional properties of materials at an atomic level across a three-dimensional space. These functional properties of materials originate from atomic level properties such as structural, optical and electronic properties, all of which can be modified to optimise the functionality of a material. This is the reason why these atomic level properties were comprehensively studied and reported in this thesis. The introduction of atomic level impurities, via the phenomena of doping, has helped to modify the structural, optical and electronic properties of the materials investigated in this thesis. An insight into the effect and potential that high temperature solid-state doping can bring towards improving the functional properties of three materials namely titania-rutile (single crystal substrates), titanates (powders) and Magnesium Silicon Nitrides $MgSiN_2$ (powders), were gained from the experiments and results reported in this thesis. NB: titanates studied include sodium and potassium hexatitanates, sodium trititanate and caesium titanate.

Chapters 3-8 of this thesis were written with a specific focus on the spatial arrangement of dopant atoms (such as B, C, S and N) introduced into photocatalytic titania-rutile and the associated influence it has on bonding, diffusion behaviours as well as structural and electronic properties. The insight gained about these properties of titania-rutile are essential when working on an industrial scale to optimise the performance of renewable energy devices, or to at least match with that of fossil fuels. The choice of anionic dopant introduced into the titania-rutile can help to vary the structural or electronic properties in titania-rutile. Additionally, the unit cell structure that determines the surface and bulk structure of the titania-rutile single crystal substrate that was chosen was observed to also help modify the structural or electronic properties. While the carbon, sulphur and nitrogen anions were predominantly incorporated as surface dopants in titania-rutile, this was not the case with boron anions, which also showed results that were dependent on the orientation of the titania-rutile. Boron incorporation in (110)-titania-rutile led to the formation of a $TiBO_3$ surface layer, approximately 120 nm thick as per XPS data. This $TiBO_3$ layer, as per XRD data, is epitaxially arranged on the rutile (110) surface along the (108), (118) and (018) planes. While this layer was also seen on the rutile (100) surface, no

XRD evidence of $TiBO_3$ was found with the rutile (001) surface. As well as observing a shift in the XPS valence band onset, the emergence of new states and O2p orbital mixing was also observed upon anion incorporation into rutile. This study, reporting the structural and electronic effects observed as a result of doping, will be crucial when working with photocatalysts that are widely studied for the water splitting process, used to produce hydrogen, which is a 'clean' energy fuel.

The main insight gained from chapter 9 is about making use of the structure of titanate materials (e.g. in open layered and tunnelled titanates) as a scaffold, to control the spatial distribution of any given dopant. This is particularly relevant when the material being investigated is in its powdered form, with no well-defined surface or a bulk. Chapter 9 was written with a specific focus on the effect of doping temperature on the location of the incorporated nitrogen dopant (aka. structural properties), electronic and optical properties in the open layered and tunnelled titanates. While these relationships are widely reported in the literature already, the challenge that this study addresses are about carrying out nitrogen doping at three different temperatures in the same system to ensure the same ammonia flow rate, which is a parameter that is often very challenging to reproduce. This ensures reproducibility of results and therefore reliability in the conclusions. Also, this study is also more comprehensive than that reported in literature the and discusses samples that are fully characterised. The preferential incorporation of nitrogen into the Ti-O-Ti bonds than the Na-O-Ti bonds was observed in the tunnelled titanates, $Na_2Ti_6O_{13}$ and $K_2Ti_6O_{13}$, and (not in the open layered titanates $Na_2Ti_3O_7$ and $Cs_{0.68}Ti_{1.825}O_4$), is potentially what led to the creation of Ti^{3+} defects as observed in their optical absorption spectrum. The resulting Ti 3d and N 1s states observed in the XPS valence band spectrum is potentially what caused the observed band gap narrowing. The modification of the electronic, optical and structural properties of the titanates using nitrogen doping can be used to optimise the functionality of titanates e.g. when it is used as photocatalysts or as battery materials.

The main insight gained from chapter 10 is about exploring the alternative material that can replace the expensive aluminium nitride, which is known to be a promising substrate material with ideal thermal conductivity and minimal dissipation of heat. This was done by studying the change in structural properties including associated unit cell volume. The effect of the addition of varying amounts of aluminium as a dopant into the $MgSiN_2$ structure, helped to find that the phase transformation from $MgSiN_2$ to AlN-wurtzite structure is observed between 30% and 50% aluminium dopant

introduction, as per XPS and XRD. While the doubling of the magnesium reactant mass led to a single phase $MgSiN_2$, it can potentially affect particle size properties, as hinted by the XRD peak broadening observed. Increasing the aluminium content to above 50% led to unit cell volume contraction as Al^{3+} ions are smaller than the lattice Mg^{2+} ions they are substituting. These findings can help gain an understanding of the fundamental chemistry underpinning the development of cheaper, alternative materials for any applications.

Impact Statement

The analysis and insight behind the science presented in this thesis can be translated across to the commercial sector. At present, there are enormous numbers of disruptive technologies that are emerging across the semiconductor and electronics industries. With the continual focus on decreasing the size of integrated circuits and renewable energy technology devices, the need for understanding the functional properties at an atomic level across a three-dimensional space remains fundamental. This explains why the process of doping, which introduces atomic impurities into materials, has attracted research interest. Despite the large volumes of publications on doping, a comprehensive study detailing a full characterisation of the doped materials being studied has not been reported. This is what this thesis will entail with a specific focus on the spatial arrangement of dopant atoms in titania-rutile and related materials, and the associated influence it has on bonding, diffusion behaviours and electronic properties. The doped titania-rutile and titanate materials (sodium and potassium hexatitanates, sodium trititanate and caesium titanate) studied in this thesis are photocatalysts that are widely studied for the water splitting process, used to produce hydrogen, which is a 'clean' energy fuel. Therefore, the findings can contribute towards the design of new and improved photocatalytic materials. This is crucial when working with renewable technologies to optimise their performance, or at least to match with that of fossil fuels.

The knowledge shared in this thesis will be a significant contribution to science from an academic view point. It builds on the scientific database of research, which over the span of decades will become established concepts in the electronics and semiconductor photocatalysis disciplines. The communication of this study on an open platform, e.g. part of my $MgSiN_2$ study was published in the Journal of Applied Physics[*] and my XPS work published in the Journal of Power Sources[#], will help to receive more government funding into this research area. Furthermore, it will encourage further interest in the research community to explore complex and facile methodologies into the synthesis and application of the materials being investigated in this thesis.

The benefits of my research can be brought about within academia as well as industry in several ways. Firstly, government funding bodies such as the EPSRC should invest more into PhD studentships involving academia-industry collaborations, so that the fundamental chemistry discovered in academia can be translated and tested in

industry straightaway. Secondly, focus groups can be used to generate awareness amongst businesses and the public to generate awareness about research into renewables outlining the benefits it will reap over time, e.g. a stable energy source and low energy bills following the high initial investment capital. This approach can also help to meet UK's initiative in increasing its reliance on carbon neutral forms of energy, as agreed during the Climate Change agreement in Paris in 2015. Thirdly, incorporating the latest advances in renewable energy technology into high school curriculums, along with the opportunity for students to meet scientists who conduct this research at universities can bring about a new generation of people interested in sustainable science. Thus, we can boost innovation and interest in this field. Powering an island, a country or a continent using sustainable energy can make it self-sufficient, which can become convenient in the times of disaster management.

* M. Råsander, J. Quirk, T. Wang, S. Mathew, R. Davies, R. Palgrave and M. Moram, *Journal of Applied Physics*, 2017, 122, 085705

Drosos, C. Jia, S. Mathew, R. Palgrave, B. Moss, A. Kafizas and D. Vernardou, *Journal of Power Sources*, 2018, 384, 355-359.

Acknowledgements

I would like to sincerely thank my supervisor, Dr Robert G. Palgrave for all his encouragement, teaching and invaluable guidance. I am also grateful to my secondary supervisor, Dr David J. Payne for all his support and assistance in getting access to research equipment at Imperial College London. I would like to also thank Professor Stephen Skinner and Dr Neil Curson, the Directors of the Centre for Doctoral Training in Advanced Characterisation of Materials, for their mentoring as well as all the valuable opportunities they provided me over the four years of my PhD.

I would like to thank the technicians who provided training for me on various research instruments. Thanks to Dr Steve Firth, Mr Martin Vickers, Mr Tom Gregory, Mr Crosby Medley and Martyn Towner for SEM, XRD and UV-Vis training at UCL departments of Chemistry and Archaeology. Thanks to Dr Sarah Fearne for SIMS and LEIS training at the department of Materials at Imperial College London. Also, thanks Mr Andrew Weston, for the CHN analysis service at UCL Pharmacy.

I would like to thank Dr Nicolas Constantino from LCN for his assistance with measuring XPS crater depths using DekTek Profilometer. Thanks to Mr Muhammad Kammaluddin for AFM images. Thanks to Dr Andrew Ballantyne for XRD of single crystal substrates and to Mr Jonathan Rackham for the Reciprocal Space map measurement.

Thanks to Dr James B. Quirk and Dr Shelly Moram from the department of Materials at Imperial College London for the collaborative work and useful discussions on Magnesium Silicon Nitrides.

I wish to thank everyone who I interacted with during the first couple of years of my PhD, which is when I learnt the most and stressed the most. Though the results of it do not appear in this thesis, I gained a lot of learning. I thank Dr Seyeh Koohpayeh from John Hopkins University, U.S.A, for the single crystal samples he synthesised. Thanks to Professor David McPhail for his mentoring and Cameca SIMS measurements of my samples from the University of Western Sydney. I would like to especially thank Dr Emily Glover and Mr Satyam Ladva, who were instrumental to helping me become confident in using the XPS and for their huge amount of support and friendship, which also made my PhD days very enjoyable. Thanks also to my colleagues, Dr Francesco di Maggio, Dr Sreenivas Gadipelli, Dr William Travis, Dr

Andrew Breeson, Dr Yaomin Li, Miss Delphine Malarde, Dr Merina Corpinot and Dr Diana C. Teixeira who have been supportive and motivating.

Thank you to Pappa, Mummy and my brother, Martin for their enormous amounts of encouragement, love and prayers during the challenging first year of my PhD, when I found the Master to PhD jump very alien and felt like quitting. Thank you to Mummy and Daddy for their love and prayers as well as for the numerous initiatives they took despite the discomforts to ensure that I am helped in every possible way in my final lap of completing my PhD. Last but certainly not the least, I would like to thank my husband, Alex for being the pillar of my strength, for being understanding and patient every step of the way in every way possible, especially during difficult times. I would like to dedicate this thesis to my loving and supportive family, without whom nothing would have been possible.

Table of Contents

Table of Figures

Table of Tables

Chapter 1: Introduction

This chapter gives a background and literature review for the investigations reported in Chapters 3, 4, 5, 6, 7, 8 and 9 of this thesis.

1.1 Research Question and Aims

A detailed characterisation of titania-rutile, titanates (to include: sodium and potassium hexatitanates, sodium trititanate and caesium titanate) and $MgSiN_2$, doped using a high temperature solid-state method is discussed in this thesis, in terms of their structural, electronic and optical properties. Introducing dopant atom(s) into these materials at different permutations and combinations can help tune these functional properties to suit their potential in many technological applications.

Since achieving stable dopant distributions in powders remains a challenge, single crystal substrates of titania-rutile were chosen for investigating anionic doping behaviour in Chapters 3, 4, 5, 6 and 7. Three decades of research on titania has reported the influence of doping on its improved photoactivity, exploring parameters such as the titania particle size and morphology as well as the dopant concentration and stoichiometry. However, these reports neither entail any comprehensive study on achieving a control over the spatial distribution of dopants of varying chemical nature in the titania lattice nor on how this distribution can potentially influence the photocatalytic properties. Chapters 3, 4, 5, 6 and 7 addresses this gap in research and reports the synthesis and a detailed characterisation of various stable anionic dopant distributions with different chemical states and electronic properties in titania-rutile. This knowledge is significant for the understanding of structure-function relationship that is essential for designing materials with optimised photoactivity.

Investigation into powdered forms of titania is important due to the high photoactivity yielding from their high surface area. While single crystal substrates serve as ideal models for understanding the diffusion of dopants in titania, achieving a stable and reproducible dopant distribution in powders remains a challenge. Chapter 8 addresses this challenge by using a structural approach involving the use of layered titanate materials (to include: sodium and potassium titanates, caesium titanate and sodium trititanate). Titanate frameworks consist of titania layers, which are spatially separated with interlayer galleries in between. These frameworks thus serve as structural “scaffolds” that can allow a spatial control of the distribution of dopants.

Although, it is still difficult to probe this spatial aspect, it is important to characterise these titanate samples fully, as detailed in Chapter 8, for it to be stepping stones for future research.

The investigation of aluminium doping into $MgSiN_2$ powders is of interest, due to the prospects of aluminium nitride being a promising reactant material. Although the synthesis of $MgSiN_2$ is reported widely, there are no publications on a detailed characterisation covering the formation of solid solutions of $MgSiN_2$ and AlN, by varying the concentration of aluminium doping being introduced into $MgSiN_2$, which is what Chapter 9 will cover.

1.2 Doping Titania – The Concept

The electronic structure, polymorphs and crystal structure of titania are explored below. It is then used to reason the existence of native defects and their diffusion in the titania lattice, appreciating the concept of doping.

1.2.1 Electronic Structure of Titania

A fundamental understanding of the electronic structure semi-conductors such as titania (TiO_2) is required to understand semi-conductor photocatalytic water splitting[1,2,3,4,5,6]. The electronic structure of a semiconductor such as titania consists of a Conduction Band (CB), which is separated from a Valence Band (VB) by the Band Gap (E_g). Upon irradiation of the semi-conductor, an electron in the VB gets promoted into the CB, leaving behind a positive hole (h^+) in the VB and a negative electron (e^-) in the CB. These photogenerated h^+ and e^- then migrate to the surface of the semi-conductor and take part in oxidation and reduction processes required for splitting water into hydrogen and oxygen (Figure 1). For successful and efficient water splitting, the photogenerated carriers (h^+/ e^-) should be prevented from recombining[7,8,9,10, 11].

The magnitude of the band gap can be calculated using Plank's[12] formula (Equation 1) and can be tuned for achieving favourable photocatalytic efficiencies. The band gap of titania is approximately 3.0 eV for titania-rutile and 3.2 eV for titania-anatase[13]. These values allow optical absorption in the UV-light region, at ~413 nm and ~387 nm respectively, of the electromagnetic spectrum. Shifting this absorption to the visible light region by reducing the band gap[14, 15, 16] is favourable in terms of the

efficiencies achieved, especially when sunlight is used to harness energy from the semiconductor water splitting process (Equation 2). This is because, visible light constitutes about 50% of the solar spectrum while UV light constitutes only about 4%[17].

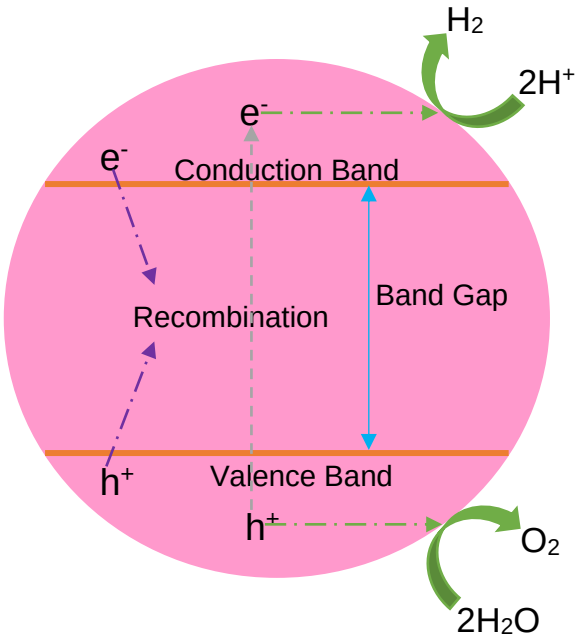

Figure 1 Role of the electronic structure of semi-conductors in photocatalytic water splitting

$$E = h\,v$$

Equation 1: Plank's equation where E is the energy of the absorbed photon of light, *h* is Plank's constant and v is the frequency of the absorbed wavelength of light

$$2H_2O \xrightarrow[\text{Titania photocatalyst}]{\text{Sunlight}} 2H_2 + O_2$$

Equation 2: Chemical equation of photocatalytic water splitting

1.2.2 Polymorphs of Titania

Anatase and rutile are the most intensely studied polymorphs of titania used for photocatalytic applications[18]. They both have a tetragonal crystal structure, consisting of Ti atoms octahedrally coordinated to O atoms, except that they differ in the way how the octahedra are connected[19,20] (Figure 2). Among these, only rutile is commercially available in single crystal substrate forms. This is because single crystal growth employs temperatures of ~700 ^{o}C to 1000 ^{o}C,[21] between which anatase is reported to transform into the more stable rutile[22]. Therefore, anatase single crystal substrates are challenging to grow. Although thin films of anatase can be epitaxially

stabilised onto substrates,[23,24] it cannot match the high crystallinity that single crystal substrate forms possess.

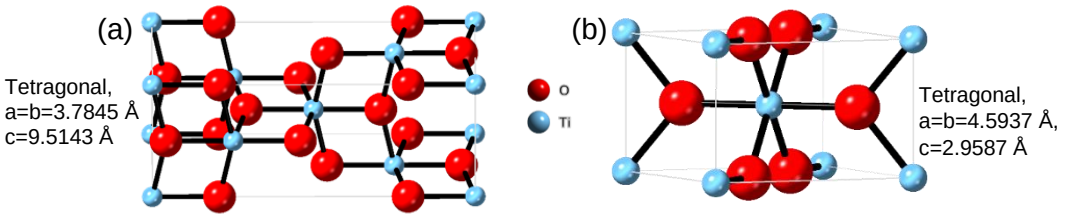

Figure 2 Crystal structure of (a) anatase and (b) and rutile forms of titania

1.2.3 Model Photocatalytic Surface of Titania

Although powdered titania yields high photocatalytic efficiencies, due to their inherently high surface area[25], single crystal substrates of titania-rutile are used as models to understand semi-conductor photocatalysis better. This is because photocatalysis is a surface reaction and single crystal substrates allow the possibility of investigating the different surfaces of the titania-rutile structure at better resolution as these substrates have a well-defined surface and a bulk[26]. With regards to research reported in this thesis, the use of these substrates will help to achieve well-defined dopants spatially as well as chemically across different substrates of varying orientations. This study then becomes crucial to gain an understanding of diffusion behaviours in surface reactions in photocatalytic powders on an atomic and molecular scale.

The (110) surface of rutile is reported to have a model photocatalytic surface and therefore, is the reason for it to be widely studied in the literature[27, 28,29]. However, it is observed to reconstruct under oxidising and reducing conditions as well as at high temperatures[30]. The deduction that the (110) surface is the most stable in titania-rutile stems from computational calculations[31] and from the findings that surfaces such as the (100) is observed to become thermodynamically more stable by transforming into the (110). The least stable (001) surface is however is seen to stabilise by transforming into the (101) or (011) surface. These surfaces in order of lowest energy are reported to be: (110) < (100) < (001) and exposes different atomic arrangements in titania (Figure 3), which is known to have different photocatalytic behaviours[32].

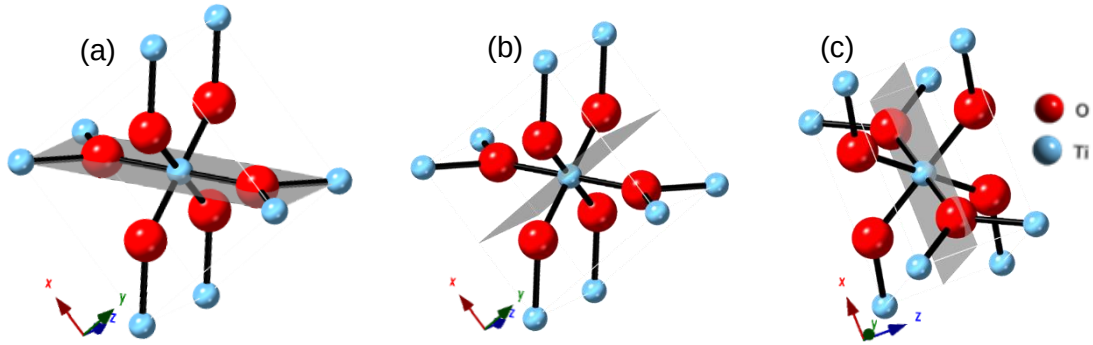

Figure 3 Crystal structure of rutile, where the grey plane in (a), (b) and (c) indicates the (110), (100) and (001) surfaces respectively

1.2.4 Defects in Titania

The two main lattice defects in titania are Ti interstitials (Ti^{3+} at an interstitial site) and oxygen vacancies, written in the Kröger-Vink notation as $Ti_i^{\bullet\bullet\bullet}$ and $V_o^{\bullet\bullet}$ respectively. These defects are formed in the titania lattice under oxidising and reducing conditions respectively (Equation 3 and 4). Achieving charge neutrality in a titania lattice, requires four $Ti_i^{\bullet\bullet\bullet}$ for every two $V_o^{\bullet\bullet}$ defects. These defects have been shown to affect the electronic structure of titania-rutile[33, 34].

$$O_o \rightleftharpoons V_o^{\bullet\bullet} + 2e^- + \tfrac{1}{2}O_{2\,(g)} \qquad \textbf{Equation 3}$$

$$TiO_2 \rightleftharpoons Ti_i^{\bullet\bullet\bullet} + 4e^- + O_{2\,(g)} \qquad \textbf{Equation 4}$$

1.2.5 Defect Diffusion in Titania

Defect equilibrium in the titania lattice is an important aspect to understand, to investigate diffusion behaviours. The diffusivity of lattice oxygen in titania is found to be proportional to the concentration of $V_o^{\bullet\bullet}$, which is reported to increase when atoms are substitutionally doped into titania[35]. While aliovalent dopants such as Al and Nb can control the type and concentration of titania lattice defects, isovalent dopants such as Sn^{4+} and Zr do not have much effect on the defect equilibria[36]. A concurrent diffusion of $Ti_i^{\bullet\bullet\bullet}$ and $V_o^{\bullet\bullet}$ or TiO units is possible in anatase, which has an open structure, possessing the ability to incorporate additional anions and cations into its lattice[37].

Diffusion within particles in titania powders is an important aspect that may affect photocatalytic behaviours. Reports show that oxygen deficient titania powders are more photoactive than its stoichiometric counterparts[38]. In a titania particle, the oxygen diffusion from its edges to its centre can be limited. This suggests that

diffusion controls the oxygen content and stoichiometry on the spatial scale inside the titania particle. The edges of titania particles have a stoichiometric composition, due to its constant exposure to air. On the other hand, the non-stoichiometric composition in the centre of the particle accounts from short diffusion lengths. These stochiometric surfaces and oxygen deficient bulk can be challenging to study in isolation, in powders. Therefore, these aspects can be modelled by annealing single crystal substrates of titania under intensive vacuum conditions. The lattice diffusion of oxygen is suggested to have the potential to rate limit the movement of grain boundaries in polycrystalline titania powders. The reason for this is proposed to be due to the large ionic radius of oxygen, which makes it the least mobile species in the titania lattice[39]. Thus, diffusion is an important area of study.

Fick's second law of diffusion[40] can be used to model an infinitesimally small change in concentration of a defect species over the thickness of a rutile single crystal substrate (Equation 5).

$$\frac{\partial \mathrm{x}}{\partial \mathrm{t}} = \mathrm{D}\left(\frac{\partial^2 \mathrm{x}}{\partial^2 z}\right)$$

Equation 5: Fick's second law of diffusion where *∂*x/ *∂*t is the change in the concentration of species (x) as a function of time (t), D is the diffusivity of the species N into the substrate, *∂*^{2}x/ *∂*^{2}*z* indicates a small infinitesimal change in the concentration of species N over the substrate of thickness *z*

The diffusion of dopants into a single crystal substrate with a well-defined surface and a bulk, can be described by a solution to Fick's Law[89] (Equation 5.1).

$$\mathrm{c}(\mathrm{x},\mathrm{t}) = c_0 erfc\left(\frac{\mathrm{x}}{2\sqrt{(\mathrm{Dt})}}\right)$$

Equation 5.1: Solution to Fick's Law where c (x, t) refers to the dopant concentration, c at depth x and time t; c_o is the concentration at the surface at t=0; D is the diffusion coefficient; eryfc (x) refers to the complimentary error function of the depth x.

Typically, a diffusion plot of Depth^2, x^2 versus the natural log of the dopant yield or concentration is used to determine the dopant diffusion coefficient(s). This plot will have distinctively looking straight line segment(s) from which the diffusion coefficients could be calculated from their line gradients. These values of diffusion coefficient(s) can then be used to model diffusion curves using Equation 5.1.

1.2.6 Anionic Defects in Titania

Anions such as nitrogen, sulphur, carbon and boron can be introduced into the titania-rutile lattice through doping, to encourage the formation of defects[41, 42, 43, 44, 45] discussed earlier. These anions can be introduced using several doping techniques, where the precursor source and annealing conditions vary with the chosen anion or their volatility for example (Table 1, 2, 3 and 4). Amongst all the techniques, the high temperature solid-state synthesis is employed for the investigations reported in this thesis. This is because of its facile nature that will enable the synthesis of dopant diffusion profiles in single crystal substrates with ease. More importantly, this synthesis technique has relatively few parameters, which can increase the reproducibility of these dopant distributions in titania-rutile.

Table 1 Dry and wet processes reported for nitrogen doping of titania

Doping technique	Parameters	Effect on structural and electronic properties
DRY PROCESSESS		
Oxidative annealing of TiN powder	- Annealing time of 90 min - O_2 gas flow rate of 10 slm - Annealing temperature of 550 ^oC - Heating rate is not mentioned	- 0.1 atomic% of substitutional N into rutile (XPS) - Caused N2p-O2p mixing, suggested (FLAPW calculations) - Shifted absorption edge to lower energy to the visible light region (UV-vis)[46]
Nitrification of TiO_2 under NH_3 gas flow	- Annealing time of 5 mins - Heating rate of 7K/ min - Annealing temperature of 870 K - NH_3 gas flow rate not mentioned	- 0.6 atomic% of N incorporated into rutile (XPS), - Interstitial N caused a shift of the optical absorption into visible light region by 0.6 eV (UV-vis)[47]
Ti particles treated with N_2 plasma using a barrel-plasma-treatment system	- Vacuum pressure in the Ti sample chamber of < 1 x 10-3 Pa - N_2 gas pressure of 10 Pa - Plasma treatment time of 15 to 1440 min - RF power levels of 50-300 W - Barrel oscillation at 5 rpm over an angular range of ±751^o - Size of the Ti particles - Temperature of the sample	- Suggested that a layer of stoichiometric TiN formed on the surface of the Ti particles, but depth profiling of particles is changing to achieve, as they do not have a well-defined surface and a bulk (XPS) - This resulted in the surface hardness of the particles to be increased by 5 times (nanoindentation measurements)[48]
Radio frequency magnetron sputtering using a N_2/ Ar sputtering gas mixture	- Concentration of the N_2 and Ar in the sputtering N_2/ Ar gas mixture - Base vacuum and working pressure of 5.0 x 10-4 Pa and 2.0 Pa respectively - Position of the substrate and the TiO_2 target - Substrate temperature of 873 K - RF power of 300 W	- Concentration of substitutional N is in the range 2.0-16.5 atomic% (XPS) - which was suggested to have a key role in the band gap narrowing observed (XPS, XRD) - N concentration of 6 atomic% gave the best photocatalytic activity under visible light irradiation[49]

Doping technique	Parameters	Effect on structural and electronic properties
WET PROCESSESS		
Mechanochemical wet ball milling of amorphous TiO_2 and a N source e.g. any one out of NH_4F, NH_4HCO_3, $NH_3 \cdot H_2O$, NH_4COOCH_3, and $CH_4\ N_2O$).	- Amount of TiO_2, N source and deionized (DI) water - Size of the agate balls used: 12x 10.0 mm diameter and 40 x 5.0mm diameter ones - Precursor grinding time of 180 min and a speed of 580 rpm - Drying temperature of the ground powder of 105 ^oC in air for 5 h - Calcination temperature of the dried powder at 400 ^oC for 2 h, with a heating rate of 3 $^oC\ min^{-1}$	- N species gave rise to a new mid-gap level within the band gap, slightly above the O 2p state within the valence band, but not suggestive of O2p-N1s mixing - Suggested that the photocatalytic activity after ball milling has reduced, suggesting that the process may have destroyed the TiO_2 surface structure[50]
Sol-gel synthesis of N doped TiO_2 powders using N sources such as ammonium nitrate	- Amount of tetra butyl titanate, ethanol, DI- water - Size of 10 agate stirring granules were 1 cm in diameter - Temperature of rotary evaporator was 25 ^oC - Air blower rate of 40 L min^{-1} - Reaction time of 3 h - Emulsion distillation temperature of 50 ^oC for 15 min under vacuum - Annealing temperature of the resulting product at varying temperatures for 2 h	- 6% theoretical molar ratio of N resulted in - an increase in the TiO_2 surface area - Band gap narrowed to 2.05 eV[51]

Doping technique	Parameters	Effect on structural and electronic properties
Hydrothermal synthesis of N doped TiO_2 powders using N sources such as triethanol amine	- Amount of TiO_2 powder, triethanol amine - Duration of ultrasound irradiation of 15 min - Annealing conditions inside the autoclave of 140 ^oC for 24 h - Washing resultant product with DI-water and absolute ethanol several times - Drying conditions of the powder at 200 ^oC in air for 10 h	- N found to substitute for Ti as O-N-O, but N-Ti-O is also present (XPS) - N concentration to be as high as 21% (molar ratio), $Ti_{1-y}O_{2-x}N_{x+y}$ where x=0.36, y=0.27 to give $Ti_{0.73}O_{1.64}N_{0.63}$ - Increased photocatalytic activity observed with the nitrogen doping of TiO_2[52]
Solvothermal synthesis of TiO_2 using the ethylenediamine N source	- Amount and concentration of tetrabutyl orthotitanate, ethanol, acetic acid, ethylenediamine, DI-water - Stirring and ageing time of solution mixtures - Annealing conditions in the autoclave of 120 ^oC for 20 h - Washing of resultant powder with water and ethanol several times - Drying temperature of 80 ^oC - Annealing conditions of 450 ^oC for 3 h in air	- TiO_2 powder with a N: Ti molar ratio of 1.0 gave the highest photoactivity - Formation of Ti^{3+} observed with N doped TiO_2 (EPR spectroscopy), - which is suggested to have a key role in the observed enhancement in the visible light absorption (UV-vis)[53]

Table 2 Dry and wet processes reported for sulphur doping of Titania

Doping technique	Parameters	Effect on structural and electronic properties
DRY PROCESSESS		
Oxidative annealing of TiS_2 powder	- Annealing conditions of 300 ^oC or 500 ^oC for 5 h in air - Heating rate not mentioned	- Substitutionally occupied S found in S doped TiO_2 and existed as Ti-S bonds, - which shifted the absorption edge to lower energy - Band gap narrowing observed caused by S 3p states mixing with the valence band, which resulted in an increase in the width of the valence band (ab initio calculations)[54]
WET PROCESSESS		
Atmospheric pressure chemical vapour deposition (APCVD) using carbon disulphide as the S source	- Custom built CVD reactor was used - Temperature and flow rate of the pre-treated nitrogen carrier gas for $TiCl_4$ were 150 ^oC and 0.5 L min^{-1} - Cleaning protocol for preparing the glass substrate being used involving water, acetone, petroleum ether and propan-2-ol - Substrate heating temperature rate of 10 ^oC min^{-1} to reach 500 ^oC for <45 min - Bubblers heated to 70 ^oC and 40 ^oC for a molar mass flow ratio of 1:2	- Sulphur doped thin films achieved with APCVD for the first time - <0.19 atomic% of S observed to be incorporated into the lattice (XPS), - as a cation S^{6+} potentially replacing the lattice Ti^{4+} ions - S oxidation potentially happened during the deposition causing an increase in the S oxidation state from (2-) to (6+) (XPS) - Compared to the industrial products Activ and BIOCLEAN, the films made had superior photoactivity and photo-induced superhydrophilicity, where - the latter is potentially caused by the red-shift of the band onset towards the visible light region[55]

Doping technique	Parameters	Effect on structural and electronic properties
Dip coating of a glass substrate using a sol-gel TiO_2 mixture, which also contains a S source such as sulphuric acid	- Tween80, isopropyl alcohol (iPrOH), Titanium (IV) isopropoxide (TTIP) used as precursors for the sol-gel - Molar ratio of Tween80: i-PrOH: TTIP: sulphuric acid of 1:45:1:1 - Stirring time of the precursor mixture as 24 h	- S incorporated into the TiO_2 as S^{2-}, replacing the lattice O^{2-} anions and as $S^{6+/\ 4+}$ and not as cations but as sulphate groups (XPS, EDX, FT-IR) - Significant shift of the optical absorption to the visible light region - Calcination parameters of 350 ^{o}C for 2 h gave the highest S incorporation, porosity, surface area and pore volume and the smallest crystallite size and a smooth uniform surface[56]

Table 3 Dry and wet processes reported for carbon doping of titania

Doping technique	Parameters	Effect on structural and electronic properties
DRY PROCESSESS		
Oxidative annealing of TiC powder	- Initial oxidation conditions at 350 ^{o}C for 36 h in air - Annealing conditions under O_2 flow at 600 ^{o}C for 5 h	- C doped into TiO_2 in the Anatase phase - C substituted into O lattice sites, - which caused the absorption edge to be shifted to higher wavelengths - Band gap narrowing is recorded, and the valence band appeared to shift upwards to the negative potential on the band diagram - Suggested further work focussing on the best C content for the application[57]
WET PROCESSESS		
Electrochemical anodizing conditions to incorporate C as a dopant	- Choice and concentration of electrolytes - Anodising conditions: potential ramp from 0 V to 15 eV at 1 V s^{-1} and maintaining the desired potential at different times in 1 M $(NH_4)H_2PO_4$ + 0.5 wt % NH_4F - Resulting powder annealed at 450 ^{o}C for 1 h	- Decreased the band gap by the incorporation of C into TiO_2 nanoarrays - Controlled the morphology by control on the aspect ratios to optimise photoactivity[58]
Hydrothermal synthesis using a C source such as Glucose	- Amount and concentration of Titanium isopropoxide in ethanol, aqueous potassium chloride - Stirring ang ageing time of the precursor mixtures, of 10 min for 24 h respectively	-C doped TiO_2 had a larger surface area, - which gave absorption in the visible light region, greater than that recorded in P25 and undoped TiO_2 - Suggested the potential of the carbon doped TiO_2 synthesised for industrial production of a visible light photocatalytic material[59]

Doping technique	Parameters	Effect on structural and electronic properties
	- Amount of TiO_2 powders (synthesised) and glucose - Autoclave conditions of 160 ^oC for 12 h - Drying temperature of resultant powders, of 60 ^oC	
Sol-gel synthesis where the C source is from a Resorcinol-Formaldehyde condensation	- Amount and concentration of Titanium tetraisopropoxide, 1, 3-dihyroxy benzene and formaldehyde, isopropanol - Annealing conditions of 350 ± 5 ^oC for 3 h	- C doped into the lattice and existed as Ti-C (XRD) - Red shift in the optical absorption edge, resulting in band gap narrowing - C doped TiO_2 reported to have excellent photoactivity[60]
Single source chemical vapour deposition using $Ti(OC_4H_9)4$ as the C source, also used as the Ti and O source	- Amount and concentration of hydrochloric acid, distilled water - Vacuum drying at 40 ^oC - Distance between the Ti plates and C source of 10 cm - Ultrapure Ar flow rate of 200 sccm for 4 h - A predetermined temperature was maintained for 2 h - Annealing conditions of 500 ^oC for 1 h	- C doped TiO_2 microspheres with pore sizes ranging from 100 nm to several micrometres in diameter, - which is reported to be controlled using the flow rate of the carrier gas - high photoactivity in the visible light region is reported - Band gap narrowing observed after carbon doping: 2.78 eV for microspheres and 2.72 eV for nanotubes[61]

Table 4 Dry and wet processes reported for boron doping of titania

Doping technique	Parameters	Effect on structural and electronic properties
DRY PROCESSESS		
Reactive Magnetic Sputtering	- Distance between substrate holder and targets of 100 mm - Base pressure of 4.0 × 10-5 Pa maximum - Substrate temperature of 100 ^{o}C - 99.9% Ti and TiB_2 metal targets - Varying target powers of 30, 60, 90, 120, 150, 180 W - Ar/ O_2 plasma - Ar gas flow rate of 20 sccm - O_2 gas flow rate of 8 sccm - Sputtering time with Ar plasma of 10 min	- Observed B incorporation into TiO_2 as BO_3 and Ti_2BO_2 - which resulted in a red-shift of the absorption edge - Although B_2O_3 was also present on the surface of the films, most of this composition evaporated during the annealing process, but resulted in the nonporous structure of the surface - This surface structure improved the photocatalytic activity in the UV range[62]
WET PROCESSESS		
Sol-gel synthesis using B containing precursor such as H_3BO_3	- Amount of titanium tetra-n-butyl oxide and DI-water - Stirring time of precursor solutions for 12 h - Drying conditions of the precursor solutions at 100 ^{o}C for 8 h in air - Annealing time in air of 1 h at high temperature (not mentioned)	- Doped boron was observed as B^{3+}, incorporated into the interstitial sites of the TiO_2 lattice, as Ti-O-B - Suggested the formation of a layer of diboron trioxide phase on the surface of the TiO_2 particles, at a certain temperature and B concentration. The diboron trioxide is formed from the B that came out of the total amount of B that was incorporated into the Anatase-TiO_2 lattice - This layer was suggested to prevent the diffusion between TiO_2 particles, resulting in reducing their ability to act as surface nucleation sites for Rutile - B doped TiO_2 annealed at 500 ^{o}C gave the best photocatalytic activity under UV irradiation, which resulted from the UV range

Doping technique	Parameters	Effect on structural and electronic properties
		intense absorption and due to the quantization effect - B: Ti molar ratio of 5% gave the best photocatalytic activity[63]
Microwave-assisted synthesis using B containing precursor such as boric acid	- Amount of titanium tetraisopropoxide (TTIP), benzyl alcohol, boric acid, oleic acid (OA) - Ratio of TTIP: OA ratios - Stirring time of the precursor mixture of 45 min - Reaction temperature and time of 210 ^{o}C for 45 min	-The doping procedure involving the use of the OA allowed to control Anatase nanorod morphology formation - Nanorod size and aspect ratio controlled using the amount of B source precursor and OA - Increased photocatalytic activity was observed in the B doped TiO_2 with increasing surface areas, lower XRD aspect ratios, higher TEM aspect ratios, smaller nanocrystalline domains indicated by the lower Raman shift of the E_g band[64]
Atmospheric pressure-plasma enhanced chemical vapour deposition	- Concentration of titanium ethoxide diluted in hexane of 0.5M - Precursor flow rate of 10 $\mu mL min^{-1}$ - Precursor droplet diameter ranging between 10 μm and 20 μm - Droplet carrier gases Ar and O_2 with a flowrate of 0.9 and 1 $L min^{-1}$ respectively - Amount of boron isopropoxide - Deposition time of B-TiO_2 films on polymer substrates 10 mins	- B doping of TiO_2 gave higher photocatalytic dye degradation rates - However, the optical properties remained the same - Suggested more work to be done with controlling the exact amount of B dopant incorporated into the TiO_2 lattice, by modifying the parameters involved in the doping process[65]

Doping technique	Parameters	Effect on structural and electronic properties
Hydrothermal synthesis using a B source such as Boric acid	- Amount and concentration of n-tetrabutyl titanate in a solution of boric acid - Amount of DI-water - Temperature at which the titanate solution was added dropwise to boric acid, was 80 ^{o}C - Synthesis conditions of 220 ^{o}C for 36 h - Drying conditions of the resultant powder of 450 ^{o}C for 15 h, 5 ^{o}C min^{-1}	- The photocatalytic degradation rate constant of the B doped TiO_2 was two times that of the undoped powders - The average crystallite size remained the same at 20-50 nm (XRD, TEM, SEM) - B species was incorporated as B_2O_3 (or H_3BO_3) indicated by the XPS peak at 193.1 eV. Also, since the peak at 192.2 eV is neither the B-O bond nor the Ti-B bond, it was suggested to be a B-O-Ti bond - O1s XPS peak are is indicative of chemical environments, Ti-O (530.6 eV) and O-H (532.6 eV), which were also present in the undoped samples, but also B-O (533.75 eV), which appeared after B incorporation[66]

1.2.6.1 Nitrogen Doping

Titania can be doped with nitrogen to make it optically active in the visible light region[67]. There are several defect formation mechanisms reported in the literature that the incorporation of nitrogen into the titania lattice can result in.

1. Since the N^{3-} and O^{2-} has similar ionic radius, nitrogen can be doped substitutionally into a vacant oxygen lattice, $V_o^{\bullet\bullet}$, resulting in $N_o^{'}$. Therefore, some nitrogen doping procedures involve an initial reduction step, which encourages $V_o^{\bullet\bullet}$ formation. The nitrogen incorporated titania lattice can achieve charge neutrality by having two $V_o^{\bullet\bullet}$ for every nitrogen substituted into the oxygen lattice site[68].

2. Nitrogen can also be incorporated at interstitial sites, $N_i^{'''}$, where charge neutrality can be achieved from the formation of $Ti_i^{\bullet\bullet\bullet}$ species.[69,70]

The defect equilibrium can help to understand diffusion behaviours (as discussed in Section 1.2.5); moreover, it can influence the electronic structure in titania[71,72]. The lattice Ti^{4+} are seen to be reduced to Ti^{3+}, due to the presence of a large concentration of $V_o^{\bullet\bullet}$ formed from nitrogen incorporation and associated surface reconstructions. These Ti^{3+} species accommodate themselves into an interstitial site, $Ti_i^{\bullet\bullet\bullet}$ or a substitutional site, $Ti_{Ti}^{'}$[73]. This explains the Ti 3d states observed near the Fermi level in the electronic structure of titania upon nitrogen doping. It has been reported that the Ti 3d states is suppressed in titania, which was nitrogen doped using ion implantation, as per Ultra-Violet Photoelectron Spectroscopy (UPS) data. This suggested that the electrons from the $V_o^{\bullet\bullet}$ creation were filled into the N 2p states located at the top of the VB than into the Ti 3d states in the CB[74]. On the other hand, the $N_i^{'''}$ dopants associated with the band gap narrowing were suggested to be due to the introduction of N-O localised states with a π* character above the VB. With regards to the optical absorption across the band gap, the N_o 2pπ to Ti dxy transition is expected to be more dominant than the N_i-Nπ* to Ti dxy transition[75]. Some reports suggest that the $N_i^{'''}$ dopants are possible sites for trapping photogenerated h^+, leading to less oxidation of the adsorbed surface species on titania[76]. Computational studies suggest that other reactive sites for recombination are potential bonding states below O 2p and anti-bonding states deep within the band gap[77].

The concentration of nitrogen dopant is another factor that is found to influence the electronic structure of titania[78]. The electron concentration in the bulk can be seen to be increased with doping nitrogen heavily into the titania lattice. This is predominantly due to the nitrogen reducing the formation energy of the $V_o^{\bullet\bullet}$. Consequently, the fermi level is shifted from being in the band gap to above the conduction band minimum. Processes such as vacuum annealing, thermal treatment and sputtering can also increase the electron concentration in the bulk. This is through the creation of Ti^{3+} species and therefore, the charge neutrality of the lattice is achieved due to the $V_o^{\bullet\bullet}$ creation[79]. It is reasonable to expect a greater optical shift to the visible region with greater nitrogen dopant concentration[80]. However, reports suggest that this is not necessarily always the case; for instance, the electron-hole recombination rates are seen to become faster with increasing nitrogen content[81]. Although more N 2p states were occupied with greater nitrogen concentration, only a small shift in the absorption band edge was observed, suggesting that $N_o^{'}$ only made a small contribution towards band gap narrowing[82]. Another study reported that low nitrogen dopant levels (~1.2 atomic%) were associated with localised N 2p states above the VB and high dopant levels (~4.2 atomic%) with N2p-O2p mixing[**75**]. These nitrogen dopants have been described in another investigation as diamagnetic and paramagnetic bulk impurity centres to explain what happens upon visible light irradiation. Their findings suggested that upon bulk reduction, a reversible electron transfer from the Ti^{3+} ions to the nitrogen in the bulk (N_b) forms Ti^{4+} ions. Thus, the N_b significantly reduces the formation energy of $V_o^{\bullet\bullet}$. Upon irradiation (437 nm), these N_b species get excited and either get irreversibly transferred into the delocalised CB states or reacts with the surface adsorbed oxygen species (Figure 4). The amount of oxygen radicals that form as a result corresponds to the difference between the amount of N_b at the start and end of the reaction. This reinforces the explanation that the electrons are excited from the N_b states that lie at least 0.1 eV above the VB of titania. The bulk N_b are thought to be photoactive centres in nitrogen doped Anatase, synthesised using sol-gel method. It is quite possible that this explanation is valid for systems prepared using other methods, however, the reverse explanation is also possible[83].

The technique and conditions used for nitrogen doping in titania is known to influence the type of lattice defect that is formed and consequently the electronic state. Anion rich conditions led to the formation of $Ti_i^{\bullet\bullet\bullet}$ from Ti indiffusion during the growth of epitaxial Rutile (110) films on Al_2O_3 (0001) substrates, using plasma assisted molecular beam epitaxy. This was accompanied by the observation of hybridised Ti-

N states on the top of the VB, causing a shift of the optical absorption into the visible light region[84]. As per the study involving the use of a wet colloidal synthesis technique, which reports N dopant concentrations of 2 to 17 atomic%, the location of a N dopant incorporated into the titania lattice can be controlled using the type of amine used as the nitrogen precursor[85]. The reduction in the band gap, by 0.6 eV, observed in nitrogen doped Rutile (with 0.6 atomic% of N) annealed under NH_3 (g) was suggested to be due to $N_i^{'''}$ bound to hydrogen, in disagreement with assignments in other reports. Upon doping, the Rutile single crystal substrate changed colour from yellow to blue, indicating the reduction of titania, caused by the molecular H_2 evolved from the decomposition of the NH_3 on the titania surface[47].

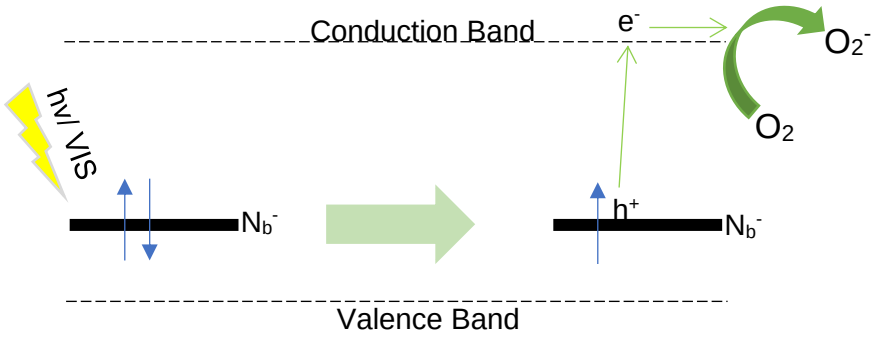

Figure 4 Processes proceeding visible light irradiation upon N_b containing titania. Adapted from reference 64

A visible light optical response was reported for the first time with titania synthesised using a wet chemical method and had an unintentional NO_x impurity[86], as per XPS data. This initiated the interest into nitrogen doping of titania and the proceeding trail of research. The NO_x impurity was observed to be volatile at annealing temperatures of 600 ^oC and was only observed at 400 ^oC. This led to more research into the effect of nitrogen incorporation into titania using different synthesis techniques, which can be categorised into dry or wet processes (Table 1, 2, 3, 4). While some synthesis involves the addition of the nitrogen precursors at the titania pre-treatment stage[87], other synthesis techniques adds the nitrogen precursors at the titania post-treatment[88] stage. The associated parameters in all these techniques were found to influence the defect states and their equilibria, which are suggested to have a correlation with their photocatalytic behaviours.

An understanding of the diffusion of $N_o^{'}$ and $N_i^{'''}$ in the titania lattice are necessary to identify ways of gaining control over dopant distributions and behaviours on an atomic and molecular level. The oxidative annealing investigations on nitrogen doped rutile

(110) single crystal substrates reveal that the $N_o^{'}$ species is more surface confined and diffuses to the surface and into the gas phase with a small diffusion coefficient of 9.50×10^{-9} $\mu m^2 s^{-1}$. On the other hand, the $N_i^{'''}$ species is suggested to be less surface confined as suggested by its larger diffusion coefficient of its asymmetric diffusion into the titania bulk. These findings suggest that the oxidative annealing process triggers the formation of disorder on the titania surface and therefore, the two diffusion coefficients may correspond to the fast grain boundary diffusion and the slow volume diffusion[89].

The variation in the concentration of nitrogen species across the thickness of the titania substrate is important to study, focussing on both the surface and the bulk. This is because the physical properties of materials are generally governed by the bulk whilst the surface composition is also equally important since photocatalysis is a surface process. In the nitrogen doped Rutile (110) thin films deposited on Al_2O_3 (0001) substrate, which were synthesised using N,N,N',N'-Tetramethylethylenediamine (TMEDA) and NH_3 (g) nitrogen sources, the N dopants migrated from the bulk to the surface upon annealing. Moreover, the nitrogen concentration reduced by 90% after depth profiling, suggesting that the nitrogen distribution across the depth of the substrate is an important aspect that determines functionality[90].

The morphology and topography of nitrogen doped titania surfaces are significant for applications. The epitaxial films of nitrogen doped anatase (001), synthesised using plasma assisted molecular beam epitaxy, followed a columnar growth fashion with small angle grain boundaries and had a rough surface. The poor morphology observed was explained to be due to the presence of twins in the $LaAl_2O_3$ (001) substrates used and the report suggests the use of $SrTiO_3$ (001) instead with lower growth temperatures as they can give a better morphology and higher nitrogen concentration[91].

The prospects of $N_o^{'}$ incorporation without the Ti^{4+} reduction has been investigated but remains a challenge due to the unavoidable surface reconstruction that occurs upon annealing of titania as part of the nitrogen doping process[92].

1.2.6.2 Sulphur Doping

Unlike nitrogen, the sulphur atom can be doped substitutionally into either the cationic or anionic sites of titania. The use of titanium rich conditions favours anionic substitution, where the lattice O^{2-} is replaced with the much larger S^{2-}, leading to lattice distortion. On the other hand, having oxygen rich conditions encourages cationic substitution, where lattice Ti^{4+} is replaced with either S^{4+} or S^{6+}, to give S_{Ti}^{x} and $S_{Ti}^{\bullet\bullet}$. The charge neutrality on the surface and the bulk du S^{6+} substitution of lattice Ti^{4+} is achieved the formation of SO_4^{2-} ions and S-Ti-O bonds respectively[93]. Like what is observed with nitrogen doping, the chemical environment of the sulphur species incorporated into titania can be controlled using the choice of precursors and the experimental conditions employed. For example, TiS_2 precursors can give anionic doping[94] predominantly, while thiourea precursors can yield cationic doping[95]. Sulphur doping is also reported to increase the surface area of titania, increasing its active sites, resulting in enhanced photoactivity[93].

The incorporation of the sulphur dopant species can have several effects on the electronic structure of titania. Firstly, the mixing of the newly formed S 3p states increases the width of the VB, as found in oxidatively annealed TiS_2 powder[94]. Increased band gap narrowing was also suggested to be observed with increasing the concentration of these sulphur dopants[96]. However, the sulphur sites have also been reported to encourage photogenerated hole trapping in titania, which was doped using a solution-based method involving thiourea[95]. This can diminish the oxidising power of these holes, making it not ideal for photocatalytic reactions. Secondly, the oxygen atom in the Ti-O-S bond, formed upon sulphur incorporation into titania, becomes an electron deficient centre, preventing the recombination of photogenerated charge carriers. Thirdly, the empty s and p orbitals of the S^{6+} ions incorporated into the titania lattice allow shallow trapping of the photogenerated electrons and released them onto the adsorbed oxygen molecules on the titania surface to attain its originally empty and stable state. This can prolong the lifetime of the photogenerated charge carriers. Lastly, these S^{6+} ions cause the formation of Ti-O-S surface states below the CB, which extends the optical response to the visible light region.

1.2.6.3 Carbon Doping

Carbon doping into the titania lattice is not as widely studied as nitrogen or sulphur doping. This is predominantly due to the synthesis technique itself, which usually require multiple processes and expensive reagents[97].

The incorporation of carbon into titania result in structural changes. With oxygen poor conditions and low carbon concentrations, $V_o^{\bullet\bullet}$ and $C_o^{"}$ are favoured. On the other hand, oxygen rich conditions favour $C_o^{"}$ and $C_i^{""}$; however, $C_i^{""}$ formation is only a possibility since carbon is usually more covalent than ionic. The type of carbon species doped into the titania lattice can be controlled by the synthesis technique employed. However, both interstitial and substitutional carbon species are reported to be achieved with the magnetron sputtering technique employing CO_2 as the carbon source. These carbon species cause narrowing of the band gap to as low as 2.02 eV and can prolong the lifetime of the photogenerated charge carriers[98]. Computational studies report that carbon doping introduces occupied C 2p states above the VB as well as unoccupied states within the band gap of titania[99].

1.2.6.4 Boron Doping

The visible light activity and the improved UV light activity observed in boron doped titania has been of research interest. However, boron doping is not as widely studied as nitrogen.

The literature reports suggestions about the bonding of boron as a dopant in the titania lattice. Boron was found to be incorporated into the interstitial as well as substitutional sites of the titania lattice, as $B_o^{'}$ and $B_i^{'''}$ [100]. Substitutionally doped boron species incorporated into titania films, synthesised using Atmospheric Pressure Chemical Vapour Deposition, have been observed to cause structural changes such as unit cell contraction[101]. From electron microscopy images, it was deduced that substitutional boron was doped into titania as local defect clusters. These clusters were modelled to understand that the boron atom is in a 3-fold coordination to three oxygen atoms, making up one of the phases of an empty octahedron. These BO_3 triangles form line defects along the (100) plane of titania. These defects are also observed to be agglomerated, forming extended structures consisting of ordered unit cell intergrowth consisting of planar TiO_2 and calcite-type $TiBO_3$ parallel to the rutile (101) plane. The reports conducted prior to these findings suggested that the boron could be located at an interstitial site in a tetrahedral coordination, but there was no structural evidence

to support this[102]. The lattice parameters calculated indicated that the boron is present at an interstitial site as B^{3+}, in a Ti-O-B chemical environment[63].

The doping of boron has resulted in changes to the microstructure, plane orientation and phase of titania. The crystal growth inhibition was observed along with the increase in surface area, in boron doped titania nanopowders. The surface of the rutile (200), (211) and (220) planes were observed to be increasingly textured upon boron doping. The degree of orientation of the (101) plane in nanocrystalline rutile was found to be increased upon boron doping[101]. A similar effect was also observed with the (110) plane, which is known to be the most active reductive site for photocatalytic surface reactions. A progressive transformation from anatase to rutile is observed upon increasing the doping levels of boron[103].

The creation of anionic defects from introducing boron dopants into titania affects the stoichiometric composition of the lattice. The boron doping itself requires a partial reduction of the lattice Ti^{4+} to Ti^{3+}, which results in a $3Ti'_{Ti} + B_i^{\bullet\bullet}$ lattice. In the presence of boron, the rutile lattice is stabilised to two orders of magnitude lower than that of the undoped rutile lattice. The concentration of boron incorporated into the titania lattice is seen to be inversely proportional to the oxygen fugacity, fO_2. The largest boron concentration of 0.33 wt% is observed at the lower fO_2 phase boundary. The literature also reports boron doped titania, where no evidence for Ti^{4+} reduction is observed. However, phonon confinement effects and oxygen deficiencies are indicative from the blue shift observed in their Raman spectra, which resulted from cell volume expansion due to the incorporation of both substitutional and interstitial boron dopant species[101]. In the boron doped titania synthesised using a solution-based method employing BH_3 as the boron source, ~1.13 atomic% boron was present in different chemical environments. The enhancement in the photoactivity resulted from the substitutionally occupied boron species that was suggested to be the “active” boron and not from the boron oxide like species which was suggested to be the “inactive” boron[104].

1.3 Doping Titanates – The Concept

The importance that the concept of doping titanates pose is explored by discussing the crystal structure of layered titanate structures.

1.3.1 Rationale of Structure Choice

It remains a challenge to diffuse dopants into the bulk of powdered forms of titania as powders do not have a well-defined surface or a bulk as supposed to a single crystal substrate. While these substrates can serve as ideal models to study photocatalytic characteristics in powders, it is also important to study powders, which yield high photocatalytic efficiencies from their inherently high surface area that a single crystal substrate do not possess. This is where titan**ates** are suitable models for achieving dopant diffusion into the bulk of powders, due to similar reasons that make titanates ideal for use in electrode materials. The layered framework with the interlayer galleries of the titanates[105] make it easier for dopants to get access to the bulk structure as well as the surface structure compared to the non-layered titania framework. The titanate and titania structure is composed of edge sharing and corner sharing TiO_6 units, linked together to form three dimensional structures. Since the brookite and rutile structures are rich in corner sharing TiO_6 units than edge sharing TiO_6 units[106], it can be said that the titanate structure is more anatase-like (Figure 5).

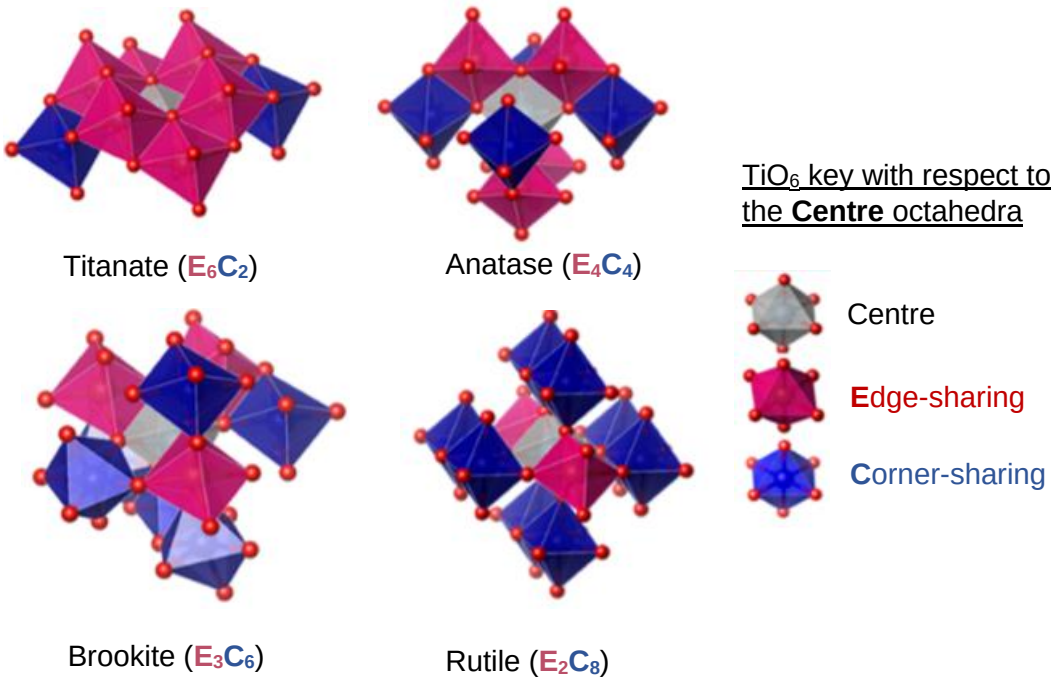

Figure 5 The TiO_6 connectivity in titanates and titania polymorphs where E_x and C_y denote the number of edge-sharing and corner-sharing units respectively. These representations are from Reference 108

1.3.2 Choice of Titanate Structures

A typical alkali metal, layered titanate has a framework consisting of puckered TiO_2-anatase like layers and have a monoclinic structure with the general formula $A_2Ti_nO_{2n+1}$, where the b parameter corresponds to the magnitude of the repeating units between the layers[107]. Structures with small n values of 2,3 or 4 gives an open layered structure with a stepped feature e.g. $Na_2Ti_3O_7$ (Figure 6), which can be explored for intercalation and is reported to be used for cation exchange reactions and catalysis[108]. Although $Cs_{0.68}Ti_{1.825}O_4$ does not follow this formula it also gives an open layered structure[109] but not a stepped structure as is the case with $Na_2Ti_3O_7$. On the contrary, structures with large n values of 6, 7 or 8 results in a tunnelled structure e.g. $Na_2Ti_6O_{13}$ and $K_2Ti_6O_{13}$ [108] (Figure 7), which are reported to have high chemical stability, are insulating and has good mechanical properties[110].

The connectivity of the TiO_6 units in an open layered structure is different to that in a tunnelled structure. The TiO_6 layers in the open layered $Cs_{0.68}Ti_{1.825}O_4$ (Figure 6a) has ridges and troughs consisting of anions in 2 co-ordination and 4 co-ordination respectively[111]. However, in the open layered $Na_2Ti_3O_7$ (Figure 6b), the edge sharing, distorted TiO_6 units are connected to each other to form $(Ti_3O_7)^{2-}$ layers, which make up each of the steps in the structure. These $(Ti_3O_7)^{2-}$ layers are linked to the positively charged sodium cations located in two main crystallographic sites within the structure[112]. The $Na_2Ti_6O_{13}$ tunnelled structure is also made up of steps consisting of three TiO_6 edge-sharing distorted octahedra units[113] (Figure 7b). However, unlike in $Na_2Ti_3O_7$, all the terminal corners of these steps are shared to form a tunnel, where a row of interstitial atomic positions and sodium ions lie[114]. This tunnelled framework is reported to be stable enough to accommodate for any structural changes because of doping[113]. The tunnelled $K_2Ti_6O_{13}$ structure (Figure 7a) also consist of three distorted TiO_6 octahedra. However, in its TiO_6 units, the Ti is positioned slightly off the centre of the octahedron to be in the direction facing the opposite sites where the nearest Ti neighbour is positioned. This TiO_6 unit is repeated in a zig-zag pattern along the b-axis and the potassium atoms are positioned in the void space inside the tunnels of this structure[115].

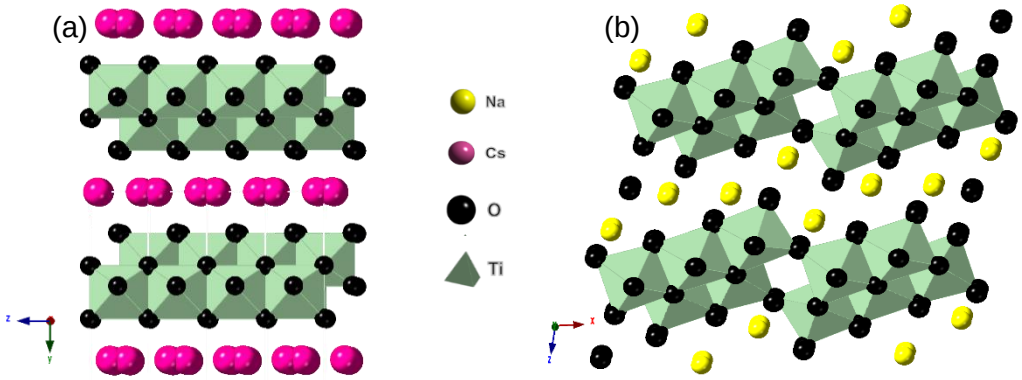

Figure 6 Open layered framework of (a) $Cs_{0.68}Ti_{1.825}O_4$ and (b) $Na_2Ti_3O_7$

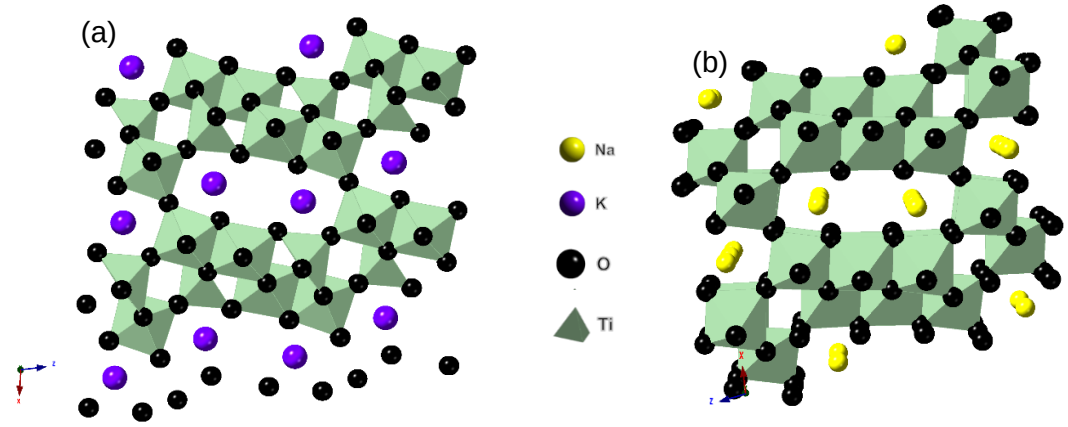

Figure 7 Tunnelled structure of (a) $K_2Ti_6O_{13}$ and (b) $Na_2Ti_6O_{13}$

1.3.3 Choice of Titanate Synthesis

Titanate frameworks such as sodium trititanate and sodium hexatitanate have been reported to be synthesised using several techniques[116]. The high temperature solid state synthesis involves annealing stoichiometric quantities of Titania and sodium carbonate or sodium oxide. On the other hand, the hydrothermal synthesis involves the use of sodium hydroxide while sol-gel synthesis uses alkoxide precursors. Using a high sintering temperature for sol-gel synthesis is found to result in the sodium hexatitanate phase, while lower temperatures are observed to give the sodium trititanate phase[117]. The rhodium doped barium titanates synthesised using hydrothermal synthesis were found to have higher photoactivity than that synthesised using the conventional high temperature synthesis. Hydrothermal synthesis allows the possibility of controlling the titanate characteristics using various permutations and combinations of several parameters such as precursor ratios and post-annealing conditions[118]. However, solid-state synthesis is chosen for the investigation carried out on doping titanates, which is reported in Chapter 8 of this thesis. This is because

of the facile nature of this technique, which has minimal parameters and therefore, increases the reproducibility of the samples prepared.

1.3.4 Doping Effects on Titanate Properties

In semiconductors, each structural and spatial arrangement of dopants have been suggested to make different modifications to the electronic structure, optical absorption, redox potential and photogenerated charge carrier mobility. There are several reports in the literature on inhomogeneous nitrogen doping in titania, introducing localised states in the intrinsic band gap[119]. Therefore, it is important to fully characterise nitrogen doped layered titanates, which the existing literature has not done, so that the relationship between the dopant bonding, dopant arrangement in the lattice and the functionality can be better understood in titania. Although layered titanate frameworks can theoretically induce homogeneous doping, it remains a challenge to characterise this aspect to prove that this is the case. There exists a literature report that uses XPS data to claim that nitrogen was homogeneously doped into caesium titanate powders[120]. This claim is mostly not valid since etching powders using XPS is not very reliable or reproducible. The reason for this is because powders do not possess a well-defined surface/ bulk compared to a single crystal substrate and this was the motivation for investigating the diffusion of dopants into substrates, which is reported in Chapters 3, 4, 5, 6 and 7 of this thesis. The literature reports the synthesis of a titanium electrode possessing gradient surface layers with the composition of nitrogen doped titanates[121]. Prior to annealing, the nitrogen concentration was measured to be increasing with increasing depth into the electrode, with the lowest nitrogen concentration on the surface. Upon increasing the annealing temperature to 800 ^{o}C, the surface concentration of nitrogen was seen to be increased while that of oxygen and hydrogen was observed to be decreased. The same nitrogen diffusion behaviour is observed with the oxidative annealing of nitrogen doped single crystal substrates of titania-rutile, suggesting that titania is a possible model for studying titanates and vice-versa.

The chemical nature of the dopant species incorporated into the titanate and the morphology of the host lattice is observed to vary with the synthesis technique used for doping. Plasma based methods were found to achieve 20 atomic% of nitrogen dopant loading, while keeping the titanate crystal structure and tubular morphology intact. Nitrogen can be doped into the substitutional sites of the titanate lattice using N_2^+ bombardment and plasma-based methods involving NH_3. These titanate samples

were also observed to have the presence of surface bound NH_4^+ species, which was also present in titanates synthesised using thermal methods[122]. Ammonolysis is a facile and popular technique used for doping nitrogen into materials and involves annealing the chosen material under a dynamic flow of ammonia gas[89]. The annealing temperature, time, ammonia gas flow rate and oxygen partial pressure inside this set-up are the potential factors that influence the chemical nature and concentration of the nitrogen incorporated into the samples. The likelihood of leaks in this reaction set-up is inevitable and therefore, will let oxygen into the system, making it challenging to reproduce the same ammonia flow rate for every experiment carried out, for example, for a study investigating the effect of doping temperature. This is the motivation behind designing a modification to the ammonolysis reaction set-up in Chapter 8, for synthesising nitrogen doped layered titanate frameworks with the same ammonia flow rate, for studying the effect of doping temperature on the crystal structure, optical absorption and electronic properties.

Employing different nitrogen dopant concentrations can result in different modifications to the titanate electronic structure. Nitrogen concentrations in $Cs_{0.68}Ti_{1.83}O_{4-x}N_x$ where x=0 to 0.31 has been reported to help shift the absorption edge to the visible light region. Moreover, this shift is observed to be proportional with the concentration of nitrogen dopant incorporated into the substitutional sites of the lattice. Although, this increase is not seen to correspond to the material having a higher oxidation potential, the narrowing of the band gap is observed, which is suggested to be due to the upshift of the valence band minimum from the mixing of the O2p-N2p states. The molar ratio of the Cs^+ and Ti^{4+} is observed to decrease by 11.7%, with the incorporation of nitrogen. The loss of the Cs^+ is seen to have a negligible effect on the titanate CB, which consists of Ti 3d and O 2p states. It has also been reported that the OH radicals taking part in photo-oxidation reactions are suggested to originate from the photogenerated holes than the photogenerated electrons in this nitrogen doped caesium titanate[123].

The chemical nature of the dopant within the titanate host lattice also varies with the choice of dopant ion used. Boron is another anionic dopant that has been studied and found to be incorporated into the interstitial sites of the titanate lattice, in Ti-O-B co-ordination. This boron doping has transformed the titanate morphology from being tubular to rod-like nanostructures. It was also observed that a small proportion of the boron caused the formation of boron titanates via an ion exchange reaction. Additionally, a phase transformation from trititanate to anatase was also observed[124].

The literature also reports the study on cationic dopants such as rhodium into barium titanate nanocrystals. It was found that the suppressing of the barium defect formation during the synthesis has helped to improve the crystallinity and resulted in high photocatalytic activity. The compositional homogeneity achieved was also suggested to contribute towards the photoactivity observed[125].

1.4 Doping $MgSiN_2$ – The Concept

The concept of doping in $MgSiN_2$ is discussed below in terms of its crystal structure and in the context of its application.

1.4.1 Choice of Material

There is an ongoing interest in the development of integrated circuits of decreasing size in the electronic industry. This suggests the need for substrate materials that have improved thermal conductivity and minimal dissipation of heat. AlN is a promising material for this purpose, however, it is expensive. Thus, interest grew into the study of ternary compounds based on AlN. A suitable alternative compound for AlN that has been reported in the literature is $MgSiN_2$, where two of the Al^{3+} is replaced by a combination of Si^{4+} and Mg^{2+} [126]. $MgSiN_2$ is known to have good fracture toughness, high electric resistance, strength and hardness. Both $MgSiN_2$ and AlN has an orthorhombic crystal structure[127].

1.4.2 $MgSiN_2$ Synthesis

The literature reports the challenge of preparing phase pure $MgSiN_2$ powders using one-step synthesis techniques. The magnesium content in the reaction mixture is often observed to be evaporated off easily, as reported in the direct nitridation of Si/ Mg or of binary nitrides as well as in combustion reactions. Therefore, the magnesium content used in these reactions is usually higher than the stoichiometric amounts. The impurity is then removed in an additional reaction step, which involves acid washing. The reaction mixture, for the direct nitridation synthesis, containing Mg, Si_3N_4 and N_2, using a 5 wt% or 10 wt% of magnesium in excess can react all the Si_3N_4 while some of magnesium reacts with N_2 to make Mg_3N_2. The final $MgSiN_2$ product is found to also have MgO, which comes from the oxidation of Mg_3N_2. The oxygen contamination is suggested to be from the starting materials, from any contamination that was picked up during the synthesis or mixing procedures or from the N_2 gas that was used. Decreasing the N_2 gas pressure from 5 MPa to 0.5 MPa has been shown to decrease

the combustion temperature. As a result, the amount of magnesium being lost from evaporation was also seen to be reduced, however not completely. It has been reported that HCl washing has helped to remove MgO impurity to leave $MgSiN_2$ as the sole product[127]. The literature shows that $MgSiN_2$ synthesised from magnesium, rather than Mg_2Si, results in less oxygen impurity. However, using Mg_2Si in large excess is also suggested to give a phase pure product. Having $Mg_2Si/Mg >= 3$ and $Si_3N_4/Si_{total} >= 0.5$ has been found to result in a single phase $MgSiN_2$ in an unsealed system. While the nitridation at low temperatures (< 1100 ^oC) can be accelerated by reducing the size of the Si particles to < 0.5 μm, the oxygen impurities can be reduced with the addition of CaF_2 and C to the reaction mixture at 2 wt% and 0.75 wt% respectively[128].

Although a two-step process has the potential to remove impurities in the $MgSiN_2$ synthesised, it can introduce more parameters into the study being investigation. Therefore, a facile one-step, high temperature solid-state synthesis was employed in Chapter 9 for keeping the number of associated parameters to a minimum. The amount of oxygen impurity in the final product was addressed by the addition of the magnesium reactant in excess.

The current literature does not present any investigations into the effect of doping $MgSiN_2$ with aluminium. This is significant to understand the point at which the $MgSiN_2$ structurally transforms into AlN. Therefore, the incorporation of aluminium into $MgSiN_2$ and the effect of different amounts of magnesium excess on the phase purity of aluminium doped $MgSiN_2$ was being investigated and reported in Chapter 9.

Chapter 2: Characterisation Techniques

This chapter discusses all the instruments used for the characterisation of the samples reported in this thesis.

2.1 X-ray Photoelectron Spectroscopy (XPS)

XPS is a technique used to analyse the chemical composition and electronic structure of materials, predominantly in the solid form.

2.1.1 XPS Spectrum Collection

First, a chosen sample is loaded into the analysis chamber of the XPS spectrometer. X-rays are then shone on the sample and this results in the ejection of core electrons from the sample with characteristic kinetic energies (K.E.). These photoelectrons then travel to the hemispherical analyser that have electrostatic fields, which allows photoelectrons of only a certain pass energy to reach the detector. The analyser measures the K.E and relative number of photoelectrons. The K.E. is then used to calculate the binding energy (B.E.) (Equation 6).

$$\text{B.E.} = E_{photon} - \text{K.E} - \Phi$$

Equation 6: Formula based on the photoelectric effect where B.E is dependent on the element present, the orbital where the ionisation occurred and the chemical state of the element. The work function, denoted as Φ, is a constant and is calibrated and differs for each spectrometer.

2.1.2 XPS Spectrometer

An overview of how the main parts of the XPS spectrometer functions to produce an XPS spectrum is detailed below.

1. **X-ray source**

Firstly, a tungsten filament is heated to produce high energy electrons, which are bombarded onto an Aluminium anode. This produces non-monochromatic X-rays, which have an energy that is dependent on the metal anode being used and intensity that is dependent on the energy of the bombarded electrons as well as the current with which these electrons are striking the anode. These X-rays are then monochromatized by diffracting and focussing them using a crystalline quartz of

(1010) orientation. This produces X-rays with a wavelength of 8.3386 Å (~1486.7 eV), which is the energy of the Al K-alpha X-ray radiation source used for the ionisation of elemental electrons of the sample being measured. The Bremsstrahlung radiation that is produced along with the Al K-alpha radiation can result in peak broadening in the XPS spectrum. By monochromatizing the X-rays, this undesirable radiation is also removed, increasing the energy resolution.

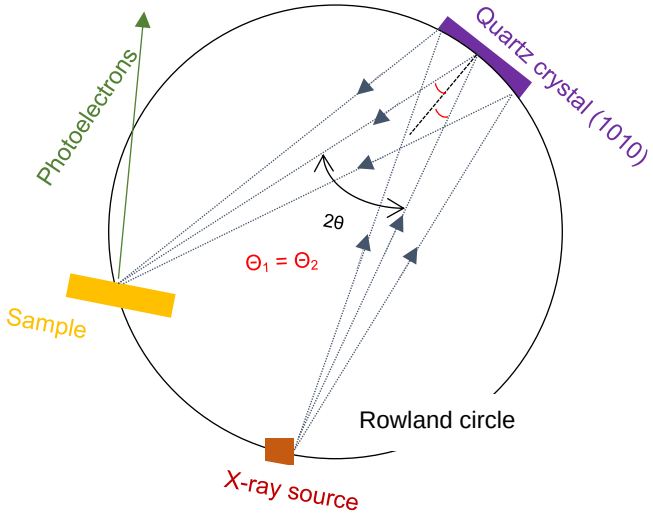

Figure 8 Schematic diagram of the X-ray monochromator

2. **Flood gun**

Since the XPS spectrometer uses monochromatic X-rays, there are limited number of electrons to neutralise the build-up of positive charge on the surface of insulating samples. This charging of the sample surface can result in shifts peaks in the XPS spectrum to higher binding energies. Therefore, a flood gun can be used to inject electrons to the sample surface for charge compensation.

3. **Photoelectron analyser**

An energy analysis of the photoelectrons ejected from the sample is carried out in the photoelectron analyser (Figure 9). An electrostatic lens directs the photoelectrons into the entry slit of the hemisphere, which is made up of two concentric hemispheres. A potential is applied across these hemispheres to control the trajectory of the photoelectrons and disperse it as a function of a chosen kinetic energy, called the pass energy. This is important as a low pass energy can give better energy resolution, which can also affect the Full Width Half Maximum (FWHM) of the principal core line peak.

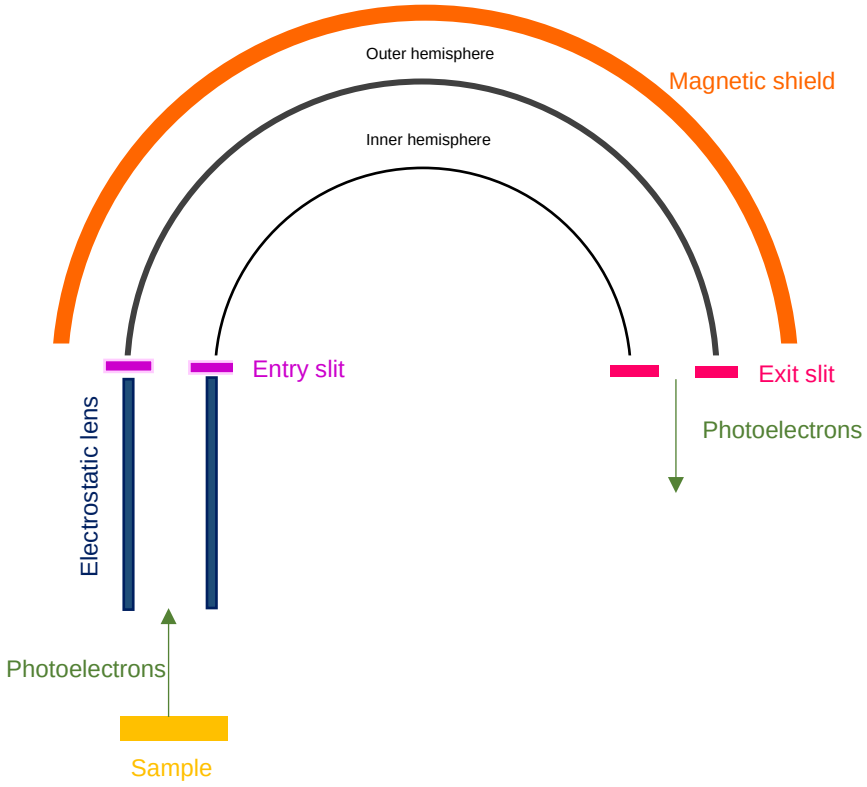

Figure 9 Schematic diagram of the XPS photoelectron analyser

4. **Vacuum pumps**

The XPS measurements are run under high vacuum conditions, i.e. the analysis chamber is maintained at a pressure of ~5x10^{-8} mbar during XPS data collection. This is to keep away any reactive contaminant species, which may be present in the chamber, from adsorbing onto the sample surfaces being measured. This low-pressure atmosphere also helps to prevent any hindrances that may slow down the kinetic energy of the photoelectrons in the hemisphere analyser, allowing these electrons to have longer path lengths.

5. **Ion gun**

A monoatomic ion gun source such as Ar^+ is accelerated at the sample by up to 3 kV, to etch material off the sample surface. Thus, a depth profile of the sample can be measured (Figure 10). Due to the Ar^+ bombardment, the new surface exposed after each etch cycle of the ion gun may have insulating properties. This is minimised by setting a time delay step after each etch cycle.

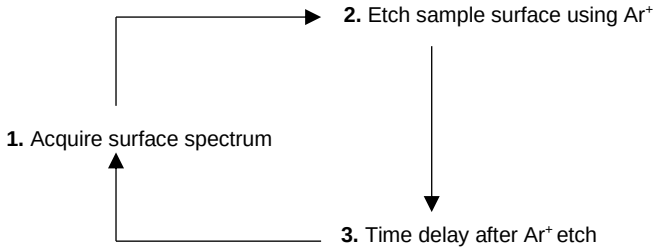

Figure 10 Steps for measuring the XPS depth profile of a sample

2.1.3 The XPS Spectrum

An XPS spectrum is produced by analysing predominantly the photoelectrons that escape from the sample surface without losing their characteristic kinetic energy, also known as the mean free path. These photoelectrons mostly emerge from the top ~10 nm of the sample surface and thus yields surface sensitivity in the measured XPS data.

1. **Basics**

In a typical XPS spectrum, the binding energy of the photoelectrons (X-axis) is plotted against its intensity (Y-axis). Each of the peaks in the spectrum can be assigned to an element in the sample and the core orbital (of the element) from which the photoelectron is ejected. Thus, the chemical composition of the sample can be determined.

2. **Peak ratio**

Orbitals with a principal quantum number, n, > 1 and an angular momentum quantum number, *l*, > 0 gives rise to spin-orbital splitting. This means that the photoelectrons in these orbitals (namely the *p*, *d* and *f* orbitals) can be in two different states, with two different binding energies and therefore, two different peaks in the XPS spectrum (also known as a doublet peak). The ratio between these two peaks is different for photoelectrons emerging from different orbitals in any given element (Table 5).

Table 5 Spin-orbit states and resulting XPS peak ratios of photoelectrons in *p*, *d* and *f* orbitals

Orbital	Spin-orbit states of photoelectron	Peak ratio
2 *p*	2 $p_{3/2}$: 2 $p_{1/2}$	2:1
3 *d*	3 $d_{5/2}$: 3 $d_{3/2}$	3:2
4 *f*	4 $f_{7/2}$: 4 $f_{5/2}$	4:3

3. **Peak Intensity**

The intensity of an XPS peak corresponds to the intensity of the photoelectrons, I, and can be influenced by five other parameters (Equation 7).

$$I = J \rho \sigma K \lambda$$

Equation 7: The intensity of the photoelectrons is dependent on the photon flux, J; the ionisation cross-section of the elemental orbital that the photoelectron is emerging from, ρ; the instrumental factors, K and the electron attenuation length, λ.

[The ionisation cross section is usually accounted for using the corresponding sensitivity factor value and the electron attenuation length usually refers to the path length that the photoelectron travels without being inelastically scattered].

4. **Peak position**

The presence of the unavoidable thin film of adventitious carbon contamination, on all surfaces exposed to air, can cause a shift in their XPS spectrum. Therefore, an energy calibration can be performed to apply charge correction to the XPS spectrum. This involves setting the C 1s principal core line XPS spectrum to 285 eV and applying this shift to all the other core line spectra of the sample being measured. Although 285 eV is the value used for the data in this thesis, there are reports in the literature, where values in the range 284.5 eV to 285 eV were used.

The position of the peak is dependent on the chemical environment of the element in the sample. Also, an increase in the elemental oxidation state can result in a shift of the associated peak to a higher binding energy. For example, core electrons in Fe^{2+} are further away from the nucleus than that in Fe^{3+} (Table 6); therefore, the electrons in Fe^{2+} can be more easily photo-ionised. This will result in the Fe^{2+} electrons having a lower binding energy than Fe^{3+} electrons. Due to this same reason, an element in its cationic state will have a higher binding energy than when it is in its anionic state.

Table 6 Orbital electron configuration of Fe in different oxidation states

Ion	Orbital electron configuration
Fe^{3+}	$1s^2\ 2s^2\ 2p^6\ 3s^2\ 3p^6\ 3d^5$
Fe^{2+}	$1s^2\ 2s^2\ 2p^6\ 3s^2\ 3p^6\ 3d^6$

5. **Spectrum background**

The photoelectrons that loses energy during its mean free path contributes to the background of the XPS spectrum. These photoelectrons can also undergo multiple energy loss processes, where they are termed as a secondary electron. Inelastic scattering of the photoelectrons can cause large tail-like features in the spectrum.

6. **Peak shape**

A *Gaussian-Lorentzian* function is used for the deconvolution of peaks in the XPS spectrum, to help identify the stoichiometry of any given sample. There are several physical factors that contribute to this function.

Gaussian:

i) X-ray source, which will never be perfectly monochromatic
ii) Shake-up and shake-off processes that cause energy loss of the core electron. It is the interaction of the photoelectron (which is excited to a higher energy level) and a valence electron (which is excited to a lower energy level).
iii) Instrumental resolution, which includes the energy resolution of the hemispherical analyser for example
iv) Non-homogeneous stoichiometry and defect density across the sample surface

Lorentzian:

i) Since electrons are ionised from quantised atomic orbitals, photoelectrons with more than one energy is observed. This will result in the photoelectron to have a finite peak width, which is dependent on the lifetime of the core hole, as per Heisenberg's uncertainty principle.

7. **Elemental analysis**

The quantification of the elemental ratios (atomic%) from the XPS spectrum will be carried out as follows. To calculate the titanium: oxygen concentration for example in TiO_2, first:

1- Divide the area under the titanium principal core line XPS peak (Ti 2p) by the sensitivity factor of the Ti 2p orbital.

2-Divide the area under the oxygen principal core line XPS peak (O 2p) by the sensitivity factor of the O 2p orbital.

3-Add the result from step 1 and step 2
4-For Ti (atomic%), divide the result from step 1 by the result from step 3
5-For O (atomic%), divide the result from step 2 by the result from step 3

Uncertainties in XPS composition

In the 70 years that the XPS technique has existed, there has not been a solution to the problem of quantifying uncertainties in composition. Quantification in XPS is achieved by comparing peak intensities scaled with a sensitivity factor specific to each element and orbital. Some factors that affect the uncertainty of the composition measurement are well understood and can be quantified to a good degree – examples are the signal to noise ratio which assuming Poisson statistics can be accounted for using standard statistical methods. However, some factors vary considerably between samples and includes the following cases.

i) It transpires that the signal intensity is exponentially dependent on the depth of the emitting species in the sample. Thus the composition on the nanometer scale has a strong influence on the recorded intensity. The world leading expert on XPS analysis, named Touggard, who has a widely used XPS quantification function named after him described the problem as follows:

   ‘’Analysis of spectra is often done under the assumption that the surface composition is homogeneous within the outermost few nanometer in which case the composition is proportional to the intensity of the corresponding peaks. Samples are however rarely homogeneous within a few nanometer and this limits the accuracy of the XPS analysis. Improvements to this analysis can easily be made if the depth composition of the sample is known prior to the analysis. But this is seldom the case in practice and the determined compositions are therefore rather uncertain’’.[129]

ii) The sensitivity factors are not known accurately and can vary depending on the matrix. Sensitivity factors can be derived from theoretical considerations, i.e. by computing the probability of a particular electronic transition induced by a photon of a specific energy (most famously Schofield sensitivity factors). This is challenging as the simple approximation of a 1 particle model is known to give significantly incorrect results, for example, when several final states are available. Empirical determination of sensitivity factors using standards is more common but suffers from poor transferability between different instruments and matrix

effects, i.e. the intensity of a signal from emitting species can vary based on the matrix it is embedded within.

The above two problems are compounded by a third, that is not easily possible to measure the ‘’true’’ surface composition using a different technique, hence it is difficult to determine even for one sample the deviation of the XPS error from the true value.

In summary, the XPS composition accuracy is limited by surface inhomogeneity on the nanometer scale, poorly defined sensitivity factors, and what is worse, deviation from the true value cannot be measured as no other technique can reliably give the surface composition.

How then do XPS analysts proceed? Discussing general XPS analysis, Woodruff and Delchar stated that, ‘’Despite these problems, quantitative studies are possible using XPS as a means of compositional analysis, and by taking great care in the mode of calibration, analyses accurate to even 5% or 10% are claimed’’.[130]

In summary, there is no ideal way to quantify errors associated with XPS compositional measurements. A widely adopted method, which has been followed, is to state errors of around 10%, but this is based on accumulated experience and not a robust physical model or statistical treatment; as such a thing has not been accomplished in XPS yet.

2.2 X-ray Diffraction (XRD)

XRD is a technique used to characterise the atomic and molecular structure that constitutes the bulk of crystalline solids.

2.2.1 Powder X-ray Diffraction (PXRD)

PXRD was used to characterise all the powder samples discussed in this thesis. It was mainly used for phase identification and to check for phase purity.

2.2.1.1 PXRD Pattern Collection

First, the powder sample was loaded onto the diffractometer in the path of the incident X-ray beam, θ. While the sample is rotating, the X-rays which are diffracted through the sample at an angle of 2θ are collected by the detector (Figure 11). Thus, the sample is scanned through a range of θ angles to get diffracted X-rays with a range of 2θ angles. This is done to cover all the possible diffraction directions of the lattice, due to the random orientation of the powder.

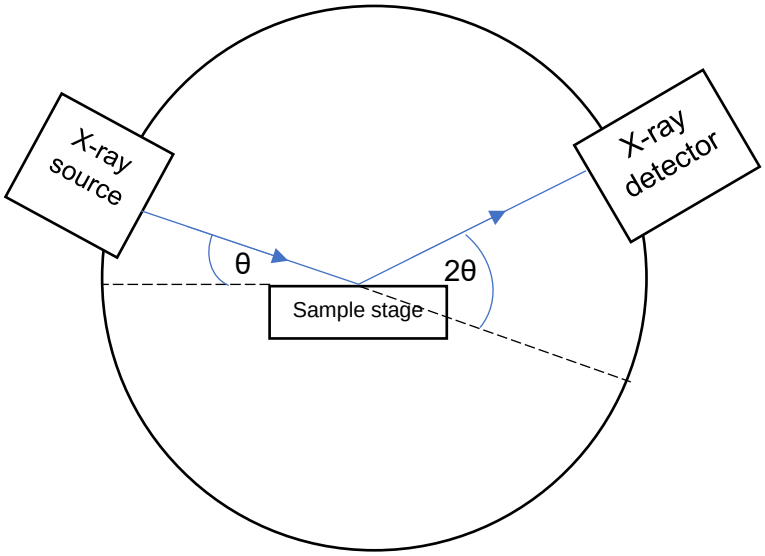

Figure 11 Basic schematic of a powder X-ray diffractometer

2.2.1.2 Powder X-ray Diffractometer

An overview of how the main parts of the X-ray diffractometer functions to produce a spectrum is detailed below.

1. **X-ray source**

X-rays are used as their wavelength is of the order of Angstroms, which is roughly equal to the distance between atoms in crystalline materials. At first, electrons are produced by heating a tungsten filament. They are then accelerated, by applying a voltage, and bombarded onto the target material. When these electrons have enough energy to knock off inner shell electrons in the target, characteristic X-rays are produced. Each target material will have a characteristic X-ray wavelength they produce. The resulting X-rays will have different wavelengths namely $K_{\alpha 1}$, $K_{\alpha 2}$ and K_{β}, which all have different intensities. A monochromator is then used to filter out the $K_{\alpha 1}$ and $K_{\alpha 2}$ wavelengths. Copper is the most commonly used target material and has the Cu $K_{\alpha 1}$ wavelength equal to 1.5418 Å. Once these X-rays are collimated, they are directed onto the powder sample. The intensity of the X-rays reflected off the sample are recorded in the PXRD pattern. A peak appears in the PXRD pattern only when the incident X-rays follow Bragg's Law. Bragg's Law states the condition for constructive interference of X-rays. In a crystalline material, constructive interference between diffracted X-rays occurs only in the directions where the path difference between these rays (2d sin θ) equals an integer multiple of the wavelength of X-rays (Equation 8, Figure 12).

$$n\,\lambda = 2d \sin\theta$$

Equation 8: Braggs Law where λ is the wavelength of the incident beam, n is the order of magnitude, d is the distance between the atomic planes in the crystalline material and θ is the angle of the incident X-ray beam

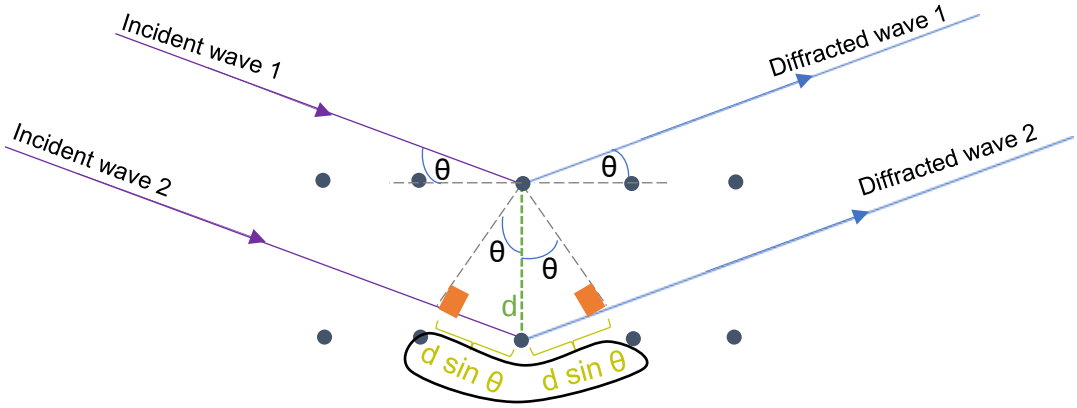

Figure 12 Crystalline lattice where incident waves with a path difference of 2d sinθ gives constructive interference, as per Bragg's Law

2. **Goniometer**

During the PXRD pattern collection, the sample is rotated in the path of the collimated X-ray beam at an angle of θ and the X-ray detector is rotated at an angle of 2θ using the goniometer.

3. **X-ray detector**

The detector processes the diffracted X-ray signal and converts it into a count rate. Typically, the 2θ range used for data collection is ~10^{o} to ~80^{o}.

2.2.1.3 PXRD Pattern

The 2θ values of the diffracted peaks recorded in the PXRD pattern can be used to calculate the corresponding d-spacings, which can be compared with standard reference patterns to identify the material being measured.

2.3 Raman Spectroscopy

The chemical structure, phase and crystallinity of the samples discussed in this thesis were also assessed using their Raman spectrum.

2.3.1. Raman Spectrum Collection

At first, the sample is irradiated with a highly intense laser light source. This incident light is scattered by the atoms or molecules in the sample. Most of the scattered light has the same wavelength as that of the laser source and is known by the term Rayleigh scattering; however, the remaining ~0.0000001% of the scattered light has different wavelengths compared to the laser source and is known as Raman scattering. The wavelengths of the Raman scattered light are dependent on the vibrational properties of the chemical structure that makes up the sample.

2.3.2. Raman Spectrometer

The main components that constitutes the Raman spectrometer is outlined below.

1. **Light source**

A high intensity, monochromatic, laser light source must be used in a Raman spectrometer to ensure that the scattered Raman light had an intensity that was high enough to be measured with a reasonable signal-to-noise ratio. Examples include argon and krypton ion sources, which can emit in the blue (488 nm) and green (530.9 nm) and red (647.1 nm) regions of the electromagnetic spectrum.

2. **Filter**

A filter is used to separate the Raman scattered light from the Rayleigh scattered light.

2.3.3. Raman Spectrum

The Raman spectrum of a sample consists of the different wavelengths of the Raman scattered light (X-axis) against their intensities (Y-axis) where each peak corresponds to the characteristic vibration of a chemical bond present in the sample.

2.4 UV-vis Spectroscopy

Since all the samples discussed in this thesis are solid powders, which reflect light off their surfaces, their diffuse-reflectance (Figure 14) spectrum was recorded using UV-vis spectroscopy. This spectrum was used to calculate the optical band gap of the materials being measured.

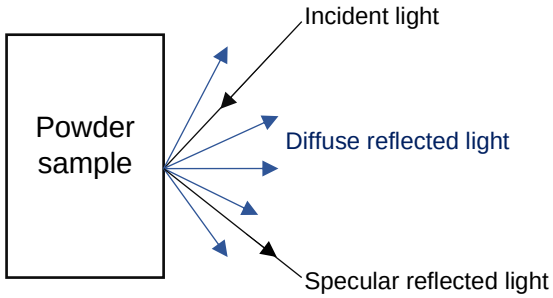

Figure 13 Diffuse reflection and specular reflection of an incident ray of light shone on a solid sample

2.4.1 UV-vis Spectrum Collection

The light reflected off the powdered sample is collected and processed to get the diffuse-reflectance UV-vis spectrum.

2.4.2 UV-vis Spectrometer

The main component of the UV-vis spectrometer that is crucial for diffuse reflectance measurements are detailed below.

1. **Integration sphere**

The integrating sphere can be thought as a white reflective surface, which has an inside of barium sulphate. A baseline spectrum measurement is obtained first by using three of these integrating spheres (Figure 15a), of which the reflectance is taken as 100%. Then, one of these spheres is replaced by the sample (Figure 15b), in front of the incident light window, and the reflected light is concentrated onto the detector, using these integrating spheres and mirrors. It is to be noted that the measured reflectance of the sample is the reflectance relative to that of the integrating sphere. When the incident light is directed at the sample at an angle of 0^{o}, the diffuse reflectance is measured by the detector. The specular reflected light (Figure 14) exits the integrating sphere at this point and therefore, is not measured by the detector.

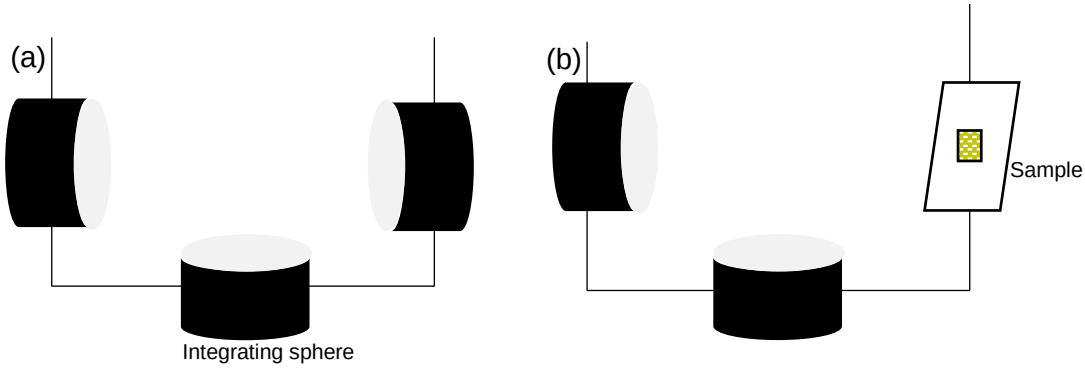

Figure 14 The integrating sphere set-up for (a) baseline and (b) sample measurement

2.4.3 UV-vis Spectrum

The UV-vis spectrum has the function of diffuse reflectance, F (R), (Y-axis) plotted against the wavelength of the diffuse reflected light (X-axis). F (R) takes account of the internal inhomogeneities of the powder, which results in the scattering of light at different points in its path. The Kubelka-Munk function is used to model this scenario. It condenses all these inhomogeneities into the scatter coefficient parameter, s. For an infinitely thick sample, where the transmission of light is 0%, the diffuse reflectance can be calculated (Equation 9).

$$R_\infty = \frac{s}{k + s + \sqrt{k(k + 2s)}}$$

Equation 9: Diffuse reflectance of an infinitely thick powder where the absorption coefficient, $k = 4\pi\left(\frac{k}{\lambda}\right)$ in which λ is the wavelength of the light.

For the scenario where all the light is reflected (i.e. there is no absorption), $R_\infty \rightarrow 1$, and there is no scattering (i.e. all the light is either transmitted or absorbed), $S \rightarrow 0$, the Kubelka-Munk function can be rewritten (Equation 10).

$$F(R_\infty) = \frac{(1 - R_\infty)^2}{2R_\infty}$$

Equation 10: Kubelka-Munk function where there is no scattering and all the light is reflection

The Kubelka-Munk function can be used to draw a **tauc plot**, which is used to determine the value of the direct and indirect optical bands. A tauc plot has the energy, hv, of the absorbed wavelengths of light by the sample (in eV) plotted on the x-axis and $(F(R)*h\nu)^n$ plotted on the y-axis, where F(R) is the Kubelka-Munk function, and n = 2 for indirect allowed transitions whereas n = ½ for direct allowed transitions. The direct and indirect **optical band gap values** which result from these transitions can be extracted from their respective tauc plots by drawing a tangent to the slope, as shown in Figure V below, and extrapolating this tangent towards the x-axis and reading the x-axis intercept (see red cross in Figure V below) of the extrapolated tangent. Thus, the indirect and direct band gaps can be thus be read off from the graphs ($[F(R) * Energy]^2$ versus *Energy*) and ($[F(R) * Energy]^{1/2}$ versus *Energy*) respectively.

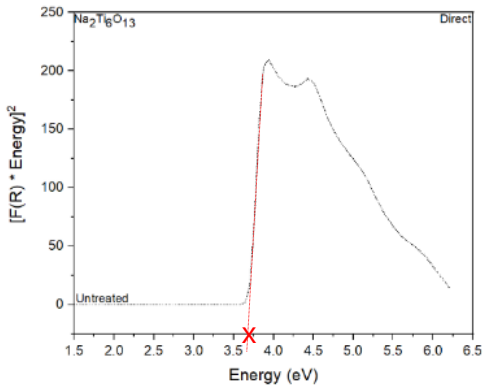

From Figure V in Appendices section

The error in the band gap measurements from the tauc plot is taken to be as the standard errors of a linear fit,[131] using the equation standard error = $\sqrt{(\frac{\sum(y-y1)^2}{n-2})}$, where y is the estimated value from the extrapolated regression line, y1 is actual value and n is the number of actual values in total. The error in the optical band gap values used in this thesis are ±0.01 eV.

2.5 CHN Analysis

The quantification of the nitrogen content in the powder samples discussed in this thesis were carried out using the CHN analysis technique.

2.5.1 CHN Data Collection

The sample is combusted and converted into the gas phase. The detector then measures a signal that is proportional to the concentration of carbon, hydrogen and nitrogen.

2.5.2 CHN Analysis Instrument

The sample is stored in a tin container, which is placed inside the autosampler drum and purged with a dynamic flow of helium gas. The samples are then dropped into the combustion reactor (at 900 ^{o}C). When the inside of this reactor is under an oxygen enriched atmosphere, the tin that the sample container is made of encourages a violent reaction and melts the tin and the sample. The combustion gases that are produced from this flash combustion reaction are then directed to pass over a layer of catalyst first and then over copper. This is to remove any oxygen excess and to allow the reduction of oxides of nitrogen to elemental nitrogen. The mixture of gases

is then separated using a chromatography column and detected by the thermal conductivity detector. This detector measures a signal that is proportional to the concentration of carbon, hydrogen and nitrogen content present in the sample being measured.

2.5.3 CHN Data

The CHN data consists of three values which indicate the concentration of carbon, hydrogen and nitrogen (in weight%) that is present in the sample.

2.6 Atomic Force Microscopy (AFM)

The surfaces of the substrates discussed in this thesis were characterised using AFM.

2.6.1 AFM Imaging

A sharp tip attached to a cantilever is made to raster across the surface of the sample. The interaction between the tip and the surface causes the cantilever to deflect. This deflection is recorded using a laser and a photodiode and used to image the surface of the sample.

2.6.2 Atomic Force Microscope

The main components of the atomic force microscope are outlined below.

1. **Tip**

The tip is usually made of silicon. It is very important to ensure that this tip is sharp, with a curvature of the order of nanometres.

2. **Cantilever**

The tip is attached to a cantilever, which helps to raster the tip across the surface of the sample. When the tip is made very close to the sample, the forces between them causes the cantilever to deflect, as per Hooke's law (Equation 11). This force is not measured directly but is measured from the deflection of the cantilever (Figure 16).

$$F = - k x$$

Equation 11: Hooke's law for the cantilever deflection where F is the force (in N), k is the spring constant (in Nm^{-1}) and x is the increase in length (m)

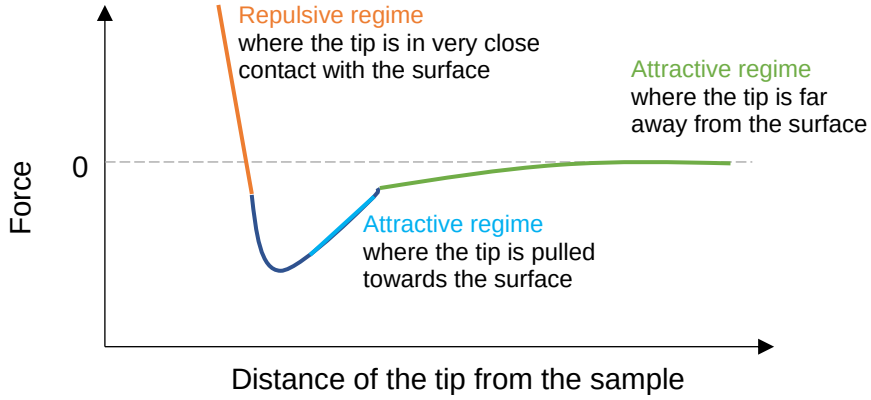

Figure 15 Force-distance curve showing the deflection of the cantilever in an AFM

3. **Laser**

The laser reflected off the end of the cantilever is used to control the force between the tip and the cantilever. The position of this laser is mapped onto the photodetector and varies as the tip is made to raster across the sample surface (Figure 17). The feedback loop uses this laser position to track the position of the tip to enable imaging of the sample surface.

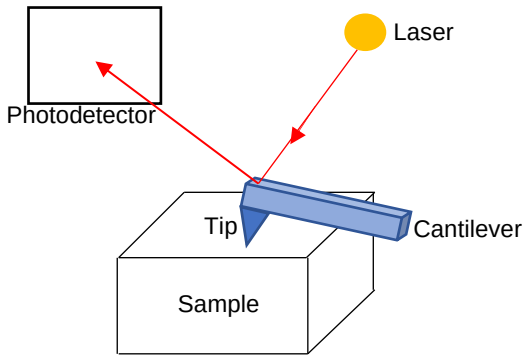

Figure 16 Schematic showing the use of laser reflection to track the position of the tip on the sample surface

2.6.3 AFM Images

The tapping mode is used to image all the sample surfaces discussed in this thesis. It involves keeping the frequency and amplitude of the signal that is used to drive the cantilever constant. This frequency is usually at or near the resonance frequency of the cantilever and this amplitude is on the range of several nm to up to 200 nm. Keeping these parameters constant, helps to keep the cantilever oscillating at a constant amplitude, given that there is no tip-surface interaction and no drift. As the tip is made to become close to the sample surface, the forces between them cause the oscillating amplitude of the cantilever to change. The feedback loop uses this new

amplitude value to adjust the height between the tip and the sample surface so that the cantilever oscillates at the set amplitude, enabling the imaging of the sample surface.

2.7 Profilometry

The depth of the crater formed from the XPS study of samples discussed in this thesis was measured using a stylus profilometer.

2.7.1 Profilometer Data Collection

The probe tip is physically moved across the surface of the sample to acquire the surface height of the sample.

2.7.2 Stylus Profilometer

The main components that make up the stylus profilometer is outlined below.

1. **Stylus tip**

The shape and size of the tip can affect the lateral resolution of the measurements (Figure 18). The tip is physically moved across the sample surface in the x, y and z directions, while in contact with the sample surface.

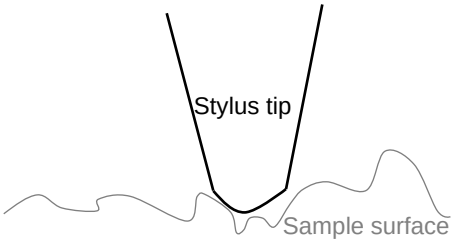

Figure 17 Schematic of the shape of the stylus tip against that of the sample surface

2. **The arm**

As the tip attached to the arm is moved across the sample surface, the force that is pushing against the tip is measured. The feedback loop uses this measured force to adjust the z height of the arm, ensuring that the arm has the setpoint force. The differences in the z height of the arm across the sample surface is used to reconstruct the surface height across the sample.

2.7.3 Profilometer Measurements

Performing profilometry on a sample gives a graph where the depth of the crater (Y-axis) is plotted against the length of the crater (X-axis).

Chapter 3: Anionic Diffusion in Rutile single crystal substrates – Experimental Procedures

This chapter will cover specific details of the instruments used for sample characterisation, the surface cleaning protocol and anion doping method employed for the as-received rutile substrates and the procedure followed for calibrating the XPS crater measurements into the depth scale.

3.1 Characterisation

The surface topography was probed using the Bruker Dimension Icon AFM, on the tapping mode, with a silicon cantilever and force constant of ~40 Nm^{-1}. The resulting AFM images were analysed using the WSXM software. The XRD patterns were recorded using the Philips Panalytical X-Pert MRD 4-circle diffractometer, with Cu K_α 1.541 Å and Cu K_β 1.387 Å, Ge 022 4-bounce monochromator, ¼ degree divergence slit and x'celerator 1D detector. The Raman spectra were measured using the Renishaw inVia spectrometer, with an Argon laser wavelength of 785 nm. The chemical composition and the valence band spectrum were recorded using ThermoScientific K-alpha photoelectron spectrometer, with 72 W monochromatic Al K-alpha source with 1486.6 eV photon energy, dual beam flood gun, instrument related sensitivity factors for normalising data and carbon correction reference done by positioning the adventitious carbon peak at 285 eV. The angle resolved facility of the ThermoScientific Theta Probe was used for collecting relatively more surface sensitive chemical composition data and a valence band spectrum with relatively better resolution was obtained using the theta probe's UV source facility.

3.2 Materials

As-received Titania-Rutile single crystal substrates of the orientations (110), (100) and (001) were purchased from Pi-Kem ltd. All these substrates were of the dimensions 0.5 mm x 0.5 mm x 0.5 mm and were mechanically polished on both sides.

3.3 Surface Cleaning Protocol

Some preliminary data was collected on the purchased substrate samples. This included the surface XPS spectrum of the rutile (100) substrate, which indicated the presence of zinc (Figure 19a).

3.3.1 Steps

A surface cleaning protocol, involving chemical etching, was employed for removing these surface bound metal impurities on the Rutile (100) surface (Figure 18). The effect of the choice of solvent (in step 1) in the removal of zinc impurities was investigated. The solvents investigated include acid piranha, 37% hydrochloric acid and 1:1 ethanol-acetone mixture. The acid piranha was prepared using 3 parts of concentrated sulphuric acid and 1 part of hydrogen peroxide.

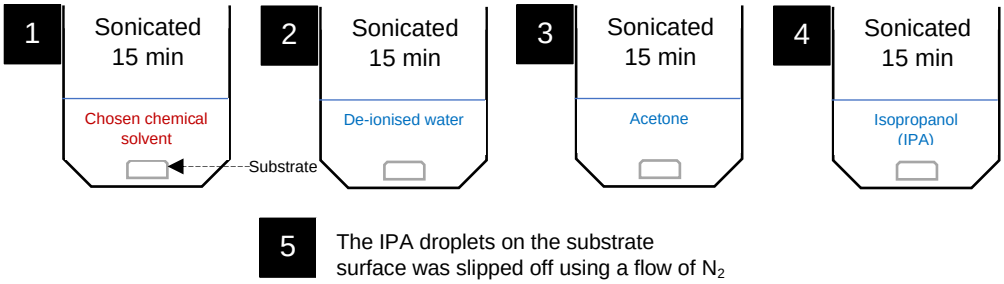

Figure 18 Surface cleaning protocol for titania substrates

3.3.2 Effectiveness

The effectiveness in the use of a different chemical solvent in step 1 of the surface cleaning protocol (Figure 18) is discussed as follows. A high-resolution Zn 2p XPS core line spectrum was recorded from two points, point #1 and point #2, on the surface of the substrate before and after surface cleaning. The presence of the Zn metal impurity was indicated by the peaks at 1044.45 eV and 1021.26 eV, which corresponds Zn $2p_{1/2}$ and Zn $2p_{3/2}$ respectively. Upon employing the surface cleaning protocol involving either the acid piranha or the hydrochloric acid or the ethanol-acetone mixture in step 1, the zinc impurities were observed to be removed, as indicated by the disappearance of the zinc peaks in the Zn 2p XPS spectrum (Figure 19). Therefore, any of these three solvents could be employed for the removal of the zinc impurities from the surface of the rutile substrates of any orientation.

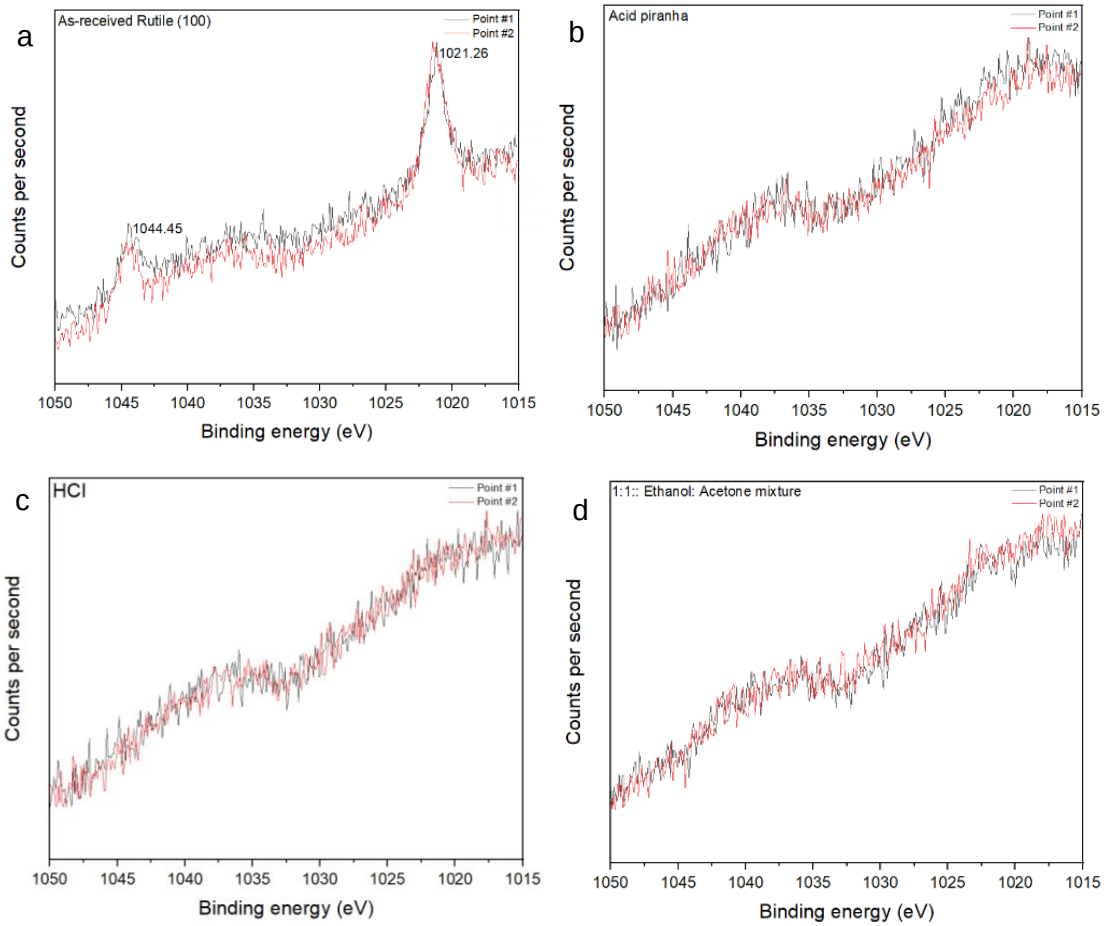

Figure 19 The Zn 2p XPS principal core line spectrum of two different points on (100) rutile substrate (a) as-received and (b), (c), (d) after surface cleaning using four different solvents

3.4 Anion Doping Method

First, the surface of the rutile substrates of the orientations (110), (100) and (001) were cleaned by employing the surface cleaning protocol, using hydrochloric acid in step 1 (section 3.3). The anionic dopant sources chosen for the boron, carbon, nitrogen and sulphur doping were TiB_2, TiC, TiN and TiS_2 respectively. This was because these compounds only contained the dopant atom and one another atom which is Titanium, which is also present in the substrate sample. The procedure employed for anionic doping of the rutile substrates (Figure 20) are as follows.

1. Into a quartz ampule sealed at one end, a chosen dopant source powder, e.g. TiB_2 powder, is placed.
2. Then the rutile substrate of a chosen orientation, e.g. (110), is placed into the same ampule.
3. The ampule is then filled with more dopant source powder, enough to bury all the sides of the substrate.

4. The inside of the ampoule was then put under vacuum, ~10^{-2} mbar, and then sealed at the open end using an oxy-propane torch.
5. Ensuring that the entire substrate remains covered by the dopant source powder, the ampule was placed into a box furnace and heated at 650 ^{o}C for the weekend (72 hours).
6. Once the ampule was cooled to room temperature, the substrate was taken out and cleaned using the steps 3, 4 and 5 of the surface cleaning protocol (section 3.3.1).
7. Boron, nitrogen, sulphur and carbon anions were individually investigated as dopants in rutile single crystal substrates of the orientations (110), (100) and (001). This was done was carrying out the above steps 1 to 6.

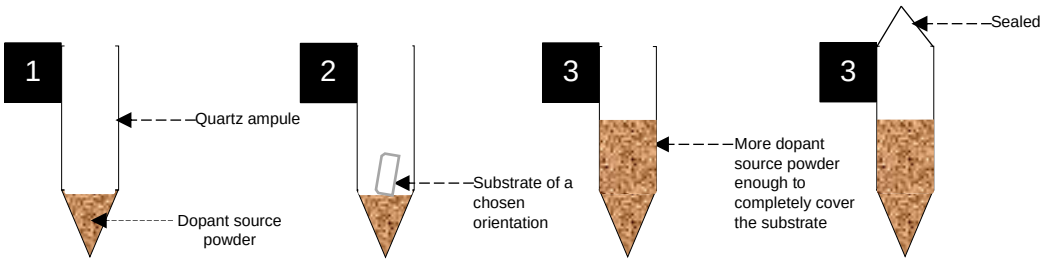

Figure 20 Procedure for anionic doping of titania substrates

3.5 Depth Calibration

A typical XPS depth profile graph has the elemental concentration (Y-axis) plotted against the sputter time (X-axis). The sputter rate of the XPS etching was calculated to calibrate the sputter time into the depth scale.

Firstly, an as-received rutile single crystal substrate, of the dimensions 3.2 mm x 3.2 mm x 0.5 mm, was ion etched on the XPS spectrometer for 2 h. Secondly, the depth of the resulting XPS crater was measured using a stylus profilometer. The right side of the crater has reached the end of the crystal and so the crater depth was deduced from the left side of the crater. The depth of the ~1.8 mm wide XPS crater was approximated to be 800 nm. The area indicated with a red square in Figure 21 indicates the flat unsputtered areas of the substrate. The distance between the minimum and the maximum point on this part of the graph is ~100nm. Therefore, 100 nm is the error associated with the depth values measured using the profilometer. An XPS crater of depth 800 nm ± 100 nm and the associated sputter time of 2 h gives a sputter time of 0.11 nm s^{-1} (Equation 12). The associated error value is within 5%, as this is within the ‘’experimental uncertainty of sputtering yields’’.[132] This sputter rate

was used for depth calibration of all the XPS depth profile measurements of the rutile substrates discussed in this thesis.

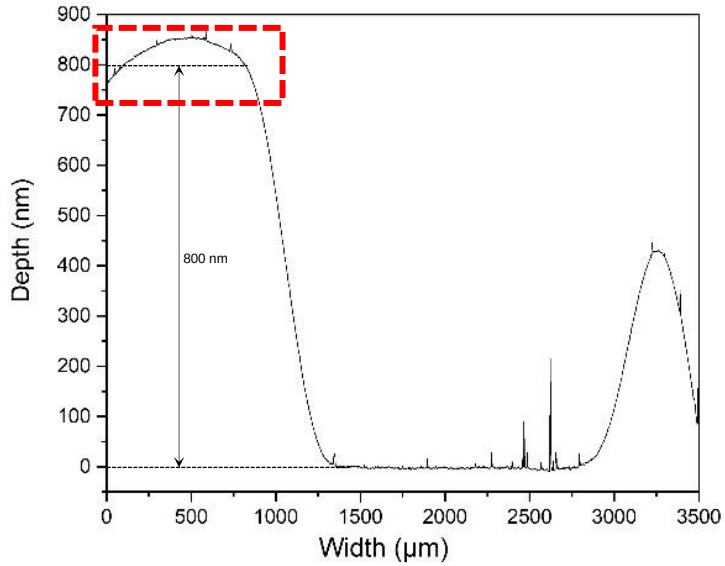

Figure 21 Profile showing the crater depth of the rutile substrate

$$\text{Sputter rate (nm } s^{-1}) = \frac{Crater\ depth\ (nm)}{Sputter\ time\ (s)}$$

Equation 12: Formula for estimating the XPS sputter rate of materials

Chapter 4: Boron Diffusion in Rutile single crystal substrates

A detailed characterisation of the rutile substrates of the orientations (110), (100) and (001) treated using the TiB_2 dopant source powder (referred to as TiB_2 treated rutile) is discussed below.

4.1 Results and Discussion

The topography, composition and bonding on the surface and the bulk of the TiB_2 treated rutile substrates were carried out.

4.1.1 Surface Topography

Upon TiB_2 treatment, the surface topography of the as-received (110), (100) and (001) rutile substrates (Figure A in Appendices) were observed to be significantly roughened, as per AFM images (Figure 22). The treated (110) substrate has a surface consisting of uniformly distributed nanoparticular features (~200 nm). On the other hand, these features are seen to be much larger (2 μm) on the treated (100) surface and less well-defined as well as non-uniform on the treated (001) surface. The tallest roughened features are observed on the (100) surface and the shortest on the (001) surface (Figure B in Appendices). The different levels of roughening observed here with the different surfaces of rutile is characteristic of what is reported to be an effect of the substrate orientation on the microstructure of a film deposited on a substrate.

The roughening of the substrate surfaces was quantified and compared by measuring their RMS roughness values which were extracted by loading the AFM images onto the WSxM 5.0 Develop 8.5 software. The RMS roughness (R_q) values are essentially the standard deviation of the z elevation values within the area being measured (5 μm x 5 μm) and is calculated using the equation[133], $R_q = \sqrt{\frac{\sum(z_i - z\_ave)^2}{N}}$, where z_i is the elevation z at a given point on the AFM image, $z_{\_ave}$ is an average of all the z values within the area being measured and N is the number of z points that are being measured. Since the rutile substrate samples being measured were single crystal substrates, which is known to have high crystallinity as supposed to thin films, the single AFM image presented for each of the sample could be truly representative of the overall morphology of the surfaces. However, any future studies to confirm this could be recommended to incorporate AFM images from different areas of the same

sample surface. The considerations in this paragraph hold for all the AFM analysis presented in Chapters 5, 6 and 7.

The surface roughening of the rutile substrates is confirmed by the observed increase in RMS roughness values of the as-received (110), (100) and (001) surfaces from being < 1 nm to become 23 nm, 227 nm and 30 nm (Table 7) respectively. These values also indicate that the (100) surface is the most roughened and the (110) surface is the least roughened, suggesting that the latter is more stable and therefore, could be the reason why it is considered to have the model photocatalytic surface[134].

Table 7 A comparison of the surface roughness of rutile substrates before and after TiB_2 treatment

	RMS roughness (nm)		
	(110)	(100)	(001)
Untreated	0.58	0.86	0.45
After TiB_2 treatment	23	227	30
Increase in roughness	**22**	**226**	**66**

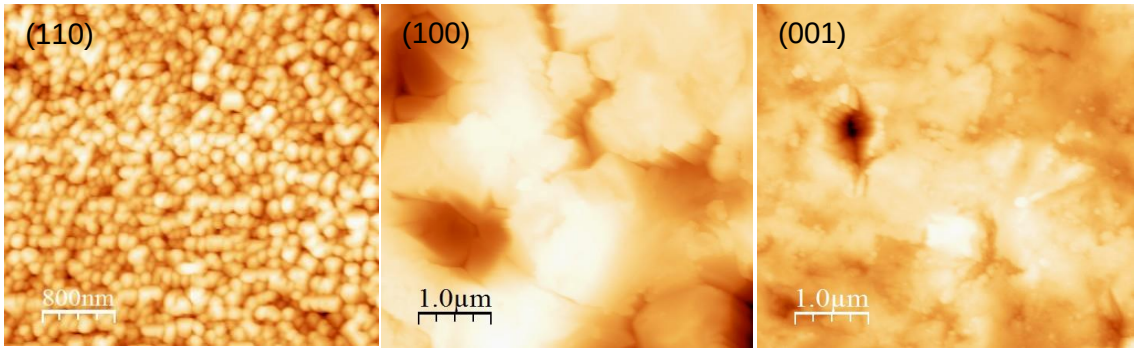

Figure 22 AFM images showing the differences in the morphology of the roughened surfaces of TiB_2 treated rutile substrates (110), (100) and (001)

4.1.2 Surface Bonding

The as-received (110), (100) and the (001) rutile substrates show two main Raman peaks at 446 and 610 cm^{-1} (Figure 23), which match well with the literature pattern of rutile[135]. The vibration at 446 cm^{-1}, corresponding to the E_g, asymmetric bending mode is caused by the movement of the O atoms in opposite directions across the O-Ti-O bonds in the (001) plane[136]. It should be noted that in the (001) orientated substrate, the vibration at 446 cm^{-1} is weak as compared with that of the (110) and (100) orientations. On the other hand, the vibration at 610 cm^{-1} is caused by the A_{1g}

symmetric stretching resulting from the movement of O atoms in the adjacent O-Ti-O bonds along the (110) plane. Upon TiB_2 treatment, both these characteristic peaks in the (110), (100) and (001) rutile are seen to be broadened significantly, suggesting the weakening of the oxygen bonds attached to the Ti atom along the (001) and (110) plane in the rutile lattice. Thus, the crystallinity of the surfaces is reduced, as indicated by the nanometer scale roughening in their AFM images. The magnitude of the broadening observed in the treated surfaces, in order of their increasing broadening is (001) > (100) > (110). This order corresponds with the size of the features: the most broadened peaks are observed with the treated (110) surface that has the smallest sized features. According to the three-dimensional phonon confinement model, phonons with a q value that is not equal to zero will have the uncertainty in its phonon momentum to be greater for samples with smaller grain sizes, resulting in increased broadening of their Raman peaks[137]. So, as per literature, the peak broadening may potentially be a grain size effect. The as-received rutile (110), (100) and (001) substrates also has peaks at 1361 cm^{-1} and 1600 cm^{-1} (figure 23), which are not reported in the literature for rutile[135] or anatase[138]. These peaks correspond to any mixed sp^2/ sp^3 carbon contamination on the surface [139, 140]. Carbon contamination such as this is challenging to avoid in samples such as this that are exposed to air and the Raman peaks of these materials are very strong so that even small amounts of contamination can lead to measurable peak intensities.

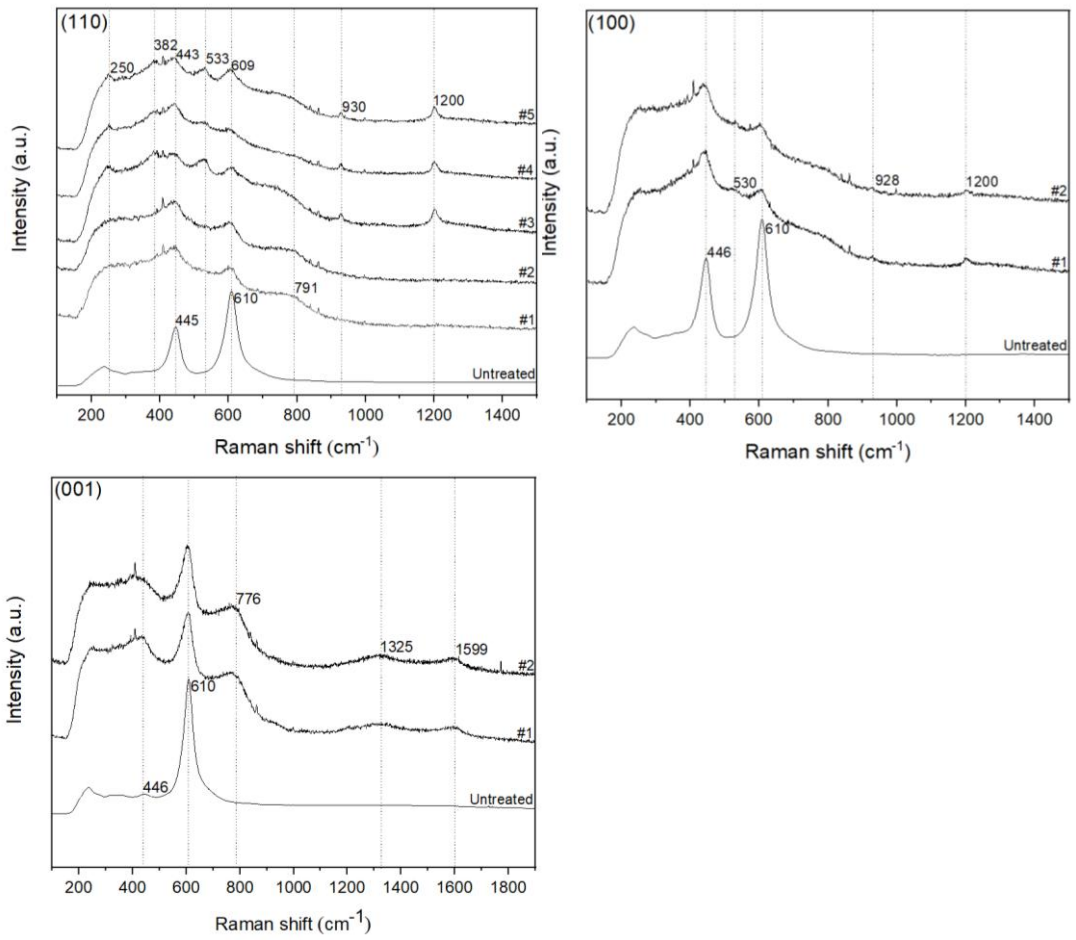

Figure 23 Raman spectrum of the TiB_2 treated titania substrates of the orientations (110), (100) and (001), where #1, #2 and so on indicates different areas on the substrate surface

With the TiB_2 treated (110) surface, there are extra peaks observed at 250, 382, 930 and 1200 cm^{-1}, corresponding to the $TiBO_3$ structure[141]. Moreover, these peaks are present only in some areas of the treated (110) surface, labelled as #3 #4 #5 (Figure 23), indicating a non-uniform distribution of $TiBO_3$ composition across the (110) surface. In the areas with $TiBO_3$, an additional peak at 533 cm^{-1} is also observed whereas in the areas with no $TiBO_3$, an additional peak at 791 cm^{-1} is observed. These peaks neither correspond to $TiBO_3$ nor to the Rutile structure. In the literature, a peak at 533 cm^{-1} is reported to be assigned to diborate, B_2O_5[142], and a peak at 801 cm^{-1} is assigned to B_2O_3[143].

In the TiB_2 treated rutile (100) substrate, there are peaks located at 928 and 1200 cm^{-1} corresponding to the $TiBO_3$ structure uniformly distributed across the surface. Likewise, was the case with the $TiBO_3$ containing areas of the TiB_2 treated (110) substrate, a peak was observed at ~530 cm^{-1}, which neither corresponds to $TiBO_3$ nor to rutile or the TiB_2 structure. Therefore, it is possible that the ~530 cm^{-1} peak could

potentially be caused by the $TiBO_3$ formation and not dependent on the orientation of the rutile substrate. The literature suggests that this peak is potentially diborate, B_2O_5.

With the TiB_2 treated (001) substrate, no $TiBO_3$ Raman peaks were observed, unlike the case with the (110) and (100) substrates. However, there were peaks located at 776, 1325 and 1599 cm^{-1}, which corresponded to neither the $TiBO_3$, nor the rutile. The literature reports the similar peaks at 1353 cm^{-1} and 1585 cm^{-1} to be assigned to any mixed sp^2/ sp^3 carbon contamination on the surface of the rutile substrates[139, 140]. The peak at 776 cm^{-1} could potentially be assigned to B_2O_3[143], which in the literature is reported to have a peak at 801 cm^{-1}.

The Raman spectrum has identified the dependence of substrate orientation on the possibility for $TiBO_3$ formation. This was evident from the $TiBO_3$ surface formations, which were found to be more uniform on the (100) substrate compared to that on the (100) substrate. This suggests that the (110) substrate is relatively less reactive and therefore, more stable than the (100) substrate and this suggestion is already known for pristine TiO_2. On the other hand, the (001) substrate did not have any $TiBO_3$ formation on its surface. Another finding that the Raman spectroscopy data has identified is the formation of B_2O_5 that is found to be accompanying the $TiBO_3$ formation. This was the case with the (100) substrate and with the $TiBO_3$ containing areas of the (110) substrate. The Raman data has also revealed the formation of B_2O_3 in areas where there was no $TiBO_3$ formation, as was the case with the (001) substrate and the non-$TiBO_3$ containing areas of (110) substrate. This suggests that the $TiBO_3$ formation is dependent on the substrate orientation while the B_2O_5 or B_2O_3 formations are dependent on whether $TiBO_3$ is formed on the rutile substrate.

4.1.3 Crystal Structure

The crystal structure and orientation of the rutile (110) substrate is observed to be retained after TiB_2 treatment. The XRD pattern measured of the untreated rutile (110) substrate (Figure 24) shows a 2θ peak at 27.5° with a d-spacing of 3.24 Å (Table 8). This corresponds to the (110) reflection in the literature pattern of Rutile, with a peak location of 27.3° with a d-spacing of 3.27 Å[144]. Upon TiB_2 treatment (Figure 24), this peak is seen to remain unshifted at 27.5° (3.24 Å), in agreement with the measured values of as-received untreated rutile substrate. The XRD pattern measured of the untreated rutile (110) substrate also shows a peak at 56.6° (1.63 Å). This corresponds to the (220) reflection in the literature pattern of rutile, with a peak location and d-

spacing of 56.4° and 1.63 Å respectively. Upon TiB_2 treatment, the peak position is seen to remain unshifted at 56.6° (1.63 Å), in agreement with the measured values of the as-received untreated rutile substrate. It is to be noted that the broad peak at 22.5° present in almost all the XRD patterns discussed in this chapter is an artefact.

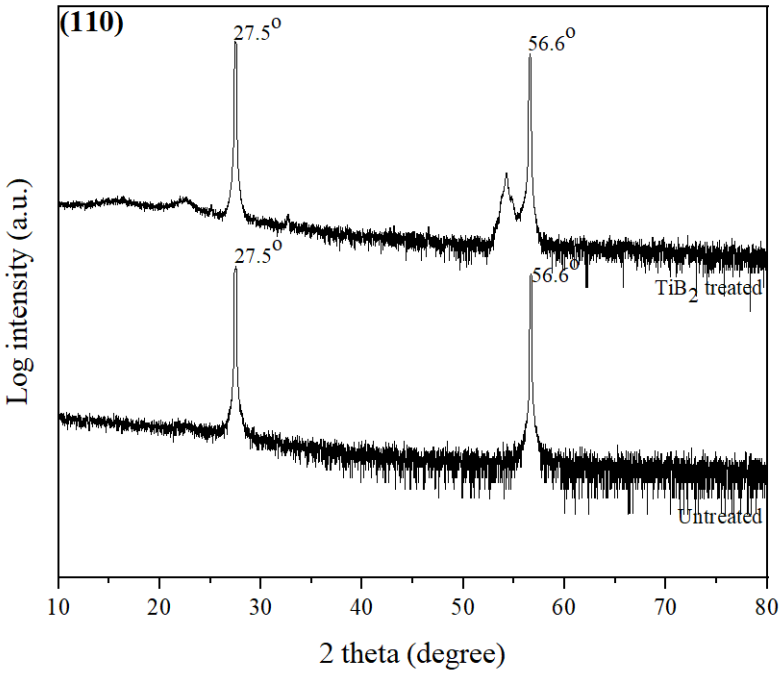

Figure 24 XRD pattern of the rutile (110) substrate before and after TiB_2 treatment

Table 8 Measured 2θ and d-spacing values (in brackets) of the rutile characteristic peaks in the as-received (110) substrate before and after TiB_2 treatment, compared with the literature data

2θ (°)			
Literature Rutile powder	**Measured as-received Rutile (110)**	**Measured TiB_2 treated Rutile (110)**	**Δ d spacing (Å) – Rutile before and after TiB_2 treatment**
27.3° (3.27 Å)	27.5° (3.24 Å)	27.5° (3.24 Å)	0.00
56.4° (1.63 Å)	56.6° (1.63 Å)	56.6° (1.63 Å)	0.00

In addition to the rutile characteristic peaks observed with the treated (110) substrate, an additional seven $TiBO_3$ characteristic peaks (Figure 25) with d-spacings that are only a maximum of ±0.01 Å away from the literature data[145] (Table 9), are also seen.

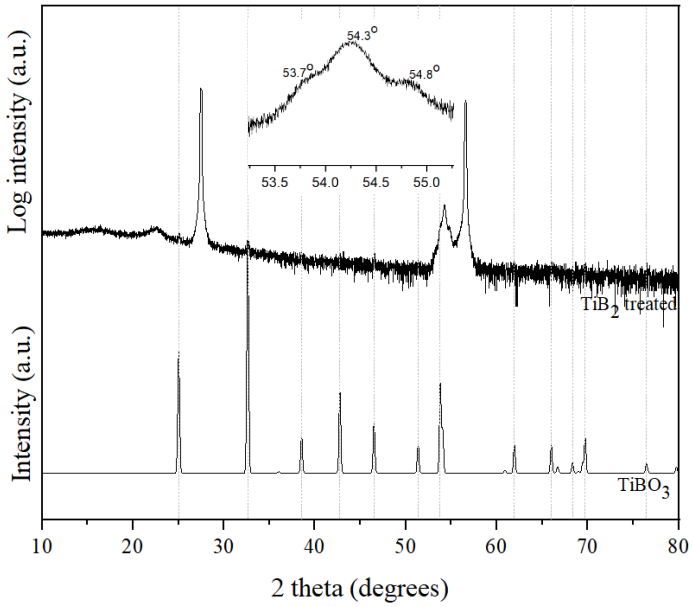

Figure 25 XRD pattern of the TiB_2 treated Rutile (110) substrate and literature-reported XRD pattern of $TiBO_3$ powder

Table 9 Measured 2θ and d-spacing (in brackets) values of the $TiBO_3$ peaks present in the TiB_2 treated rutile (110) substrate, compared with the literature data

2θ (°)		
Literature $TiBO_3$	**Measured TiB_2 treated Rutile (110)**	**Δ d spacing (Å)**
25° (3.56 Å)	25.1° (3.55 Å)	-0.01
32.6° (2.75 Å)	32.7° (2.74 Å)	-0.01
38.5° (2.34 Å)	38.5° (2.34 Å)	0.00
46.5° (1.95 Å)	46.6° (1.95 Å)	0.00
53.8° (1.70 Å)	53.7° (1.71 Å)	+0.01
54.1° (1.70 Å)	54.3° (1.69 Å)	-0.01
54.8° (1.68 Å)	54.8° (1.68 Å)	0.00

On the treated (110) rutile substrate, $TiBO_3$ is epitaxially arranged predominantly in the (108), (118) and (018) orientations (Table 10), since these are the reflections corresponding to the most intense $TiBO_3$-2θ peaks, which emerge at 53.7°, 54.3° and 54.8°. Each of these reflections are seen to have a twinned characteristic on the reciprocal space map (Figure 26). Since the difference in omega between each of the two components that make up each of the twinned feature is ≤1°, it can be suggested to represent three sets of twinned crystals, out of which two of them appear to be prominent at omega values of 29.5° and 26°.

Table 10 Measured 2θ and d-spacing (in brackets) values of the $TiBO_3$ peaks with the strongest intensity observed in the TiB_2 treated rutile (110) substrate and their corresponding reflections

Measured 2θ and d-spacing of TiB_2 treated Rutile (110)	Corresponding reflections in literature-reported $TiBO_3$ PXRD pattern
25.1° (3.55 Å)	(112) (102) (012)
32.7° (2.74 Å)	(014) (114) (104)
38.5° (2.34 Å)	(210) (120) (110)
46.6° (1.95 Å)	(222) (202) (022)
53.7° (1.71 Å)	(116), (216), (126)
54.3° (1.69 Å)	(108), (118), (018)
54.8° (1.68 Å)	(225)

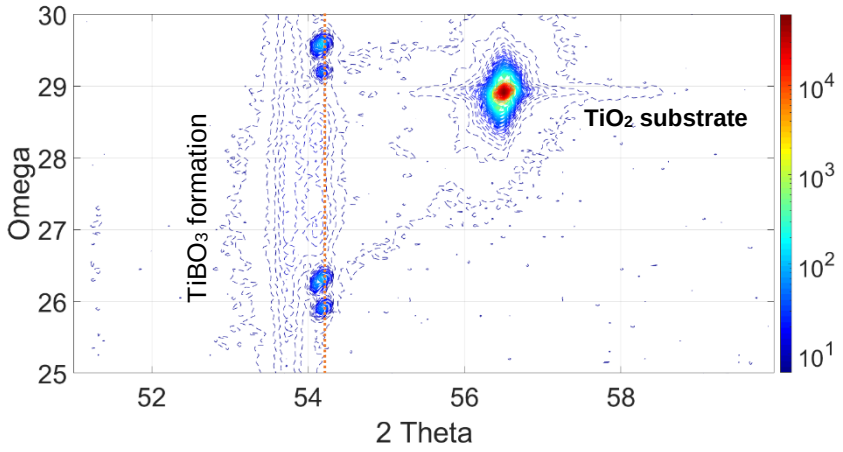

Figure 26 Reciprocal space map of the TiB_2 treated rutile (110) substrate. To see this figure on an extended scale and for the raw data collected, see Figure C and D in Appendices respectively

The XRD pattern measured of the rutile (100) substrate shows the presence of a peak at 39.3° with a d-spacing of 2.29 Å (Table 11). This corresponds to the peak at 39° (2.31 Å) in the literature data of the rutile (Figure 27). Upon TiB_2 treatment, the rutile (100) substrate peak remains at 39.3° (2.29 Å).

Table 11 Measured 2θ and d-spacing values (in brackets) of the rutile characteristic peaks in the as-received (100) substrate before and after TiB_2 treatment, compared with the literature data

2θ (°)			
Literature Rutile powder	Measured as-received Rutile (100)	Measured TiB_2 treated Rutile (100)	Δ d spacing (Å) - Rutile before and after TiB_2 treatment
39° (2.31 Å)	39.3° (2.29 Å)	39.3° (2.29 Å)	0.00

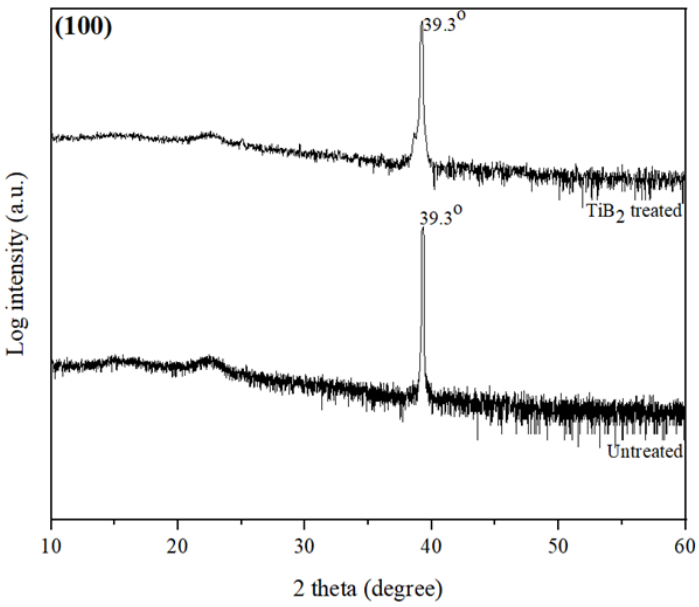

Figure 27 XRD pattern of the rutile (100) substrate before and after TiB_2 treatment

The XRD pattern of the TiB_2 treated (100) substrate shows the presence of a peak at 38.6º with a d-spacing of 2.33 Å (Figure 28). This matches with the $TiBO_3$ peak at 38.5º with a d-spacing of 2.34 Å, with the (210), (120) and (110) reflections (Table 12).

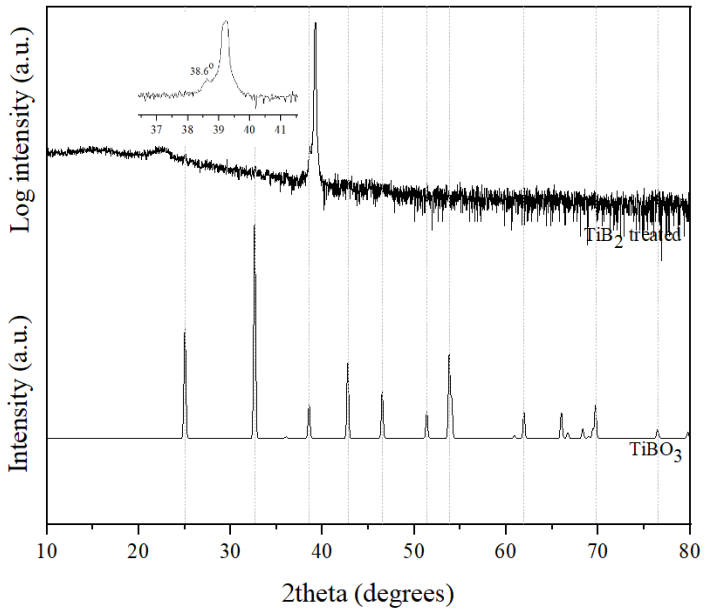

Figure 28 XRD pattern of the TiB_2 treated Rutile (100) substrate and literature-reported XRD pattern of $TiBO_3$ powder

Table 12 Measured 2θ and d-spacing (in brackets) values of the $TiBO_3$ peaks with the strongest intensity observed in the TiB_2 treated rutile (100) substrate and their corresponding reflections

2θ (°)		Δ d spacing (Å)
Literature $TiBO_3$	Measured TiB_2 treated Rutile (100)	
38.5° (2.34 Å)	38.6° (2.33 Å)	-0.01

The XRD peak of the untreated (001) substrate shows the presence of a 2θ peak at 62.8° with a d-spacing of 1.48 Å, which corresponds to the peak in the literature pattern of rutile which is located at 62.9° with a d-spacing of 1.49 Å (Table 13). Upon TiB_2 treatment, the presence of an additional peak at 63.4° with a d-spacing of 1.47 Å is also observed, which does not correspond to $TiBO_3$ a peak. The other possibilities are anatase or rutile (Table 14), which do not match either.

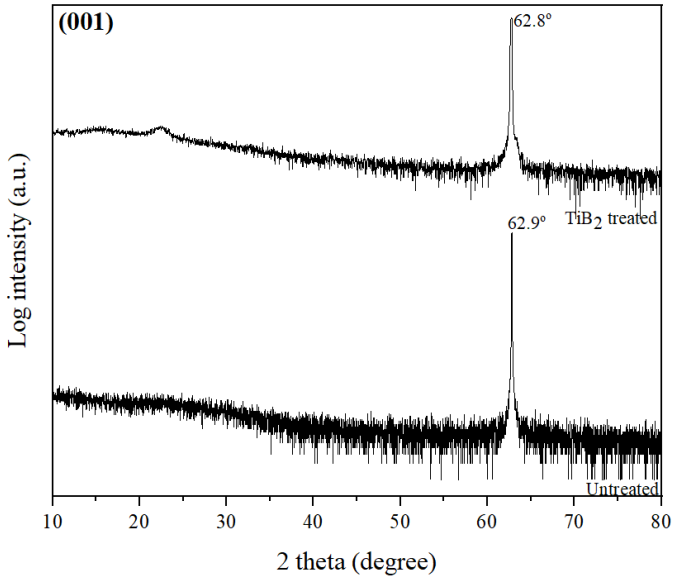

Figure 29 XRD pattern of the rutile (001) substrate before and after TiB_2 treatment

Table 13 Measured 2θ and d-spacing values (in brackets) of the rutile characteristic peaks in the as-received (001) substrate before and after TiB_2 treatment, compared with the literature data

2θ (°)			
Literature Rutile powder	Measured as-received Rutile (100)	Measured TiB_2 treated Rutile (100)	Δ d spacing (Å) - Rutile before and after TiB_2 treatment
62.9° (1.49 Å)	62.9° (1.48 Å)	62.8° (1.48 Å)	0.00

Since the rutile peak at 62.8° is only 0.6° away from the measured peak (Table 14) while the anatase peak at 62.7° is 0.7° away[146], the measured peak is potentially associated with rutile since the d-spacing remains the same for both these anatase and rutile peaks. Also, since the measured peak is 0.6° away from the rutile peak at 62.8°, the measured peak of the (001) treated rutile could potentially be due to boron

doped rutile. This suggests that the Raman peak observed at 776 cm^{-1} in the TiB_2 treated (001) substrate that was discussed to be corresponding to B_2O_3 (in section 4.1.2), are possible surface-bound species as evidence for these structures are not observed in the XRD data.

Table 14 Measured 2θ and d-spacing values (in brackets) of the TiB_2 treated (001) rutile substrate, compared with the literature data of anatase and rutile

2θ (°)		
Literature-reported value	**Measured TiB_2 treated Rutile (001)**	**Δ d spacing (Å)**
Anatase @ 62.7° (1.48 Å)	63.4° (1.47 Å)	-0.01
Rutile @ 62.8° (1.48 Å)		-0.01

The orientation of the incorporated $TiBO_3$ is found to be dependent on the orientation of the rutile single crystal substrates. On the treated (110) rutile substrate, $TiBO_3$ is epitaxially arranged predominantly in the (108), (118) and (018) orientations, while on the treated (100) rutile substrate, $TiBO_3$ is arranged in the (210), (120) and (110) orientations. On the other hand, there are no $TiBO_3$ XRD peaks observed.

4.1.4 Chemical Environments on the Depth scale

The chemical composition of the TiB_2 treated (110), (100) and (001) rutile substrates were studied using XPS. The concentration of B, Ti and O on the surface of these substrates were compared with that in their near surface or bulk. This was done by etching the surface off at periodic time intervals and measuring the chemical composition of the thus exposed surface. The resulting XPS depth profiles show the concentration of B, Ti and O at certain depths into the substrate, where 0 nm corresponds to the surface and anything > 0 nm corresponds to the surfaces exposed upon etching.

1. **Boron environment**

The as-received TiB_2 powder used for the anionic doping of rutile substrates, has two main XPS B1s peaks at 192.3 eV and 187.7 eV (Figure 29), corresponding to the B-O in B_2O_3 and Ti-B in TiB_2 respectively[147].

The presence of the surface-bound B_2O_3 was observed only on the surface of the (100) substrate, at 192.2 eV (Figure 30) as this XPS peak matched with the B_2O_3 XPS peak in the literature at 192.3 eV[147]. It is possible to distinguish between B_2O_3 and

$TiBO_3$ chemical environments in XPS spectrum as a peak at 192.6 eV has been found to correspond to H_2BO_3 (dihydrogen borate, $[BO(OH)_2]^-$ [148]. This information about surface-bound B_2O_3 was only picked up on the XPS data due to its surface sensitivity and not on the Raman spectrum. Therefore, it can be deduced that the B_2O_3 in the (100) substrate is relatively more surface-bound and its concentration is relatively less compared to that found in the (110) and (001) substrates. The deduction made earlier with the Raman data that B_2O_3 is absent in $TiBO_3$ containing areas can now be re-written as: B_2O_3 concentration is relatively lower in the presence of $TiBO_3$. The XPS B1s spectrum of the (110) substrate does not show any presence of a B_2O_3 chemical environment. It can be reasoned that this XPS data was collected from the non-$TiBO_3$ containing areas of the (110) substrate surface, where the $TiBO_3$ is non-homogenously distributed as per Raman data. The presence of B_2O_3 environment although was expected in the (001) substrate, as per Raman results, there is none observed in the XPS data. This potentially suggests that the B_2O_3 is non-uniformly distributed across the (001) surface.

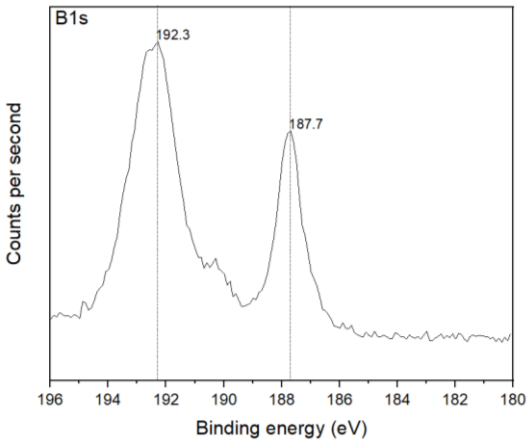

Figure 30 XPS B1s principal core line spectrum of the as-received TiB_2 powder used for anionic doping of the rutile substrates

The presence of interstitially located boron is observed only on the surface of (110) and the (001) substrate, at 192.0 eV (Figure 31). This incorporated boron is a surface bound species, as there is no evidence for its presence in the XRD or Raman data, which are less surface sensitive than the XPS. However, this peak at 192.0 eV also matches with the B_2O_3 XPS peak found in the literature at 192.1 eV.

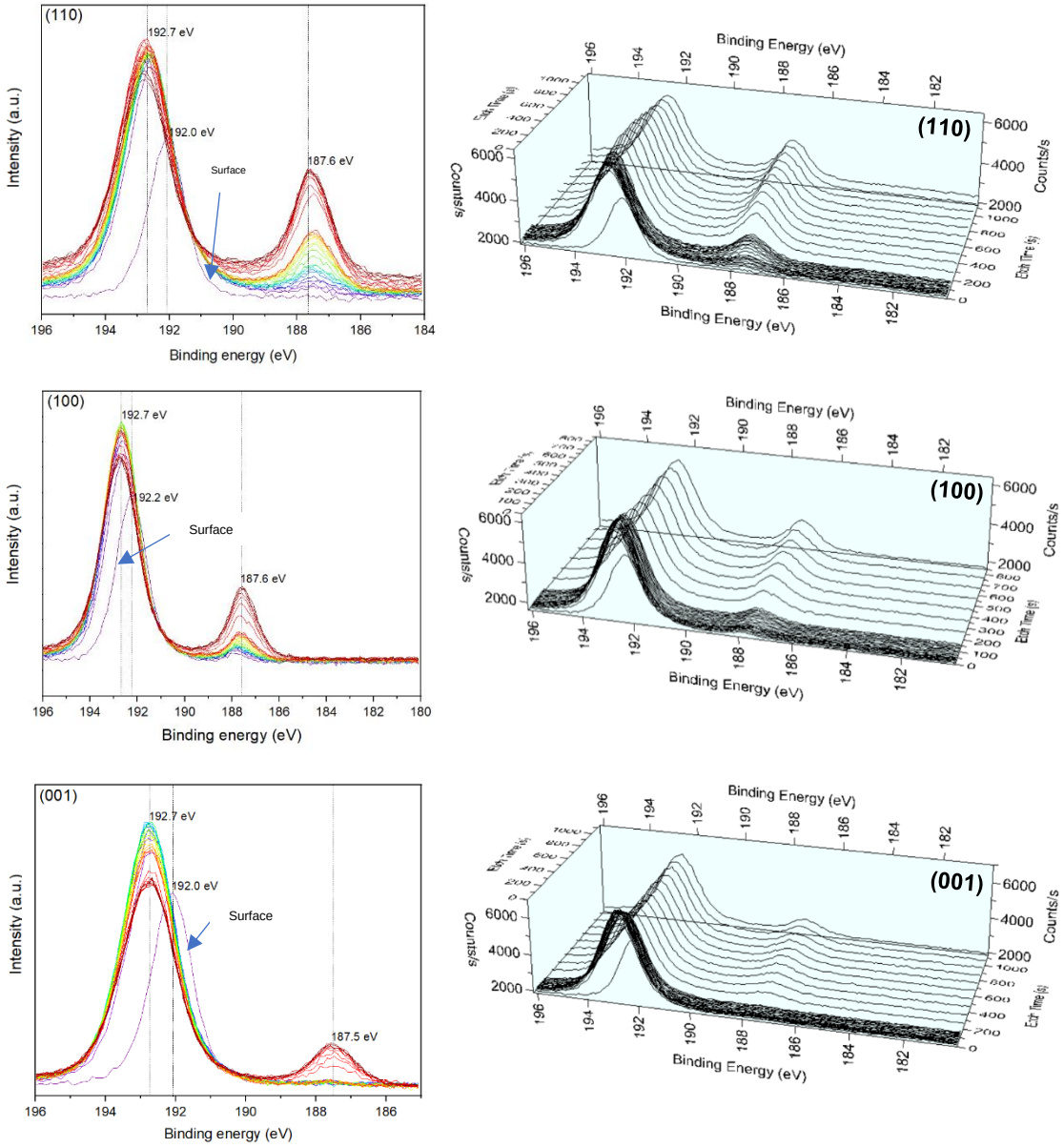

Figure 31 XPS B1s core line depth profile of the TiB_2 treated rutile (110), (100) and (001) substrates: (left) on a 2D scale and (right) on a 3D scale.

The XPS peak at 187.5 eV, which correspond to the TiB_2 chemical environment (187.7 eV), is seen to be present on the surface of the (110) and (100) substrates. Since, this is not indicated on the Raman or XRD data, it can be deduced that this chemical species is surface bound. On the other hand, the XPS of the (001) surface do not indicate this TiB_2 species, which was found in its Raman data. This suggests that the (001) may potentially have a non-uniform distribution of TiB_2 on its surface. The XPS peak at 192.7 eV observed in all the three substrates correspond to the H_3BO_3 chemical environment, which has a peak at 192.6 eV[148]. This environment may potentially be indicating the presence of $TiBO_3$. Since the XPS of the (001) substrate also shows this peak, it can be suggested that $TiBO_3$ may be present in low

concentrations, which may have been below the detection limit of Raman spectroscopy.

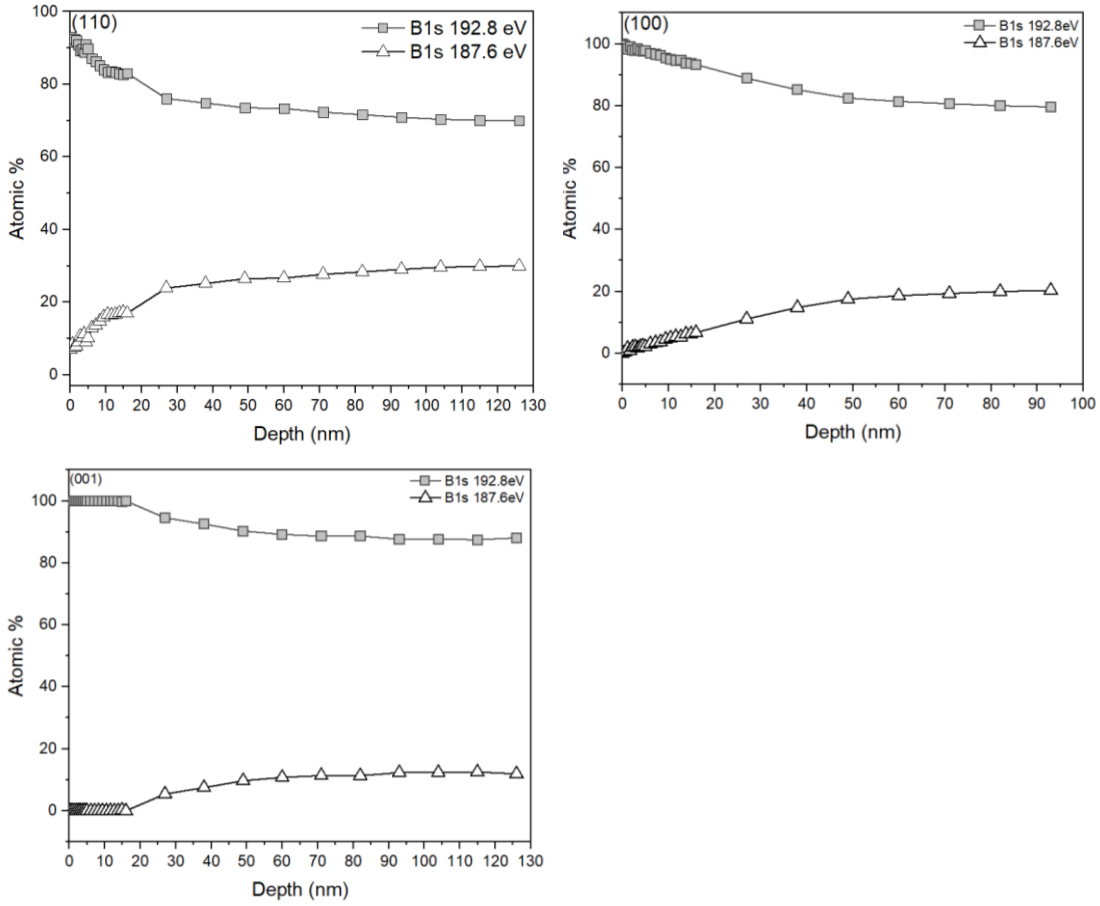

Figure 32 XPS depth profile of two types of boron environments in the TiB_2 treated (110), (100) and (001) substrates. The plots here indicate the ratio of the areas (in atomic%) for the two peaks observed in the B1s XPS spectrum

The $TiBO_3$ chemical environment (192.8 eV) is found be highest on the surface of all the three substrates (Figure 32). On the other hand, the TiB_2 chemical environment concentration (187.5 eV) is found to be lowest on the surfaces of all the three substrates. In all the three substrates, the $TiBO_3$ concentration decreases deeper into the substrate and the TiB_2 concentration increases deeper into the substrate. While the former observation could be rate limited by the diffusion of boron species into the rutile substrate, the latter observation could have a contribution from the reduction of the lattice from the XPS argon etching process.

2. **Titanium environment**

The Ti2p XPS principal core line spectrum of the as-received TiB_2 powder used for the TiB_2 treatment of the rutile substrates indicate the presence of two sets of doublet peaks (Figure 33). The doublet at 464.8 eV and 459.1 eV matches with the $Ti2p_{1/2}$

and $Ti2p_{3/2}$ orbital states in TiO_2, which are reported to be in the literature to be at 464.8 eV and 459 eV respectively. The peak at 454.6 eV matches with the $Ti2p_{3/2}$ chemical environment in TiB_2; whereas the doublet peaks at 459 eV and 464.8 eV matches with the $Ti2p_{3/2}$ and $Ti2p_{1/2}$ chemical environment in TiO_2[149]. The pure TiO_2 has a Ti2p spectrum with a doublet peak where the Ti $2p_{3/2}$ is positioned at 458.5 eV and the Ti $2p_{1/2}$ is positioned at 464.2 eV[150].

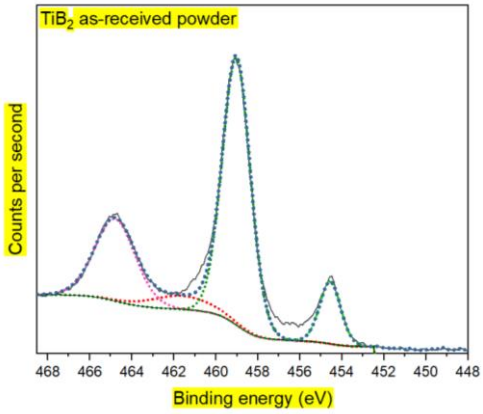

Figure 33 XPS Ti2p principal core line spectrum of the as-received TiB_2 powder used for anionic doping of the rutile substrates

The XPS Ti2p surface spectrum of the TiB_2 treated Rutile (110), (100) and (001) substrates (Figure 34) indicate the presence of TiO_2 environments. In the (110) substrate, these peaks are located at 458.5 eV and 464.2 eV, which are both +0.1 eV away from that seen in the pure TiO_2. In (100) substrate, these peaks are at 464.4 eV and 458.8 eV, which are +0.2 eV and +0.3 eV away from the pure TiO_2 peaks respectively. Similarly, in the (001) substrate, these peaks are situated at 464.4 eV and 458.5 eV, which is +0.2 eV and +0 eV away from the peaks in pure TiO_2 spectrum. These shifts are potentially due to the incorporation of boron in the TiO_2 lattice.

Beneath the surface, these characteristic TiO_2 peaks appear to be additionally shifted. With the (110) substrate, the Ti2p peaks are seen to be located at 464 eV and 458.1 eV, i.e. they are shifted by -0.2 eV and -0.4 eV respectively. With the (100) substrate, these peaks are seen to be located at 464 eV and 458.4 eV, i.e. they are shifted -0.2 eV and +0.1 eV from the pure TiO_2 peaks. On the other hand, with the (001) substrate, the Ti2p spectrum shows these peaks at 463.9 eV and 458.2 eV, which is -0.3 eV away from the peaks in pure TiO_2. The shifting of the Ti2p peaks observed is caused by the reduction of the lattice Ti^{4+}, which is caused by XPS ion gun etching.

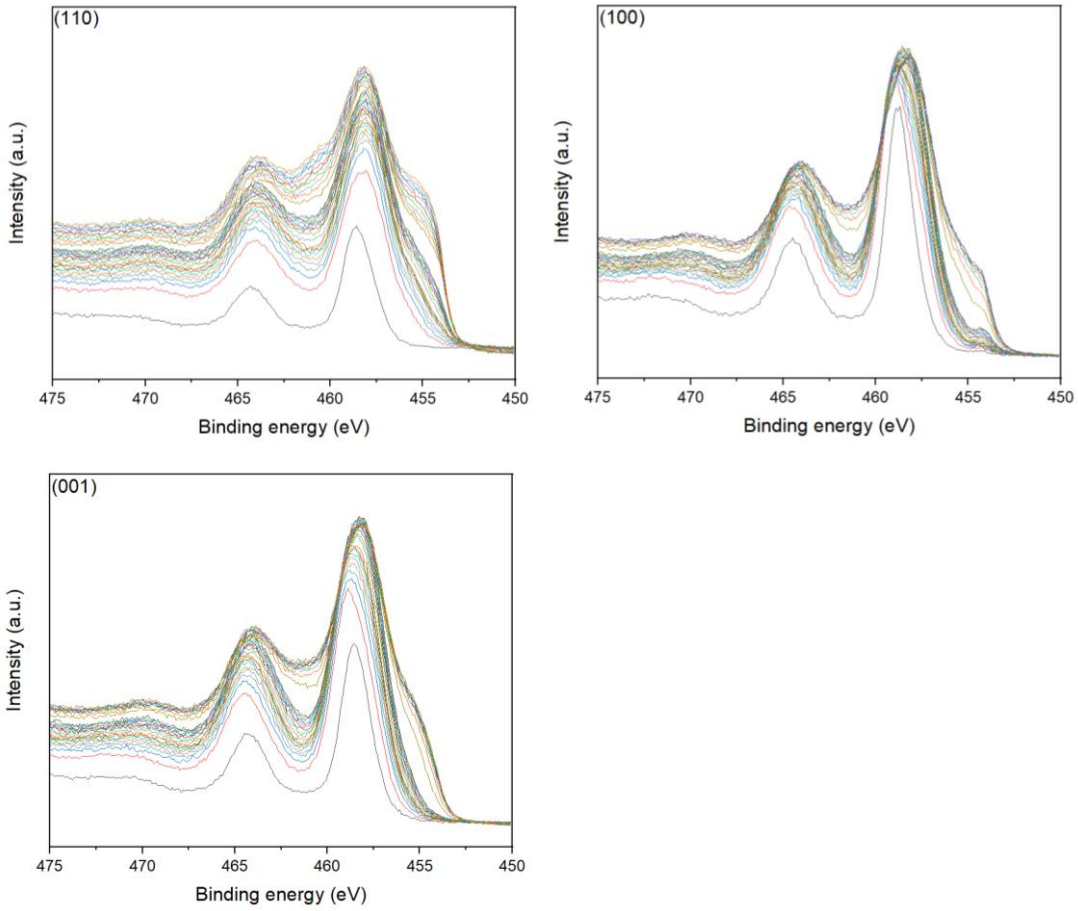

Figure 34 XPS Ti2p core line depth profile, 0 nm (surface, black curve) to 120 nm (bulk, coloured line), of the TiB_2 treated Rutile (110), (100) and (001) substrates. NB: The graph in black indicates the titanium concentration on the surface of the titania substrate and the coloured graphs indicate the titanium concentrations beneath the surface. The concentration of titanium changes with increasing depth – please refer to figure 36 for the corresponding graph of Ti concentration against depth.

In the TiB_2 treated TiO_2 (110), (100) and (001) substrates, the Ti is seen to be in two different chemical environments, as observed by the two sets of doublet peaks, one of which is the pure TiO_2, as discussed above, and the other which becomes prominent with increasing depth into the bulk of the substrates. The latter chemical environment is potentially Ti^{3+}. The ratio of Ti^{4+} compared to Ti^{3+}, is observed to decrease with increasing depth into the substrate and the presence of Ti^{4+} is observed on the surface as well as beneath the surface (Figure AF in Appendices).

3. **Oxygen environment**

The presence of the $TiBO_3$ chemical environment is also seen from the asymmetricity of the O1s core line at ~532 eV in the (110), (100) and (001) substrates (Figure 35). However, the XPS O1s spectrum is not widely used in the literature for reliable deductions on the chemical environments present.

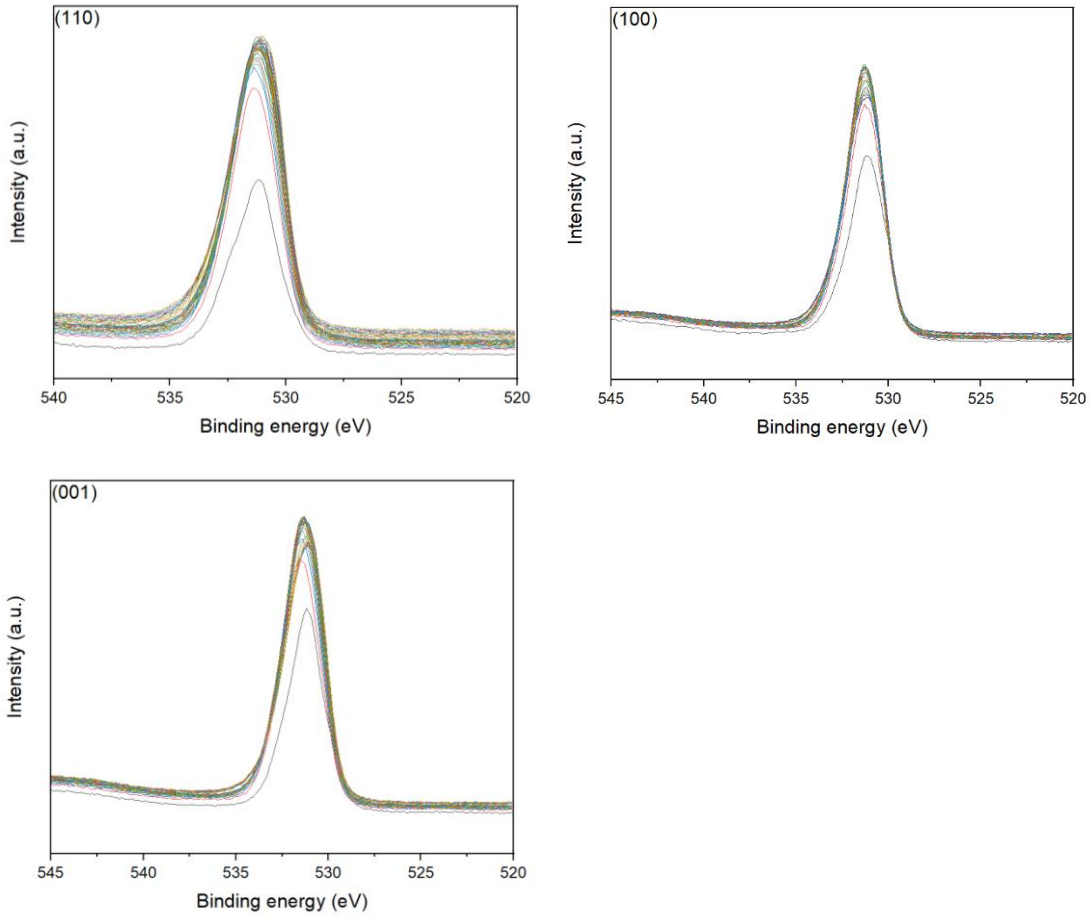

Figure 35 XPS O1s core line depth profile of the TiB_2 treated Rutile (110), (100) and (001) substrates. NB: The graph in black indicates the oxygen concentration on the surface of the titania substrate and the coloured graphs indicate the oxygen concentrations beneath the surface. The concentration of oxygen changes with increasing depth – please refer to figure 36 for the corresponding graph of O concentration against depth.

4. **Relative elemental concentration**

The TiB_2 treated rutile (110), (100) and (001) substrates have a chemical composition that is close to the $TiBO_3$ stoichiometry. Elemental ratios, O: Ti: B, in these substrates are observed to be 60: 20: 20 ± 8% (Figure 36, see Figure E in Appendices). This can be reasoned using the findings already discussed earlier. The stoichiometric similarity observed is because the $TiBO_3$ chemical environment (192.8 eV) is found be highest on the surface of all the three substrates. In (110), the ~8% variation from this stoichiometry on the surface could be caused by the presence of surface-bound interstitial boron and TiB_2 species along with the $TiBO_3$; while beneath the surface the TiB_2 solely is responsible for the variation. With the (100) substrate, this variation is caused by the presence of surface-bound B_2O_3 and TiB_2 species, while beneath the surface, the TiB_2 species is solely responsible for the variation from the $TiBO_3$ stoichiometry. On the other hand, with the (001) substrate, the stoichiometric variation on the surface is caused by the presence of interstitial boron species, while beneath

the surface, the TiB_2 species is solely responsible. In addition to the stoichiometric variation caused from the presence of other boron species, the non-homogeneity of the roughened sample surface, as observed from the AFM images, could be a potential cause of variation from the $TiBO_3$ stoichiometry in the recorded XPS depth profiles.

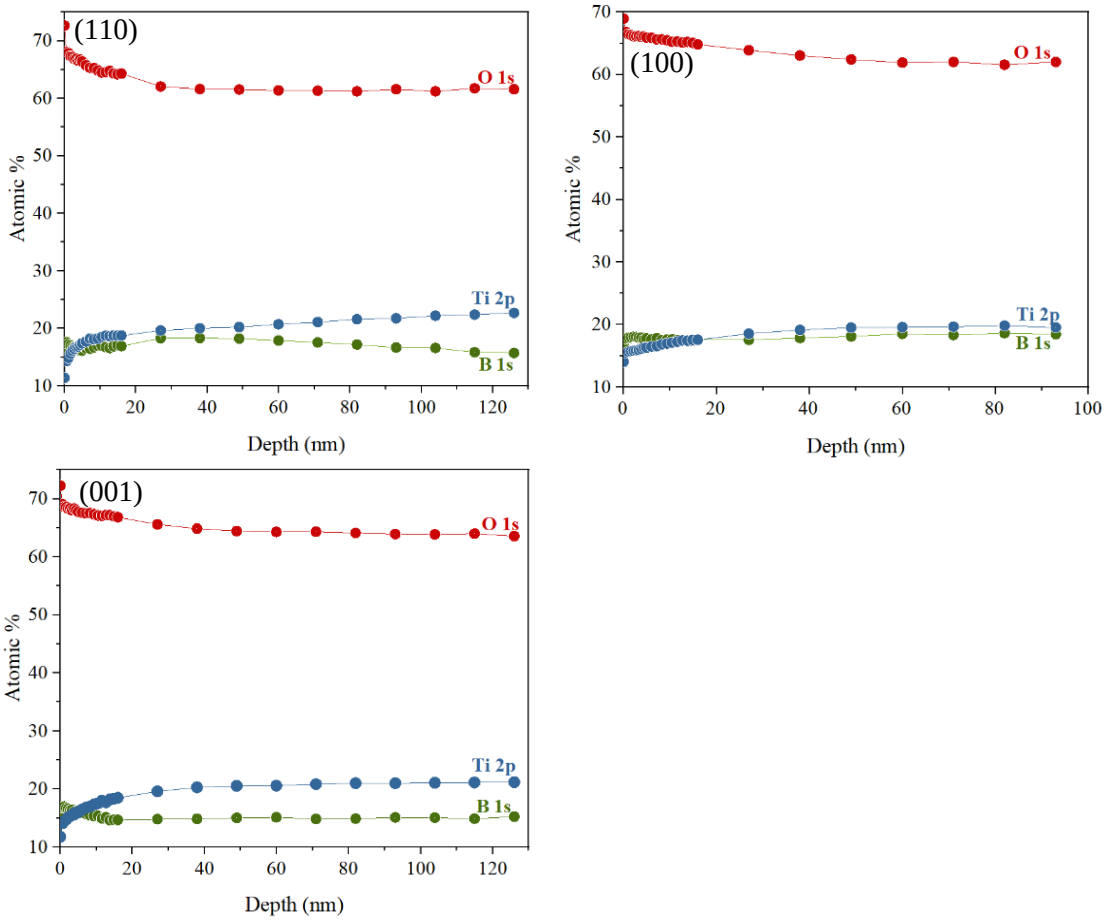

Figure 36 XPS depth profiles of TiB_2 treated Rutile (110), (100) and (001) substrates. The plots here indicate the ratio of the areas (in atomic%) for the Ti2p, O1s and B1s peaks present in the XPS spectrum

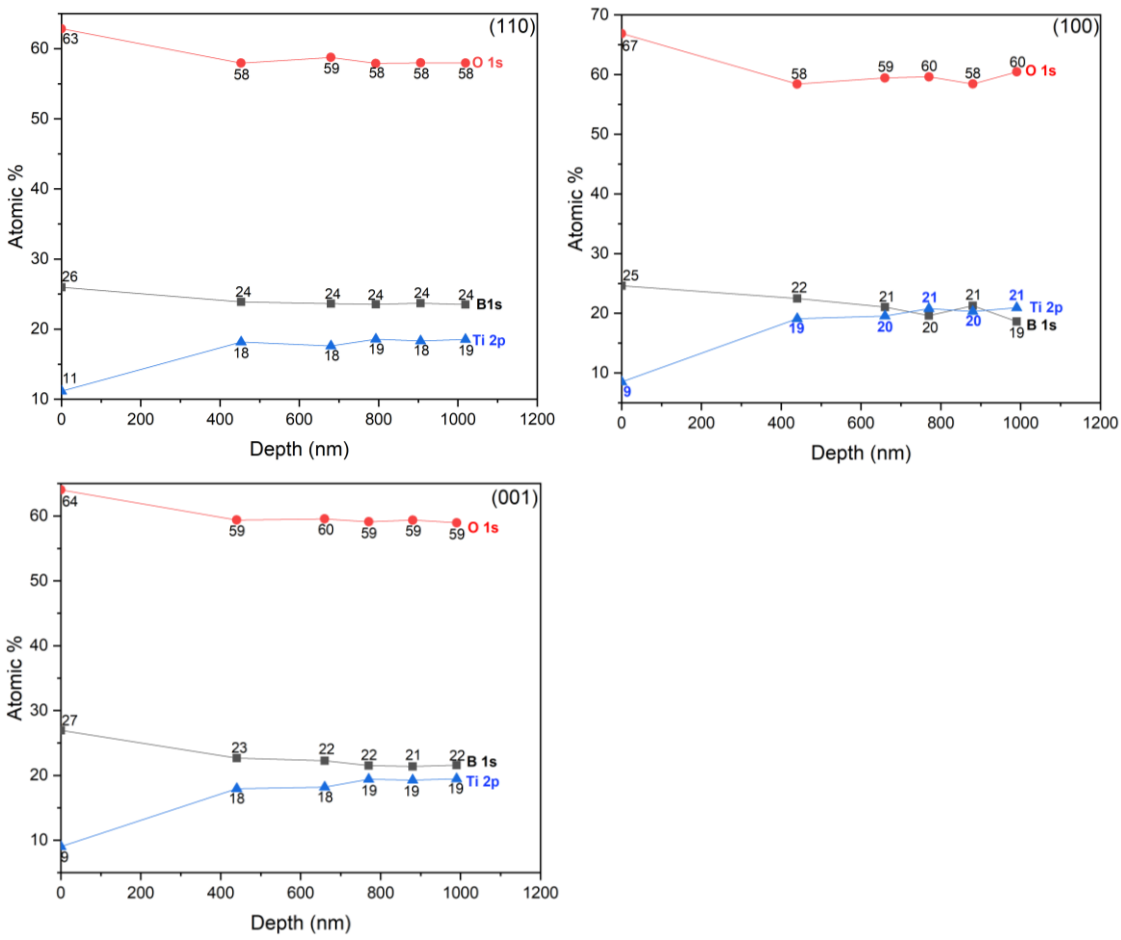

Figure 37 Extended – XPS depth profiles of TiB_2 treated rutile (110), (100) and (001) substrates

Even at 1000 nm, the boron concentration does not reach anywhere close to 0 atomic% and do not seem to meet the $TiBO_3$-TiO_2 interface (Figure 37). [*It is to be noted that the boron concentration in Figure 37 is higher than that in Figure 36. This is because the sample used to collect the data in Figure 36 was destroyed upon XPS etching and therefore, a fresh sample had to be used to collect data in Figure 37]*. This could potentially be due to at least one or more of the following hypotheses: (i) the $TiBO_3$ layer is very thick, (ii) the $TiBO_3$ layer is indestructible or (iii) the $TiBO_3$ layer is being pushed deeper into the substrate by the XPS argon etching, making it challenging to probe the $TiBO_3$-TiO_2 interface. Please note that these are hypothesis, which means that it is neither studied nor reported in the literature and therefore has future research scope. On the other hand, the TiB_2 concentration increases deeper into the substrate. This could be an effect of the reduction of the TiB_2 treated Rutile, caused by the XPS argon etching. All the XPS B1s depth profiles would look the same if this was the case and this certainly is not the case. The XRD data of the (001) substrate do not indicate the presence of $TiBO_3$ while the XPS elemental depth profile (Figure 36) shows the presence of $TiBO_3$ even at depths of 1000 nm. From this, it can

be deduced that the small concentration of $TiBO_3$ present on the (001) substrate surface (as observed on its surface scan) may have been pushed into substrate during the XPS argon etching process. Therefore, further considerations in future work for avoiding this scenario would be to use a cluster gun source. It is to note that the concentration of boron, titanium and oxygen in the depth profiles in Figure 36 is ~10% less than that observed in the extended depth profiles in Figure 37. This is potentially because the depth profiles in Figure 36 was measured in the scanning mode while that in Figure 37 was measuring the snapshot mode, where some of the qualitative resolution may have been lost. Also, since XPS depth profiling is a destructive technique, therefore it is expected to see differences observed between the XPS and Raman data for example.

4.1.5 Chemical Environments on the Near surface

The relatively more surface sensitive angle resolved XPS was also used to study the chemical composition of the surface of the TiB_2 treated (110), (100) and (001) Rutile substrates. This technique is non-destructive unlike the K-alpha XPS used for recording the depth profiles above. Due to this same reason, the elemental concentrations measured using both these instruments will have a variation. Additionally, the non-homogenous characteristic of the substrate surfaces could also contribute to this variation. In the angle resolved XPS depth profile, small angles indicate bulk sensitive data whereas higher angles indicate surface sensitive data. It is to be noted that the strongest signal in these measurements is achieved with the emission angle of 90^o to the normal and the weakest signal with the lowest emission angle. This means that the intensity of the XPS signal decreases with smaller emission angles. Therefore, it is important that the elemental concentrations deduced from these measurements should be discussed with respect to another element that is present in the sample.

1. **Boron environment**

The angle resolved XPS depth profile of the B1s principal core line shows the presence of only one peak in the rutile (110), (100) and (001) substrates (Figure 38). In the (100) and (001) substrate, this peak is located at 192.5 eV, which corresponds to the B-O chemical environment. As per the K-alpha XPS depth profile, these could possibly correspond to the $TiBO_3$ in (100) and interstitial boron species in the (001) substrate. It is to be noted that the TiB_2 species observed in the K-alpha XPS depth profile of the surface of the (110) and (100) substrates are not observed in the angle

resolved XPS data. This suggests that the TiB_2 concentrations on the surface are below the detection limit of the angle resolved XPS instrument.

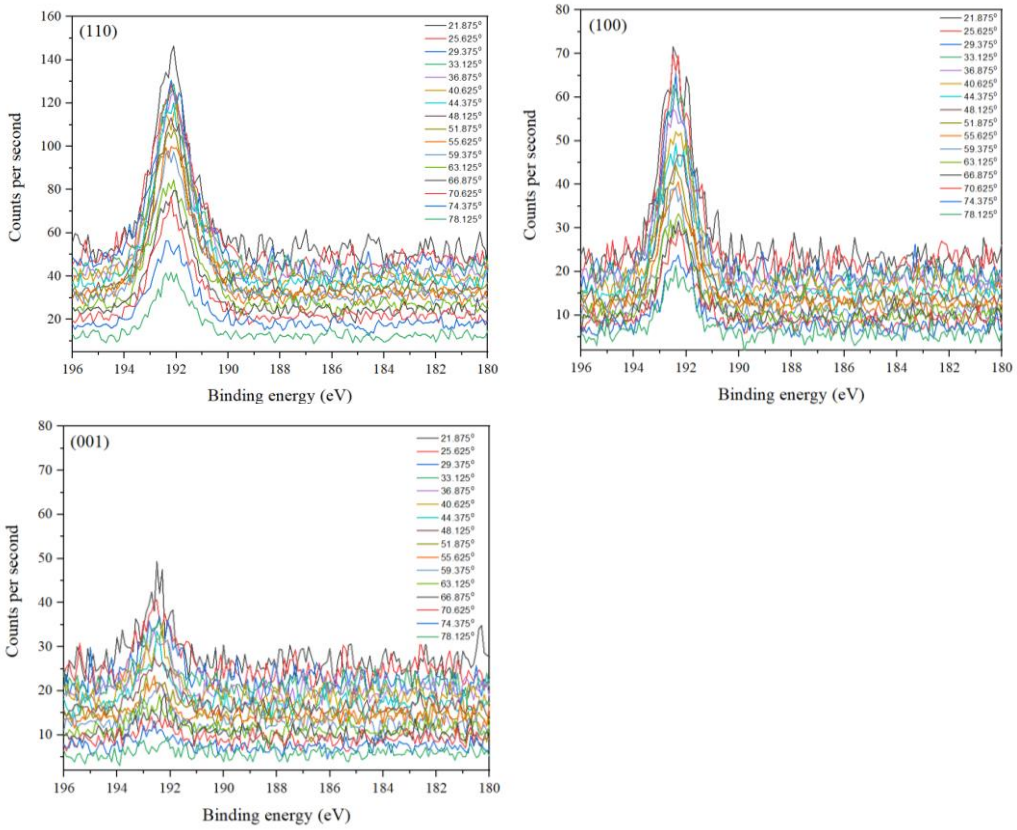

Figure 38 Angle resolved XPS B1s depth profile of the TiB_2 treated rutile (110), (100) and (001) substrates

2. **Titanium environment**

The Ti-O and Ti-B chemical environments are seen in all the three substrates (Figure 39). It is to be noted that the asymmetry of the Ti 2p peak is more evident with the (110) and (100) spectrum than with the (001) substrate. This is expected from the Raman spectrum and XRD data of the (001) substrate, which do not indicate the presence of any $TiBO_3$. Therefore, the $TiBO_3$-like environment that is observed in the K-alpha XPS data could be beneath the surface that is probed by the angle resolved XPS and may have a lateral non-homogenous arrangement.

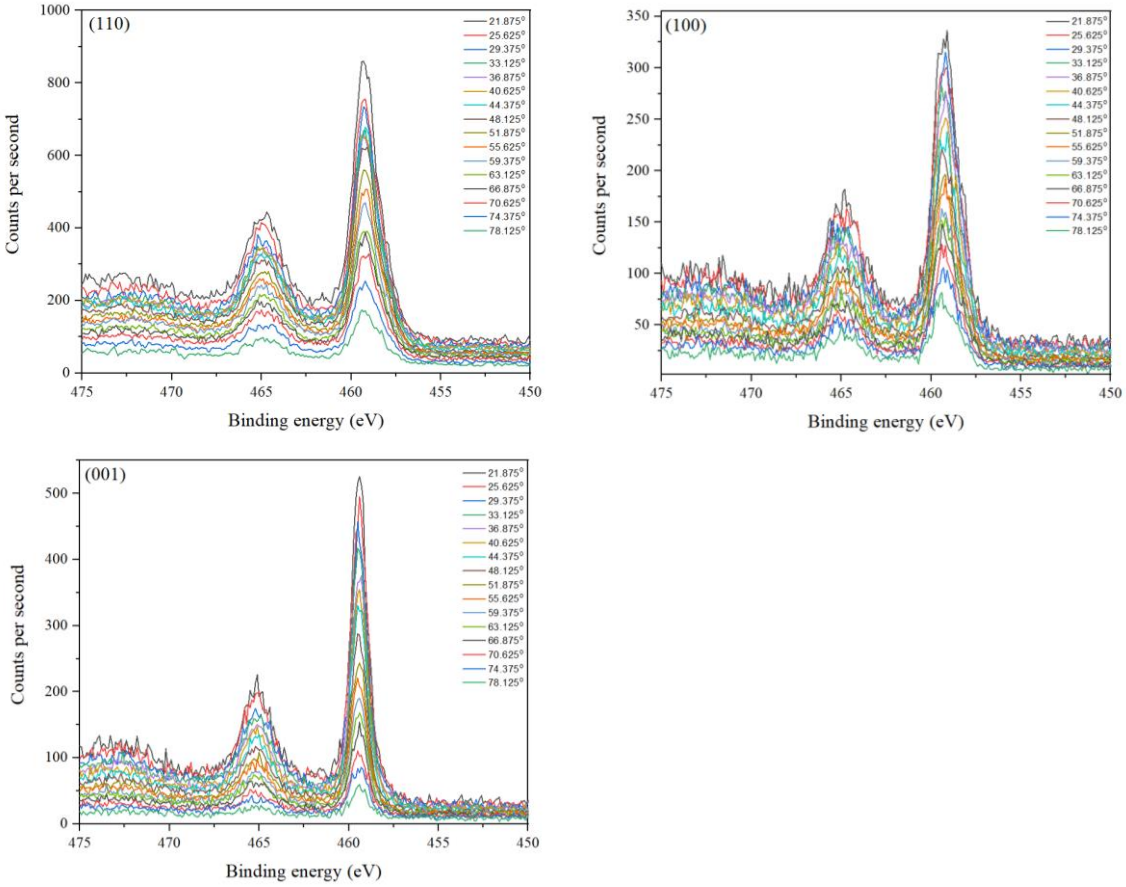

Figure 39 Angle resolved XPS Ti2p depth profile of the TiB_2 treated rutile (110), (100) and (001) substrates

3. **Oxygen environment**

The angle resolved O1s XPS spectrum of the Rutile (110) and (100) substrates show two peaks at ~533 eV and ~532 eV (Figure 40), which correspond to the B_2O_3 and $TiBO_3$ environments respectively. In the (001) substrate however, there is a peak located at ~533 eV, which corresponds to the non-homogeneously distributed interstitial boron species (as per Raman data); and the peak located at ~531 eV corresponds to TiO_2 environment on the substrate surface that are not covered with the interstitial boron species.

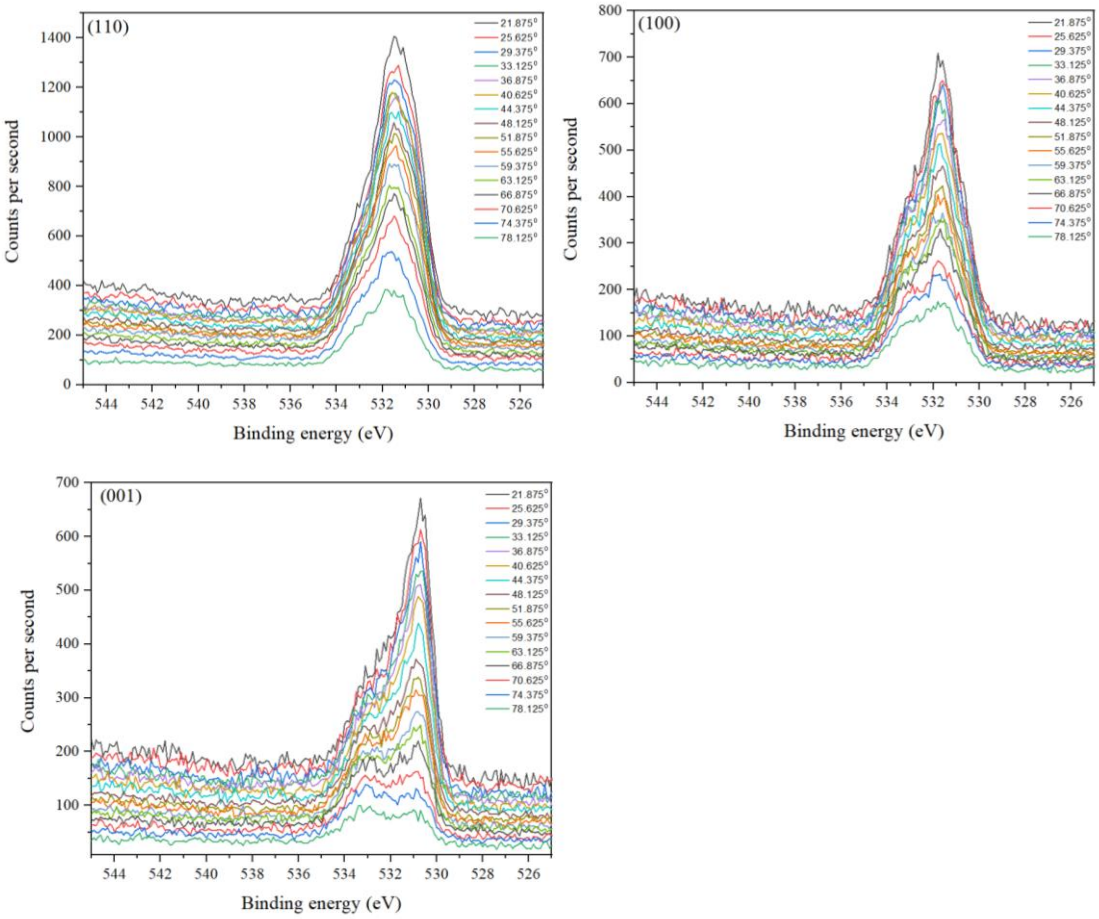

Figure 40 Angle resolved XPS O1s depth profile of the TiB_2 treated rutile (110), (100) and (001) substrates

4. **Relative elemental concentrations**

An angle resolved XPS spectrum of the surface of TiB_2 treated (110), (100) and (001) substrates indicate that the ratio of O: Ti: B is 60: 20: 20 ± 10 atomic% (Figure 41). This ~10 atomic% variation from the $TiBO_3$ stoichiometry could be caused by the presence of other boron containing species. In the (110) substrate, it could be caused by the non-homogeneously distributed $TiBO_3$ species. In the (100) substrate, it could be caused by the presence of the B_2O_3 species along with the $TiBO_3$ species. On the other hand, with the (001) substrate, it could be caused by the presence of the interstitial boron species and relatively low concentrations of the $TiBO_3$ species compared to the (110) and (100) substrates.

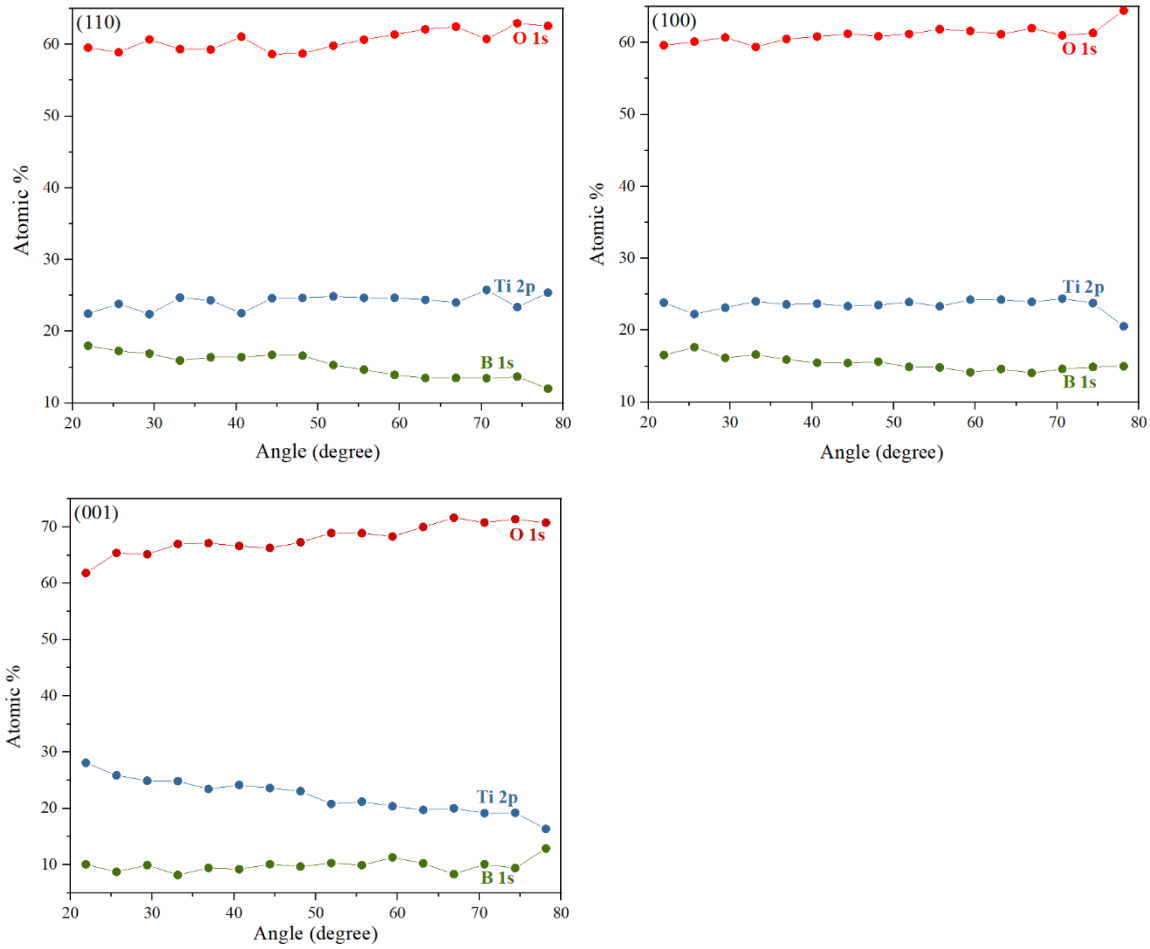

Figure 41 Angle resolved XPS elemental depth profile of the TiB_2 treated rutile (110), (100) and (001) substrates

4.1.6 Electronic Structure

The valence band can be measured using the XPS, where an X-ray source is used, and a UPS, where a UV source is used.

1. **XPS valence band**

NB: The XPS valence band onset is extracted from an XPS Valence band spectrum by extrapolating the straight-line region of the lower end of the spectrum towards the x-axis and reading off the x-axis intercept, as indicated in the TiB_2 spectrum in Figure 42.

Upon TiB_2 treatment, the XPS valance band onset measured of the surface of the rutile (110), (100) and the (001) substrates (Figure 42) have shifted to higher binding energies (Table 15). The greatest shift of 0.49 eV was observed with the (110) substrate, which appears to be the most disordered surface with B_2O_3, TiB_2, interstitial boron species and a clearly distinguishable non-uniformly distributed $TiBO_3$ (i.e. seen in the Raman, XRD and XPS data). On the other hand, the smallest shift of 0.07 eV

is observed with the (001) oriented substrate, which appears to have the least disorder surface consisting of interstitial boron species and a not very clearly distinguishable $TiBO_3$ species (i.e. only seen in the XPS data). The literature suggests that the blue shift in the valence band onset observed is due to the interstitially doped boron[151]. The blue shift has also been reported to be observed in TiB_2 core/ TiO_2 shell particles, with a B_{int} concentration gradient in the shell, where the electrons in the B_{int} contributed towards a band bending effect[152]. However, this cannot be the case as the (100) substrate surface characterisation did not show any evidence for the presence of interstitial boron. This surface however, indicated the presence of B_2O_3, and a clearly distinguishable uniformly distributed $TiBO_3$ (i.e. seen in the Raman, XRD and XPS data). This shows that the (110) substrate has four different boron species, the (100) substrate has three while the (001) substrate potentially has two different types of boron species. This suggests that the (110) substrate surface is the most disordered and therefore, has experienced the most shift in its electronic valence band onset.

Table 15 XPS valence band onset of TiB_2 treated rutile (110), (100) and (001) substrates

Titania substrate orientation	XPS Valence Band (eV)	
	Untreated	TiB_2 treated
(110)	1.20	1.69
(100)	1.18	1.62
(001)	1.19	1.26
TiB_2 dopant source powder	2.72	N/A

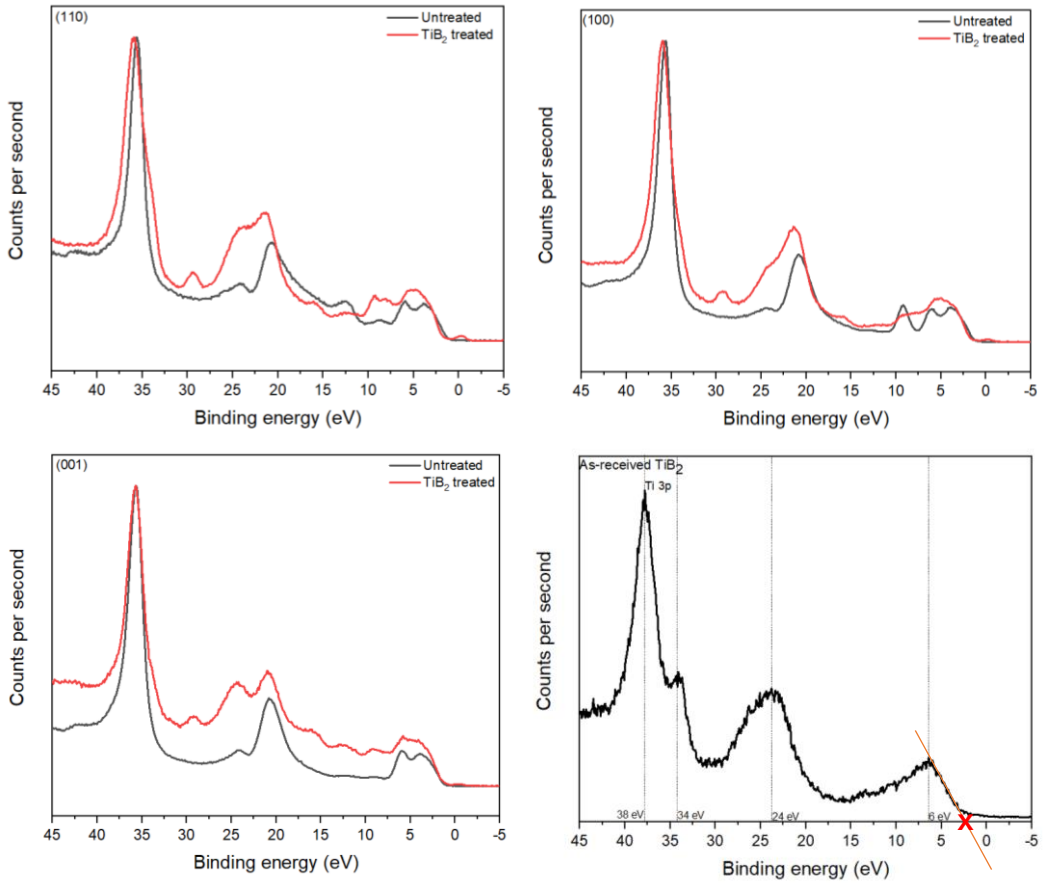

Figure 42 XPS valence band spectrum of the TiB_2 treated rutile (110), (100) and (001) substrates along with that of the TiB_2 powder used for the TiB_2 treatment

In the XPS valence band spectrum, 0 eV corresponds to the fermi level and the region >0 eV corresponds to the valence band, which is mainly made of O2p, and the region < 0 eV correspond to the conduction band, which is reported to be mainly constitute of Ti3d, Ti4s and Ti4p[153].

The XPS valence band of the untreated (110), (100) and (001) substrates looks similar except for the following features. The (100) orientation has a very intense peak at 10 eV, which is slightly visible in (110) substrate, but not at all visible in the (001) substrate. In the Raman spectra of these untreated substrates, discussed earlier (see section 4.1.2), the asymmetric bending mode {caused by the movement of the O atoms in opposite directions across the O-Ti-O bonds in the (001) plane} in the (001) substrate was seen to be weak unlike the untreated (110) and (100) substrates. This suggests that the feature at 10 eV in the valence band spectrum could be related to this O-Ti-O asymmetric bending mode. Upon TiB_2 treatment, this peak is observed to be split into 2 peaks in (110) substrate, broadened in the (100) substrate, and become

more intense in the (001) substrate. This could suggest that the boron is incorporated into these O-Ti-O bonds.

The rest of the peaks that appear in the XPS valence band spectrum are the same in the as-received rutile (110), (100) and (001) substrates and can be assigned using literature data. The peak at ~36 eV can be assigned to Ti 3p, arising from any inherent Ti^{3+} defects in the pure rutile lattice, which is also reported to be found in Ti_2O_3 [154]. The peaks in the range 27 eV to 15 eV, centred at ~24 eV and ~21 eV corresponds to O 2s[155]. The peaks located in the 10 eV to 7 eV range, centred at ~6 eV and ~4 eV corresponds to the O 2p orbital contribution, which can be deconvoluted into the O 2p σ and O 2p π contributions[156].

The broadening of the O 2s peak between ~24 eV and 21 eV upon TiB_2 treatment is similar in the (110) and (100) substrates, with the greatest broadening observed with the (110). The broadened peak can be deconvoluted into two distinct peaks at 24 eV and 21 eV. The valence band spectrum of the as-received TiB_2 dopant source powder (Figure 42) shows the presence of the peak at 25 eV with a similar shape as that of the broadened peak at 24 eV. From this it can be deduced that the increase in contribution observed at ~24 eV is potentially caused by the mixing of the O2s state with B1s states arising from the surface-bound TiB_2 species present in both these substrates, as per XPS surface spectrum. On the other hand, in the (001) substrate this broadening does not occur to the same extent but does occur to the 24 eV peak and therefore, may correspond to the surface-bound interstitial boron species. Since the new state indicated by the peak at 30 eV appears in all the three substrates, it can be suggested to correspond to the Ti3p state associated with the $TiBO_3$ surface-bound defect species. Since the $TiBO_3$ has been found to be non-homogeneously distributed across the surface of the Rutile substrate, as per Raman data, the peak at 36 eV could be corresponding to the Ti3p orbital contribution from the host rutile lattice.

The 10 eV to 3 eV region is dominated by O2p contribution of the valence band in pure TiO_2. Upon TiB_2 treatment of the (110) and (100) substrates, the two-humped peak in this region is observed to be broadened into a single peak, like what is observed in the XPS valence band spectrum of the as-received TiB_2 dopant source powder. This suggests that the broadening is caused by the mixing of the B1s states arising from the surface-bound TiB_2 defect species with the O2p states from the host rutile-TiO_2 lattice. On the other hand, upon TiB_2 treatment of the (001) substrate, this

two-humped peak in the 10 eV to 3 eV region is seen to be broadened but is not seen to transform into a single peak like the (110) and (001) substrate. This suggests that the broadening is caused by the presence of interstitial boron species with the B1s states in the rutile-TiO_2 lattice. The small peak at 10 eV in the (001) substrate is seen to remain the same, suggesting that the O2p contribution from the pure rutile lattice remains the same. However, in the treated (100) substrate the intense peak at 10 eV is seen to be broadened. This means that the O-Ti-O bonds along its (001) plane, which the intense 10 eV peak is thought to correspond to, is weakened. Since the shape of the broadened peak looks like but not exactly the TiB_2 valence band spectrum, it can be deduced that the broadening is caused by the contribution from the cationic boron species in the $TiBO_3$ which is mixing with the O2p states. On the other hand, in the TiB_2 treated (110) substrate, a two-humped peak is observed at 10 eV, which may have resulted from the epitaxially arranged $TiBO_3$ on the host Rutile lattice. This feature may have potentially come from the O2p and cationic boron species contributions from the $TiBO_3$.

There is also a metal like feature observed just below the Fermi level (= 0 eV), upon TiB_2 treatment in all three substrates, but this feature is seen to be more prominent in the (110) and (100) substrate, where $TiBO_3$ formation was more clearly observed. This suggests that the metal like contribution, which makes up the conduction band, could be from the Ti3d orbitals of $TiBO_3$.

2. **UPS valence band**

The UPS valence band of the as-received rutile substrate shows two main characteristic peaks centred at 6 eV and 8 eV, which are reported to correspond to the π O2p and σ O2p orbitals[157] respectively. In addition, there is a peak centred at ~13 eV, which is seen to be most intense with the (110) substrate, which may potentially be due any inherent Ti^{3+} defects in the pure rutile lattice. Upon TiB_2 treatment, the peaks at 6 eV and 8 eV are seen to merge into a single peak in (110) (Figure 43). This suggests the presence of the mixing of the O2p orbitals with the new B1s state arising from the surface-bound TiB_2 species. The same is observed with the (001) substrate, except that it is caused by the surface bound interstitial boron defect species. On the other hand, with the (100) substrate, the peak at 8 eV is slightly broadened while the peak at 6 eV is not broadened. This suggests that the mixing of the B1s states from the surface-bound TiB_2 species occurs predominantly with the σ O2p states and not much with the π O2p states.

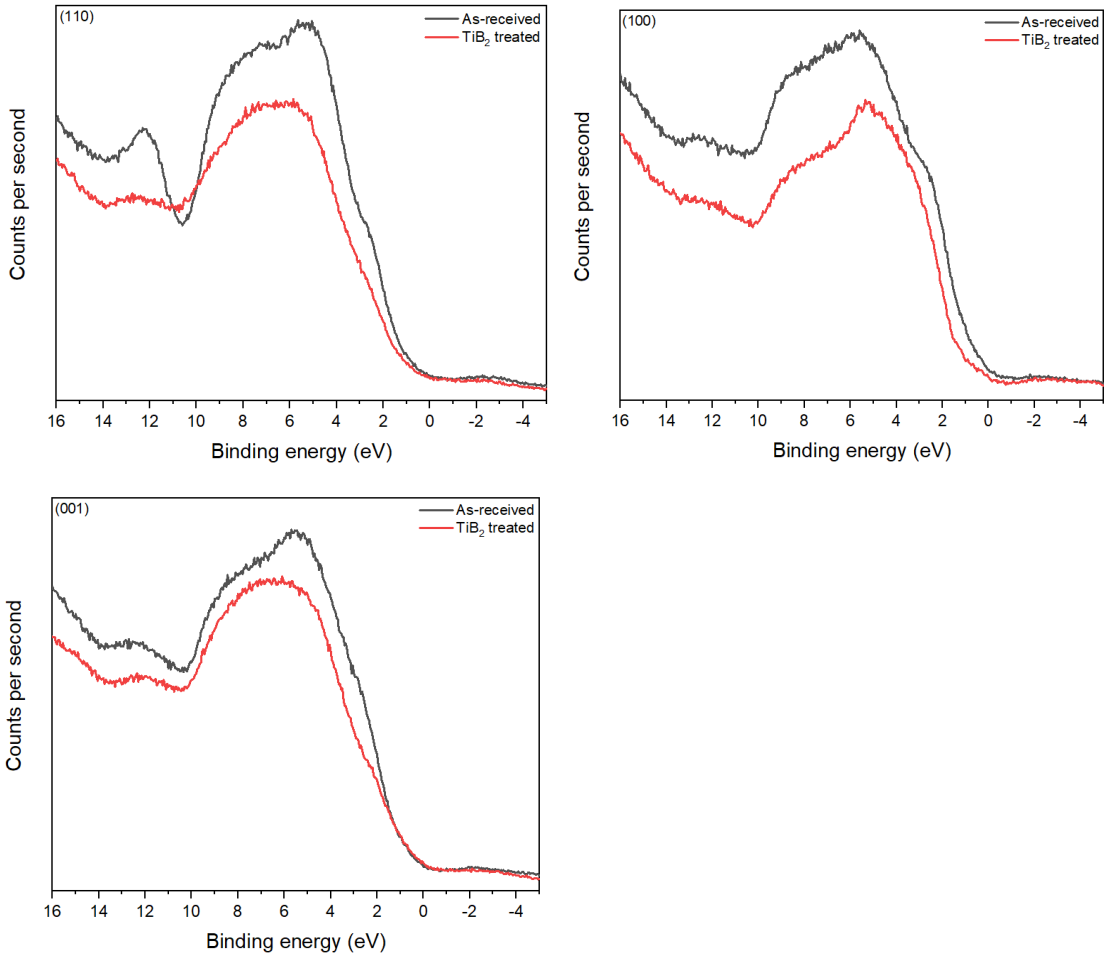

Figure 43 UPS valence band spectrum of the TiB_2 treated Rutile (110), (100) and (001) substrates measured using He (II) source

4.2 Summary of Findings

The boron is observed to be incorporated into the rutile substrates of the orientations (110), (100), (001) upon treatment with TiB_2, but not as a dopant. The asymmetric O-Ti-O bonds in the rutile substrate were weakened to different extents, as indicated by the differences in morphology of the roughened surfaces, which was found to be dependent on the substrate orientation. The $TiBO_3$ surface formation is dependent on the substrate orientation while the B_2O_5 or B_2O_3 surface formations are dependent on the concentration of $TiBO_3$ formed on the rutile substrate. The $TiBO_3$ is epitaxially arranged, predominantly in the (108), (118) and (018) orientations, onto the rutile (110) substrate. However, on the (100) substrate, the $TiBO_3$ is epitaxially arranged in the (210), (120) and (110) orientations. On the other hand, the XRD peak shift observed in the (001) substrate, indicates the incorporation of boron into the lattice, as boron doped rutile. Surface bound boron containing defect species were present in concentrations below the detection limit of Raman was observed in the K-alpha XPS data. For example, in the (100) substrate, the presence of surface bound B_2O_3 and TiB_2 was observed, while surface bound interstitial boron species were observed in the (110) and (001) substrate. The XPS depth profiles also indicated stoichiometry across the depth scale to be close to that of $TiBO_3$ with ~10% variation, which could be caused by the presence of the other boron containing defect species other than $TiBO_3$. The greatest blue shift in the XPS valence band was observed with the (110) surface, which had four different boron containing defect species, while the (001) had the smallest blue shift from its two different boron defects. The surface-bound TiB_2 species has resulted in B1s-O2s and B1s-O2p orbital mixing in the (110) and (100) substrates, while the surface-bound boron interstitial species caused it in the (001) substrate. New O2p and B1s states were formed at ~10 eV from the $TiBO_3$ in the (110) and (100) substrates. New Ti3d states arising from $TiBO_3$ were found below the fermi level in all the three substrates. A new Ti3p state from the $TiBO_3$ is also observed alongside the Ti3p state from the host rutile lattice, suggesting the significance of the bulk and surface crystal structure in the electronic structure of a material. The B1s sates were found to be mixed with the σ O2p states more than with the π O2p states in the (100) substrate.

4.3 Future Considerations

The future work that can be carried out as an extension to the work reported in this chapter is:

1.**Effect of XPS argon etching**

The effect of XPS argon etching on the $TiBO_3$ layer located on the Rutile (110), (100) and (001) substrates can be investigated using a cluster or a single ion source. The effect upon varying the ion energy and other etching parameters can also be investigated.

Chapter 5: Carbon Diffusion in Rutile single crystal substrates

A detailed characterisation of the rutile substrates of the orientations (110), (100) and (001) treated using the TiC dopant source powder (referred to as TiC treated rutile) is discussed below.

5.1 Results and Discussion

The topography, composition and bonding on the surface and the bulk of the TiC treated rutile substrates were carried out.

5.1.1 Surface Topography

Upon TiC treatment, the surface topography of the as-received (110), (100) and (001) rutile substrates (Figure A in Appendices) were observed to be significantly roughened, as per AFM images (Figure 44). However, this roughened topography caused by the TiC treatment is different compared to that caused by the TiB_2 treatment. This shows the effect of the choice of anion (e.g. carbon or boron) on the extent and type of roughening caused on the rutile surface.

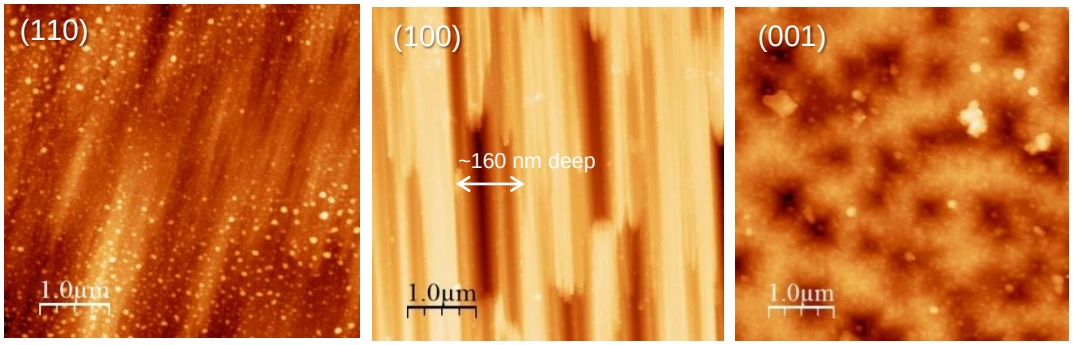

Figure 44 AFM images showing the differences in the morphology of the roughened surfaces of TiC treated rutile substrates (110), (100) and (001)

Different levels of roughening are observed in the (110), (100) and (001) rutile substrates, suggesting the effect of the rutile substrate orientation on the extent and type of surface roughening caused. The RMS roughness values of the (110), (100) and (001) substrates, after the TiC treatment, were observed to increase from being < 0 nm to become 3.3 nm, 36 nm and 46 nm respectively (Table 16). However, the increase in roughness upon TiC treatment is relatively less compared to that observed upon TiB_2 treatment (Table 7). With the (110) oriented substrate, the surface is observed to be modified by the formation of trenches (Figure F in Appendices), which

are ~2 μm wide. The (100) surface is modified by the formation of ~2-3 μm wide trenches too but with better defined edges, where the deepest trench is seen to have a depth of ~160 nm (Figure 45). On the other hand, the trenches observed with the (001) surface are circular in shape.

Table 16 A comparison of the surface roughness of rutile substrates before and after TiC treatment

	RMS roughness (nm)		
	(110)	(100)	(001)
Untreated	0.58	0.86	0.45
After TiC treatment	3.3	36	46
Increase in roughness	**3**	**35**	**46**

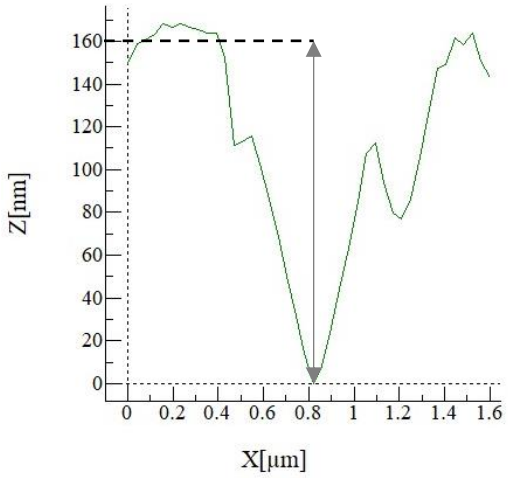

Figure 45 Line profile indicating the depth of one of the trenches on the TiC treated (100) rutile substrate, marked and labelled in figure 45

5.1.2 Surface Bonding

Upon TiC treatment, the position of the rutile characteristic peaks in the Raman spectrum of the (110), (100) and (001) substrates remained the same at 444 cm^{-1} and 608 cm^{-1} (Figure 46). This suggests that any changes in the rutile structure were not detectable using Raman spectroscopy. However, this was not the case with the peaks located at 1361 cm^{-1} and 1600 cm^{-1}, which still correspond to any mixed sp^2/ sp^3 carbon contamination on the surface[139 140]. In the (110) substrate, these peaks are seen to disappear after TiC treatment, while in the (100) and (001) substrates, these peaks are seen to almost disappear and are shifted to lower wavenumbers. This may suggest that the defect is being removed upon TiC treatment, increasing the crystallinity of the rutile substrates (Figure G, H, I in Appendices). A homogeneous

composition of the surface is thought to be achieved with the TiC treated (110), (100) and (001) substrates. This is because the spectra were found to be reproducible.

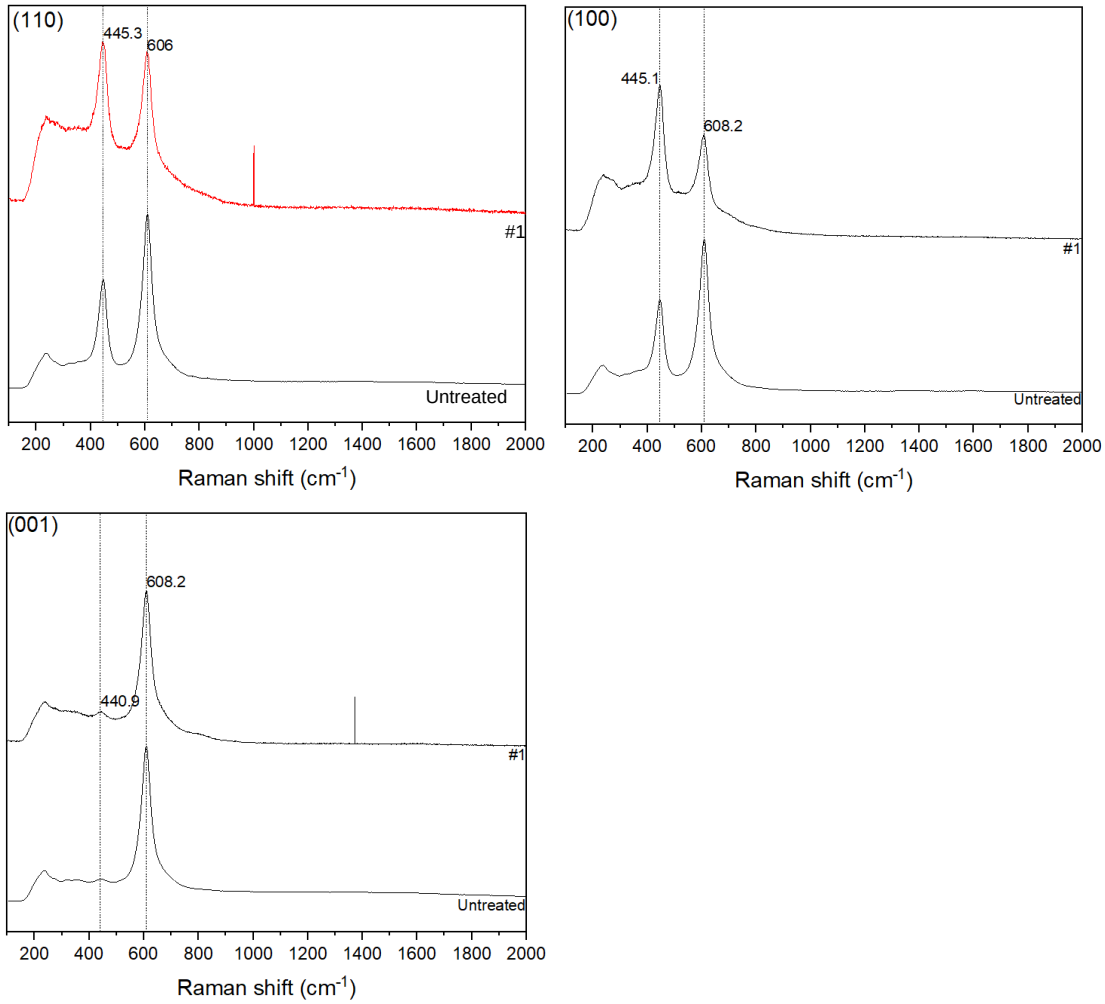

Figure 46 Raman spectrum of the untreated and TiC treated rutile substrates of the orientations (110), (100) and (001), where #1 indicates an area on the substrate surface

The position of the Raman peaks is characteristic of the bonding vibrations in materials. Since there are no peak shifts observed upon TiC treatment of the (110), (100) and (001) substrates, it can be deduced that the rutile bonding structure is retained upon TiC treatment. Therefore, the change in peak intensities observed in the (110) and (100) substrates could be due to the decomposition of the rutile bonding structure caused by the TiC treatment, which is what is suggested for similar Raman data observed in the literature for nitrogen doped titania[158]. With the (110) substrate, the intensity of the 445 cm^{-1} peak becomes like that of the 606 cm^{-1} peak, suggesting that the asymmetric vibration of the O-Ti-O bond in the (001) plane has similar magnitude as the symmetric vibration of the O-Ti-O bonds in the (110) plane.

With the (100) substrate, the 445 cm^{-1} peak becomes more intense than the

606 cm^{-1} peak, suggesting that the asymmetric vibration of the O-Ti-O bond in the (001) plane has larger magnitude than the symmetric vibration of the O-Ti-O bonds in the (110) plane. On the other hand, no such changes are observed with the (001) substrate upon TiC treatment. There are no additional Raman peaks observed upon TiC treatment of the substrates. This suggests that no new phases are formed, and the possibility of carbon incorporated as a dopant, which may have caused the observed weakening of the rutile host lattice bonds.

5.1.3 Chemical Environments on the Depth scale

The concentration of the carbon incorporated into the surface and the bulk of the rutile substrates and the possibility of carbon diffusion is investigated using XPS.

1. **Relative elemental concentration**

The elemental XPS depth profile shows a smooth diffusion of carbon from the surface into the bulk of the TiC treated rutile (110), (100) and (001) substrates (Figure 47).

The carbon concentration is found to be highest on the surface for all the substrates, with ~55 atomic% in (110), ~39 atomic% in (100) and ~41 atomic% in (001). This also shows that the carbon concentration was the greatest on the (110) surface and least on the (100) surface. The carbon concentration is observed to be < 5 atomic% at ~5 nm into the (110) substrate, at ~0.2 nm in the (100) substrate and at ~10 nm into the (001) substrate. This shows that the carbon concentration in the near-surface was greatest in the (001) substrate and lowest in the (100) substrate. So, overall (100) has incorporated the least amount of carbon which lie predominantly in the top 0.2 nm and most of the carbon in the (110) substrate is predominantly in the top 5nm while most of the carbon in the (001) substrate is in the top 10 nm. When the carbon concentration is < 5 atomic%, the O: Ti ratio becomes close to that found in pristine TiO_2, i.e. 67: 33 ± 2 atomic%, in all the three substrates. This suggests that the incorporated carbon is predominantly surface-bound in all the three substrates. Even at a depth of ~120 nm, the carbon concentration is seen to remain at ~0.2 atomic% in all the three substrates, suggesting that the carbon diffusion trail into the bulk of the substrate continues (Figure 47 right).

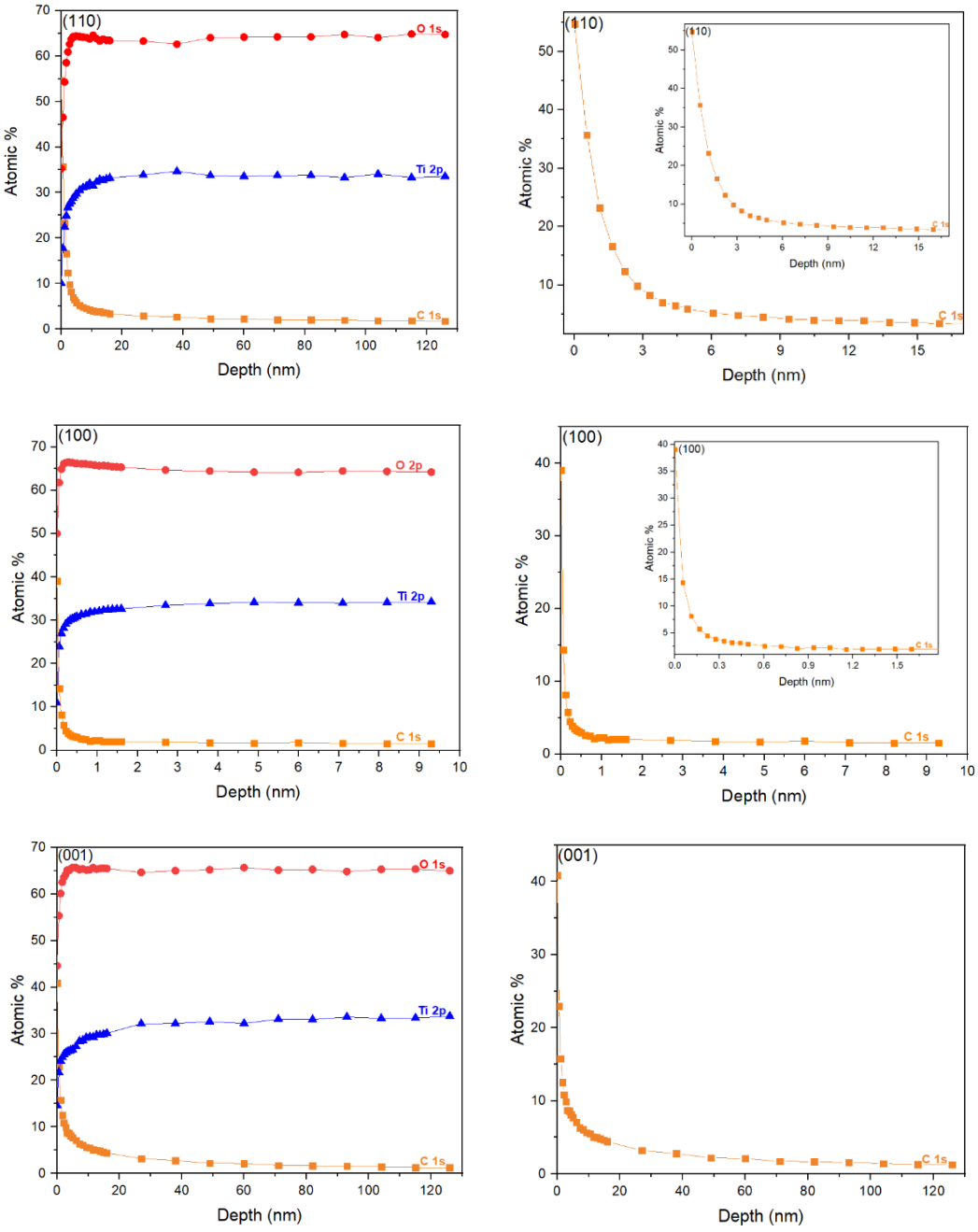

Figure 47 XPS depth profile of TiC treated rutile (110), (100) and (001) substrates showing (left) the O, Ti and C elemental profiles and (right) a zoomed in version of the carbon depth profile by itself, showing the carbon concentrations more clearly

The carbon is diffused into each of the substrates with more than one diffusion rate, which is usually deduced from the diffusion coefficient calculated using Fick's second law of diffusion[89]. The carbon diffusion coefficients extracted from the carbon diffusion plots (Figure 48, 49 and 50) are summarised in Table 17.

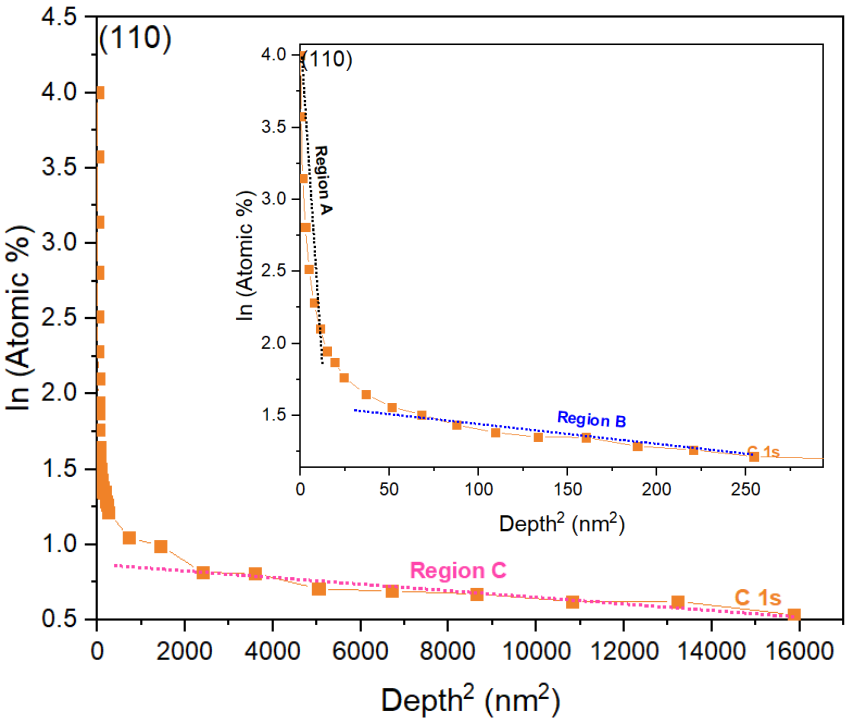

Figure 48 The carbon diffusion gradient of the TiC treated (110) rutile substrates

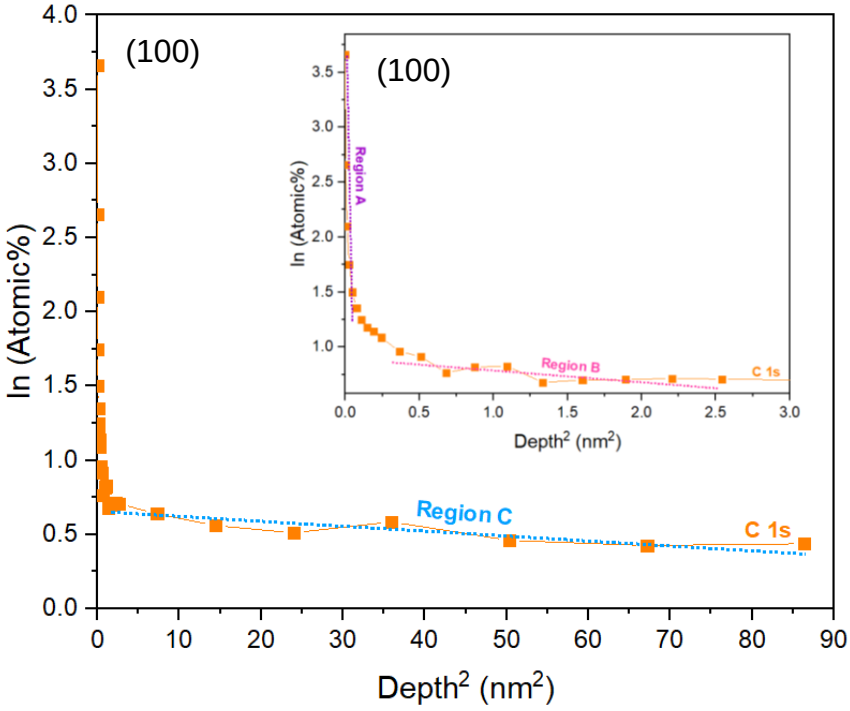

Figure 49 The carbon diffusion gradient of the TiC treated (100) rutile substrates

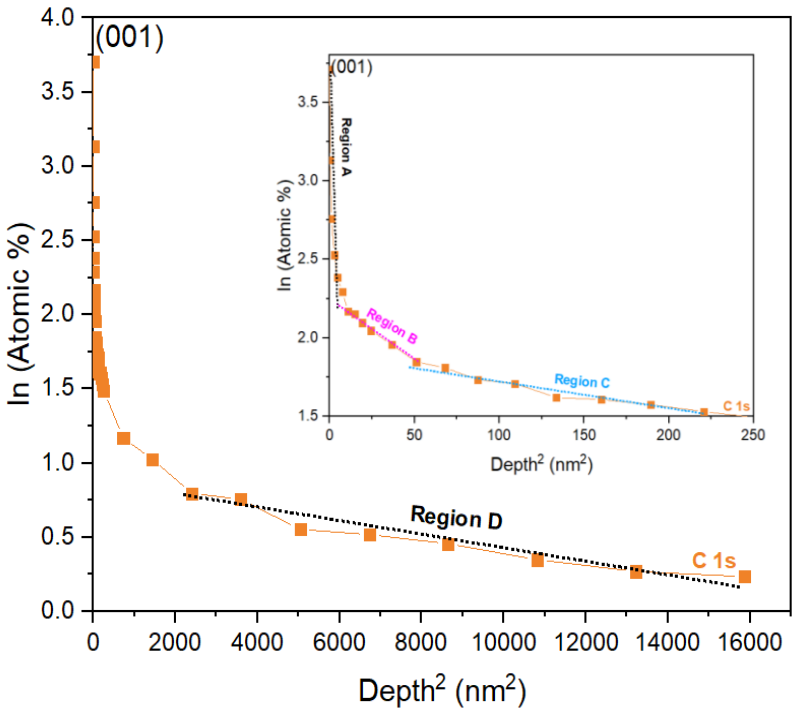

Figure 50 The carbon diffusion gradient of the TiC treated (001) rutile substrates

Table 17 The carbon diffusion coefficients and carbon concentrations at different depths into the TiC treated rutile (110), (100) and (001) substrates

Fastest carbon diffusion			
	110	**100**	**001**
Depth into the substrate	~44 nm and ~120 nm	~9 nm and ~2 nm	~15 nm and ~7 nm
Carbon concentration	0.2 atomic%	~0.2 atomic%	~5 atomic%
Diffusion coefficient	-2.1421 x 10^{-5} nm^2 s^{-1}	-0.0032 nm^2 s^{-1}	-0.0017 nm^2 s^{-1}
Second fastest carbon diffusion			
	110	**100**	**001**
Depth into the substrate	~7 nm and ~16 nm	~2 nm and ~1 nm	~7 nm and ~1 nm
Carbon concentration	~0.3 atomic%	~0.2 atomic%	~10 atomic%
Diffusion coefficient	of -0.00135 nm^2 s^{-1}	-0.1133 nm^2 s^{-1}	-0.0075 nm^2 s^{-1}
3rd fastest carbon diffusion			
	110	**100**	**001**
Depth into the substrate	0 nm and 7 nm	<1 nm	< 1nm
Carbon concentration	~55 atomic%	~36 atomic%	~41 atomic%
Diffusion coefficient	-0.1893 nm^2 s^{-1}	-73.4 nm^2 s^{-1}	-0.435 nm^2 s^{-1}
Slowest carbon diffusion			
	110	**100**	**001**
Depth into the substrate			~120 nm and ~45 nm
Carbon concentration			0.2 atomic%
Diffusion coefficient			-4.4833 nm^2 s^{-1}

The fastest and slowest carbon diffusion rates are not found at the same depths in the (110), (100) and (001) rutile substrates (Table 17). The fastest carbon diffusion is

observed to occur with the lowest carbon concentration of 0.2 atomic%, which is located deepest in the (110) and (100) substrates, i.e. between ~44 nm and ~120 nm in the (110) and between ~9 nm and ~2 nm in the (100) substrate. The slowest carbon diffusion is observed with the highest carbon concentration, 55 atomic% in (110) and 36 atomic% in (100) substrate, which is located on the surface, between 0 nm and 7 nm in (110) while between 0 nm and 1 nm in the (100) substrate. On the other hand, with the (001) substrate, the fastest carbon diffusion is seen between depths of ~15 nm and ~7 nm, for the carbon concentrations of up to 5 atomic%; while the slowest carbon diffusion is observed for the lowest carbon concentration (0.2 atomic%) located deepest within the substrate at depths between ~120 nm and ~45 nm.

2. **Carbon environment**

The chemical environment of the surface-bound carbon incorporated into the rutile substrates are deduced from their XPS core line spectra.

The as-received TiC powder used for the TiC treatment of the rutile substrates, has four main XPS C1s peaks (Figure 51). The peak at 282 eV corresponds to the C-Ti[159] chemical environment in TiC, while the other three peaks correspond to the environments typically found in adventitious carbon contaminated surfaces. These three peaks are positioned at 289 eV, 286.5 eV and 285 eV and corresponds to the O-C=O, C-O-C[160] and C-C [159] carbon environments respectively.

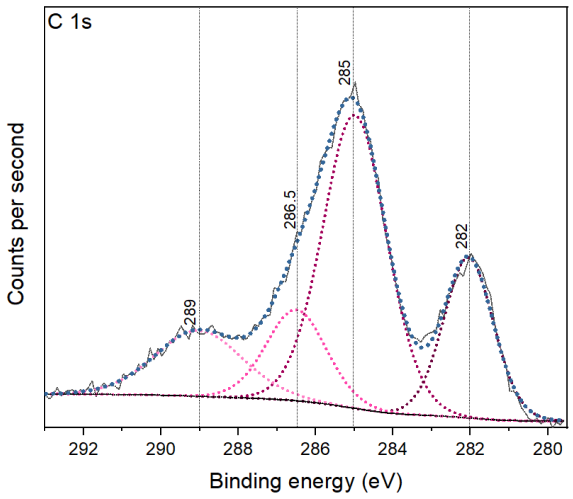

Figure 51 XPS C1s principal core line spectrum of the as-received TiC powder used for anionic doping of the rutile substrates

The carbon in the rutile (110), (100) and (001) substrates are observed to be in chemical environments that correspond to those found in adventitious carbon contamination, as per their XPS C1s core line spectrum (Figure 52). With the (110) and (001) substrates, the carbon is in the O-C=O and C-C environments, indicated by the peaks at ~289 eV and ~285 eV respectively. However, with the (100) substrate, the carbon is in the O-C=O, C-O-C and C-C environments, indicated by their peaks at ~288 eV, ~287 and ~285 eV. Therefore, one may deduce from this that the carbon observed here is from adventitious carbon contamination and not from the TiC dopant source powder. However, adventitious carbon contamination cannot induce the modifications in the chemical bonding vibrations observed in the Raman spectrum. Also, the carbon concentration is observed at least to a depth of 120 nm into substrate. Therefore, it can be suggested that the carbon from the TiC treatment has incorporated carbon into the rutile lattice.

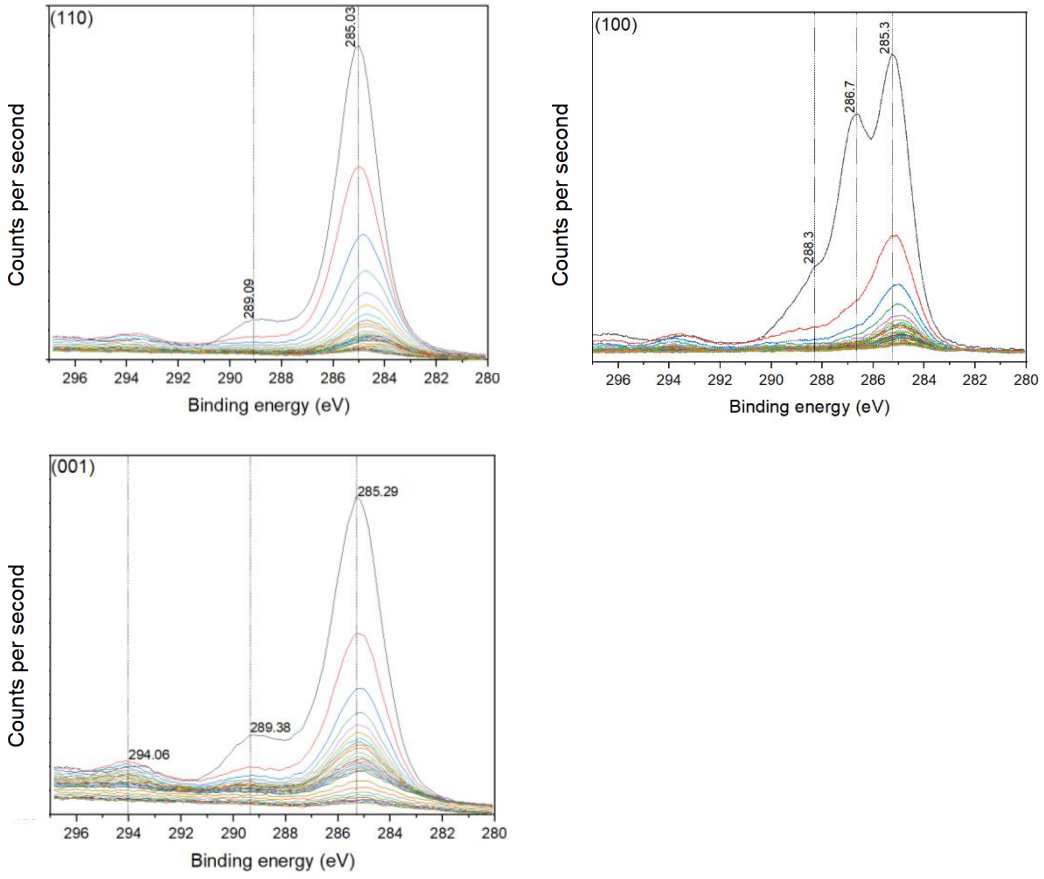

Figure 52 XPS C1s principal core line spectrum of the TiC treated rutile (110), (100) and (001) substrates. NB: The graph in black indicates the carbon concentration on the surface of the titania substrate and the coloured graphs indicate the carbon concentrations beneath the surface. The concentration of carbon decreases with increasing depth – please refer to figure 47 for the corresponding graph of C concentration against depth.

3. **Titanium environment**

The Ti2p XPS principal core line spectrum of the as-received TiC powder used for the TiC treatment of the rutile substrates indicate the presence of two sets of doublet peaks (Figure 53). The doublet at 464.6 eV and 458.8 eV matches with the $Ti2p_{1/2}$ and $Ti2p_{3/2}$ orbital states in TiO_2, which are reported to be in the literature to be at 464.8 eV and 459 eV respectively. The doublet peak at 455.4 eV and 461.2 eV matches with the $Ti2p_{3/2}$ and $Ti2p_{1/2}$ found in the literature at 454.7 eV and at 460.7 eV respectively, corresponding to a TiC chemical environment[159].

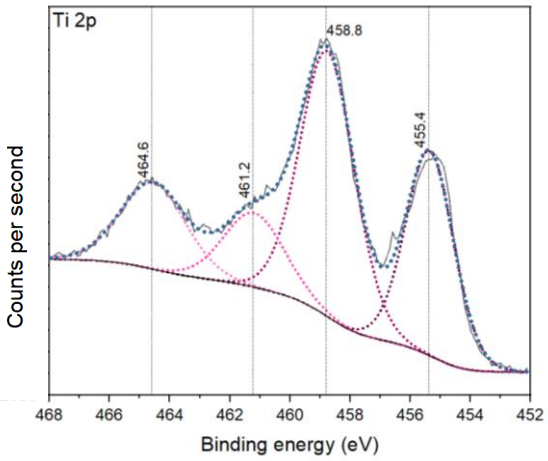

Figure 53 XPS Ti2p principal core line spectrum of the as-received TiC powder used for anionic doping of the rutile substrates

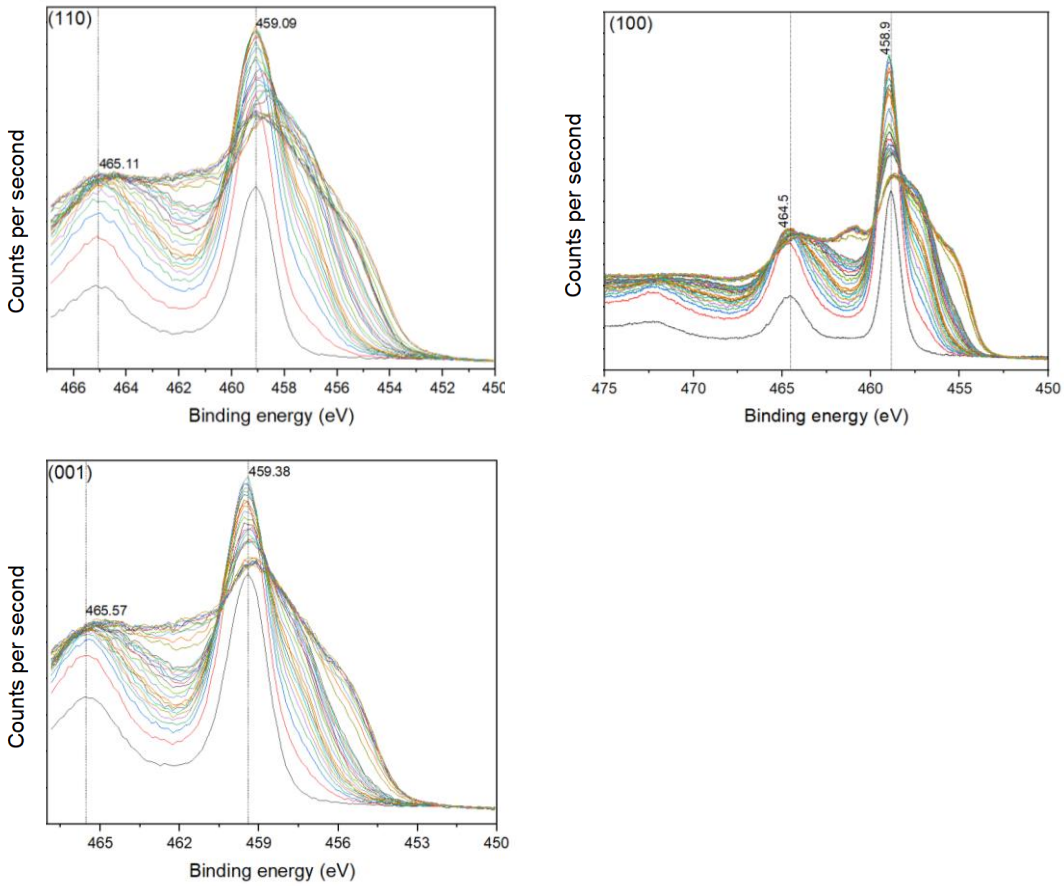

Figure 54 XPS Ti2p core line depth profile of the TiC treated rutile (110), (100) and (001) substrates. NB: The graph in black indicates the titanium concentration on the surface of the titania substrate and the coloured graphs indicate the titanium concentrations beneath the surface. The concentration of titanium changes with increasing depth – please refer to figure 47 for the corresponding graph of Ti concentration against depth.

The Ti2p XPS surface spectrum of the TiC treated rutile (110), (100) and (001) substrates (Figure 54) indicate the presence of TiO_2 environments. In the (110) substrate, these peaks are located at 465.1 and 459.1, which are +0.3 eV and +0.1 eV away from the pure TiO_2 peaks respectively. In the (100) substrate, these peaks are at 464.5 eV and 458.9 eV, which are -0.3 eV and -0.1 eV away from the pure TiO_2 peaks respectively. Similarly, in the (001) substrate, these peaks are situated at 465.6 eV and 459.4 eV, which are +0.8 eV and +0.4 eV away from the pure TiO_2 peaks. These shifts are potentially due to the incorporation of carbon into the TiO_2 lattice and confirms that the carbon environments observed in the C1s XPS core line depth profile are not from adventitious carbon sources but from the TiC dopant powder source (Figure 53) as discussed earlier.

Beneath the surface, these characteristic TiO_2 peaks do not appear to be additionally shifted in any of the substrates. This is potentially because the concentration of carbon beneath the surface is seen to decrease, as observed in the XPS elemental depth profile of carbon discussed earlier. At depths close to 120 nm, the TiC treated (110) and (100) substrates show the emergence of peaks at ~462 eV and ~465 eV, which

correspond to the Ti-C chemical environment. However, this TiC environment is not observed in the C1s XPS spectrum of the substrates. From this, it can be deduced that the TiC environment observed near the 120 nm depth of the substrate is not due to the carbon dopant diffusion but due to the XPS argon etching process which may have reduced the carbon doped TiO_2 into TiC.

4. **Oxygen environment**

The O1s XPS spectrum of the TiC treated (110), (100) and (001) substrates has a peak at 530 eV, which corresponds to the O-Ti environment of TiO_2 (Figure 55). It is only on the surface of these substrates that the peak around 532 eV is observed, which is also seen in the O1s spectrum of the as-received TiC powder used for the TiC treatment. This peak corresponds to O-C, as per the literature reports. As per this, there is no carbon environment beneath the surface. However, the O1s XPS spectrum is not used widely in the literature for validati fi ngs from other data or instrument.

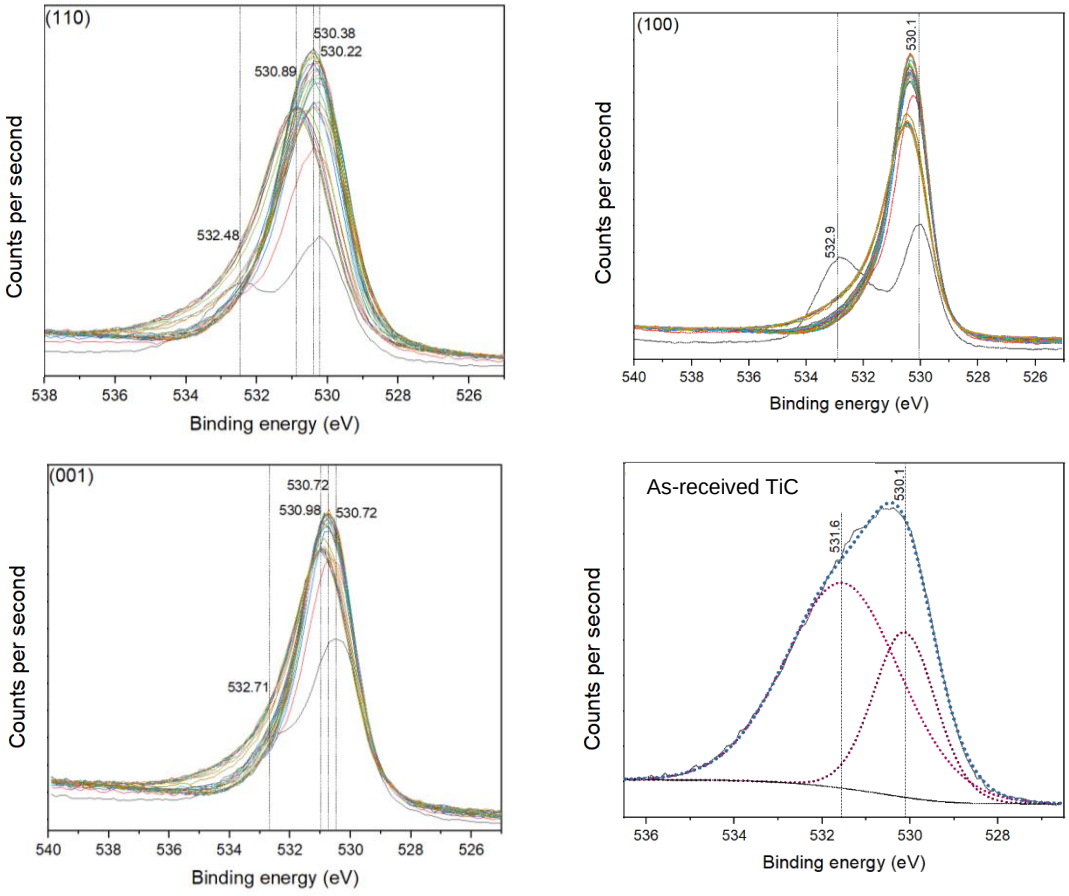

Figure 55 XPS O1s core line depth profile of the TiC treated Rutile (110), (100) and (001) substrates and of the as-received TiC powder. NB: The graph in black indicates the oxygen concentration on the surface of the titania substrate and the coloured graphs indicate the oxygen concentrations beneath the surface. The concentration of oxygen changes with increasing depth – please refer to figure 47 for the corresponding graph of O concentration against depth.

The valence band analysis carried out using XPS and UPS is discussed below.

1. **XPS valence band**

Upon TiC treatment, the XPS valance band onset measured of the surface of the Rutile (110), (100) and the (001) substrates (Figure 56) have shifted to higher binding energies (Table 18). The greatest shift by +2.22 eV was observed with the (100) substrate, which as per the Raman data, has a stronger asymmetric vibration of the O-Ti-O bond in the (001) plane than the symmetric vibration of the O-Ti-O bonds in the (110) plane. On the other hand, the smallest shift of +1.75 eV was observed with the (001) substrate, where any changes to the O-Ti-O bonding vibrations were not large enough to be detectable using Raman spectroscopy. Although this blue shift in the valence band onset is reported in the literature to be caused by interstitial dopant species, this is not the case as no evidence for interstitial carbon species is observed in the XPS data. The carbon incorporated into the (110) and (001) substrates were in O-C=O and C-C environments, while with the (100) substrate, the carbon incorporated were in O-C=O, C-O-C and C-C environments. This shows that the (100) substrate had three different carbon species while the (110) and (001) substrates had two different types of carbon species. This suggests that the (100) surface is the most disordered from the incorporated carbon and therefore, might be the reason why it experienced the most shift in the electronic valence band onset.

The shift in the XPS valence band spectrum of 2.0 to 2.4 eV discussed above is not due to charging of the substrate, as all the spectrum has been charge-corrected before analysis. This could be due to the following reason. The literature mentions that ‘’in most oxides, oxygen vacancies lead to n-doping via filled band gap states and this shifts all the energy levels down to higher binding energy’’.[161] The magnitude of the shift observed here is not commonly observed, however a shift of 2.0 eV to lower binding energy (which is opposite to the case here) has been reported to be observed in ZrO_2.[161]

Table 18 XPS valence band onset of TiC treated rutile (110), (100) and (001) substrates

Rutile substrate orientation	XPS Valence Band (eV)	
	Untreated	TiC treated
(110)	1.20	3.17
(100)	1.18	3.40
(001)	1.19	2.94
TiC dopant source powder	1.79	N/A

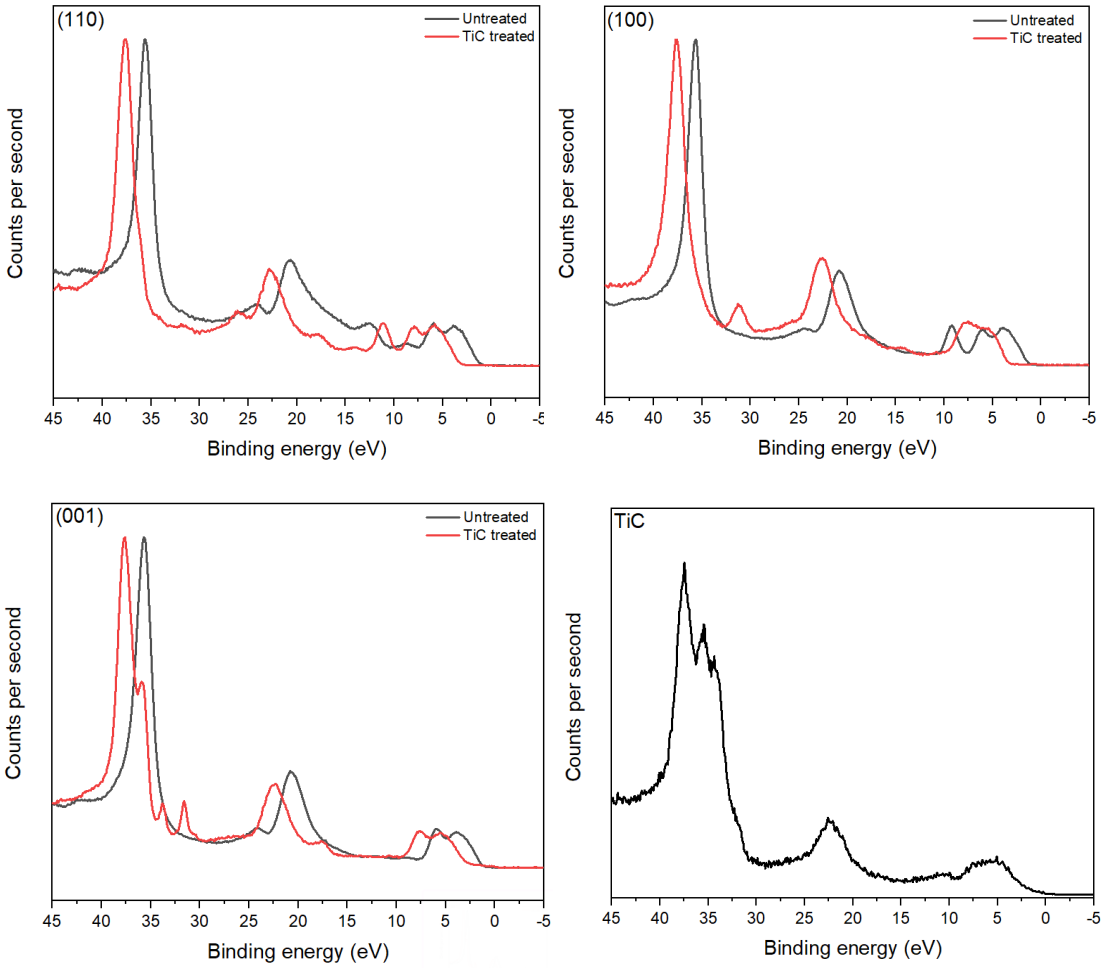

Figure 56 XPS valence band spectrum of the TiC treated rutile (110), (100) and (001) substrates along with that of the TiC powder used for the TiC treatment

The intense peak at 10 eV in the as-received valence band spectrum of the (100) rutile substrate was assigned in Chapter 3A to be potentially caused by the O-Ti-O asymmetric bending vibration. Upon TiC treatment, this peak is observed to disappear. This suggests that the asymmetric O-Ti-O bond is weakened, which is also observed by the decreasing intensity of the corresponding peak in its Raman spectrum. However, upon TiC treatment of the (110) rutile substrate, this peak is observed to become as intense as that found in the as-received (100) substrate. This suggests the strengthening of the asymmetric O-Ti-O bond in the TiC treated (100) substrate, which is also observed by the increasing intensity of the corresponding peak in its Raman spectrum. The peak at 36 eV, in the valence band spectrum of the as-received TiC powder, corresponds to the Ti3p orbital in Ti_2O_3, which has been arisen from the typically found surface oxidation of the TiC powder, as seen in its XPS surface spectrum in figure 51. This peak is not present in the valence band spectrum

of the untreated (110), (100) or (001) rutile-TiO_2 substrates. Upon TiC treatment, this 36 eV peak is observed to emerge in the (001) substrate, suggesting the reduction of rutile-TiO_2 into Ti_2O_3 [162]and the mixing of the Ti3p orbitals with C1s orbitals. This peak is seen to be less prominent in the (110) treated substrate and not too prominent in the (100) substrate. These differences observed in the three substrates could be due to how the carbon species is incorporated into the rutile TiO_2 structure. This is also reflected in their raman spectra where in the (110) and (100) substrates, the raman peaks are observed to have altered in intensities upon TiC treatment while the raman peaks of the (001) substrate remains the same upon TiC treatment.

Upon TiC treatment, the disappearance of the 25 eV peak, corresponding to an O2p contribution, is observed in the (100) and (001) substrates. These substrates are the most roughened, as per AFM images. Therefore, it can be deduced that the disappearance of the peak must be due to the loss of any surface bound inherent-carbon-based defect species in the rutile host lattice.

Upon TiC treatment, the 10 eV to 3 eV region that is dominated by the O 2p contribution in TiO_2 is observed to be broadened only in the (100) substrate. This is potentially due to the mixing of the O2p orbitals with the C1s orbitals from the C-O-C chemical environment, which is only present in the TiC treated (100) substrate.

The emergence of a new peak at ~30 eV is observed in all the three substrates upon TiC treatment. This peak could be a new C1s state arising from the O-C=O or C-C chemical environments. The FWHM of this peak may potentially be associated the concentration and spatial distribution of the carbon defect species incorporated into the surface of the rutile substrate. The broadest peak is observed with the (100) substrate where 39 atomic% of the carbon species lie within the top 0.2 nm of the surface. However, 41% of carbon defects lie within the top 1 nm of the (001) substrate and therefore, gives the second broadest 30 eV peak. On the other hand, 55% of carbon species lie within the top 7 nm of the (110) substrate and therefore, gives the lowest FWHM for the 30 eV peak. From this, it can be deduced that the closer the carbon defects are to the surface of the rutile substrate, the higher the FWHM of the new C1s state. This suggests that the spatial distribution of the carbon defects can affect the electronic structure of rutile where the concentration of carbon species incorporated itself is related to the orientation of the rutile substrate.

2. **UPS valence band**

Upon TiC treatment of the (100) substrate, the contribution from the π O2p at 6 eV is observed to be increased in the UPS valence band spectrum (Figure 57). This suggests that the mixing of the new C1s state, associated with the O-C-O environment, occurs predominantly with the π O2p orbital. On the other hand, with the (110) and (001) substrates, the π O2p and σ O2p peaks at 6 eV and 8 eV are seen to merge into a single peak. This suggests the mixing of the new C1s state, corresponding to the O-C=O chemical environment, with these O2p orbitals.

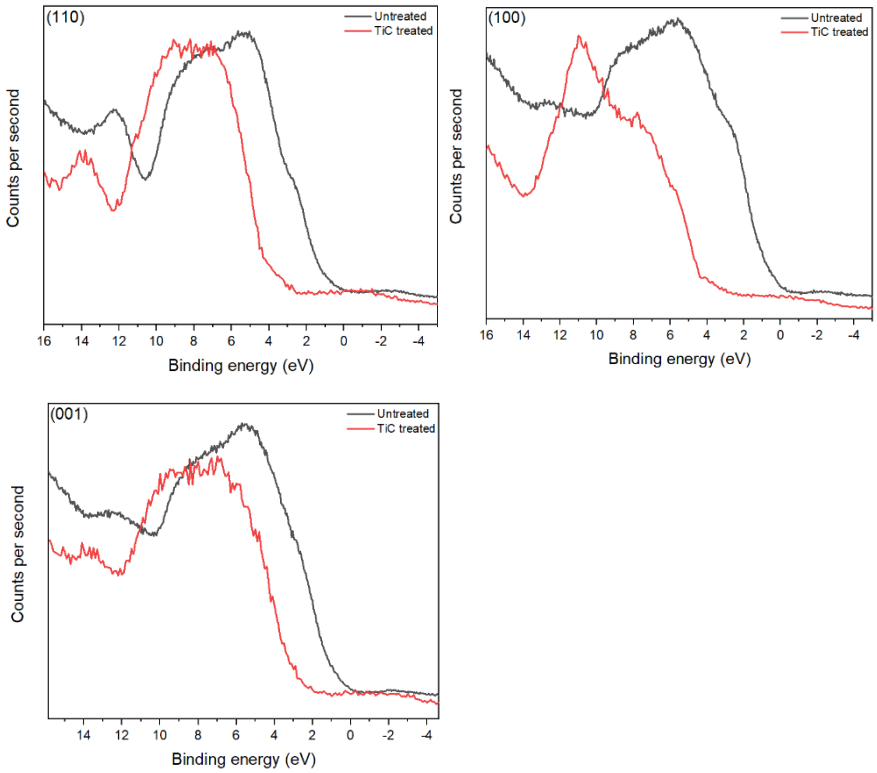

Figure 57 UPS valence band spectrum of the TiC treated rutile (110), (100) and (001) substrates measured using He (II) source

5.2 Summary of Findings

Upon TiC treatment, carbon was diffused, as a dopant, into the rutile (110), (100) and (001) substrate, unlike the case with the TiB_2 treatment which caused $TiBO_3$ formation. The Raman peaks assigned to the inherent-Ti^{3+}-defects in the rutile substrates were observed to disappear completely in the (110) substrate, while they nearly disappear in the (100) substrate and they remain, although slightly modified, in the (001) substrate. The defect free (110) substrate is observed to be the least roughened and the defect containing (001) substrate is seen to be the most roughened. The characteristic rutile peaks in the Raman spectrum remains unshifted although modifications to their intensities are observed in the (110) and (100) substrates. Upon TiC treatment, in the (110) substrate, O-Ti-O bonds along both the

(001) plane and the (110) planes are weakened, making it easier for carbon to get access to these bonds, giving a surface carbon concentration of ~55 atomic%. The O-Ti-O bonds along the (001) plane is the weakest in the as-received (001) substrate compared to the other substrates. Therefore, upon TiC treatment, a carbon concentration of ~41 atomic% is achieved. On the other hand, in the (100) substrate, only the O-Ti-O bonds along the (110) plane is seen to be weakened, which gives the lowest surface carbon concentration of ~39 atomic%. This carbon concentration falls to < 5 atomic% within ~5 nm into the (110) substrate, within ~0.2 nm in the (100) substrate and within ~10 nm into the (001) substrate. When the carbon concentration is < 5 atomic%, the O: Ti ratio becomes close to that found in pristine TiO_2, i.e. 67: 33 ± 2 atomic%, in all the three substrates. This explains why the rutile characteristic peaks in the Raman spectrum are not seen to be shifted. As per the XPS C1s spectrum, carbon is incorporated into the rutile substrates in the same environments that are found in adventitious carbon contamination. i.e. with the (110) and (001) substrates, the carbon is in the O-C=O and C-C environments, while with the (100) substrate, the carbon is in the O-C=O, C-O-C and C-C environments. The carbon concentration remains at ~0.2 atomic% even at a depth of ~120 nm into the three substrates. From this, it can be deduced that the carbon incorporated into the rutile lattice is not just from an adventitious carbon contamination source. Also, adventitious carbon would not have caused modifications to the Raman peak intensities as observed here with the TiC treated rutile (110), (100) and (001) substrates. The electronic structure of the rutile substrates is modified by the different types of carbon environments incorporated into them. Upon TiC treatment, the valence band onset was observed to be shifted the most with the (100) substrate which has three different types of carbon environments and therefore, possibly have introduced more defect levels than the other substrates. Between the (110) and (100) substrates both of which have two different carbon environments, the (110) substrate has a higher carbon concentration than the (001) substrate. Therefore, the valence band shift is observed to be greater in the (110) substrate than the (001) substrate. The weakening of the asymmetric O-Ti-O bond is observed in TiC treated (100) substrate by the decreasing intensity of the associated Raman peak and by the broadening of the 10 eV peak in the XPS valence band spectrum. On the other hand, the strengthening of this bond is observed in the (110) substrate, as per the Raman and XPS valence band spectrum. The XPS valence band spectrum helped to identify the presence of surface-bound inherent-Ti^{3+}-defect species in the (110) and (100) substrates, which were unidentifiable using Raman spectroscopy. Also, it found that these defect species found in the (001) substrates were not surface-bound and that it helped to tune the

(001) electronic structure to look like that of the TiC powder. The mixing of the C1s state, arising from the C-O-C chemical environment, in the TiC treated (100) substrate with the O2p orbitals were observed in the XPS valence band spectrum; while in the UPS valence band spectrum, this mixing was found to be predominantly with the π O2p orbital. The emergence of a new C1s state arising from the O-C=O or C-C chemical environments was observed in all the three substrates. The magnitude of the contribution from this state was found to be corresponding to how close the carbon species were near the substrate surface. i.e. the more surface-bound the carbon species, the higher the contribution from the associated new C1s state.

Chapter 6: Sulphur Diffusion in Rutile single crystal substrates

A detailed characterisation of the rutile substrates of the orientations (110), (100) and (001) treated using the TiS_2 dopant source powder (referred to as TiS_2 treated rutile) is discussed below.

6.1 Results and Discussion

The topography, composition and bonding on the surface and the bulk of the TiS_2 treated rutile substrates were carried out.

6.1.1 Surface Topography

Upon TiS_2 treatment, the surface topography of the as-received (110), (100) and (001) rutile substrates (Figure A in Appendices) were observed to be significantly roughened, as per AFM images (Figure 58). However, this roughened topography caused by the TiS_2 treatment is different compared to that caused by the TiC and TiB_2 treatment. This shows the effect of the choice of anion (e.g. carbon or boron) on the extent and type of roughening caused on the rutile surface.

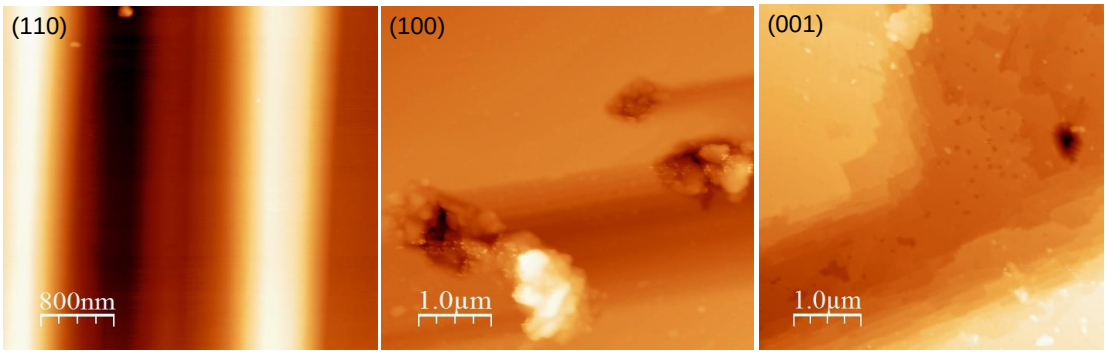

Figure 58 AFM images showing the differences in the morphology of the roughened surfaces of TiS_2 treated rutile substrates (110), (100) and (001)

The extent of surface roughening is observed to be dependent on the orientation of the rutile substrates. The (100) substrate is observed to be the most roughened as observed by the highest increase in roughness (Table 19) and the (110) surface is seen to be least roughened. The RMS roughness values of the (110), (100) and (001) substrates after the TiS_2 treatment, were observed to increase from being < 0 nm to become 23 nm, 57 nm and 33 nm respectively (Table 19). With the (110) oriented substrate, the surface is observed to be modified by the formation of a trench (Figure

J in Appendices), which is at least ~3 µm in length and ~75 nm deep (Figure 59). On the other hand, the (100) and (001) substrate surfaces are modified by the formation of long stepped features, ~5 x 3 µm in dimension. The (001) surface features are found to be significantly more layered with a step size of ~30 nm. On the other hand, in the (100) substrate, steps of the sizes 40 nm, 30 nm, 20 nm and 10 nm are observed (Figure 60).

Table 19 A comparison of the surface roughness of rutile substrates before and after TiS_2 treatment

	RMS roughness (nm)		
	(110)	(100)	(001)
Untreated	0.58	0.86	0.45
After TiS_2 treatment	23	57	33
Increase in roughness	**22**	**56**	**33**

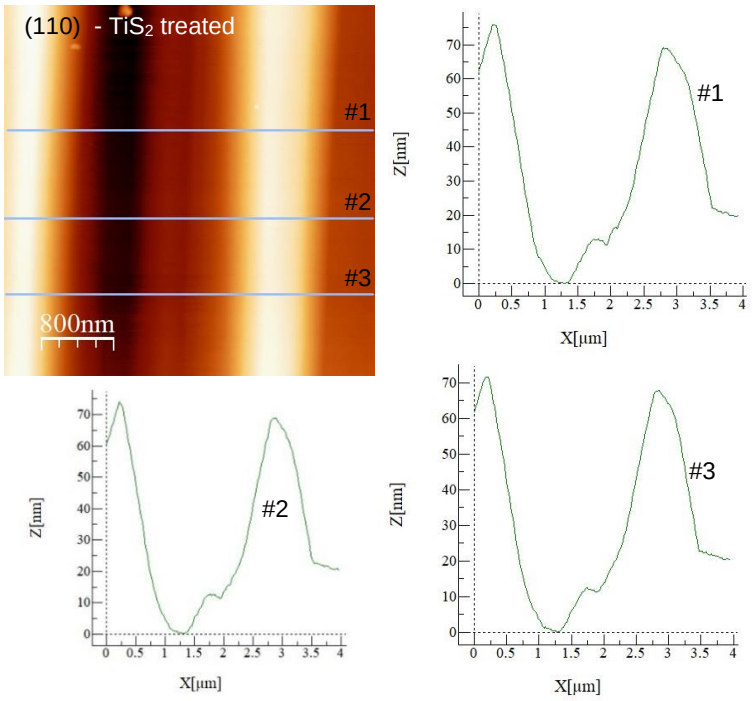

Figure 59 Line profiles #1 #2 and #3 indicating the depth of the trench on the TiS_2 treated (110) rutile substrate

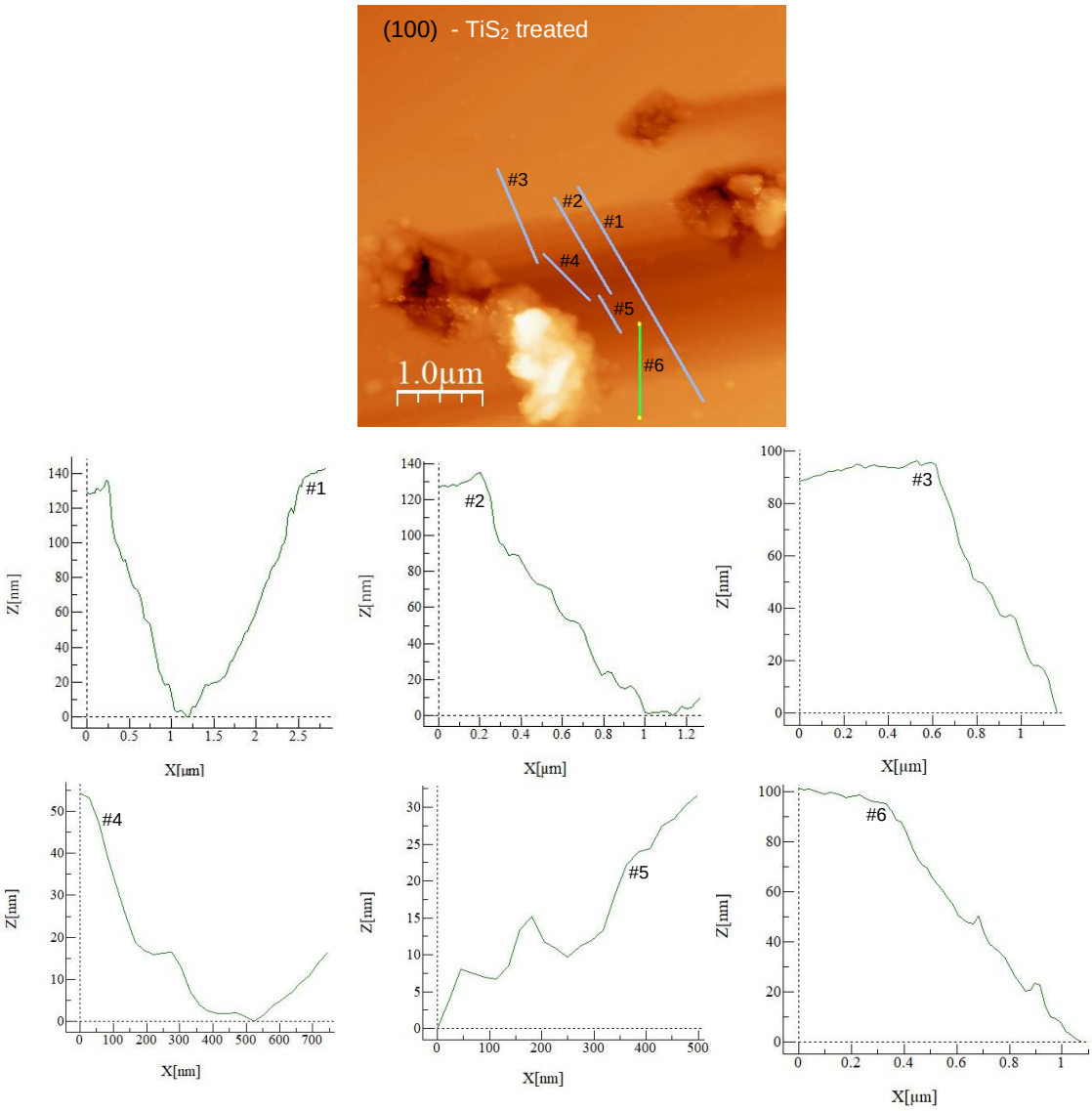

Figure 60 Line profiles, #1 to #6, indicating the height of the steps on the TiS_2 treated (100) rutile substrate

6.1.2 Surface Bonding

Upon TiS_2 treatment, the position of the rutile characteristic peaks in the Raman spectrum of the (110), (100) and (001) substrates remained the same at 444 cm^{-1} and 608 cm^{-1} (Figure 61). This suggests that any changes in the rutile structure were not detectable using Raman spectroscopy. As already discussed in Chapter 4 and 5, the peaks located at 1361 cm^{-1} and 1600 cm^{-1} These peaks correspond to any mixed sp^2/ sp^3 carbon contamination on the surface[139, 140]. Upon TiS_2 treatment, the peak at 1361 cm^{-1} is seen to disappear the (100) and (001) substrates (Figure K, L, M in Appendices). This may suggest that this defect is being removed upon treatment, potentially increasing the crystallinity of the rutile substrates. However, upon TiS_2 treatment of the (110) substrate, the peaks at 1361 cm^{-1} and 1600 cm^{-1} are observed

to shift to 1434 cm^{-1} and 1688 cm^{-1}. These peaks still correspond to any mixed sp2/ sp3 carbon contamination on the surface as the peaks in these region usually correspond to hydrocarbons [139, 140].

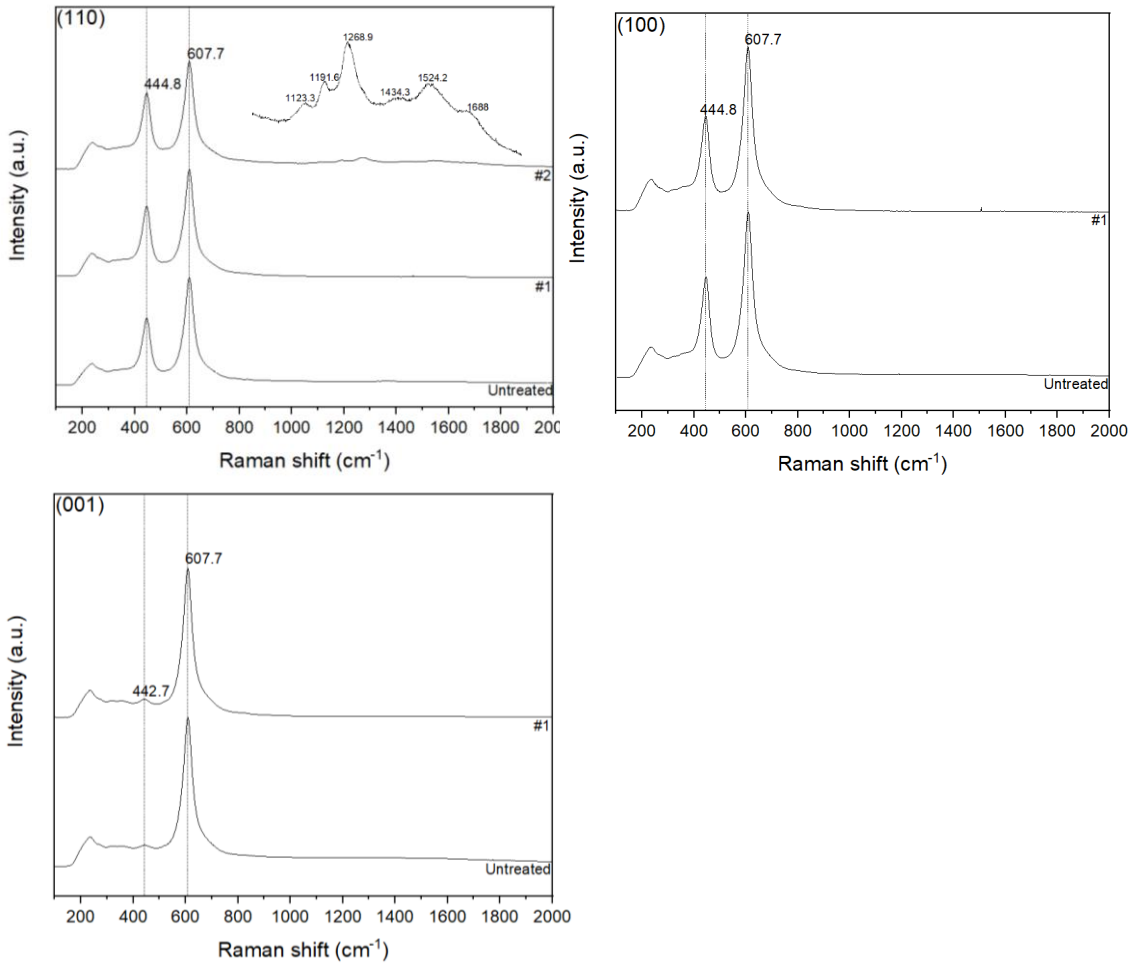

Figure 61 Raman spectrum of the TiS_2 treated rutile substrates of the orientations (110), (100) and (001), where #1 and #2 indicates different areas on the same substrate surface

The Raman spectrum was measured over seven different points across the surface of each of the substrates. It was found that one of the seven spectra measured of the surface of TiS_2 treated (110) substrate showed peaks in addition to the characteristic rutile peaks (Figure 61), suggesting a non-homogeneous chemical composition. Out of these, the peaks at 1123 cm^{-1} and 1269 cm^{-1} matches with the peaks of the sulphate group in $TiOSO_4$[163] (at 1135 cm^{-1} and 1225 cm^{-1} respectively), which is reported to be observed during the oxidative annealing of TiS_2 [54]. The other peaks are located at 1192 cm^{-1} and 1524 cm^{-1} are not observed in the literature for sulphur doped rutile or treated titania. On the other hand, the presence of $TiOSO_4$ is not observed in the (100) and (001) substrates. This may be the reason for the (100) and (001) substrate surfaces to be roughened in the same way, by forming stepped features, and for the

(110) substrate surface to be roughened differently, by forming trenches, as observed from the AFM images.

6.1.3 Chemical Environments on the Depth scale

The concentration of the sulphur incorporated into the surface and the bulk of the rutile substrates and the possibility of sulphur diffusion is investigated using XPS.

1. **Sulphur environment**

The incorporation of sulphur into the surfaces of all the three substrates is observed from their XPS S2p core line spectrum (Figure 62). The TiS_2 treated (110) and (001) surfaces have a peak at ~169 eV, indicating the presence of the SO_4^{2-} environment associated with $TiOSO_4$[164]. The evidence for this bonding was only observed in the Raman spectrum of the (110) substrate, suggesting that the $TiOSO_4$ in the (001) is only surface-bound. In (110), the $TiOSO_4$ was potentially present in the near surface too and therefore, could be the reason why it was detected in the Raman spectrum. The (001) substrate surface also indicates the presence of a sulphide environment (~162 eV), potentially arising from Ti-S bonding[164], which is also present with the (100) substrate. This environment is found beneath the surface of these substrates, as per the S2p XPS core line depth profiles. Since this environment was not detected in the Raman spectrum, it can be deduced that the (100) and (001) substrates either have a non-homogeneous surface composition or that the sulphur concentration was not high enough to be picked up by Raman spectroscopy. Instead of the $TiOSO_4$ chemical environment, the (100) substrate surface indicates the presence of the Ti-O-S environment by the presence of the peak at ~163.7 eV[165].

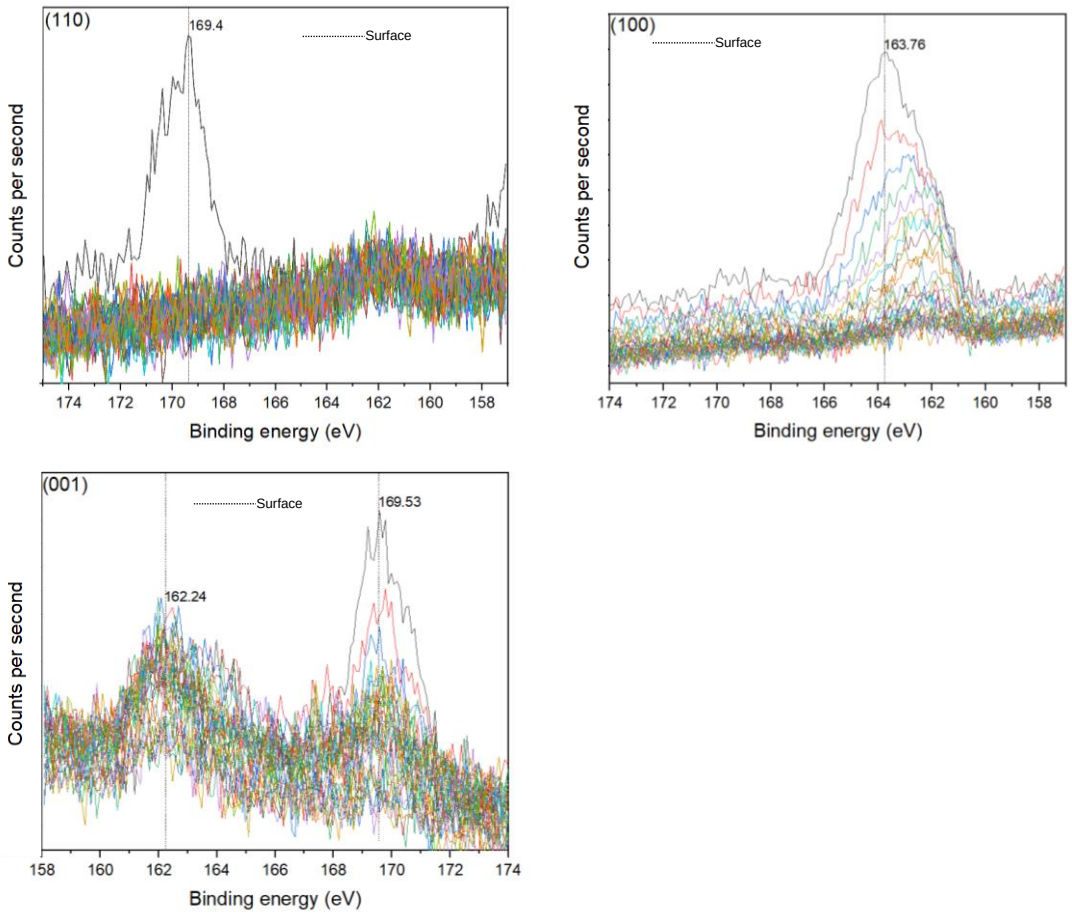

Figure 62 XPS S2p principal core line depth profile spectrum of the TiS_2 treated rutile (110), (100) and (001) substrates. NB: The graph in black indicates the sulphur concentration on the surface of the titania substrate and the coloured graphs indicate the sulphur concentrations beneath the surface. The sulphur concentration changes with increasing depth – please refer to figure 65 for the corresponding graph of S concentration against depth.

2. **Titanium environment**

The surface Ti2p XPS spectrum of all the TiS_2 treated substrates (Figure 63) indicate the substitution of lattice oxygen with SO_4^{2-}, forming a TiOS chemical environment, as per the presence of the peaks at ~464.8 eV ($Ti2p_{1/2}$) and ~459 eV ($Ti2p_{3/2}$)[165]. However, peaks corresponding to this environment was observed in the S2p XPS spectrum of only the (100) substrate. This could be because sulphur is a relatively light element compared to titanium and therefore, the TiOS chemical environment was lost among the relatively high signal to noise ratio of the S2p XPS spectrum. Beneath the surface of all the TiS_2 treated substrates, peaks at ~456 eV and ~461 eV are observed, which corresponds to the $Ti2p_{3/2}$ and $Ti2p_{1/2}$ contributions from the Ti-S chemical environment[164]. Beneath this near surface region of all the TiS_2 treated substrates, peaks at ~458 eV and ~463 eV, corresponding to the $Ti2p_{3/2}$ and $Ti2p_{1/2}$ contributions from the rutile TiO_2, are observed. This supports the Raman data where the rutile TiO_2 bonding is observed to remain intact.

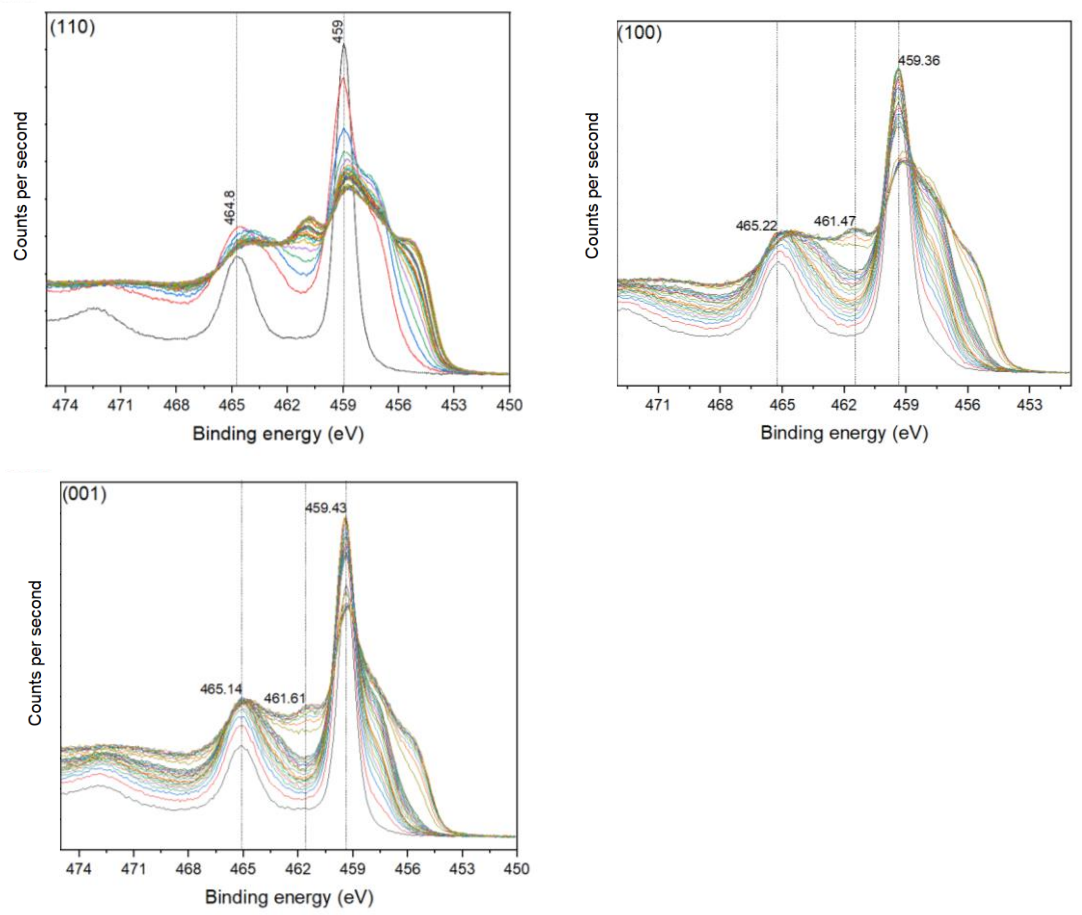

Figure 63 XPS Ti2p principal core line depth profile spectrum of the TiS_2 treated rutile (110), (100) and (001) substrates. NB: The graph in black indicates the titanium concentration on the surface of the titania substrate and the coloured graphs indicate the titanium concentrations beneath the surface. The concentration of titanium changes with increasing depth – please refer to figure 65 for the corresponding graph of Ti concentration against depth.

3. **Oxygen environment**

The TiS_2 treated rutile (110), (100) and (001) substrates indicate the presence of two chemical environments on the surface and only one beneath the surface (Figure 64). The peak at ~530 eV that is seen both in the surface as well as beneath it, matches well with that observed in pure TiO_2. On the other hand, the surface peak positioned at ~533 eV in all the three substrates, is not reported in the literature for sulphur incorporated rutile. Since the presence of the Ti-O-S chemical environment is indicated in the XPS Ti2p core line depth profile, it can be deduced that the 533 eV peak is caused by the TiOS bonding environment[165]. However, it is to be noted that the O1s XPS spectrum is not used widely in the literature for validating findings from other data or instrument.

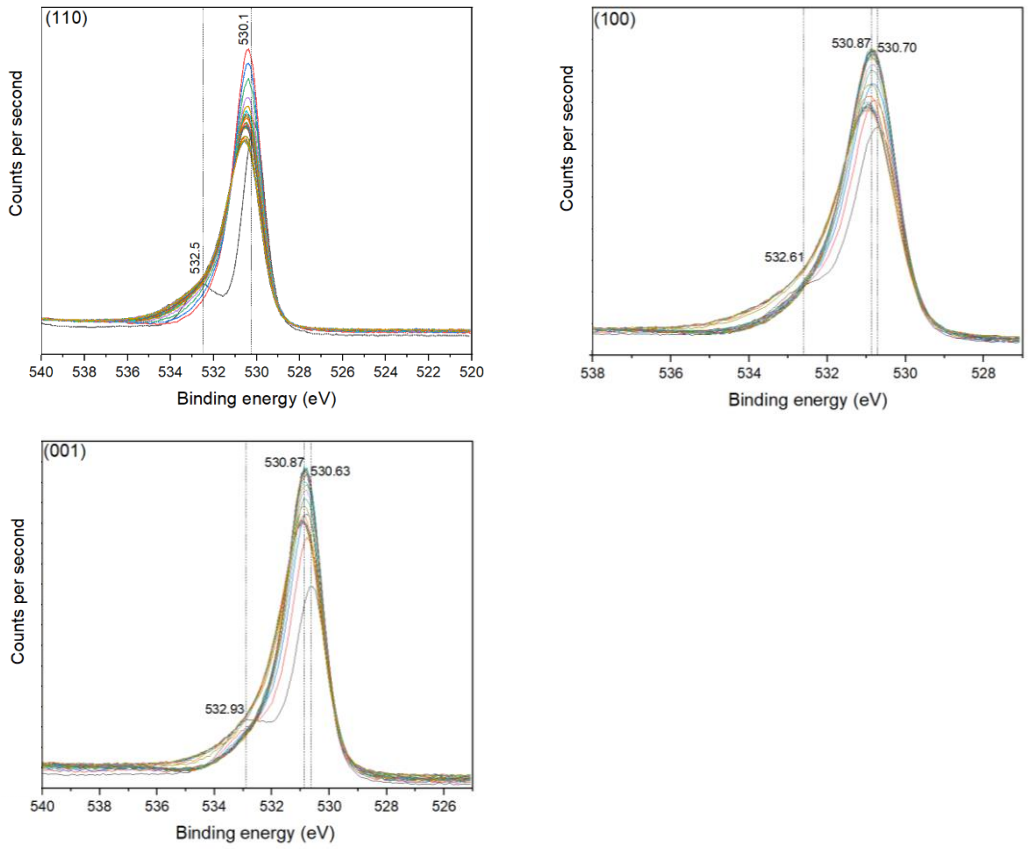

Figure 64 XPS O1s principal core line depth profile spectrum of the TiS_2 treated rutile (110), (100) and (001) substrates. NB: The graph in black indicates the oxygen concentration on the surface of the titania substrate and the coloured graphs indicate the oxygen concentrations beneath the surface. The concentration of oxygen changes with increasing depth – please refer to figure 65 for the corresponding graph of O concentration against depth.

The elemental XPS depth profile shows sulphur diffusion from the surface into the near surface of the TiS_2 treated rutile (100) and (001) substrates; while the sulphur incorporated into the rutile (110) substrate is surface-bound (Figure 65). The similarity in the behaviours of the (100) and (001) substrates is reflected in their Raman spectrum, where no new peaks are observed and in the AFM images where both the substrates are seen to be roughened with layered features. The sulphur concentration was observed to be highest on the surface for all the substrates, with ~0.01 atomic% in (110), ~1.65 atomic% in (100) and ~1.2 atomic% in (001). This also shows that the sulphur concentration is highest on the (100) substrate and least on the (001) substrate. The sulphur concentration was found to go below 0.2 atomic% just beneath the surface, i.e. at depths > 0 nm, in (110), at depths > 10 nm in the (100) substrate and at depths > 70 nm in the (001) substrate. So overall, the least amount of sulphur incorporated into the (110) substrate is on the surface and is in the $TiOSO_4$, Ti-O-S and Ti-S chemical environments as per XPS core line depth profiles. Although these same sulphur environments are also present in the (100) and (001) surfaces, these sulphur species are spatially distributed within depths of 10 nm and 70 nm

respectively into the surfaces. The ~1.65 atomic% of the sulphur distributed across the top 10 nm of the (100) substrate could be the reason for it to be more roughened than the (001) substrate which has a lower sulphur concentration of ~1.2 atomic% that is distributed within its top 70 nm. Although the (100) and (001) substrates have incorporated a higher concentration of sulphur into their surface and depths, the O: Ti ratio remained approximately the same as that found in TiO_2, i.e. 67: 33 ± 1 atomic%. This indicates that the sulphur incorporation in these cases has not affected the Ti-O bonding, which is also evident in their Raman spectrum. On the other hand, the 0.01 atomic% of sulphur incorporated on only the surface of the (110) substrate has caused the Ti: O ratio on the surface to be 70: 30 ± 1 atomic% and beneath the surface to be 80: 20 ± 6 atomic%. Here, the percentage of oxygen is greater than that found in pristine TiO_2 while it is the same as that found in $TiOSO_4$, where oxygen makes up ~71%. Therefore, this additional oxygen could be accounted for by the $TiOSO_4$ species that was formed on the surface of only the (110) substrate, as per Raman data. This could be the reason for the (110) surface to be roughened via the formation of large trenches unlike the (100) and (001) surface, which formed stepped features. This also suggests that the sulphur is potentially incorporated into the (100) and (001) as dopants while in (110) it is not, where the rutile composition observed to be is affected. Even at a depth of ~120 nm, the sulphur concentration in the (100) and (001) substrates are at 0.1 atomic% and 0.2 atomic% respectively, suggesting that the sulphur diffusion trail into the bulk of the substrate continues (Figure 65, right).

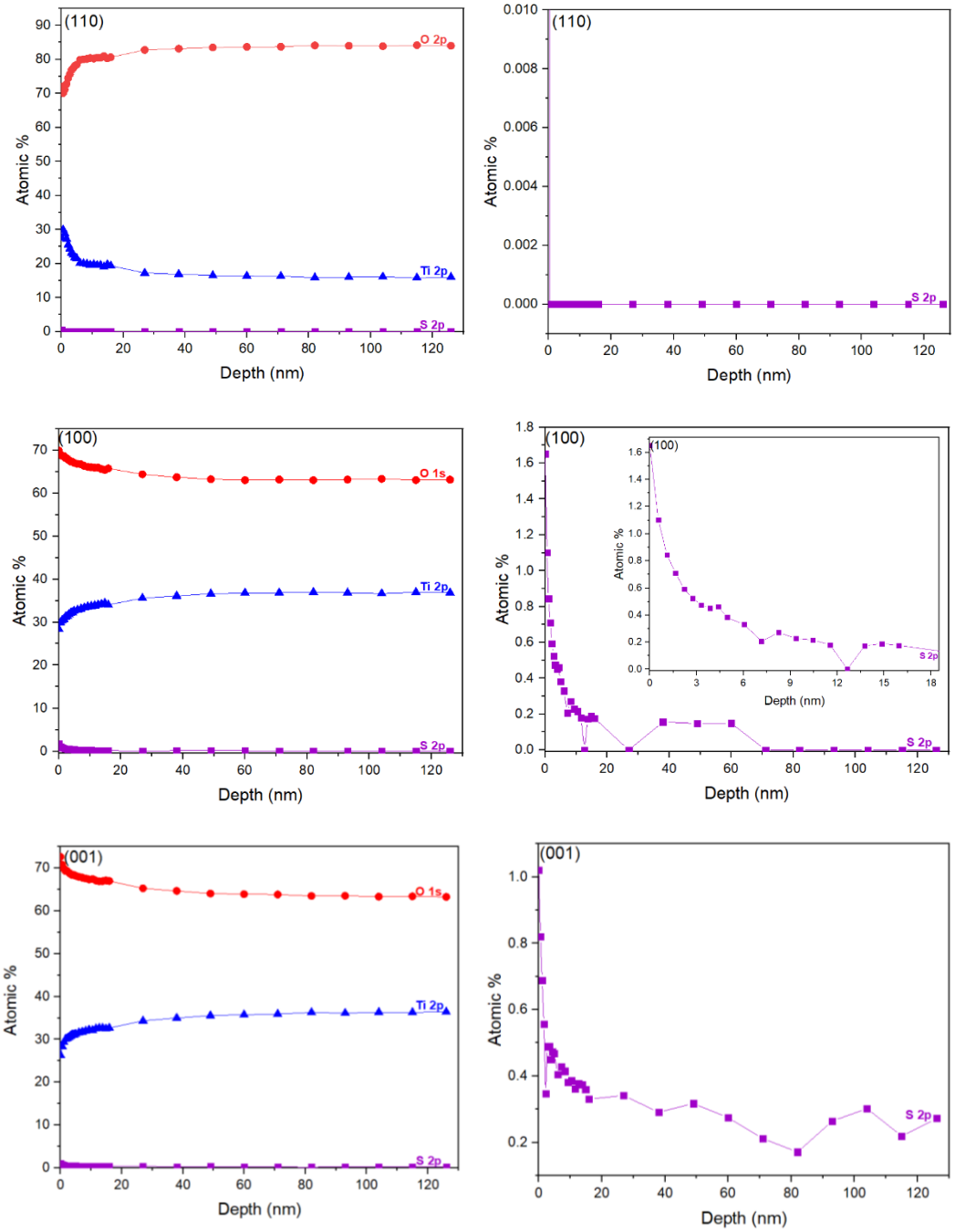

Figure 65 XPS depth profile of TiS_2 treated rutile (110), (100) and (001) substrates showing (left) the O, Ti and S elemental profiles and (right) a zoomed in version of the sulphur depth profile by itself, showing the sulphur concentrations more clearly

The sulphur is diffused into the (100) and (001) substrates with more than one diffusion rate, which is usually deduced from the diffusion coefficient calculated using Fick's second law of diffusion. The sulphur diffusion coefficients extracted from the carbon diffusion plots (Figure 66 and 67) are summarised in Table 20. Please note that in figure 67, Regions D and C look like noise in the measured signal rather than a true concentration gradient reflecting from diffusion. Therefore, it is not ideal to fit

these regions to obtain the diffusion coefficients (the fit for both these regions are indicated in figure 67 is just to indicate where these regions lie).

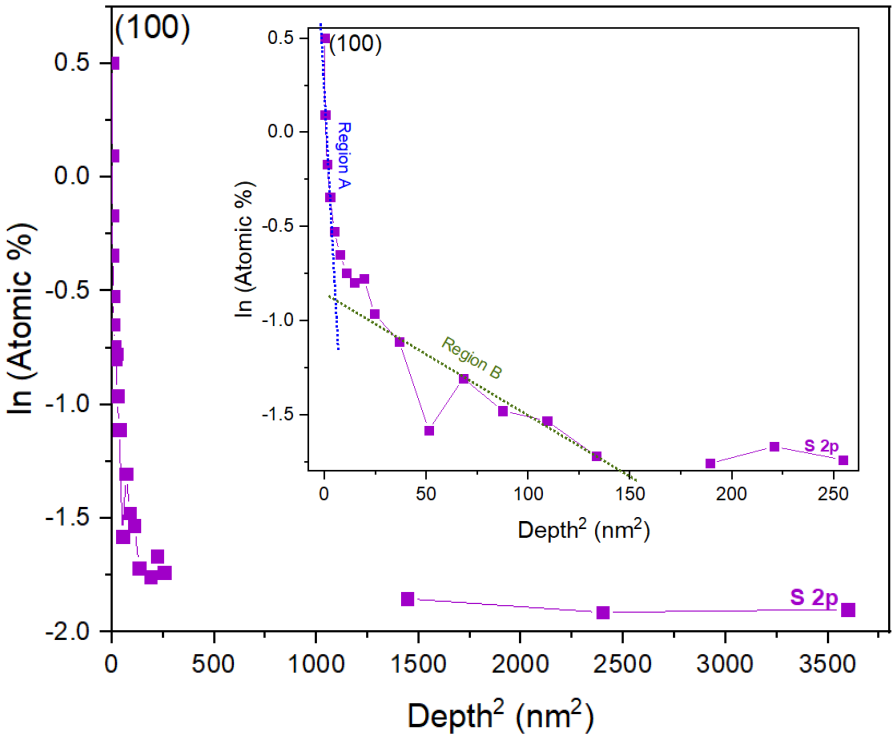

Figure 66 The sulphur diffusion gradient of the TiS_2 treated (100) rutile substrates

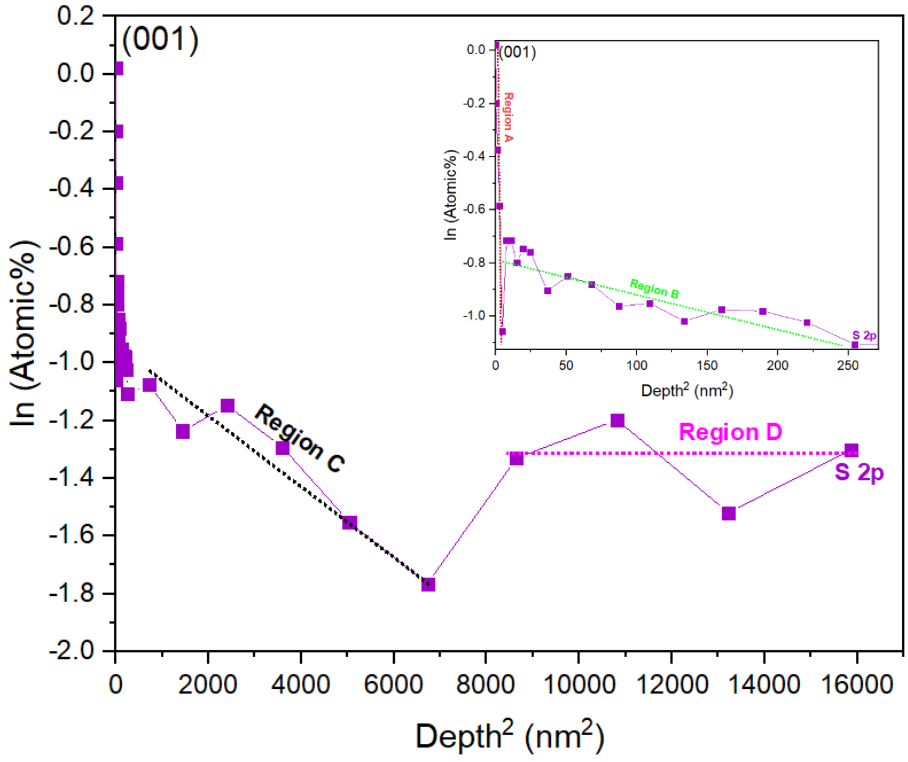

Figure 67 The sulphur diffusion gradient of the TiS_2 treated (001) rutile substrates

Table 20 The sulphur diffusion coefficients and sulphur concentrations at different depths into the TiS_2 treated rutile (100) and (001) substrates

Fastest sulphur diffusion			
	110	**100**	**001**
Depth into the substrate	--	~5 nm to ~12 nm	< ~80 nm to ~130 nm
Sulphur concentration	--	~0.4 atomic%	~1.2 atomic%
Diffusion coefficient	--	~0.006 $nm^2 s^{-1}$ (Region B)	~Noise (Region D)
Second fastest sulphur diffusion			
	110	**100**	**001**
Depth into the substrate	--	< ~4 nm	~30 nm to ~80 nm
Sulphur concentration	--	~1.6 atomic%	~0.38 atomic%
Diffusion coefficient	--	~0.19 $nm^2 s^{-1}$ (Region A)	~Noise (Region C)
3rd fastest sulphur diffusion			
	110	**100**	**001**
Depth into the substrate	--	--	~3 nm to ~16 nm
Sulphur concentration	--	--	~0.35 atomic%
Diffusion coefficient	--	--	~-0.0013 $nm^2 s^{-1}$ (Region B)
Slowest sulphur diffusion			
	110	**100**	**001**
Depth into the substrate	--	--	~0 nm to ~3 nm
Sulphur concentration	--	--	~0.38 atomic%
Diffusion coefficient	--	--	~-0.3051 $nm^2 s^{-1}$ (Region A)

The fastest and slowest sulphur diffusion rates were not observed at the same depths in the (100) and (001) substrates (Table 20). The fastest sulphur diffusion in the (100) substrate was observed with the lowest sulphur concentration of ~0.4 atomic% lying in the ~5 nm to ~12 nm region. However, the fastest sulphur diffusion in the (001) substrate was observed with the highest sulphur concentration of ~1.2 atomic% located on the surface. This could be the reason for the (001) surface to be the most roughened, as per the AFM images. On the other hand, the slowest sulphur diffusion in the (100) substrate was observed with the highest sulphur concentration of ~1.6 atomic% lying in the surface. However, the slowest sulphur diffusion in the (001) substrate was observed with the lowest sulphur concentration of ~0.38 atomic% lying in the ~120 nm region.

6.1.4 Electronic Structure

The valence band analysis carried out using XPS and UPS is discussed below.

1. **XPS valence band**

Upon TiS_2 treatment, the XPS valence band onset measured of the surface of the rutile (110), (100) and (001) substrates were observed to be shifted to higher binding energies (Table 21). The greatest shift by +2.1 eV was observed with the (110) substrate, which had the least concentration of sulphur (~0.01 atomic%) and had surface-bound $TiOSO_4$, which was observed in the XPS and Raman data. On the other hand, the smallest shift of +1.82 eV was observed with the most roughened (001) surface, which had the highest concentration of sulphur (~1.6 atomic%). This suggests that the sulphur concentration is inversely related to the shift in the valence band onset. The smaller shifts observed with the (100) and (001) substrates could also be related to the absence of the $TiOSO_4$ peaks in their Raman spectrum.

Table 21 XPS valence band onset of TiS_2 treated rutile (110), (100) and (001) substrates

Rutile substrate orientation	XPS Valence Band (eV)	
	Untreated	TiS_2 treated
(110)	1.20	3.30
(100)	1.18	3.12
(001)	1.19	3.01
TiS_2 dopant source powder	0.50	N/A

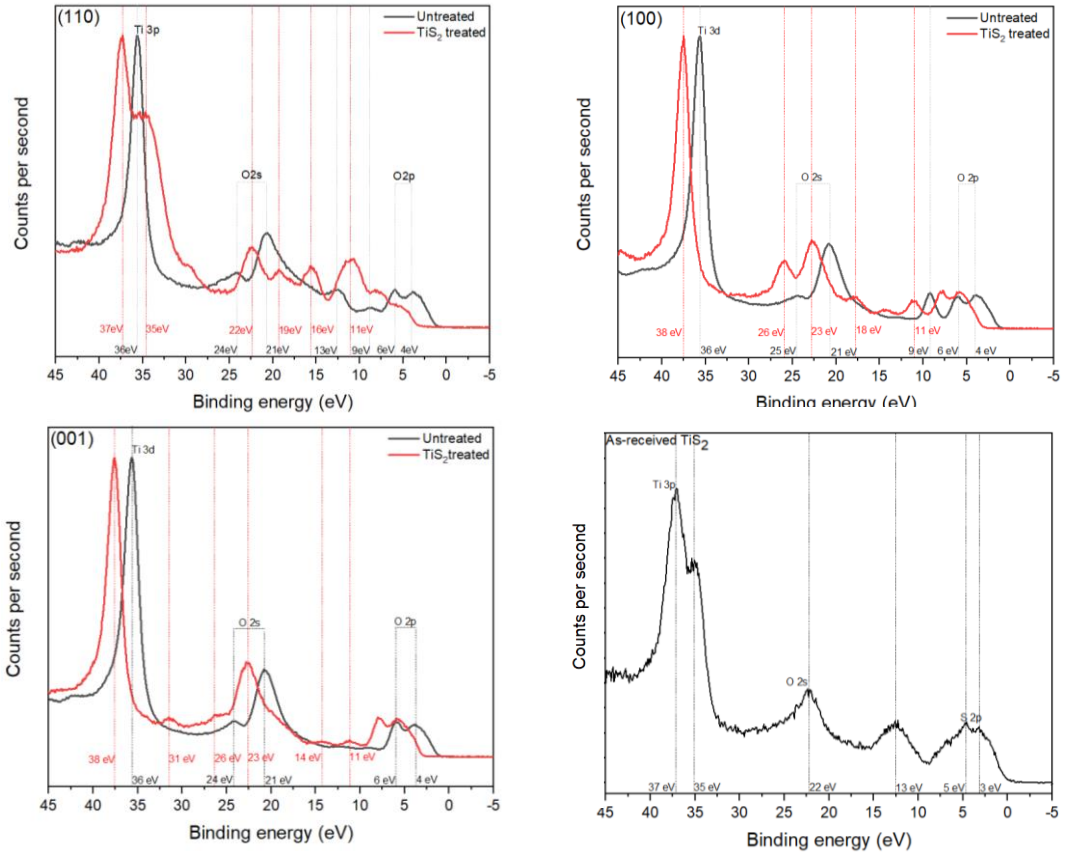

Figure 68 XPS valence band spectrum of the TiS_2 treated rutile (110), (100) and (001) substrates along with that of the TiS_2 powder used for the TiS_2 treatment

The intense peak at 10 eV in the XPS valence band spectrum, originally observed only in the as-received (100) substrate is seen in the TiS_2 treated (110), (100) and (001) rutile substrates. In the (100) substrate, its intensity is observed to be decreased, suggesting the weakening of the asymmetric O-Ti-O bonding, which this peak was associated to in the Raman spectrum (as discussed in Chapter 4). The weakening of this bond could be due to the incorporation of sulphur into the (100) rutile substrate as Ti-S, Ti-O-S and $TiOSO_4$ species, while maintaining the O: Ti ratio of 67: 33 in pristine TiO_2. On the other hand, in the (110) substrate, a peak at 10 eV is seen to emerge with intensity greater than that of (100) and (001) substrates. In this case, the sulphur is incorporated into the rutile (110) lattice as Ti-S, Ti-O-S and $TiOSO_4$ species, by disrupting the percentage of oxygen to become close to that found in $TiOSO_4$, as per XPS data. Here new O-Ti-O bonds are formed from $TiOSO_4$, without breaking the rutile O-Ti-O bonds, which are observed to remain intact as per Raman data. Therefore, the O-Ti-O bonds from both TiO_2 and $TiOSO_4$ could be the reason for the increased intensity of the 10 eV peak seen in the XPS valence band spectrum of the (110) substrate.

As per Raman data, the peaks corresponding to the inherent-Ti^{3+}-defects are shifted upon TiS_2 treatment in the (110) substrate suggesting the incorporation of sulphur by interaction with these Ti^{3+} species, and they remain in the (100) and (001) substrates. This is also reflected in the XPS valence band spectrum, where the Ti3p contribution from this Ti^{3+} species is seen to be present in the (100) and (001) substrates. On the other hand, in the (110) substrate, the Ti3p contribution is seen to transform into looking like the Ti3p contribution in the as-received TiS_2 powder (Figure 68). This suggests the mixing of the Ti3p with the S2p orbitals.

Upon TiS_2 treatment, new peaks corresponding to O2s contribution are observed in all the three rutile substrates. In the (110) substrate, new peaks are found at 19 eV and 16 eV. In the (100) substrate, the new peaks are found at 15 eV and 18 eV, while in the (001) substrate, they are found at 14 eV. The peak at ~15 eV is possibly due to the $TiOSO_4$ species, since the intensity of this peak is found be the highest in the (110) substrate, which is clearly distinguished in the XPS S2p core line spectrum. The peak at ~17 eV is potentially caused by the Ti-S chemical environment.

Upon TiS_2 treatment, the 10 eV to 3 eV region that is dominated by the O 2p contribution in TiO_2 is observed to be broadened only in the (110) substrate. This is potentially due to the formation of $TiOSO_4$ via the modification of the TiO_2 chemical composition where the percentage of oxygen was 67 (which is the case in TiO_2) to become 71 (which is the case in $TiOSO_4$).

The emergence of the new peak at ~30 eV is only observed in the (110) and (001) substrates. This could potentially be due to the presence of the $TiOSO_4$ species that is surface bound in the (110) and (001) substrates but potentially not in the (100) substrate, as per the XPS S2p core line spectrum.

2. **UPS valence band**

In the UPS valence band spectrum of the TiS_2 treated rutile (110), (100) and (001) substrates, the contribution from the π O2p at 6 eV is observed to be increased (Figure 69). In the (110) substrate, this contribution is observed be greatest, potentially corresponding to the O2p states in the $TiOSO_4$ species formed. The contribution from the σ O2p orbital in the (110) substrate is seen to be decreased drastically, which corresponds to the TiO_2 chemical composition which was observed to be modified. On the other hand, in the (100) and (001) substrates, the π O2p contribution is also observed to be increased but not as much as that observed in the

(110) substrate. In these (100) and (001) substrates, the σ O2p orbital contribution remains the same. This reflects the π O2p contribution from the $TiOSO_4$ species formed, without affecting the σ O2p orbital contribution from the TiO_2 chemical composition that was left unaffected upon TiS_2 treatment, as per the XPS elemental depth profiles.

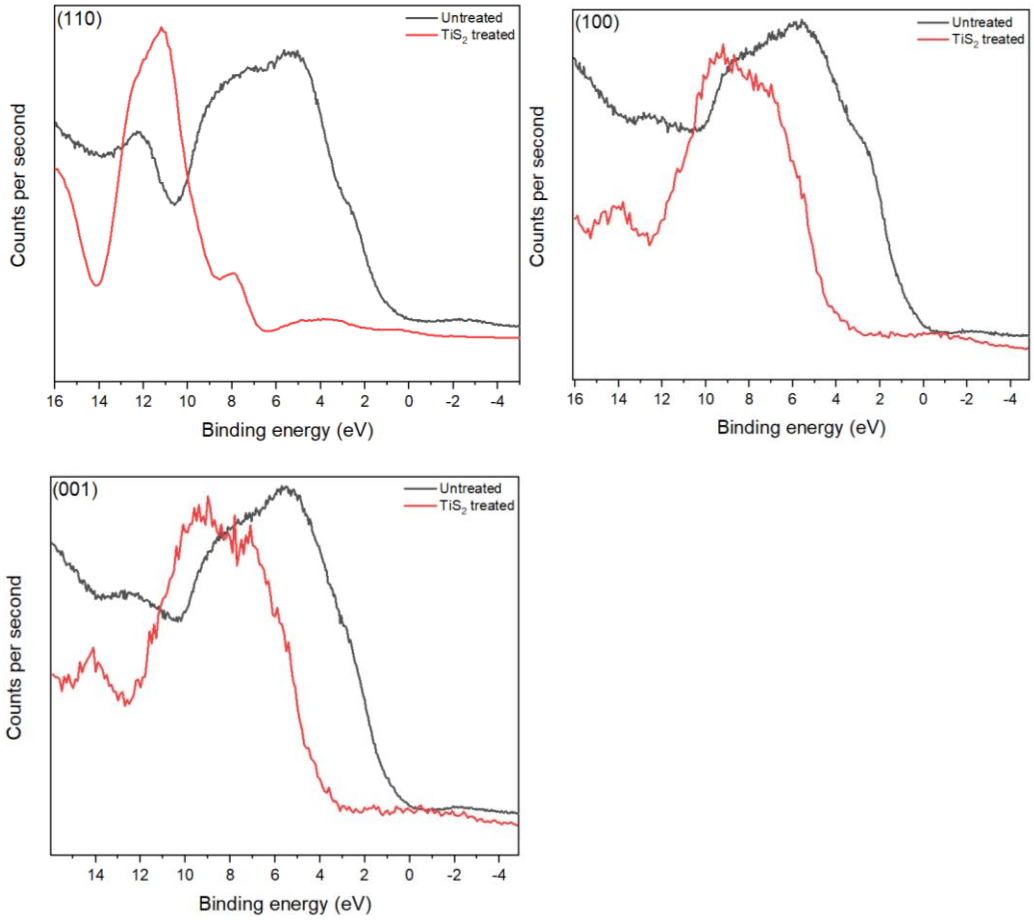

Figure 69 UPS valence band spectrum of the TiS_2 treated rutile (110), (100) and (001) substrates measured using He (II) source

6.2 Summary of Findings

The TiS_2 treatment of the rutile (110), (100) and (001) substrates resulted in the formation of $TiOSO_4$, TiOS and TiS chemical environments. However, the effects on chemical bonding, surface roughness, chemical composition and electronic valence band structure were found to be similar in the (100) and (001) substrates but not in the (110) substrate. The Raman data of the (110) substrate showed the rutile characteristic peaks remaining intact and evidence for $TiOSO_4$ formation. However, the TiO_2 chemical composition is also observed to be modified as per the XPS elemental depth profile. Since the formation of $TiOSO_4$ was only observed in 1 out of the 7 Raman spectra measured, it can be deduced that the $TiOSO_4$ is non-uniformly

distributed across the (110) substrate. This $TiOSO_4$ species is surface bound, as per the XPS S2p core line spectrum, while it is observed beneath the surface in the (100) and (001) substrates. This could be the reason for the (110) surface to be roughened differently to that in the other substrates. On the other hand, with the (100) and (001) substrates, the Raman spectrum do not indicate any additional peaks corresponding to the presence of the sulphur containing species and shows the rutile peaks to remain intact. The TiO_2 chemical composition remained the same even though the presence of sulphur was observed up to 120 nm into the (100) and (001) substrates. The fastest sulphur diffusion in the (100) substrate was observed with the lowest sulphur concentration of ~0.4 atomic% lying in the ~5 nm to ~12 nm region. However, the fastest sulphur diffusion in the (001) substrate was observed with the highest sulphur concentration of ~1.2 atomic% located on the surface. This could be the reason for the (001) surface to be the most roughened, as per the AFM images. The greatest valence band onset shift by +2.1 eV was observed with the (110) substrate, which had the least concentration of sulphur (~0.01 atomic%) and had surface-bound $TiOSO_4$, which was observed in the XPS and Raman data. On the other hand, the smallest shift of +1.82 eV was observed with the most roughened (001) surface, which had the highest concentration of sulphur (~1.6 atomic%). This suggests that the sulphur concentration is inversely related to the shift in the valence band onset. The smaller shifts observed with the (100) and (001) substrates could also be related to the absence of the $TiOSO_4$ peaks in their Raman spectrum. The π O2p contribution from the $TiOSO_4$ species formed was observed to be drastically increased in the (110) substrate while the σ O2p contribution from TiO_2 was observed to significantly reduce, which is also reflected in the XPS elemental depth profile. On the other hand, this drastic increase in the π O2p contribution is not observed with the (100) and (001) substrates.

Chapter 7: Nitrogen Diffusion in Rutile single crystal substrates

A detailed characterisation of the rutile substrates of the orientations (110), (100) and (001) treated using the TiN dopant source powder (referred to as TiN treated rutile) is discussed below.

7.1 Results and Discussion

The topography, composition and bonding on the surface and the bulk of the TiN treated rutile substrates were carried out.

7.1.1 Surface Topography

Upon TiN treatment, the surface topography of the as-received (110), (100) and (001) rutile substrates (Figure A in Appendices) were observed to be significantly roughened, as per AFM images (Figure 70). However, this roughened topography caused by the TiS_2 treatment is different compared to that caused by the TiS_2, TiC and TiB_2 treatment. This shows the effect of the choice of anion (e.g. sulphur, carbon or boron) on the extent and type of roughening caused on the rutile surface.

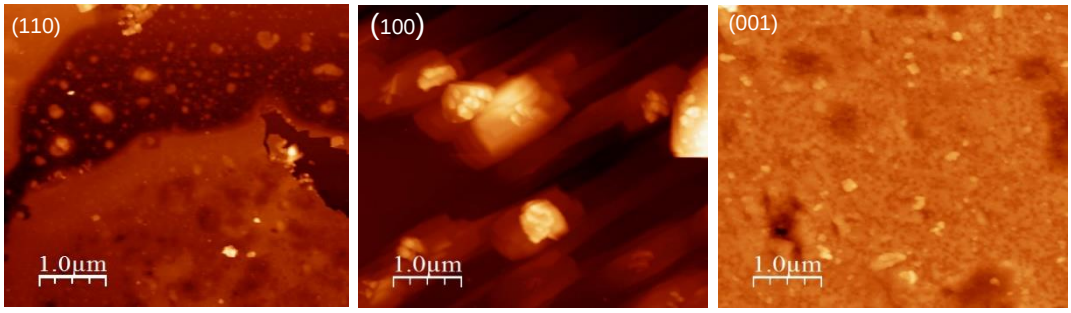

Figure 70 AFM images showing the differences in the morphology of the roughened surfaces of TiN treated rutile substrates (110), (100) and (001)

The extent to which the surface roughening occurred is found to be dependent on the orientation of the rutile substrates. The (100) surface is found to be the most roughened and the (110) surface is found to be the least roughened, as observed by the increase in their RMS roughness values (Table 23). The RMS roughness values of the (110), (100) and (001) substrates after the TiN treatment, were observed to increase from being < 0 nm to become 6.8 nm, 47 nm and 15 nm respectively (Table 22). With the (110) surface, oval shaped features with buckled edges of at least ~5 x 3 µm in size, surrounded by ~0.25 µm sized features were observed (Figure N in Appendices). However, on the (100) surface, these features are seen to be smaller

and are rectangular shaped ~1 μm sized mountains. On the other hand, the features on the (001) surface are circular, ≤ 0.5 μm in size and are less well defined like was the case with the TiB_2 treated (001) surface.

Table 22 A comparison of the surface roughness of rutile substrates before and after TiN treatment

	RMS roughness (nm)		
	(110)	(100)	(001)
Untreated	0.58	0.86	0.45
After TiN treatment	6.8	47	15
Increase in roughness	**6.2**	**46**	**14.6**

7.1.2 Surface Bonding

Upon TiN treatment, the position of the rutile characteristic peaks in the Raman spectrum of the (110), (100) and (001) substrates remained the same at 444 cm^{-1} and 608 cm^{-1} (Figure 71). This suggests that any changes in the rutile structure were not detectable using Raman spectroscopy. In the all the three TiN treated substrates, one of the peaks (1600 cm^{-1}) assigned as the peaks in these regions usually correspond to mixed sp^2/ sp^3 carbon contamination[139, 140] on the surface of the as-received rutile substrates also remain unshifted, while the other inherent defect peak at 1361 cm^{-1} was observed to disappear. This just suggests that some of the carbon contamination may have been removed by the high temperature carbon doping. It was found that 7 out of 7 Raman spectrum that was measured from different areas across each of the substrates gave the same result, suggesting a homogeneous chemical bonding characteristic.

Upon TiN treatment of the substrates, although the position of the rutile characteristic Raman peaks remains unchanged, the intensity of these peaks is observed to be modified in the (110) and (100) substrates. With the (110) and (100) substrates, the peak at 445 cm^{-1} becomes more intense than the peak at 606 cm^{-1}, suggesting that the asymmetric vibration of the O-Ti-O bond in the (001) plane has larger magnitude than the symmetric vibration of the O-Ti-O bonds in the (110) plane. On the other hand, no such changes are observed with the (001) substrate upon TiN treatment. The additional broad peak at ~708 cm^{-1} in all the three substrates does not correspond to rutile or nitrogen doped titania in the literature, suggesting the formation of a new phase from the TiN treatment.

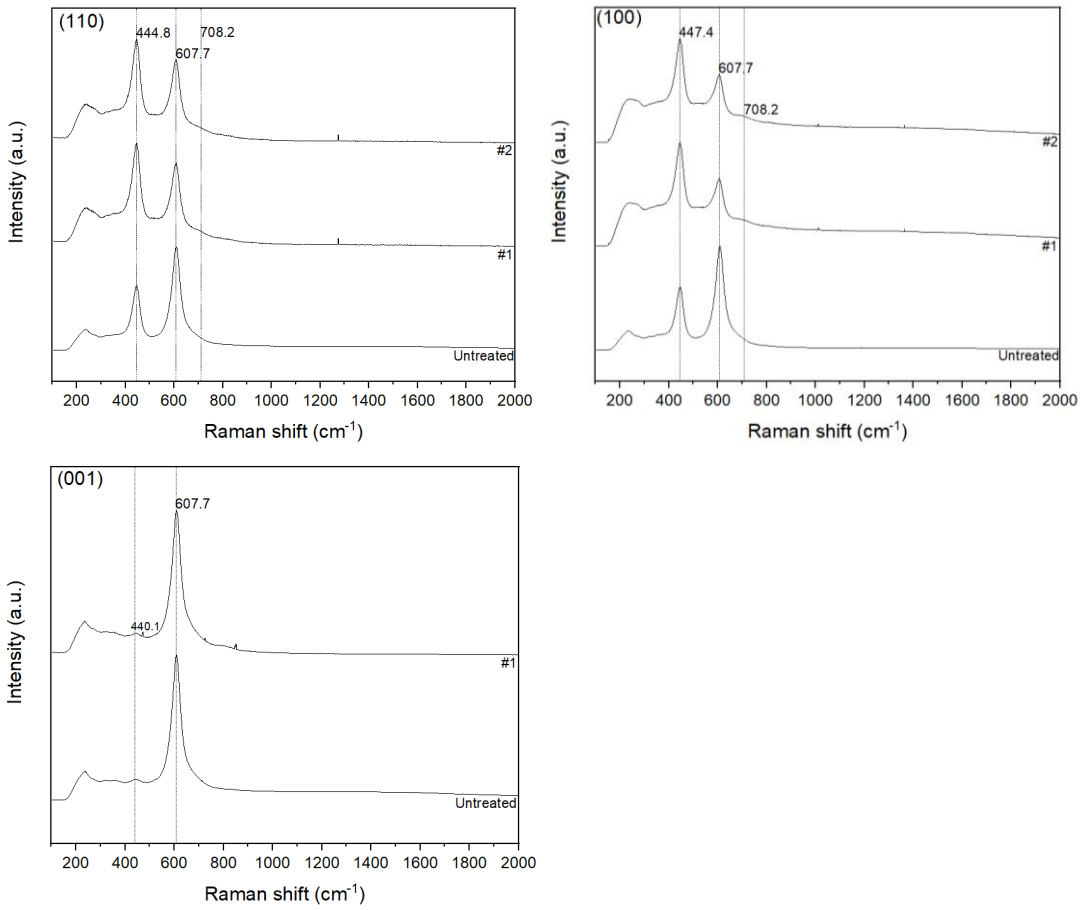

Figure 71 Raman spectrum of the TiN treated titania substrates of the orientations (110), (100) and (001), where #1 and #2 indicates different areas on the same substrate surface

7.1.3 Chemical Environments on the Depth scale

The concentration of the nitrogen incorporated into the surface and the bulk of the rutile substrates and the possibility of nitrogen diffusion is investigated using XPS.

1. **Nitrogen environment**

The incorporation of nitrogen is observed in all the three substrates, from their XPS N1s core line spectrum (Figure 72). The nitrogen incorporated into the surfaces of these substrates is predominantly in an interstitial site, potentially as N^{3-} species, as indicated by the peak at ~400 eV[166,167]. This is the nitrogen environment that is predominantly present even beneath the surface of the (110) and (001) substrates. On the other hand, the substitutional nitrogen environment (N^{-}), indicated by the peak at ~397 eV[168], is predominantly present beneath the surface of the (100) substrate.

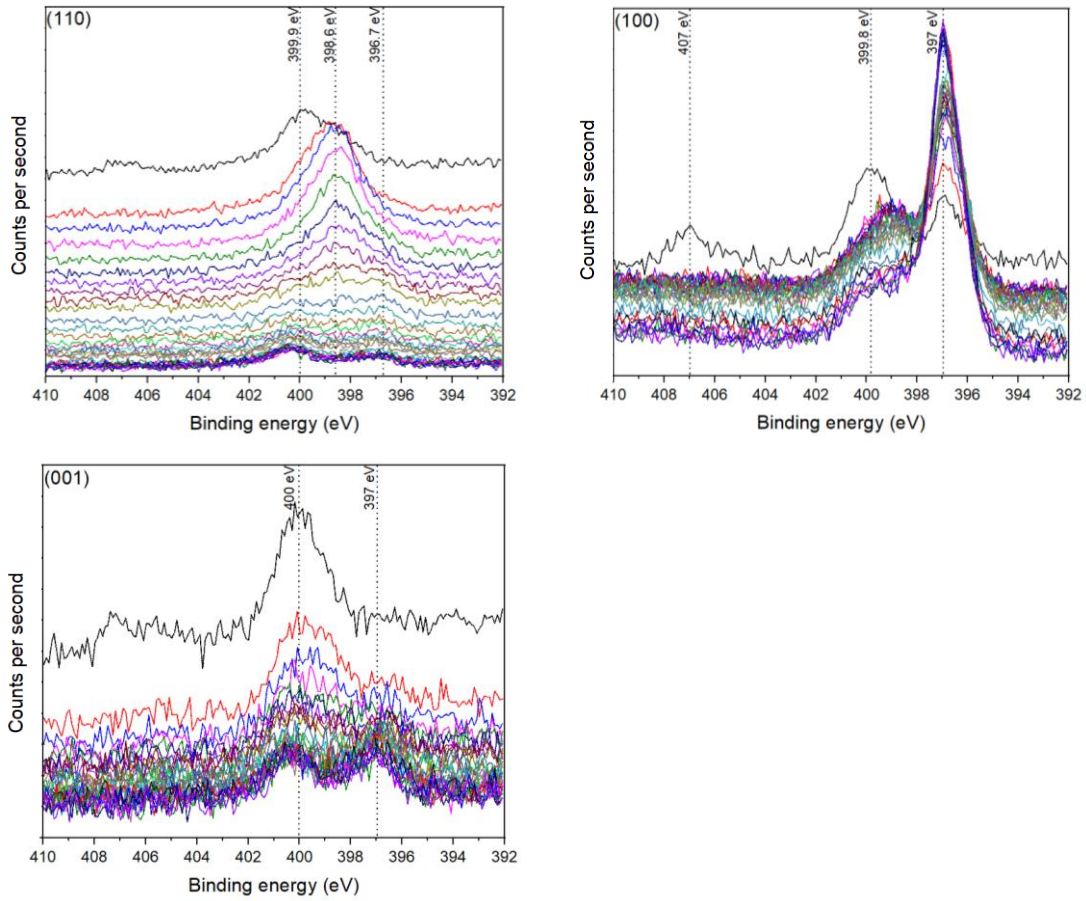

Figure 72 XPS N1s principal core line depth profile spectrum of the TiN treated rutile (110), (100) and (001) substrates. NB: The graph in black indicates the nitrogen concentration on the surface of the titania substrate and the coloured graphs indicate the nitrogen concentrations beneath the surface. The concentration of nitrogen decreases with increasing depth – please refer to figure 75 for the corresponding graph of N concentration against depth.

2. **Titanium environment**

Upon TiN treatment of the rutile (110), (100) and (001) substrates, the TiO_2 chemical environment is observed to remain. This is indicated by the peaks located at 464.6 eV and 458.9 eV (Figure 73), corresponding to the $Ti2p_{1/2}$ and $Ti2p_{3/2}$ orbital contributions in pristine TiO_2. In addition, Ti-N chemical environments are also observed, as indicated by the peaks at ~462 eV and ~455 eV, corresponding to the $Ti2p_{1/2}$ and $Ti2p_{3/2}$ orbital contributions[169].

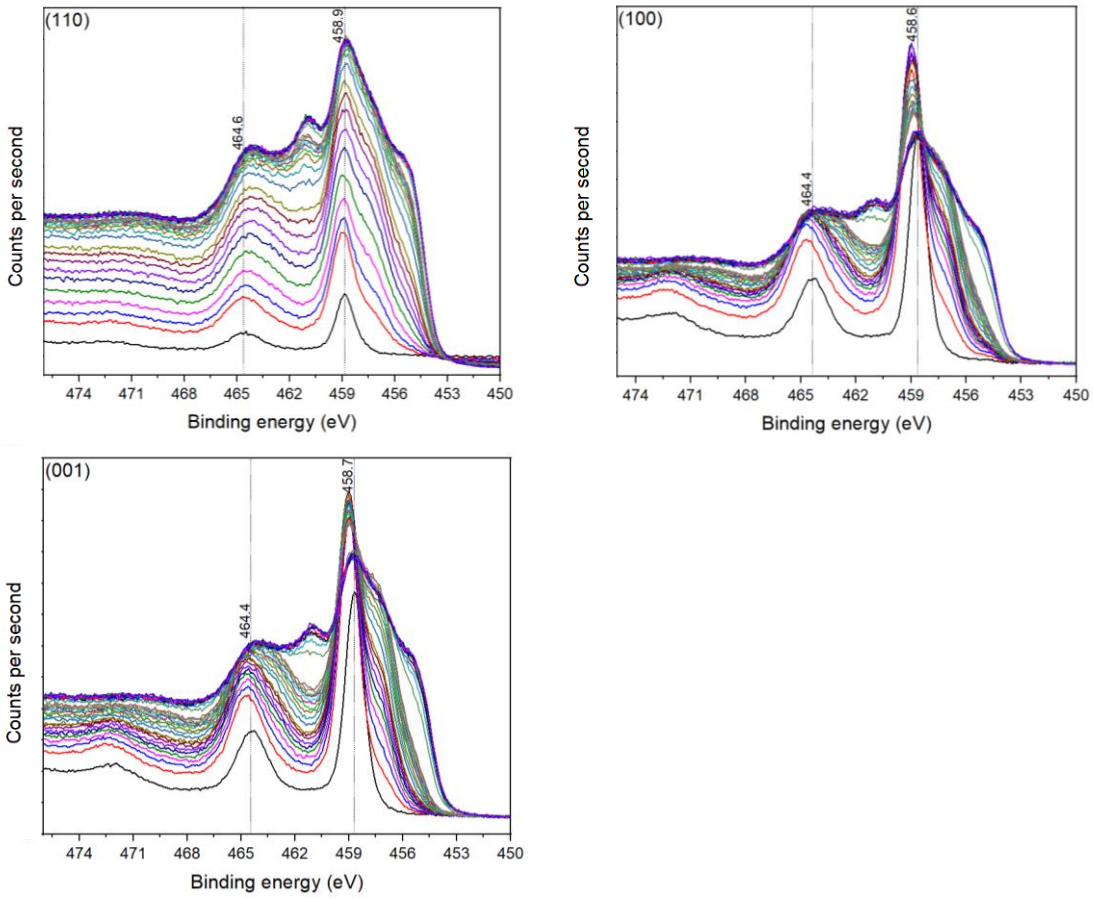

Figure 73 XPS Ti2p principal core line depth profile spectrum of the TiN treated rutile (110), (100) and (001) substrates. NB: The graph in black indicates the titanium concentration on the surface of the titania substrate and the coloured graphs indicate the titanium concentrations beneath the surface. The concentration of titanium changes with increasing depth – please refer to figure 75 for the corresponding graph of Ti concentration against depth.

The TiN treated Rutile (110), (100) and (001) substrates have a peak at ~530 eV (Figure 74) on their surface as well as beneath their surface. This peak corresponds to the O-Ti chemical environment in TiO_2. All the three substrates also have a peak at ~532 eV. Beneath the surface, this peak is observed to disappear in the (100) and (001) substrates, potentially suggesting that this is the interstitially bonded nitrogen species. In the (110) substrate, the concentration of the ~530 eV peak is lower than that of the ~532 eV peak on the surface as well as beneath the surface. However, at larger depths into the (110) substrate, the concentration of the ~532 eV peak becomes lower than that of the ~530 eV peak. This could potentially be due to the presence of N^- species in the surface and the near surface of the (110) substrate, which is not observed in the (100) and (001) substrate. Although these suggestions can be made, it is to be noted that the O1s XPS core line spectrum is not widely used in the literature to validate the presence of chemical environments.

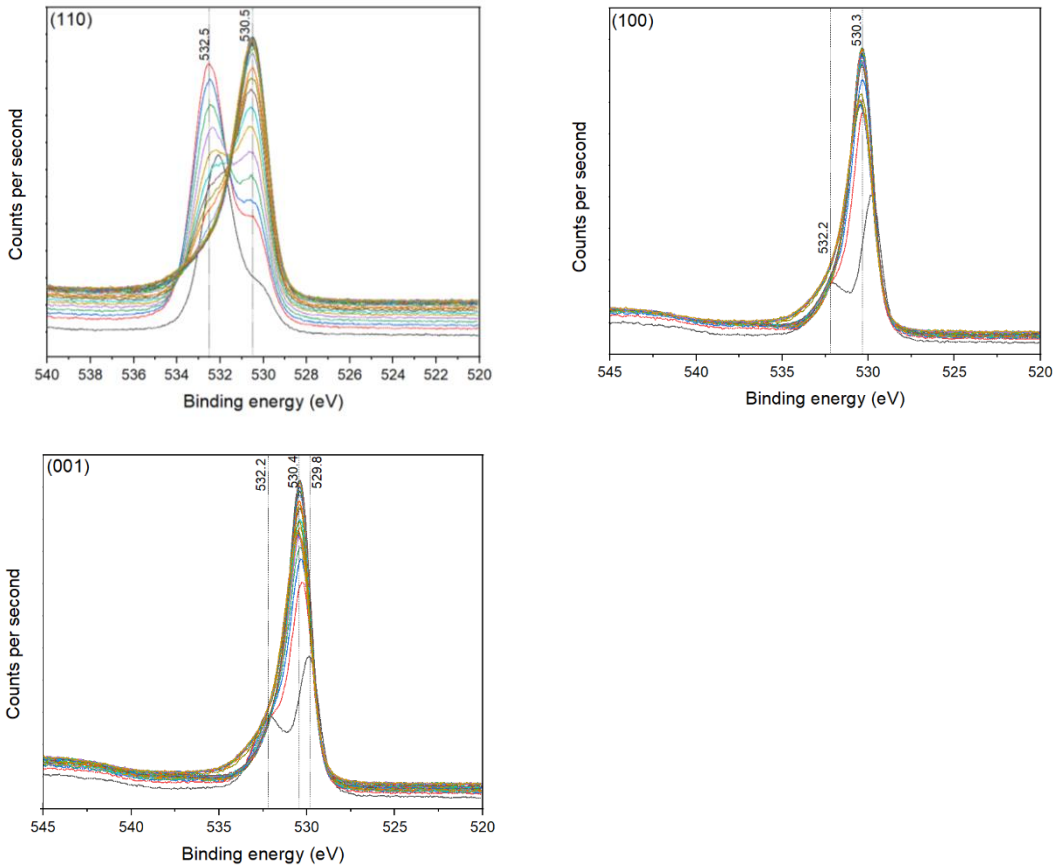

Figure 74 XPS O1s principal core line depth profile spectrum of the TiN treated rutile (110), (100) and (001) substrates. NB: The graph in black indicates the oxygen concentration on the surface of the titania substrate and the coloured graphs indicate the oxygen concentrations beneath the surface. The concentration of oxygen changes with increasing depth – please refer to figure 75 for the corresponding graph of O concentration against depth.

4. **Relative elemental concentration**

The elemental XPS depth profile shows nitrogen diffusion in the rutile (110), (100) and (001) substrates (Figure 75). The nitrogen concentrations of 2 atomic%, 1.7 atomic% and 1.2 atomic% found on the surface of the (110), (100) and (001) substrate surfaces are predominantly the interstitially located N^{3-} species, as per the N1s XPS core line spectrum. In the (110) and (001) substrates, the nitrogen concentration is found to be highest on the surface while in the (100) substrate, the nitrogen concentration is lowest on the surface. Beneath the surface of the (100) substrate, the nitrogen concentration is observed to increase, and this nitrogen is predominantly the substitutionally located nitrogen species. From these findings, it can be deduced that in the (110) and (001) substrates, the interstitial nitrogen diffusion into the surface occurs while in the (100) substrate, substitutional nitrogen diffusion towards the bulk of the substrate occurs. The nitrogen concentration is observed to go below 0.4 atomic% at a depth of ~10nm in the (110) substrate and ~1 nm in the (001) substrate. This suggests that most of the nitrogen incorporated into the (001) substrate is

surface-bound and is potentially the reason why the intensity of the Rutile characteristic peaks in the Raman spectrum remain intact unlike the case with the (110) and (100) substrates. The O: Ti ratio on the surface has been affected because of the nitrogen incorporation. However, beneath the surface, the ratio remained close to that observed in pristine TiO_2.

Please note that the (100) titania depth profile measurement is the only one that shows an initial increase in the dopant concentration with depth and with greater depths, the nitrogen concentration is not seen to level off to zero. In a similar scenario, long XPS depth profile experiments were carried out on the boron doped titania substrates in the previous chapter. However, this approach did not turn out to be useful in getting an answer to the reasoning behind why the dopant profiles were not observed to tail off at higher depths. Therefore, as already discussed in the boron doped titania chapter, further characterisation work needs to be carried out on the (100) titania that was nitrogen doped, using XPS cluster etching.

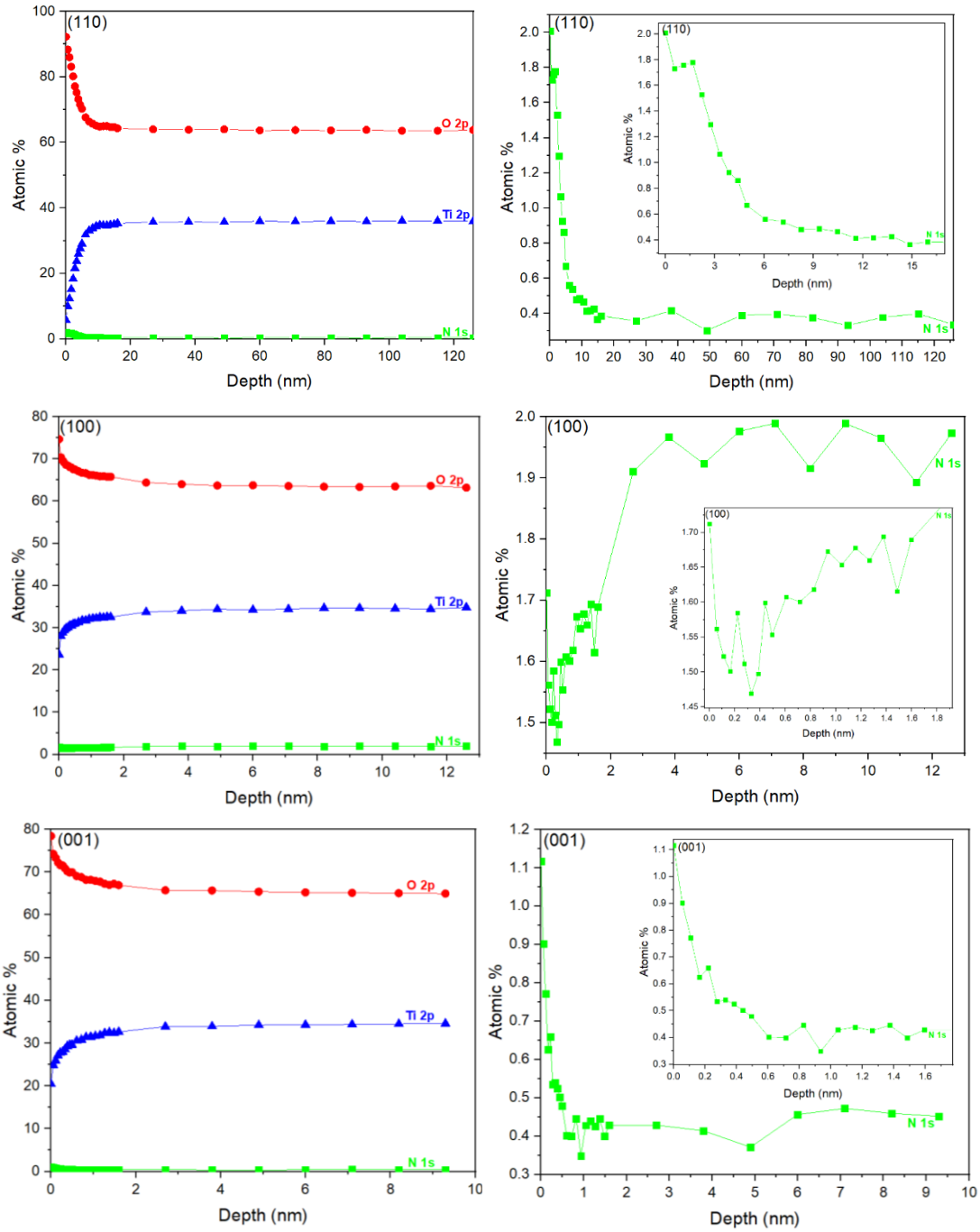

Figure 75 XPS depth profile of TiN treated rutile (110), (100) and (001) substrates showing (left) the O, Ti and N elemental profiles and (right) a zoomed in version of the nitrogen depth profile by itself, showing the nitrogen concentrations more clearly

The nitrogen diffusion in the (100) and (001) substrates is observed to have more than one diffusion rate, which is usually deduced from the diffusion coefficient calculated using Fick's second law of diffusion. The nitrogen diffusion coefficients extracted from the nitrogen diffusion plots (Figure 76, 77 and 78) are summarised in Table 24.

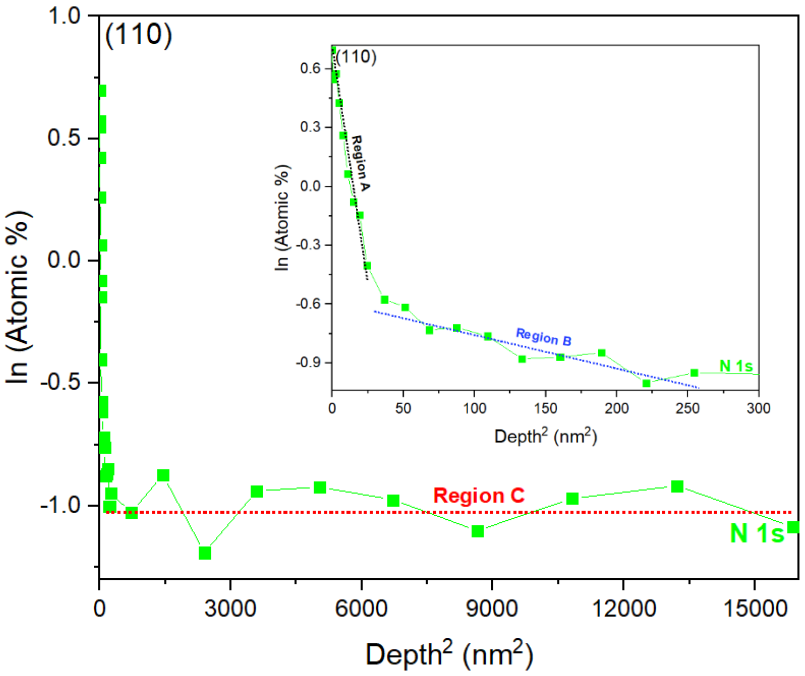

Figure 76 The nitrogen diffusion gradient of the TiN treated (110) rutile substrate. Inset: zoomed in version of the Depth^2 values from 0 nm^2 to 300 nm^2

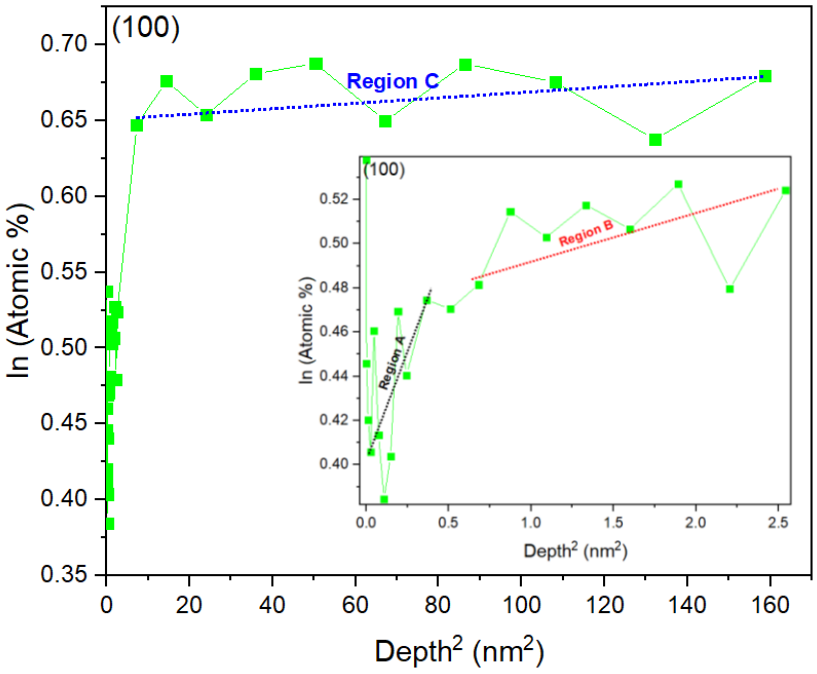

Figure 77 The nitrogen diffusion gradient of the TiN treated (100) rutile substrate. Inset: zoomed in version of the Depth^2 values from 0 nm^2 to 2.5 nm^2

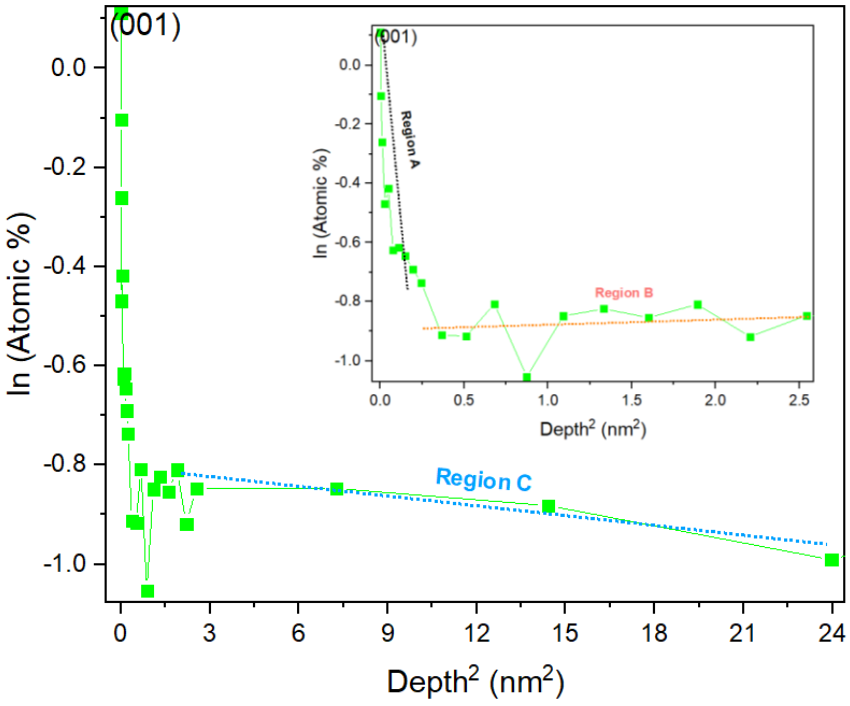

Figure 78 The nitrogen diffusion gradient of the TiN treated (001) rutile substrate. Inset: zoomed in version of the Depth^2 values from 0 nm^2 to 2.5 nm^2

Table 23 The nitrogen diffusion coefficients and nitrogen concentrations at different depths into the TiN treated rutile (100) and (001) substrates

Fastest nitrogen diffusion			
	110	**100**	**001**
Depth into the substrate	~5 nm to ~0 nm	~13 nm to ~2 nm	~0.5 nm to ~0 nm
Carbon concentration	~2 atomic%	~1.6 atomic%	~1.1 atomic%
Diffusion coefficient	~-0.0458 nm^2 s^{-1} (Region A)	~0.0002 nm^2 s^{-1} (Region C)	~-5.9087 nm^2 s^{-1} (Region A)
Second fastest nitrogen diffusion			
	110	**100**	**001**
Depth into the substrate	~16 nm to ~5 nm	~2 nm to ~1 nm	~5 nm to ~2 nm
Carbon concentration	~0.5 atomic%	~1.7 atomic%	~0.45 atomic%
Diffusion coefficient	~-0.00171 nm^2 s^{-1} (Region B)	~0.0221 nm^2 s^{-1} (Region B)	~-0.0064 nm^2 s^{-1} (Region C)
3rd fastest nitrogen diffusion			
	110	**100**	**001**
Depth into the substrate	~120 nm to ~16 nm	~1 nm to ~0 nm	~2 nm to ~0.5nm
Carbon concentration	~0.4 atomic%	~2 atomic%	~0.45 atomic%
Diffusion coefficient	~0 nm^2 s^{-1} (Region C)	~0.1933 nm^2 s^{-1} (Region A)	~0.0165 nm^2 s^{-1} (Region B)

The fastest and slowest nitrogen diffusion rates were not observed at the same depths in the (110), (100) and (001) substrates (Table 23). The fastest nitrogen diffusion in the (110) substrate was observed with the highest nitrogen concentration of ~2

atomic% lying in the top ~5 nm region. The fastest nitrogen diffusion in the (100) substrate was observed with the lowest concentration of ~1.6 atomic% in the top 1 nm region. On the other hand, in the (001) substrate, the fastest nitrogen diffusion was observed in the top 0.5 nm region with the highest concentration of nitrogen of ~1.1 atomic%.

7.1.4 Electronic Structure

The valence band analysis carried out using XPS and UPS is discussed below.

1. **XPS valence band**

Upon TiN treatment, the XPS valence band onset measured of the surface of the rutile (110), (100) and (001) substrates were observed to be shifter to higher binding energies (Table 24). All the three substrates were shifted by 2.18 eV and this could be due to the presence of nitrogen in both interstitial and substitutional sites of the Rutile lattice. This suggests that the concentration of the individual nitrogen defect species itself does not affect the shift in the valence band onset.

Table 24 XPS valence band onset of TiN treated rutile (110), (100) and (001) substrates

Rutile substrate orientation	XPS Valence Band (eV)	
	Untreated	TiN treated
(110)	1.20	3.38
(100)	1.18	3.36
(001)	1.19	3.37
TiN dopant source powder	2.26	N/A

The intense peak at 10 eV in the XPS valence band spectrum is observed to disappear in the (110), (100) and (001) substrates upon TiN treatment (Figure 79). This peak, originally assigned to correspond to the asymmetric O-Ti-O vibration in the Raman spectrum, is therefore deduced to be weakened. This could be due to the incorporation of the nitrogen into the substitutional sites, which require the breaking of the O-Ti-O bonds.

Upon TiN treatment, the Ti3p contribution from the inherent- Ti^{3+}-defect species is seen to be remain in the (110), (100) and (001) substrates.

The TiN treatment has resulted in the emergence of new peaks in the O2s region of the XPS valence band spectrum of the (100) and (001) substrates. A new peak is

clearly observed at ~17 eV in both these substrates and not in the (110) substrate. Therefore, it could be deduced that this peak is caused by the nitrogen species in the (100) and (001) substrates that are predominantly located in the substitutional sites of the rutile lattice, as per the N1s XPS core line spectrum.

The broadening of the peak in the 10 eV to 3 eV region, corresponding to the O2p orbital contribution is observed in all the three rutile substrates upon TiN treatment. This could be caused by the mixing of the N1s states arising from the interstitial nitrogen species, present in all these substrates, with the O2p state in TiO_2.

The emergence of the new peak at ~30 eV is observed in all the three substrates. This could be potentially caused by the nitrogen species incorporated in the interstitial sites of the rutile lattice. It is to be noted that this peak is not found to be present in the as-received TiN powder, and therefore suggesting that the nitrogen species which gave rise to the 30 eV peak could not have been incorporated into a TiN chemical environment after being incorporated into the rutile structure. This suggests that the 30 eV peak has resulted from an interstitially incorporated nitrogen species than a substitutionally incorporated nitrogen species, both of which are seen to be present in the XPS N1s spectra discussed earlier.

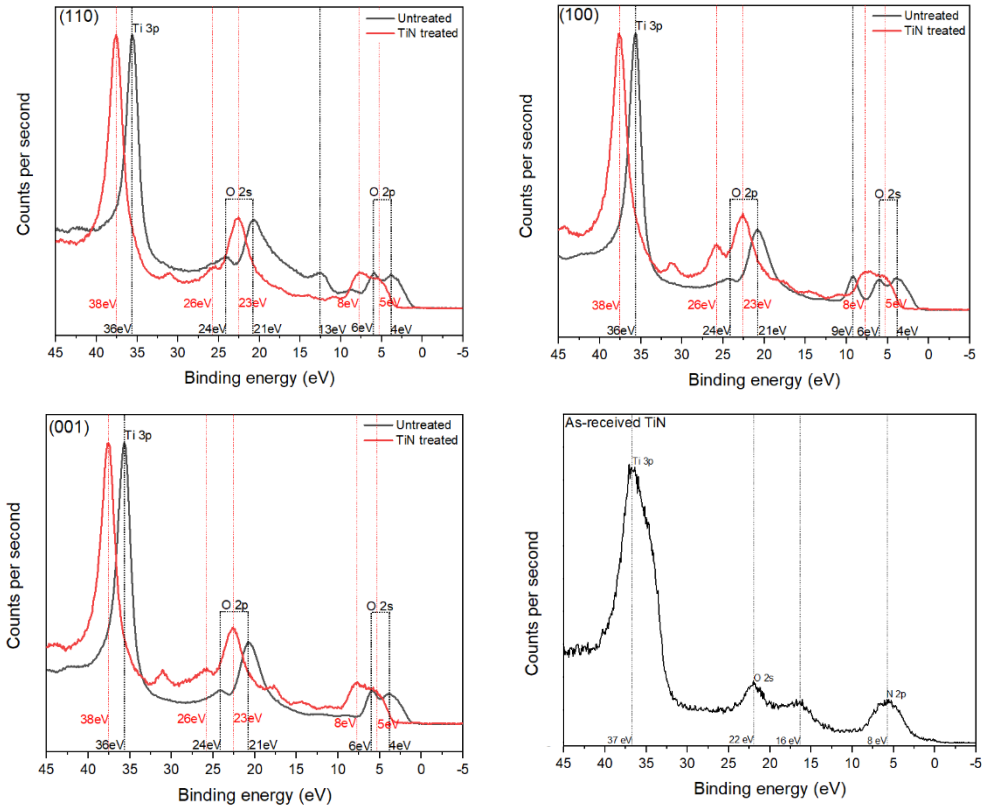

Figure 79 XPS valence band spectrum of the TiN treated rutile (110), (100) and (001) substrates along with that of the TiN powder used for the TiN treatment

2. **UPS valence spectrum**

Upon TiN treatment, the π O2p contribution (~6 eV) in the UPS valence band spectrum (Figure 80) is observed to remain the same in the (110) substrate while it is seen to increase in the (100) and (001) substrates. This could be due to the nitrogen species located predominantly in the substitutional sites of the rutile (100) and (001) substrates. On the other hand, the nitrogen species predominantly occupied in the interstitial sites of the rutile (110) substrate has not affected the π O2p or σ O2p orbital contributions.

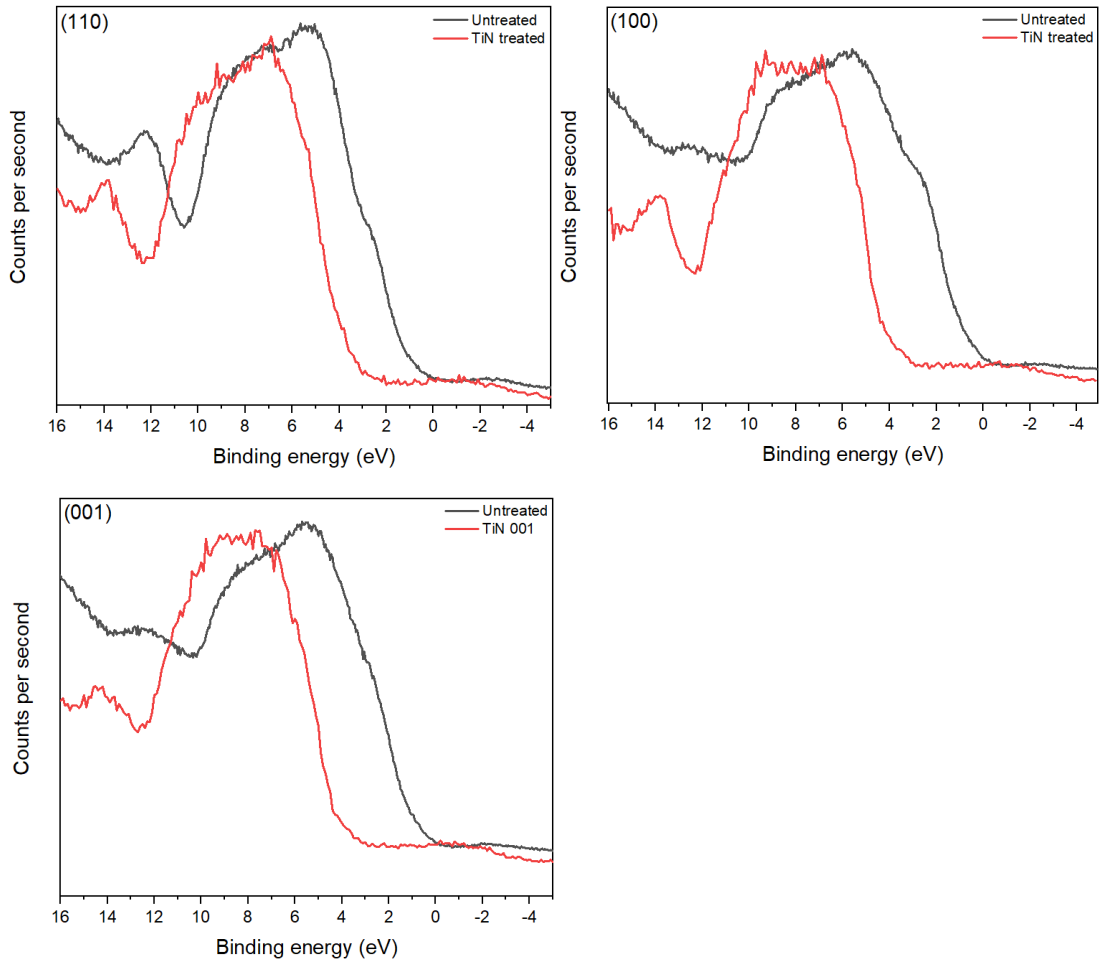

Figure 80 UPS valence band spectrum of the TiN treated rutile (110), (100) and (001) substrates measured using He (II) source

7.2 Summary of Findings

Upon TiN treatment, the nitrogen diffusion is observed in the (110), (100) and (001) substrates. The nitrogen incorporated into the (001) substrate is surface-bound, below 1 nm, and could be the reason why the intensity or position of the peaks in its Raman spectrum are not modified. On the other hand, nitrogen incorporation into the surface

as well as beneath the surface of the (110) and (100) substrates has weakened the symmetric O-Ti-O bonding vibration, as per the Raman data. These findings clearly show the different behaviours of the (110), (100) and (001) substrates towards TiN treatment, which is reflected in the different extents and ways in which their surfaces are roughened. These surfaces of all the three substrates are predominantly made up of interstitially located N^{3-} species, as per the N1s XPS core line spectrum. However, the diffusion of the interstitial nitrogen into the surface of the (110) and (001) substrates is observed, while the diffusion of the substitutional nitrogen towards the bulk of the (100) substrate is observed, as per the XPS elemental depth profile. The fastest nitrogen diffusion in the (110) substrate was observed with the highest nitrogen concentration of ~2 atomic% lying in the top ~5 nm region. The fastest nitrogen diffusion in the (100) substrate was observed with the lowest concentration of ~1.6 atomic% in the top 1 nm region. On the other hand, in the (001) substrate, the fastest nitrogen diffusion was observed in the top 0.5 nm region with the highest concentration of nitrogen of ~1.1 atomic%. The XPS valence band onset of all the three substrates were shifted by 2.18 eV and this could be due to the presence of nitrogen in both interstitial and substitutional sites of the rutile lattice. This suggests that the concentration of the individual nitrogen defect species itself does not affect the shift in the valence band onset. Upon TiN treatment, the π O2p contribution (~6 eV) in the UPS valence band spectrum is observed to remain the same in the (110) substrate while it is seen to increase in the (100) and (001) substrates. This could be due to the nitrogen species located predominantly in the substitutional sites of the rutile (100) and (001) substrates. On the other hand, the nitrogen species predominantly occupied in the interstitial sites of the rutile (110) substrate has not affected the π O2p or σ O2p orbital contributions.

Below is a summary (Table 25, 26, 27) of the effect of different anion incorporation into the rutile substrates of the orientations (110), (100) and (001). This was done since Chapters 3, 4, 5, 6 and 7 were focussed on discussing the effect of different orientations of the rutile substrates in the incorporation of each of the anions namely boron, carbon, sulphur and nitrogen.

Table 25 The effect of boron, carbon, sulphur and nitrogen incorporation on the crystal structure, chemical composition and electronic properties of the rutile (110) substrate

For Rutile substrate orientation (110)					
Effect on:		**Boron**	**Carbon**	**Sulphur**	**Nitrogen**
Topography	AFM	Surface roughness of 23 nm with uniformly distributed nanoparticle sized features	Surface roughness of 3.3 nm with several trenches with straight edges	Surface roughness of 23 nm with a trench with smooth edges	Surface roughness of 6.8 nm with oval shaped features with buckled edges
Crystal structure	Raman	Weakening of the asymmetric and symmetric O-Ti-O bonds plus $TiBO_3$, B_2O_3 and B_2O_5 peak formation	Weakening of the symmetric O-Ti-O bonds	$TiOSO_4$ peak formation	Weakening of the symmetric O-Ti-O bonds observed
	XRD	Epitaxial formation of $TiBO_3$ on the surface	n/A	n/a	n/a
Chemical composition	XPS core line depth profile	Stoichiometry over the depth scale close to $TiBO_3$ +/- 10% variation, caused by the presence of other B_2O_5 or B_2O_3 or TiB_2	C concentration falls below 5 atomic% within the top 5 nm, below which O: Ti of pristine TiO2 is seen. O-C=O and C-C environments seen.	Surface bound TiOSO4 observed, O: Ti ratio beneath the surface is close to that in pristine TiO_2	Nitrogen on the surface and beneath the surface is predominantly in the Rutile interstitial site although substitutionally occupied nitrogen is also observed
Electronic structure	XPS Valence band	Blue shift of the XPS VB onset, B1s-O2s and B1s-O2p orbital mixing from surface-bound TiB_2 species, New O2p, B1s and Ti3p states from $TiBO_3$	Blue shift of the XPS VB onset, Ti3p contribution like that in the TiC powder, the intensity of the new C1s state peak dependent on the concentration of surface-bound defects	Blue shift of the XPS VB onset, Ti3p contribution like that in TiS_2, new S2p peaks from $TiOSO_4$ in the O2p and O2s contribution regions of the XPS VB spectrum	Blue shift of the XPS VB onset, mixing of the O2p states with the N1s states in interstitial sites
	UPS valence band	O2p-B1s mixing from surface bound TiB_2 species is observed	σ O2p mixing with C1s states from O-C=O environment	O2p contribution mainly from its π orbital	Interstitial N1s states has not caused significant changes to the σ or π O2p contributions

Table 26 The effect of boron, carbon, sulphur and nitrogen incorporation on the crystal structure, chemical composition and electronic properties of the rutile (100) substrate

For Rutile substrate orientation (100)					
Effect on:		**Boron**	**Carbon**	**Sulphur**	**Nitrogen**
Topography	AFM	Surface roughness of 227 nm with round features	Surface roughness of 36 nm with several trenches with straight edges	Surface roughness of 57 nm with a trench with smooth edges	Surface roughness of 47 nm with oval shaped features with buckled edges
Crystal structure	Raman	Weakening of the asymmetric and symmetric O-Ti-O bonds plus $TiBO_3$ and B_2O_5 peak formation	Weakening of the symmetric O-Ti-O bonds	Changes to the Rutile structure not detected using Raman spectroscopy	Weakening of the symmetric O-Ti-O bonds observed
	XRD	Formation of $TiBO_3$ on the surface	n/A	n/a	n/a
Chemical composition	XPS core line depth profile	Stoichiometry over the depth scale close to $TiBO_3$ +/- 10% variation, caused by the presence of other B_2O_5 or B_2O_3 or TiB_2	C concentration falls below 5 atomic% within the top 0.2 nm, below which O: Ti of pristine TiO2 is seen. O-C=O, O-C-O and C-C environments seen.	Ti-O-S observed, O: Ti ratio beneath the suface is close to that in pristine TiO_2	Nitrogen on the surface is predominantly at the interstitial site and nitrogen beneath the surface is predominantly in the substitutional site of the Rutile lattice
Electronic structure	XPS Valence band	Blue shift of the XPS VB onset, B1s-O2s and B1s-O2p orbital mixing from surface-bound TiB_2 species, New O2p, B1s and Ti3p states from $TiBO_3$	Blue shift of the XPS VB onset, mixing of the C1s states from the C defects with the O2s and O2p orbital contributions	Blue shift of the XPS VB onset, mixing of the new S2p peaks from $TiOSO_4$ and Ti-S with the O2p and O2s contribution regions of the XPS VB spectrum	Blue shift of the XPS VB onset, mixing of the O2p states with the N1s states in interstitial sites and mixing of the O2s states with the N1s states from substitutional sites
	UPS valence band	σ O2p-B1s mixing from surface bound TiB_2 species is observed	π O2p mixing with C1s states from O-C=O environment	O2p contribution mainly from its π orbital	π O2p contribution seen to be increased potentially due to the substitutional nitrogen defects

Table 27 The effect of boron, carbon, sulphur and nitrogen incorporation on the crystal structure, chemical composition and electronic properties of the rutile (001) substrate

For Rutile substrate orientation (001)					
Effect on:		**Boron**	**Carbon**	**Sulphur**	**Nitrogen**
Topography	AFM	Surface roughness of 30 nm with round features	Surface roughness of 46 nm with circular trenches	Surface roughness of 33 nm with a stepped layered feature	Surface roughness of 15 nm with circular features
	Raman	Weakening of the asymmetric and symmetric O-Ti-O bonds plus TiB_2 and B_2O_3 peak formation	Changes to the structure are not detected using Raman spectroscopy	Changes to the Rutile structure not detected using Raman spectroscopy	Weakening of the symmetric O-Ti-O bonds observed
Crystal structure	XRD	Boron doped Rutile	n/A	n/a	n/a
Chemical composition	XPS core line depth profile	Stoichiometry over the depth scale close to $TiBO_3$ +/- 10% variation, caused by the presence of other B_2O_5 or B_2O_3 or TiB_2	C concentration falls below 5 atomic% within the top 0.2 nm, below which O: Ti of pristine TiO_2 is seen. O-C=O and C-C environments seen	Ti-S and $TiOSO_4$ observed, O: Ti ratio beneath the surface is close to that in pristine TiO_2	Nitrogen on the surface and beneath the surface is predominantly in the interstitial site of the Rutile lattice
Electronic structure	XPS Valence band	Blue shift of the XPS VB onset, B1s-O2s and B1s-O2p orbital mixing from surface-bound interstitial boron and TiB_2 species	Blue shift of the XPS VB onset, Ti3p contribution looks like that in the TiC powder, new C1s peaks from O-C=O or C-C environments	Blue shift of the XPS VB onset, mixing of the new S2p states from surface bound $TiOSO_4$	Blue shift of the XPS VB onset, mixing of the O2p states with the N1s states in interstitial nitrogen, mixing of the O2s states with the N1s states in the substitutional nitrogen
	UPS valence band	π O2p-B1s mixing from surface bound interstitial boron species observed	π O2p mixing with C1s states from O-C=O environment	O2p contribution mainly from its σ orbital	π O2p contribution seen to be increased potentially due to the substitutional nitrogen defects

Chapter 8: Nitrogen Doped Layered Titanate Structures

This chapter covers the synthesis and a comprehensive characterisation of nitrogen doped tunnelled titanates and nitrogen doped layered titanates.

8.1 Characterisation

Powder X-ray Diffraction (PXRD) was carried out on the Bruker STOE diffractometer with a monochromatic Mo K α λ = 0.7107 Å radiation to determine the crystal structure. The lattice parameters were extracted from the recorded XRD pattern using the UnitCell software. Thermoscientific Fisher K-alpha X-ray Photoelectron Spectrometer with a monochromatic Al K α source of 1486.6 eV energy was used to investigate the chemical nature and composition of the nitrogen doped titanate structures. The Renishaw inVia spectrometer with a laser wavelength of 785 nm set up with an Argon laser source was used for measuring the effect of nitrogen doping on the bond stretching and bending vibrations. An estimate of the nitrogen concentration in the bulk of the titanates were measured using the CHN analysis service at the UCL School of Pharmacy. Any shift in the optical absorption spectrum due to the doping was measured using the Perkin Elmer Lambda-950 UV/ VIS spectrometer.

8.2 Experimental

The procedures carried out for the preparation of alkali metal titanates and for the nitrogen doping of these titanates is detailed below.

1. **Layered Titanate Synthesis**

Titania Anatase powder, purchased from *Sigma Aldrich*, was ground well with the relevant group 1 carbonate powder out of Na_2CO_3, K_2CO_3 and Cs_2CO_3, purchased from *Sigma Aldrich,* using an agate pestle and mortar for the synthesis of $Na_2Ti_3O_7$, $Na_2Ti_6O_{13}$, $K_2Ti_6O_{13}$, and $Cs_{0.68}T_{1.825}O_4$. The anatase-carbonate mixture was then annealed in air at 800^o C for 60 h in a box furnace, with further grinding every 20 h to get the layered titanate powders. For the synthesis of $Na_2Ti_3O_7$, 0.7029 g of Na_2CO_3 and 1.5890 g of TiO_2 was used; for the $Na_2Ti_6O_{13}$ synthesis, 0.3917 g of Na_2CO_3 and 1.7711g of TiO_2 was used; for the $K_2Ti_6O_{13}$ synthesis, 0.4821 g of K_2CO_3 and 1.6715 g of TiO_2 was used.

2. **Ammonolysis**

The above synthesised titanate powder was then nitrogen doped using ammonolysis. The following modification to the ammonolysis set-up is made when carrying out the reaction. One end of the crucible containing the powder is aligned and placed in the middle of the tube furnace as shown in Figure 81. The powder is then annealed under a dynamic flow of ammonia gas with a flow rate of 720 cm^3 min^{-1} at 750 ^oC for 1 h.

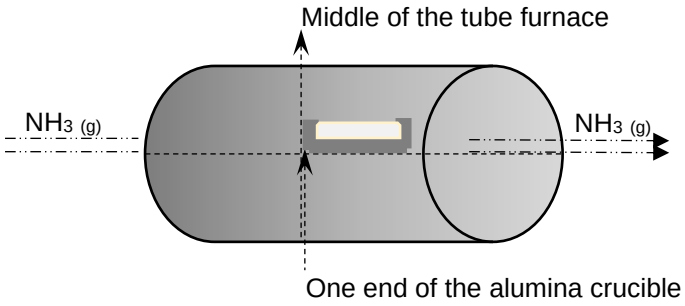

Figure 81 Modified ammonolysis reaction set-up

8.3 Results and Discussion

8.3.1 Varying the Doping Temperature

Each batch of the titanate powders that was nitrogen doped using the modified ammonolysis technique had a green-yellow-cream colour gradient (Figure 82). The green colour was observed with the titanate powders that were between 0 cm and 5.5 cm away from the middle of the furnace. The yellow colour was observed with titanate powders that were between 5.5 cm and 7 cm away from the middle of the furnace. The cream colour was observed with the titanate powders that were between 7 cm and 8.5 cm away from the middle of the furnace. The temperature of the furnace denoted by the green, yellow and cream regions were measured to be 750 ^oC, 684 ^oC and 640 ^oC respectively.

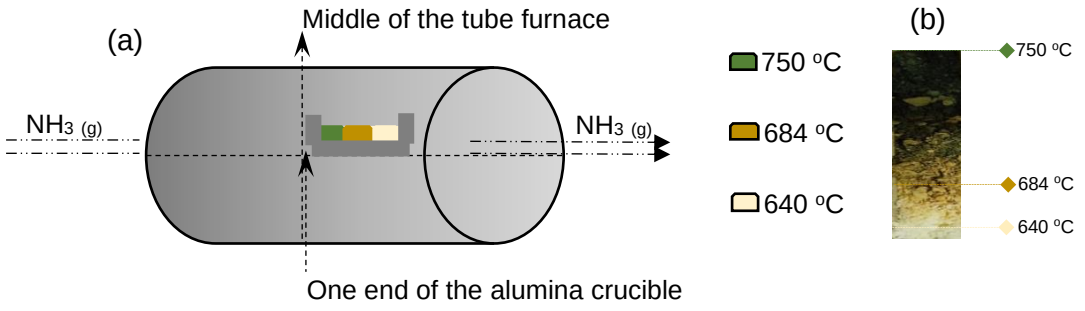

Figure 82 (a) The green-yellow-cream temperature zones of the modified ammonolysis set-up and (b) photograph of the powder obtained after ammonolysis

8.3.2 Crystal Structure

The crystal structure of the synthesised tunnelled frameworks, $Na_2Ti_6O_{13}$ and $K_2Ti_6O_{13}$, match well with the pattern found in the literature[170, 171, 172] (see Appendices Figure R and S) and is observed to be retained upon nitrogen doping. However, potential modifications to their crystallinity, morphology, chemical composition are observed from their PXRD patterns (Figure 83). In $Na_2Ti_6O_{13}$, the intensity of the peak at ~ 9° is seen to decrease with increasing doping temperature, with this peak completely absent at the highest doping temperature of 750 °C. This suggests a potential increase in crystallinity with increasing doping temperature. However, in $K_2Ti_6O_{13}$, an increase in crystallinity is also observed at all three doping temperatures, where the peak at 13.6° and 29.3° becomes sharper and well-defined. In $Na_2Ti_6O_{13}$, the new peak at 11.8° is seen to emerge at all three doping temperatures while the peak at 12.5° is observed only at 640 °C and 684 °C and so the latter peak could be caused by a nitrogen defect species that is volatile at higher temperatures. However, in $K_2Ti_6O_{13}$, the intensity of the peak at 24.3° is seen to remain the same with the doping temperature of 684 °C but seen to double with the temperatures 640 °C and 750 °C. This may suggest that the nitrogen defect formed at 640 °C is potentially volatile at 684 °C and too reactive at 750 °C. Peak broadening is observed only in $Na_2Ti_6O_{13}$ with the peak at ~10.9° at all three doping temperatures and is potentially caused by the formation of nano-sized particles.

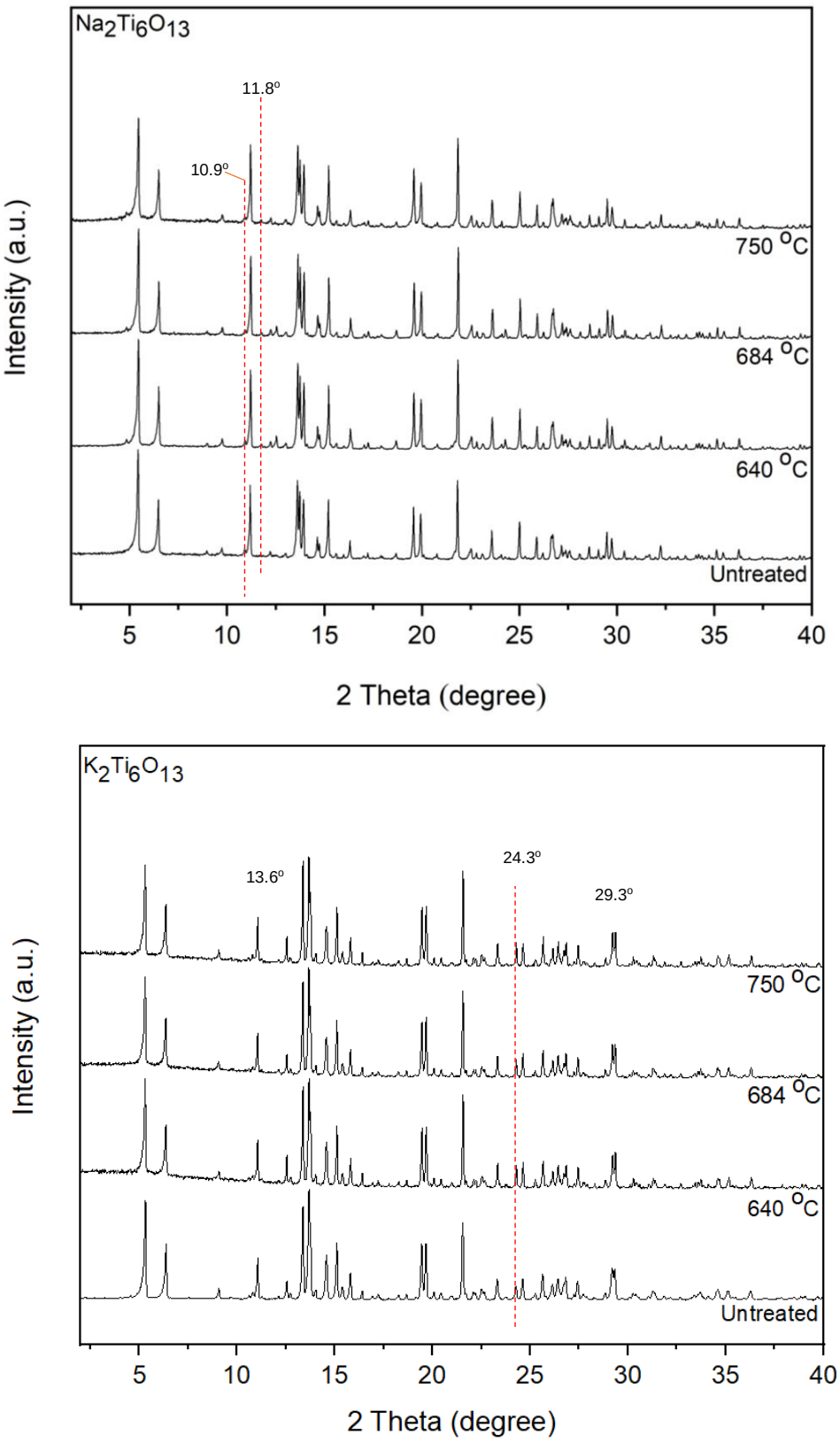

Figure 83 PXRD pattern of undoped and nitrogen doped $Na_2Ti_6O_{13}$ (top) and $K_2Ti_6O_{13}$ (bottom) tunnelled titanates at three different doping temperatures of 640 ºC, 684 ºC and 750 ºC

The crystal structure of the synthesised open layered frameworks, $Na_2Ti_3O_7$ and $Cs_{0.68}T_{1.825}O_4$, match well with the pattern found in the literature [173,174] (see Appendices

Figure T and U) and is observed to be retained upon nitrogen doping. Upon nitrogen doping, the $Na_2Ti_3O_7$ crystal structure remains the same while the $Cs_{0.68}T_{1.825}O_4$ structure is observed to have potential modifications to their crystallinity, morphology and chemical composition, according to their PXRD patterns (Figure 84). The broadening of the peaks located at ~9.3 eV, ~14 eV, ~18 eV and ~26 eV is observed to increase upon nitrogen doping and upon increasing the doping temperature from 640 ^oC and 684 ^oC. This could potentially be an effect of changes to the particle size of the titanate powders[175]. The ratio of the peak at ~13 eV with respect to the peak at ~13.2 eV, at these temperatures, are seen to be swapped. However, at 750 ^oC, this ratio decreases from being ~1: 3/4 to ~1: 1/2 and the peaks discussed above are seen to be sharper. Additionally, at all the three doping temperatures, the peaks at ~14 eV, ~18eV, ~26 eV and ~28 eV are seen to transform into a doublet, where the shape of the doublet at ~28 eV is seen to vary for different doping temperatures. All these observations could potentially be due to increase in crystallinity upon incorporation of nitrogen defect species into the $Cs_{0.68}T_{1.825}O_4$ lattice.

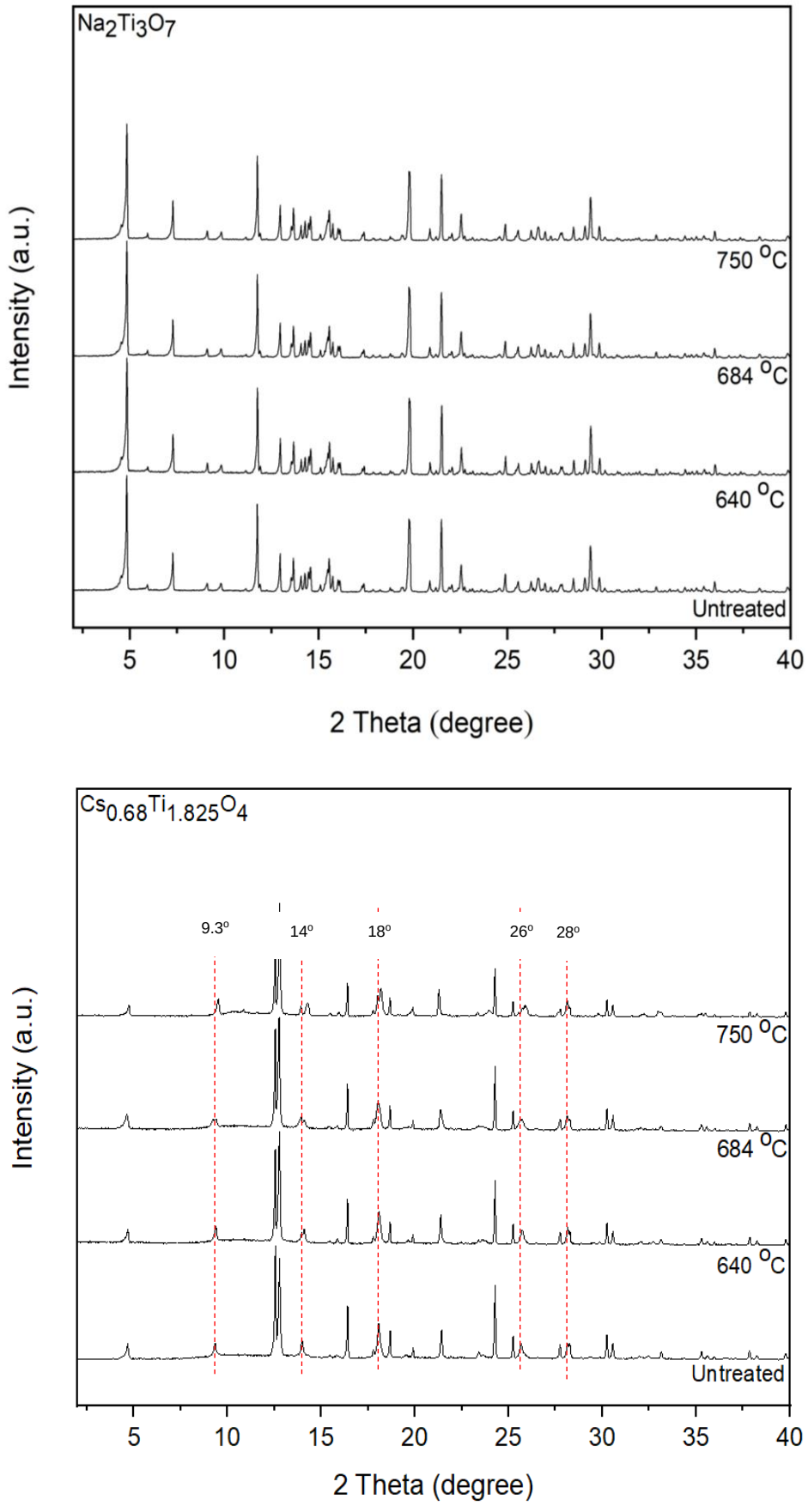

Figure 84 PXRD pattern of nitrogen doped $Na_2Ti_3O_7$ (top) and $Cs_{0.68}T_{1.825}O_4$ (bottom) open layered titanates at three different doping temperatures

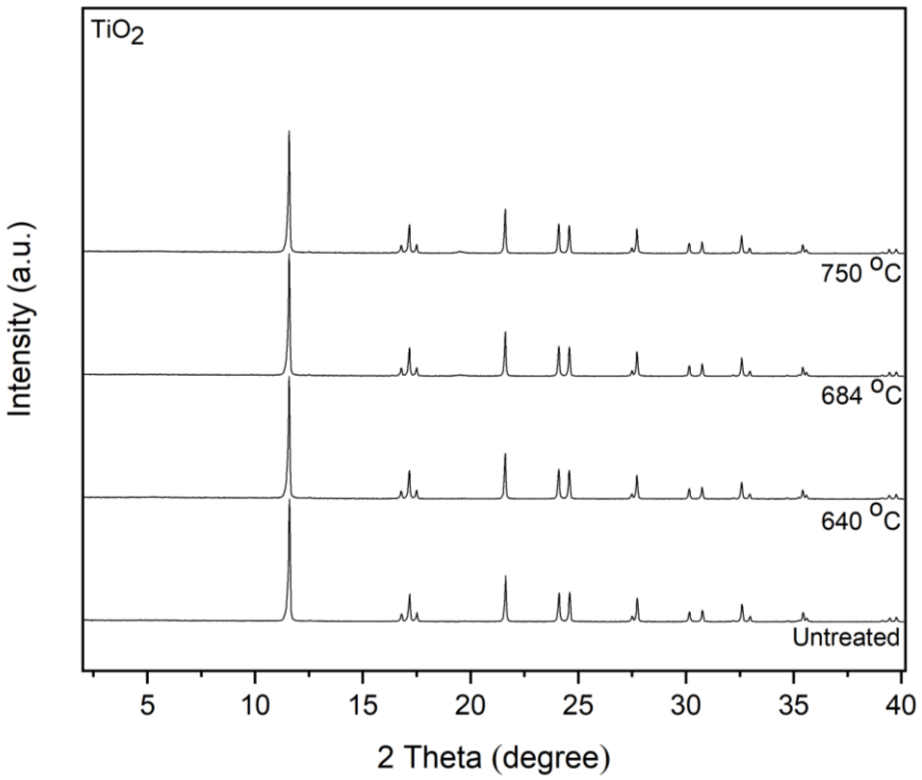

Figure 85 PXRD pattern of nitrogen doped anatase-titania

The as-received anatase-titania powders that were doped with nitrogen did not show any crystallographic structural changes at all three temperatures (Figure 85), like was the case with the open layered framework, $Na_2Ti_3O_7$.

Table 28 Calculated unit cell parameters a, b and c of the open layered titanates, tunnelled titanates and anatase-titania before and after nitrogen doping at three different doping temperatures

Sample	Doping temperature (°C)	Lattice parameter (Å)			Assumed Crystal Structure
		a	b	c	
Open layered framework					
$Cs_{0.68}Ti_{1.825}O_4$	750 °C	2.9553(3)	17.192(7)	3.8434(7)	Orthorhombic
	684 °C	2.9680(3)	17.562(8)	3.8370(8)	
	640 °C	2.9645(3)	17.458(8)	3.8271(7)	
	Untreated	2.9594(8)	17.523(7)	3.8187(7)	
Literature Untreated $Cs_{0.6}Ti_{1.84}O_4$	*(variation in lattice parameter values due to different composition than the one used in this thesis)*	3.829(3)	17.012(17)	2.962(3)	
$Na_2Ti_3O_7$	750 °C	8.462(8)	3.758(3)	9.025(7)	Monoclinic
	684 °C	8.527(7)	3.874(4)	9.191(10)	
	640 °C	8.570(7)	3.806(3)	9.135(6)	
	Untreated	8.458(6)	3.759(3)	9.026(6)	
Reference*	Literature Untreated	8.571(2)	3.804(2)	9.135(2)	
Tunnelled framework					

$K_2Ti_6O_{13}$	750 ºC	15.611(3)	3.802(1)	9.129(1)	Monoclinic
	684 ºC	15.604(4)	3.801(1)	9.129(1)	
	640 ºC	15.616(3)	3.811(1)	9.118(1)	
	Untreated	15.593(3)	3.805(1)	9.119(1)	
Reference #	Literature Untreated	15.582(6)	3.82(1)	9.112(1)	
$Na_2Ti_6O_{13}$	750 ºC	14.940(9)	3.702(3)	9.050(10)	Monoclinic
	684 ºC	14.930(8)	3.702(3)	9.024(7)	
	640 ºC	15.140(7)	3.735(3)	9.157(6)	
	Untreated	15.13 (1)	3.752(3)	9.163(8)	
Reference $	Literature Untreated	15.131(2)	3.745(4)	9.159(1)	
Non-layered framework					
Anatase-TiO_2	750 ºC	3.789(2)		9.53(1)	Tetragonal
	684 ºC	3.790(2)		9.54(1)	
	640 ºC	3.743(3)		9.40(1)	
	Untreated	3.743(2)		9.40(1)	
Reference@	Literature Untreated	3.785(1)		9.514(6)	

References:

* S. Andersson and A. Wadsley, Acta Crystallographica, 1961, 14, 1245-1249.

H. CID-DRESDNER and M. BUERGER, Zeitschrift für Kristallographie - Crystalline Materials, 1962, 117.

$ C. Wu, W. Hua, Z. Zhang, B. Zhong, Z. Yang, G. Feng, W. Xiang, Z. Wu and X. Guo, Advanced Science, 2018, 5, 1800519.

@ D. Cromer and K. Herrington, Journal of the American Chemical Society, 1955, 77, 4708-4709.

The calculated unit cell parameters of the untreated open layered titanates, tunnelled titanates and anatase-titania are found to match well with the literature values (Table 28).

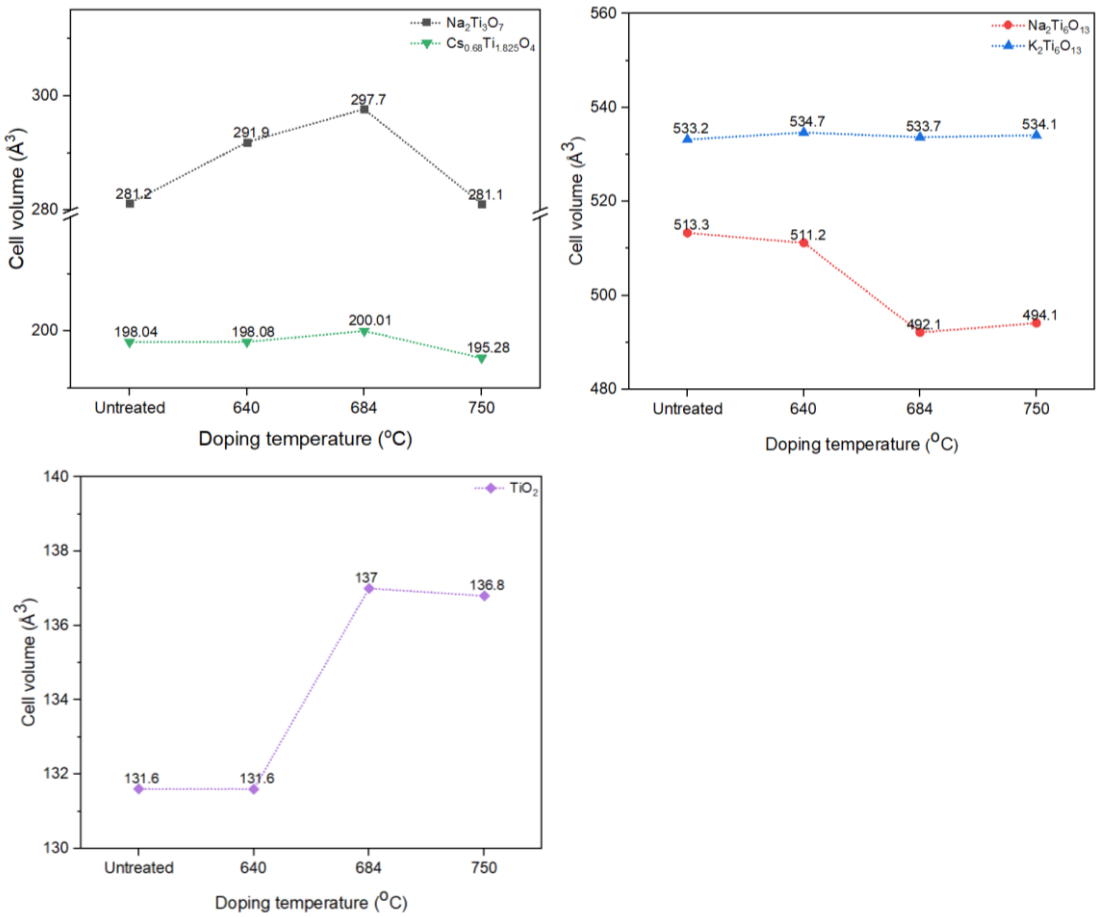

Figure 86 Calculated cell volumes of the open layered titanates ($Na_2Ti_3O_7$ and the $Cs_{0.68}T_{1.825}O_4$), tunnelled titanates ($Na_2Ti_6O_{13}$ and $K_2Ti_6O_{13}$) and anatase-titania before and after nitrogen doping at three doping temperatures

The maximum cell expansion of 16 Å^3 and 2 Å^3 is observed with the doping temperature of 684 °C in $Na_2Ti_3O_7$ and the $Cs_{0.68}T_{1.825}O_4$ respectively (Figure 86), caused by the expansion along the a, b and c axes. Beyond this temperature, the cell volume remains the same for the $Na_2Ti_3O_7$, suggesting that the maximum cell expansion has reached and further increase in temperature does not induce any further changes to the structure; whereas for $Cs_{0.68}T_{1.825}O_4$, the further increase in temperature gives cell contraction by 3 Å^3, caused by contraction along the a and b axes; and the expansion along the c axis. On the other hand, with the lowest doping temperature of 640 °C, the cell volume remains the same with $Cs_{0.68}T_{1.825}O_4$, while a cell expansion by 10 Å^3 is observed with the $Na_2Ti_3O_7$. It can be deduced from these findings that the unit cell of both these open layered structures are observed to either contract or expand from the incorporation of nitrogen. This is because the nitrogen atom has a higher ionic radius (1.55 Å) than that the lattice oxygen atom (1.52 Å) it is replacing. The modification of the unit cell volume indicates that nitrogen is incorporated into both these open layered titanates, where in $Na_2Ti_3O_7$, the crystal

structure remains intact and in $Cs_{0.68}T_{1.825}O_4$, the crystal structure is retained along with the formation of new nitrogen containing phases, as per its PXRD pattern.

With the tunnelled frameworks, $Na_2Ti_6O_{13}$ and $K_2Ti_6O_{13}$, two different cell volume characteristic behaviours are observed with increasing the doping temperature (Figure 86). With $K_2Ti_6O_{13}$, the cell volume remains the same with the doping temperature of 684 ^oC, whereas at 640 ^oC and 750 ^oC, a cell expansion by 1 $Å^3$ is observed due to the b and c axes contraction accompanied by 'a' axis expansion and contraction along the a, b and c axes respectively. This may suggest that the nitrogen defect formed at 640 ^oC is potentially volatile at 684 ^oC and too reactive at 750 ^oC, as discussed with the PXRD peak at 24.3^o earlier. With $Na_2Ti_6O_{13}$, increasing the doping temperature is seen to result in cell volume contraction, with the highest of -21 $Å^3$ observed with 684 ^oC (a, c expansion; b contraction), followed by -19 $Å^3$ with 750 ^oC (a, c expansion; b contraction) and -2 $Å^3$ with 640 ^oC (a, b expansion). Here, the unit cell is contracted to become smaller than that of the untreated $Na_2Ti_6O_{13}$ at all three doping temperatures, which is not observed in the tunnelled titanate $K_2Ti_6O_{13}$ or in the open layered structures discussed above.

The maximum cell expansion of 6 $Å^3$ is observed with the doping temperature of 684 ^oC in the non-layered anatase-titania, like with $Na_2Ti_3O_7$ and the $Cs_{0.68}T_{1.825}O_4$, caused by expansion along the a and c axes. However, unlike the case with these open layered titanates, increasing the doping temperature to 750 ^oC with anatase-titania led to unit cell expansion by 5 $Å^3$ from the a and c axes expansion. From the above observations, the nitrogen incorporation that left the crystal structure intact, without the formation of new phases was only found in the non-layered anatase and open layered $Na_2Ti_3O_7$.

8.3.3 Surface Bonding

The effect of nitrogen doping on the surface bonding characteristics in the tunnelled titanates, $Na_2Ti_6O_{13}$ and $K_2Ti_6O_{13}$, is observed to be more prominent at the highest doping temperature of 750 ^oC (Figure 87). Upon nitrogen doping at 750 ^oC, the $Na_2Ti_6O_{13}$ Raman peaks are observed to be significantly broadened compared to the samples doped at lower temperatures. The broadening appears to reach the extent of the disappearance of the peaks at 247 cm^{-1} and 409 cm^{-1}, which corresponds to the Na-O-Ti stretching vibrations. Additionally, the peaks at 524 cm^{-1}, 652 cm^{-1} and 741 cm^{-1}, corresponding to the short Ti-O stretches[176], were also found to disappear

upon nitrogen doping at 750 ^{o}C. Since the peak around 188 cm^{-1} is not as broadened as the peaks in the 500 cm^{-1} to 800 cm^{-1} regions and that beyond 800 cm^{-1}, it could be suggested that nitrogen is more favourably doped into the Ti-O-Ti and or Ti-O bonds than the Na-O-Ti bonds. Therefore, it can be deduced that in $Na_2Ti_6O_{13}$, the nitrogen dopant atom is more likely to be spatially distributed neatly in the TiO_2 anatase-like layers rather than within the Na-O-Ti bonds that make up the interlayer galleries. This could be the reason why nitrogen incorporated has resulted in unit cell contraction, as discussed earlier. However, the nitrogen is incorporated into the Na-O-Ti and Ti-O-Ti bonds has resulted in the formation of new nitrogen containing phases, as demonstrated by the formation of new peaks in its PXRD pattern. With $K_2Ti_6O_{13}$, the untreated sample has characteristic peaks in the Raman spectrum where the peaks below 500 cm^{-1} correspond to the K-O-Ti stretching vibration, the peaks at ~655 cm^{-1} to the Ti-O-Ti stretching within the edge shared TiO_6 octahedra, the peaks at ~870 cm^{-1} is assigned to short Ti-O stretching vibration within the distorted TiO_6 octahedra[177]. The peaks at ~240 and ~400 cm^{-1} is reported to be assigned to K-O-Ti and short Ti-O bonds respectively. Upon nitrogen doping at 750 ^{o}C, the peak at around 454 cm^{-1} in the untreated sample is seen to be shifted to 449.5 cm^{-1} and is seen to be increased in intensity. Also, the peak at ~609 cm^{-1} is observed to be increased in intensity. This suggests that nitrogen is potentially incorporated into the TiO_2-anatase like layers as well as into the K-O-Ti bonds within the interlayer galleries of $K_2Ti_6O_{13}$. It is to be noted that lower doping temperatures of 684 ^{o}C and 640 ^{o}C employed in $K_2Ti_6O_{13}$ were not high enough to cause changes in the local structure upon nitrogen incorporation. This could be the reason why cell expansion by only 1 Å was observed at 750^{o}C and no changes to the unit cell were observed when lower doping temperatures were employed. The incorporation of nitrogen into the K-O-Ti and Ti-O-Ti has not resulted in the formation of new nitrogen containing phases, as no new peaks were observed in its PXRD pattern.

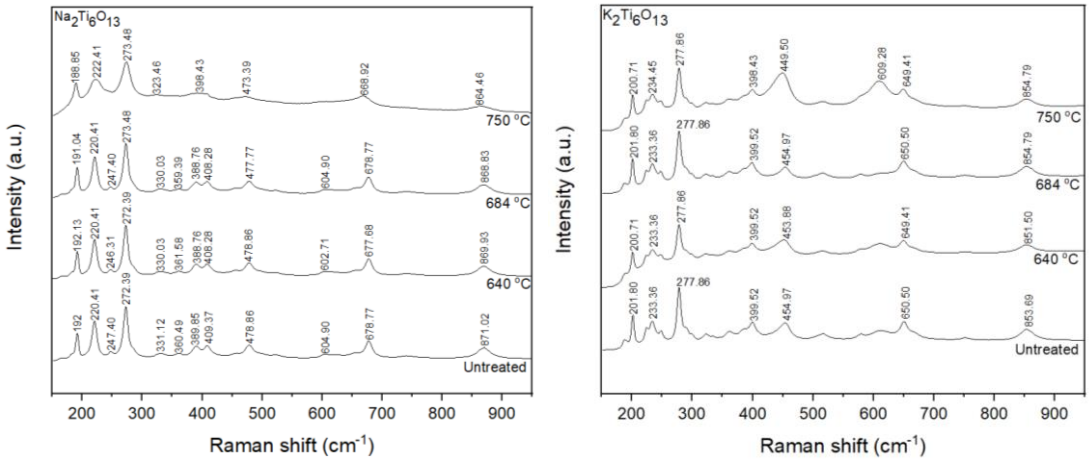

Figure 87 Raman spectra of the tunnelled structure titanates, $Na_2Ti_6O_{13}$ and $K_2Ti_6O_{13}$, before and after nitrogen doping at three doping temperatures

The $Na_2Ti_3O_7$ characteristic peaks remained the same after doping with nitrogen, as per the Raman spectra, suggesting no structural changes have occurred and that the interlayer spacings have remained intact. The doped samples have peaks at 284 cm^{-1} (Na-O-Ti), 447 cm^{-1}, 654 cm^{-1}, 740 cm^{-1} (all three corresponding to Ti-O-Ti stretch in edge shared TiO_6) and 882 cm^{-1} (short Ti-O stretch, with non-bridging O atoms)[178,179]. The peak at 882 cm^{-1} is seen to be shifted at all three doping temperatures. Since the shift in the 882 cm^{-1} and 740 cm^{-1} peaks is more than that observed in the other peaks, it can be deduced that the nitrogen dopant atoms prefer to be doped within the Ti-O-Ti and or Ti-O bonds than within the Na-O-Ti bonds. This is also the case in $Na_2Ti_6O_{13}$, as discussed earlier. This is the cause for the observed unit cell expansion in $Na_2Ti_3O_7$. The incorporation of nitrogen into these bonds have not caused the formation of any new nitrogen containing phases, as there are no additional PXRD peaks observed. However, the spatial distribution of nitrogen can be visualised to be different in $Na_2Ti_3O_7$ compared to that in $Na_2Ti_6O_{13}$. While $Na_2Ti_3O_7$ has TiO_6 layers that are connected to each other along the x axis, these layers are connected to each other along the x as well as y axes to make up the tunnelled structure framework in $Na_2Ti_6O_{13}$. Literature reports suggest structural transformation of $Na_2Ti_3O_7$ into $Na_2Ti_6O_{13}$ occurs upon thermal annealing at 800 ^oC and under at 500 ^oC (10h, under H_2). However, this was not observed in the nitrogen doped $Na_2Ti_3O_7$ samples with doping temperatures of up to 750 ^oC, again confirming that the original meta titanate structure was retained upon heating.

The Raman spectrum of $Cs_{0.68}Ti_{1.825}O_4$ shows three main characteristic peaks (Figure 88) at 276 cm^{-1}, 446 cm^{-1} and 609 cm^{-1}, which matches roughly with the literature pattern of $Cs_{0.68}Ti_{1.83}O_4$ which has peaks at 278 cm^{-1}, 435 cm^{-1} and 643 cm^{-1} [180]. The

literature does not report the assignments of these peaks to the bonds in the $Cs_{0.68}Ti_{1.825}O_4$ structure. Based on the peak assignments in the Raman spectrum of the other titanates discussed in this chapter, the Raman peaks of the $Cs_{0.68}Ti_{1.825}O_4$ structure is assigned. This means that the peaks at 276 cm^{-1} and 609 cm^{-1} correspond to the Cs-O-Ti bonding vibration while the peak at 446 cm^{-1} correspond to either the Ti-O-Ti or short Ti-O bonding vibration. Upon nitrogen doping of $Cs_{0.68}Ti_{1.825}O_4$, at 640 ^oC, the peaks at 446 cm^{-1} and 609 cm^{-1} is seen to be shifted, while at 684 ^oC, all the three main peaks are seen to be shifted. On the other hand, at 750 ^oC, the peak at 276 cm^{-1} becomes a doublet while the peak at 446 cm^{-1} is shifted. This suggests that at all doping temperatures, the nitrogen is incorporated into both the Cs-O-Ti and Ti-O-Ti or short O-Ti bonds. This is the reason why cell volume expansion of only 2 $Å^3$ is observed upon nitrogen doping. However, nitrogen incorporation into these bonds have potentially caused new nitrogen containing phases, which are indicated by the new peaks in its PXRD pattern. At 750 ^oC, the intensity of the peak at 377 cm^{-1} is also observed, which potentially suggests the formation of large particles.

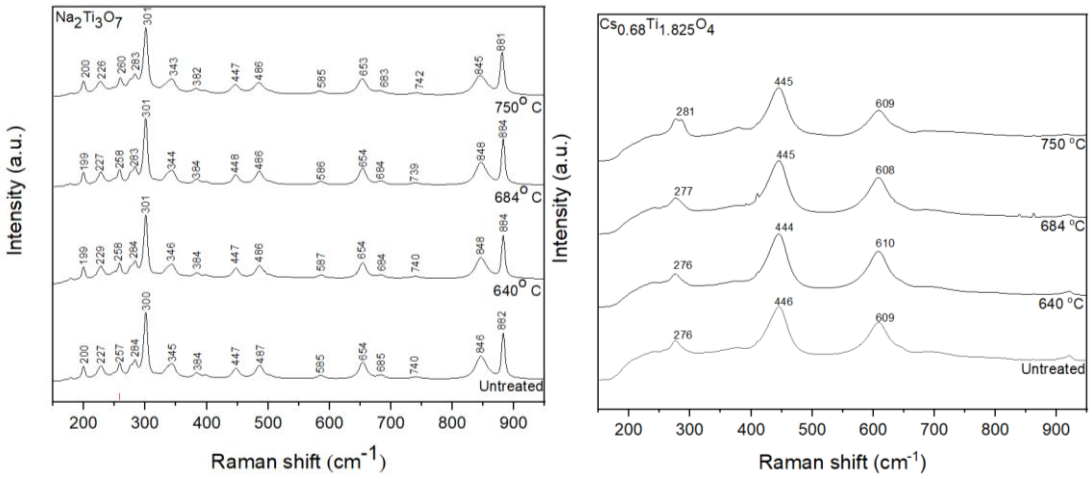

Figure 88 Raman spectra of the open layered titanates, $Na_2Ti_3O_7$ and $Cs_{0.68}T_{1.825}O_4$, before and after nitrogen doping at three doping temperatures

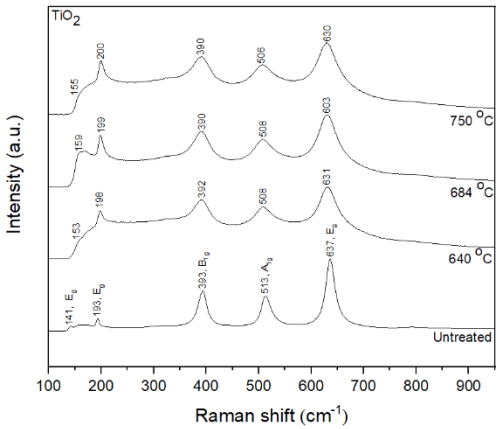

Figure 89 Raman spectra of the non-layered anatase-titania

The Raman spectrum of the as-received anatase-titania shows the six Raman active modes (Figure 89), $2A_{1g}$ (516 cm^{-1}) + $3E_g$ (639 cm^{-1}, 197 cm^{-1} and 144 cm^{-1}) + $1B_{1g}$ (399 cm^{-1}), which matches with the literature reports. Upon nitrogen doping, the intensity of the lowest frequency E_g Raman mode is seen to be shifted from 141 cm^{-1} to 159 cm^{-1} with increasing doping temperature. This suggests the incorporation of nitrogen atoms into the TiO_2 lattice. The maximum shift in this peak position is observed with 684 ^oC and not 750 ^oC doping temperature. This is reflected in the unit cell expansion of 6 Å at 684 ^oC and 5 Å at 750 ^oC. The broadening of the E_g peak mode is also observed and is greater than the shift in its peak position. This indicates the possibility of the formation of nano-sized particles. Only the E_g peak was observed to shift in the Raman spectrum, suggesting the incorporation of nitrogen into only one type of bond within the titania lattice, which as per the PXRD data does not give rise to the formation of any new nitrogen containing phases.

8.3.4 Optical Absorption

In both the tunnelled titanates, $Na_2Ti_6O_{13}$ and $K_2Ti_6O_{13}$ (Figure 90), changes in the optical absorption are observed at all the three doping temperatures. In $Na_2Ti_6O_{13}$, the absorption in the 350 nm to 800 nm is observed to be increased with increasing doping temperature. This could be potentially caused by the new nitrogen containing phases (as per the emergence of new peaks in PXRD data), arising from nitrogen incorporation into the Na-O-Ti and Ti-O-Ti bonds that was observed in the Raman spectrum, where peak broadening was seen to be the most at 750 ^oC doping temperature. On the other hand, in $K_2Ti_6O_{13}$, the highest absorption is observed at 684 ^oC. This is potentially caused by lower amounts of nitrogen incorporated into the K-O-Ti and Ti-O-Ti bonds. A new broad peak emerges in the 350 nm to 500 nm region, which was originally not present in $Na_2Ti_6O_{13}$, and is seen to increase in intensity with

increasing doping temperature. This potentially means that this new peak is associated with the incorporation of nitrogen dopant and the increasing intensity of this peak is to do with an effect of the doping temperature. As per the Raman data in this chapter, this nitrogen is potentially incorporated more into the Ti-O-Ti bonds than the Na-O-Ti bonds at the highest doping temperature of 750 ^{o}C. This is confirmed by the UV-Vis spectrum of anatase-titania (Figure 90). Only Ti-O-Ti bonds are present in titania, into which nitrogen is doped. With increasing doping temperature, the intensity of the peak emerging in the 350 nm to 500 nm is observed to increase, same as the case with $Na_2Ti_6O_{13}$.

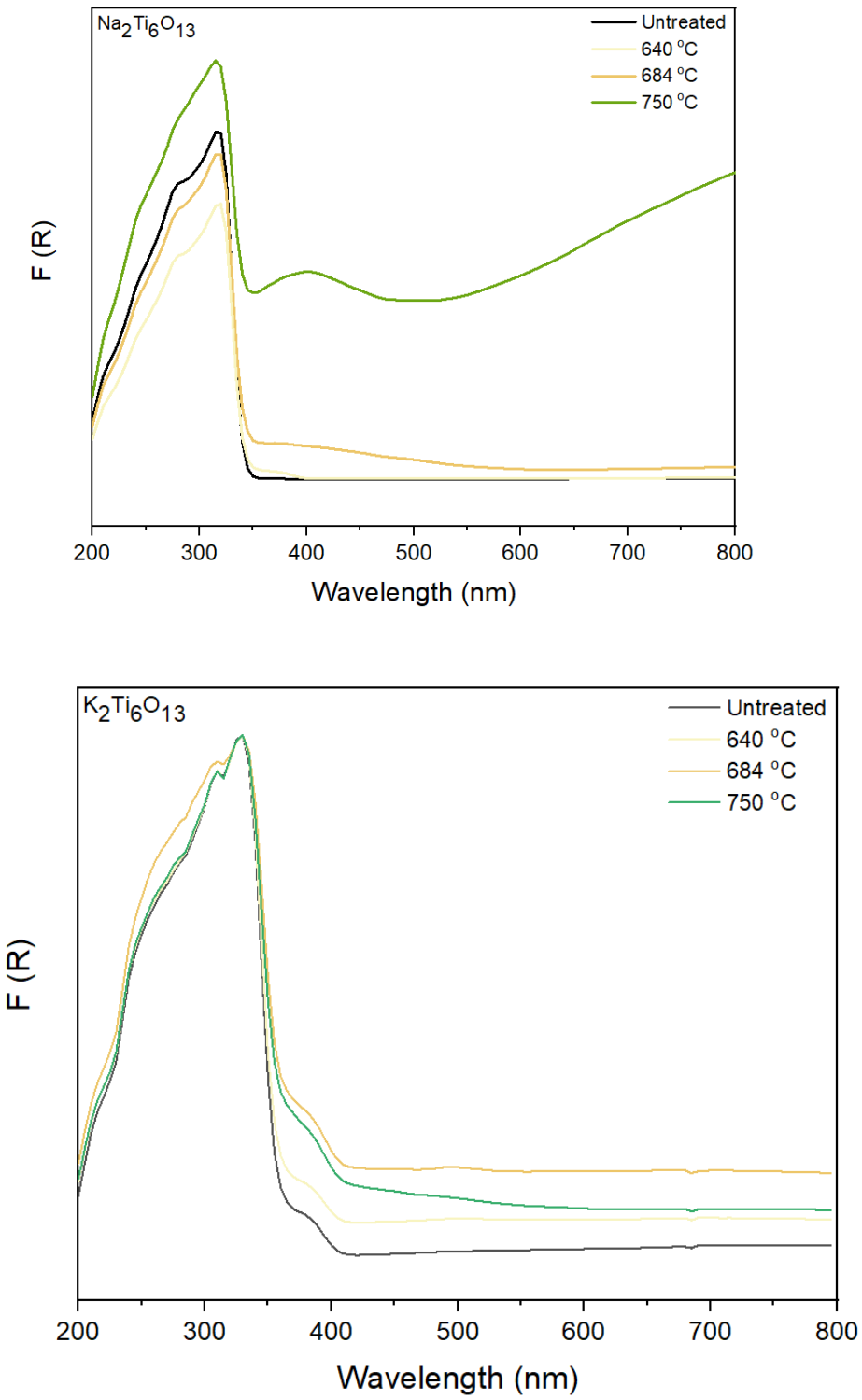

Figure 90 Optical absorption UV-Vis spectrum of tunnelled structure titanates, $Na_2Ti_6O_{13}$ and $K_2Ti_6O_{13}$, before and after nitrogen doping at three doping temperatures

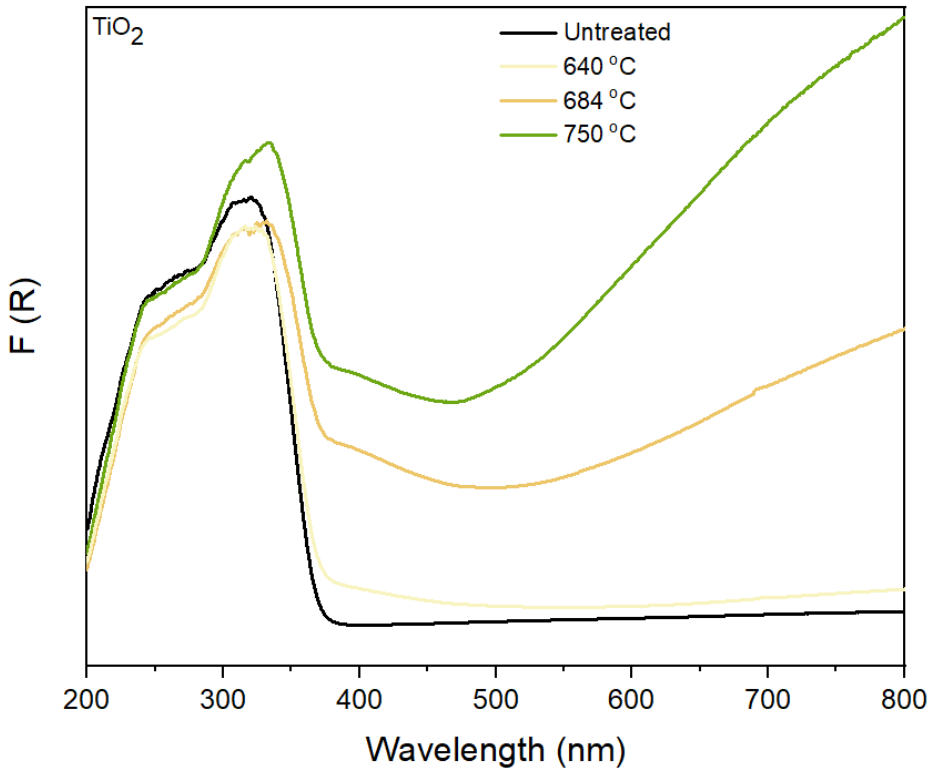

Figure 91 Optical absorption UV-Vis spectrum of anatase-TiO_2, before and after nitrogen doping at three doping temperatures

With the open layered titanates, $Na_2Ti_3O_7$ and $Cs_{0.68}T_{1.825}O_4$, too, an increase in the optical absorption is observed upon nitrogen doping (Figure 91). In $Na_2Ti_3O_7$, the lowest doping temperature of 640 °C was not high enough to induce an increase in the optical absorption. The highest optical absorption was observed with the doping temperature of 750 °C but is not as high as that observed in the tunnelled titanates. This is potentially caused by lower amounts of nitrogen incorporation, since the PXRD pattern of the nitrogen doped $Na_2Ti_3O_7$ did not show any new peaks, although there was a small increase in its unit cell volume. Even though the Raman data shows preference for the nitrogen to be doped into the Ti-O-Ti bonds in $Na_2Ti_3O_7$, no broad peaks in the 350 nm to 500 nm region in its UV-Vis spectrum is observed. This suggests that the nitrogen dopant concentration within the Ti-O-Ti bonds of $Na_2Ti_3O_7$ is lower than that in the $Na_2Ti_6O_{13}$ tunnelled structure. On the other hand, the open layered titanate, $Cs_{0.68}T_{1.825}O_4$, the optical absorption is observed to be significantly lowered with the doping temperature of 750 °C. The optical absorption is seen to be increased only with the lowest doping temperature of 640 °C. The nitrogen does not have a preference to be doped into the Cs-O-Ti or Ti-O-Ti bonds in $Cs_{0.68}T_{1.825}O_4$, as per Raman data at 750 °C. Therefore, nitrogen doping into both these bonds may potentially be the reason for the decrease in optical absorption at 750 °C and 684 °C,

while the preference for doping into the Ti-O-Ti bonds could be the reason for the increase in optical absorption at 640 °C. There are no new broad peaks emerging in the 350 nm to 500 nm region. This suggests that the nitrogen concentration within the Ti-O-Ti bonds is potentially less than that in $Na_2Ti_6O_{13}$ or that it is not high enough for Ti^{3+} species formation.

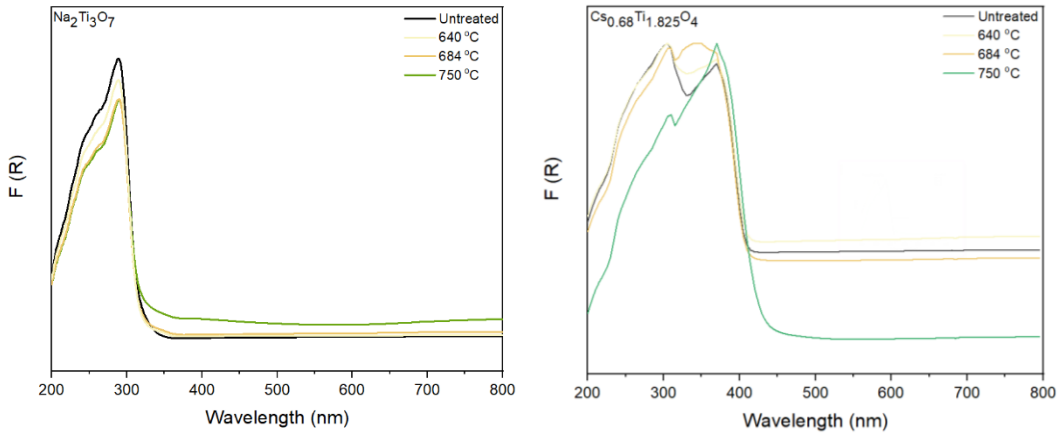

Figure 92 Optical absorption UV-Vis spectrum of the open layered titanates, $Na_2Ti_3O_7$ and $Cs_{0.68}T_{1.825}O_4$, before and after nitrogen doping at three doping temperatures

8.3.3.1 Optical Band Gap

A tauc plot is used to determine the value of the direct (see Appendices Figure V, W and X) and indirect (see Appendices Figure Y, Z and AA) optical band gap of the titanates before and after nitrogen doping. More information on how these optical band gap values were extracted from their respective tauc plots and the associated errors are explained in section 2.4.3.

1. **Direct band gap**

The direct optical band gap of the tunnelled titanates, $Na_2Ti_6O_{13}$ and $K_2Ti_6O_{13}$, were observed to be lowered upon nitrogen doping at all the three temperatures (Table 29). The $Na_2Ti_6O_{13}$ synthesised using solid-state synthesis has a band gap (3.69 eV) that is different from the literature (3.48 eV), which uses a NaCl-KCl melt technique. Increasing the doping temperature has narrowed the band gap. This is potentially caused by the formation of new nitrogen containing states within the band gap, caused by nitrogen incorporation into the Na-O-Ti and Ti-O-Ti bonds as per Raman data. While the band gap is lowered by 0.01 eV with the doping temperatures 640 °C and 684 °C, it is lowered by 0.07 eV with 750 °C. This is potentially due to the formation of the nitrogen containing states as well as the Ti^{3+} states which are predominantly found at 750 °C, as per UV-Vis data. On the other hand, the synthesised $K_2Ti_6O_{13}$ has

a direct band gap that matches with the literature value of 3.52 eV. The nitrogen doping at 640 ^{o}C, 684 ^{o}C and 750 ^{o}C has resulted in the narrowing of the band gap by 0.01 eV, 0.04 eV and 0.03 eV respectively. This is potentially due to the formation of nitrogen containing states within the band gap, caused by nitrogen incorporation into the K-OH and Ti-O-Ti bonds, which are detected by Raman spectroscopy in $Na_2Ti_6O_{13}$ doped at 750 ^{o}C, but not at 640 ^{o}C and 684 ^{o}C. Additionally, it could be caused by other states that has resulted in the increase in optical absorption, in the 350 nm to 800 nm region, observed upon nitrogen doping at all three temperatures. This is not the case with $Na_2Ti_6O_{13}$, where the optical absorption in this region is seen to be increasing with increasing doping temperature.

The direct optical band gap of the open layered titanates, $Cs_{0.68}T_{1.825}O_4$ and $Na_2Ti_3O_7$, were also observed to be lowered upon nitrogen doping at all the three temperatures (Table 29). The only exception to this was for the $Cs_{0.68}T_{1.825}O_4$ doped at 684 ^{o}C, where the band gap remained the same. The band gap of $Cs_{0.68}T_{1.825}O_4$ was seen to be narrowed least (by -0.02 eV) at 640 ^{o}C. The band gap of $Cs_{0.68}T_{1.825}O_4$ was found to be narrowed the most (by -0.09 eV) at 750 ^{o}C, which is caused by new nitrogen containing states within the band gap, caused by nitrogen incorporation into the Cs-O-Ti and Ti-O-Ti or short O-Ti bonds, as per Raman data. The synthesised $Cs_{0.68}T_{1.825}O_4$ had a band gap value (3.11 eV) that is different from the literature (3.62 eV)[180]. This is potentially due to the literature sample which had slightly different stoichiometry of $Cs_{0.68}T_{1.83}O_4$. On the other hand, with $Na_2Ti_3O_7$, the band gap is -0.04 eV away from the literature value of 3.96 eV[181] and is narrowed by -0.01 eV at all three doping temperatures, potentially caused by the incorporation of nitrogen into its Ti-O-Ti or Na-Ti-O bonds.

The literature value of anatase-titania is 3.2 eV[13], while that recorded of the as-received anatase is 3.47 eV. As per literature studies, band gap values greater than 3.4 eV, independent of the type of transition (direct or indirect), is due to the amorphous nature present in the titania as per a detailed literature study[182]. Upon nitrogen doping, the direct optical band gap value is observed to be reduced with increasing doping temperature, like was the case with $Na_2Ti_6O_{13}$. This band gap narrowing is potentially caused by the incorporation of nitrogen into the Ti-O-Ti bonds and by the presence of the Ti^{3+} species as per the Raman data and UV-Vis data respectively.

Upon nitrogen doping, the shape of the absorption edge associated with the direct optical transition remains the same in all the samples, except for a few cases (Table 30). In addition to the main absorption peak, the emergence of a relatively less intense absorption peak is also observed. These seen in nitrogen doped $Na_2Ti_6O_{13}$ (750 ^oC) gives a band gap of 2.09 eV and that in $K_2Ti_6O_{13}$ (750 ^oC and 684 ^oC) gives a band gap of 3 eV. These band gaps are smaller than that associated with the larger absorption region of the optical spectrum. The wide band gap potentially corresponds to the region between the core levels that make up the valence band and the conduction band. The smaller band gaps potentially correspond to the new high energy levels that are formed below the conduction band upon nitrogen doping.

Table 29 Calculated optical band gaps from direct allowed transitions of the tunnelled and open layered titanates in comparison with anatase-titania

Direct optical band gap (in eV)					
Doping temperature	**Tunnelled**		**Open layered**		**Non-layered**
	$Na_2Ti_6O_{13}$	$K_2Ti_6O_{13}$	$Na_2Ti_3O_7$	$Cs_{0.68}Ti_{1.825}O_4$	TiO_2-Anatase
Untreated	3.69	3.53	4.01	3.11	3.47
640 ^oC	3.68	3.52	4	3.09	3.42
684 ^oC	3.68	3.49	4	3.11	3.29
750 ^oC	3.62	3.50	4	3.02	3.27

Table 30 Calculated optical band gaps from additional direct allowed transitions of the tunnelled and open layered titanates in comparison with anatase-titania

Additional Direct optical band gap (in eV)					
Doping temperature	**Tunnelled**		**Open layered**		**Non-layered**
	$Na_2Ti_6O_{13}$	$K_2Ti_6O_{13}$	$Na_2Ti_3O_7$	$Cs_{0.68}Ti_{1.825}O_4$	TiO_2-Anatase
Untreated	n/a	n/a	n/a	n/a	n/a
640 ^oC	n/a	n/a	n/a	n/a	n/a
684 ^oC	n/a	3.0	n/a	n/a	n/a
750 ^oC	2.09	3.0	n/a	n/a	n/a

2. **Indirect band gap**

The indirect optical band gaps of the tunnelled titanates are also observed to be lowered upon nitrogen doping (Table 31). Additionally, increasing the doping temperature is also seen to reduce the band gap. With $Na_2Ti_6O_{13}$, the band gap is narrowed by -0.02 eV at 640 ^oC, by -0.03 eV at 684 ^oC and by -0.07 eV at 750 ^oC. However, with $K_2Ti_6O_{13}$, the band gap is narrowed by -0.01 eV at 640 ^oC, by -0.05 eV at 684 ^oC and by -0.06 eV at 750 ^oC. The same trend is observed with the anatase-

titania where the band gap is narrowed by -0.06 eV at 640 ^{o}C, by -0.27 eV at 684 ^{o}C and by -0.33 eV at 750 ^{o}C.

With the open layered titanates too the indirect optical band gaps are observed to be narrowed, but not at all the three doping temperatures (Table 31). With $Na_2Ti_3O_7$, a doping temperature of 750 ^{o}C has narrowed the band gap by -0.03 eV, since at 640 ^{o}C and 684 ^{o}C the band gap was observed was observed to remain the same. On the other hand, with $Cs_{0.68}T_{1.825}O_4$, the band gap only remained the same at 640 ^{o}C; while at 684 ^{o}C and 750 ^{o}C, the band gaps were narrowed by -0.01 eV and -0.12 eV respectively.

Table 31 Calculated optical band gaps from indirect allowed transitions of the tunnelled and open layered titanates in comparison with anatase-titania

Indirect optical band gap (in eV)					
Doping temperature	**Tunnelled**		**Open layered**		**Non-layered**
	$Na_2Ti_6O_{13}$	$K_2Ti_6O_{13}$	$Na_2Ti_3O_7$	$Cs_{0.68}Ti_{1.825}O_4$	TiO_2-Anatase
Untreated	3.63	3.45	3.92	3.04	3.36
640 ^{o}C	3.61	3.44	3.92	3.04	3.30
684 ^{o}C	3.60	3.40	3.92	3.05	3.09
750 ^{o}C	3.46	3.39	3.89	2.92	3.03

Table 32 Calculated optical band gaps from additional indirect allowed transitions of the tunnelled and open layered titanates in comparison with anatase-titania

Additional Indirect optical band gap (in eV)					
Doping temperature	**Tunnelled**		**Open layered**		**Non-layered**
	$Na_2Ti_6O_{13}$	$K_2Ti_6O_{13}$	$Na_2Ti_3O_7$	$Cs_{0.68}Ti_{1.825}O_4$	TiO_2-Anatase
Untreated	n/a	n/a	n/a	n/a	n/a
640 ^{o}C	3.08	n/a	n/a	n/a	2.15
684 ^{o}C	1.89	n/a	n/a	n/a	1.68
750 ^{o}C	1.23	n/a	n/a	n/a	1.31

Upon nitrogen doping, the shape of the absorption edge associated with the indirect optical transition also remains the same in all the samples, except for a few cases (Table 32). The emergence of an additional absorption peak with relatively lower intensity than the main absorption peak is observed in the nitrogen doped $Na_2Ti_6O_{13}$ and anatase-TiO_2 doped at all the three temperatures. As already discussed earlier, these samples are therefore suggested to form new states below the conduction band upon nitrogen incorporation.

8.3.5 Elemental Analysis

An understanding of the nitrogen concentration into the bulk and the surface of the titanates is studied. In addition, the chemical nature of the incorporated nitrogen is also probed.

1. **Bulk nitrogen concentration**

The incorporation of nitrogen into the bulk of $K_2Ti_6O_{13}$ and anatase-TiO_2 was observed at all the three doping temperatures (Table 33) where the nitrogen concentration in anatase in higher than that in $K_2Ti_6O_{13}$. Nitrogen can be incorporated into the Ti-O-Ti bonds of TiO_2 and $K_2Ti_6O_{13}$. However, the $K_2Ti_6O_{13}$ structure also allow nitrogen to be incorporated into its K-O-Ti bonds, as per Raman data. This means that charge neutrality of the host lattice is potentially more easily met with the TiO_2 than the $K_2Ti_6O_{13}$ composition, making nitrogen incorporation easier in TiO_2. This could be the same reason why $Na_2Ti_6O_{13}$, $Cs_{0.68}Ti_{1.825}O_4$ and $Na_2Ti_3O_7$ also have lower nitrogen concentrations than TiO_2. Increasing the doping temperature results in increasing nitrogen concentrations in only the tunnelled $Na_2Ti_6O_{13}$, the open layered $Cs_{0.68}Ti_{1.825}O_4$ and TiO_2 except for $Cs_{0.68}Ti_{1.825}O_4$ at 640 ^oC, where the nitrogen incorporation is zero. However, this nitrogen incorporation has modified the bulk crystal structure indicated by the PXRD peak shifts which is seen in all the four titanates but not the TiO_2. With $K_2Ti_6O_{13}$, the highest nitrogen concentration is seen at 684 ^oC and the lowest at 750 ^oC. With $Na_2Ti_3O_7$ however, the highest concentration is seen with 640 ^oC and the lowest at 684 ^oC.

Table 33 Nitrogen concentration in the bulk of the tunnelled and open layered titanates in comparison with anatase-titania; where nitrogen concentrations were measured using CHN analysis

Bulk nitrogen concentration (atomic%)					
Doping temperature	**Tunnelled**		**Open layered**		**Non-layered**
	$Na_2Ti_6O_{13}$	$K_2Ti_6O_{13}$	$Na_2Ti_3O_7$	$Cs_{0.68}Ti_{1.825}O_4$	TiO_2-Anatase
640 ^oC	0	0.3063	0.4545	0	0.5800
684 ^oC	0.3330	0.3381	0	0.0359	0.8293
750 ^oC	0.4938	0.2909	0.2178	0.3489	0.9392

2. **Surface nitrogen**

The incorporation of nitrogen into the surface of $Na_2Ti_6O_{13}$ and anatase-TiO_2 was observed at all the three doping temperatures (Table 34), which is slightly different to the bulk nitrogen concentrations. While with $Na_2Ti_6O_{13}$ and $Cs_{0.68}Ti_{1.825}O_4$, the nitrogen

concentration increases with increasing doping temperature, with TiO_2, the highest nitrogen concentration is seen with 684 ^oC and the lowest with 640 ^oC. With the other tunnelled structure $K_2Ti_6O_{13}$, nitrogen is only observed to be incorporated at 750 ^oC. On the other hand, with $Na_2Ti_3O_7$, nitrogen incorporation is observed to be highest at 750 ^oC and lowest with 640 ^oC. The nitrogen concentrations on the surface of all the samples are greater than that in the bulk. From this, it can be deduced that nitrogen is incorporated into the bulk some value of diffusion coefficient, which remains as a challenge to probe in powder samples. However, single crystal substrates of rutile-titania can be used as models to calculate this dopant diffusion coefficient and this is exactly what was studied in Chapter 3, 4, 5, 6 and 7.

Table 34 Nitrogen concentration in the surface of the tunnelled and open layered titanates in comparison with anatase-titania, measured using XPS core line spectra

Surface nitrogen concentration (atomic%)					
Doping temperature	**Tunnelled**		**Open layered**		**Non-layered**
	$Na_2Ti_6O_{13}$	$K_2Ti_6O_{13}$	$Na_2Ti_3O_7$	$Cs_{0.68}Ti_{1.825}O_4$	TiO_2-Anatase
640 ^oC	2.53	0	1.9	0	6.8
684 ^oC	5.35	0	0	7.32	13.57
750 ^oC	18.6	2.63	6.22	15.65	13.1

The 2.63 atomic% of nitrogen incorporated on the surface of only the 750 ^oC doped $K_2Ti_6O_{13}$ is in a substitutional lattice site, as denoted by the XPS N1s core line peak at ~396 eV (Figure 93). On the other hand, the 2.53 atomic%, 5.35 atomic% and 18.6 atomic% of nitrogen incorporated into the $Na_2Ti_6O_{13}$ at the 640 ^oC, 684 ^oC and 750 ^oC respectively is occupied in both the interstitial and substitutional sites of the host lattice. This is denoted by the presence of the XPS N1s core line peaks at ~396 eV and ~400 eV.

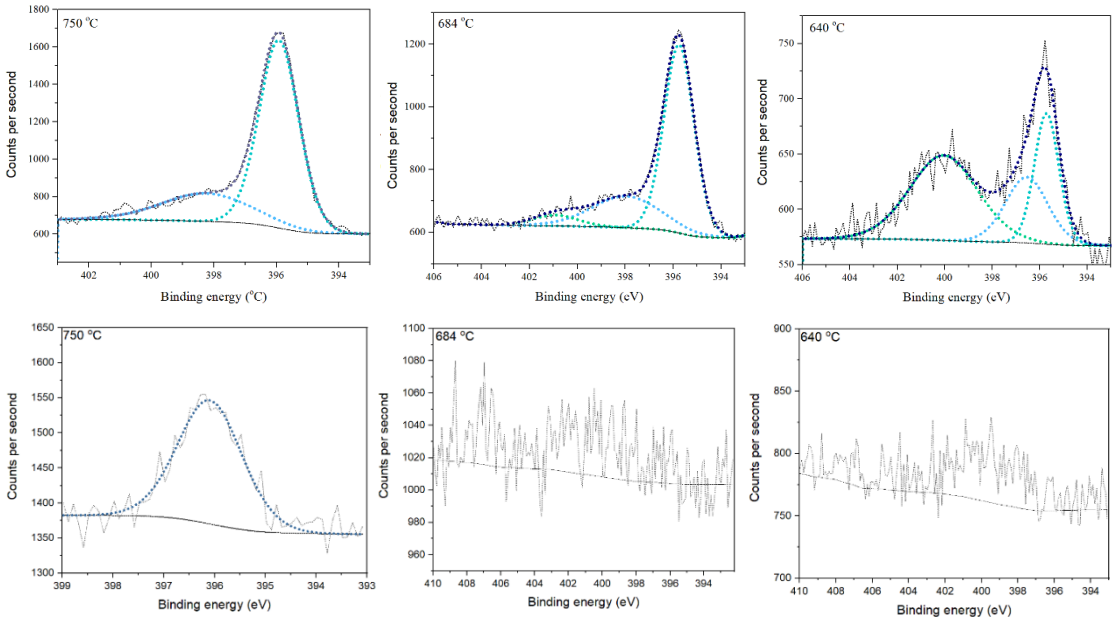

Figure 93 XPS N1s core line spectrum of the nitrogen doped tunnelled titanates, $Na_2Ti_6O_{13}$ (top) and $K_2Ti_6O_{13}$ (bottom)

The nitrogen is incorporated either into the interstitial or the substitutional or both sites of the host lattice. The 2.63 atomic% of nitrogen incorporated on the surface of only the 750 °C doped $K_2Ti_6O_{13}$ is in a substitutional lattice site, as denoted by the XPS N1s core line peak at ~396 eV (Figure 93). On the other hand, the 2.53 atomic%, 5.35 atomic% and 18.6 atomic% of nitrogen incorporated into the $Na_2Ti_6O_{13}$ at the 640 °C, 684 °C and 750 °C respectively is occupied predominantly in the substitutional sites than in the interstitial sites of the host lattice. This is denoted by the presence of the XPS N1s core line peaks at ~396 eV and ~400 eV respectively. With $Cs_{0.68}T_{1.825}O_4$, the 15.65 atomic% of nitrogen incorporated at 750 °C is predominantly in substitutional lattice sites even though it is also present at interstitial sites. The same is also observed with the nitrogen doped $Na_2Ti_3O_7$ at 750 °C and 684 °C (Figure 94). With TiO_2 however, the nitrogen is incorporated in both the sites at all the three doping temperatures (Figure 95).

The incorporation of nitrogen into the host lattice will result in p-type doping. However, this will result in an excess negative charge, which is being attempted to be compensated by the promotion of oxygen vacancies. The creation of oxygen vacancies in excess will induce a n-type doping.

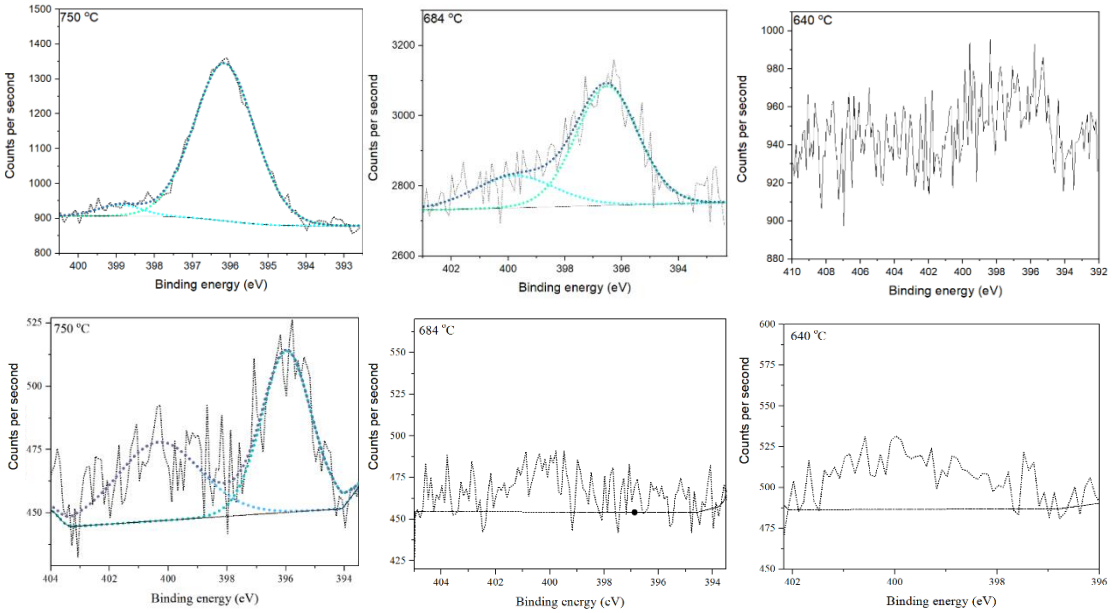

Figure 94 XPS N1s core line spectrum of the nitrogen doped open layered titanates, $Na_2Ti_3O_7$ (top) and $Cs_{0.68}T_{1.825}O_4$ (bottom)

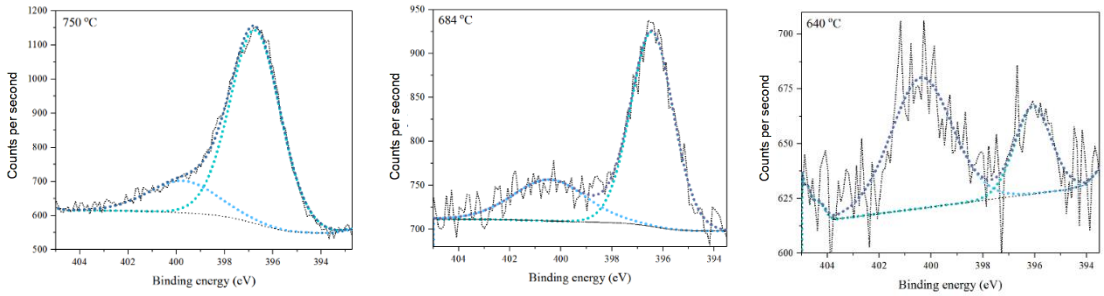

Figure 95 XPS N1s core line spectrum of the nitrogen doped anatase-titania doped at the temperatures 750 °C, 684 °C and 640 °C

8.3.6 Electronic Structure

Upon nitrogen doping, the XPS valence band onset measured of the surface of the titanates and anatase-titania were observed to be shifted (Table 35). In $K_2Ti_6O_{13}$ and anatase-titania, the shift is observed to increase with increasing the doping temperatures. In $Na_2Ti_6O_{13}$, the lowest shift of +0.03 eV is observed at 684 °C and 750 °C, while the highest shift of -0.05 eV is observed at 640 °C. With $Na_2Ti_3O_7$, the lowest shift of -0.02 eV was observed at 684 °C, while the highest shift of +0.16 eV was observed at 750 °C. On the other hand, with $Cs_{0.68}Ti_{1.825}O_4$, the highest shift of +0.44 eV was observed at 684 °C and the lowest shift of -0.01 eV was observed with 640 °C. These shifts in the valence band onset is different in each case, potentially due to the different nitrogen concentrations incorporated into the surface and bulk of the host lattice.

Table 35 XPS valence band onset of the tunnelled and open layered titanates in comparison with anatase-titania

Valence band onset (eV)					
Doping temperature	**Tunnelled**		**Open layered**		**Non-layered**
	$Na_2Ti_6O_{13}$	$K_2Ti_6O_{13}$	$Na_2Ti_3O_7$	$Cs_{0.68}Ti_{1.825}O_4$	TiO_2-Anatase
Untreated	2.96	2.52	2.76	2.63	3.04
640 °C	2.91	2.60	2.67	2.62	2.89
684 °C	2.93	2.91	2.74	3.07	2.67
750 °C	2.93	3.06	2.92	2.63	2.68

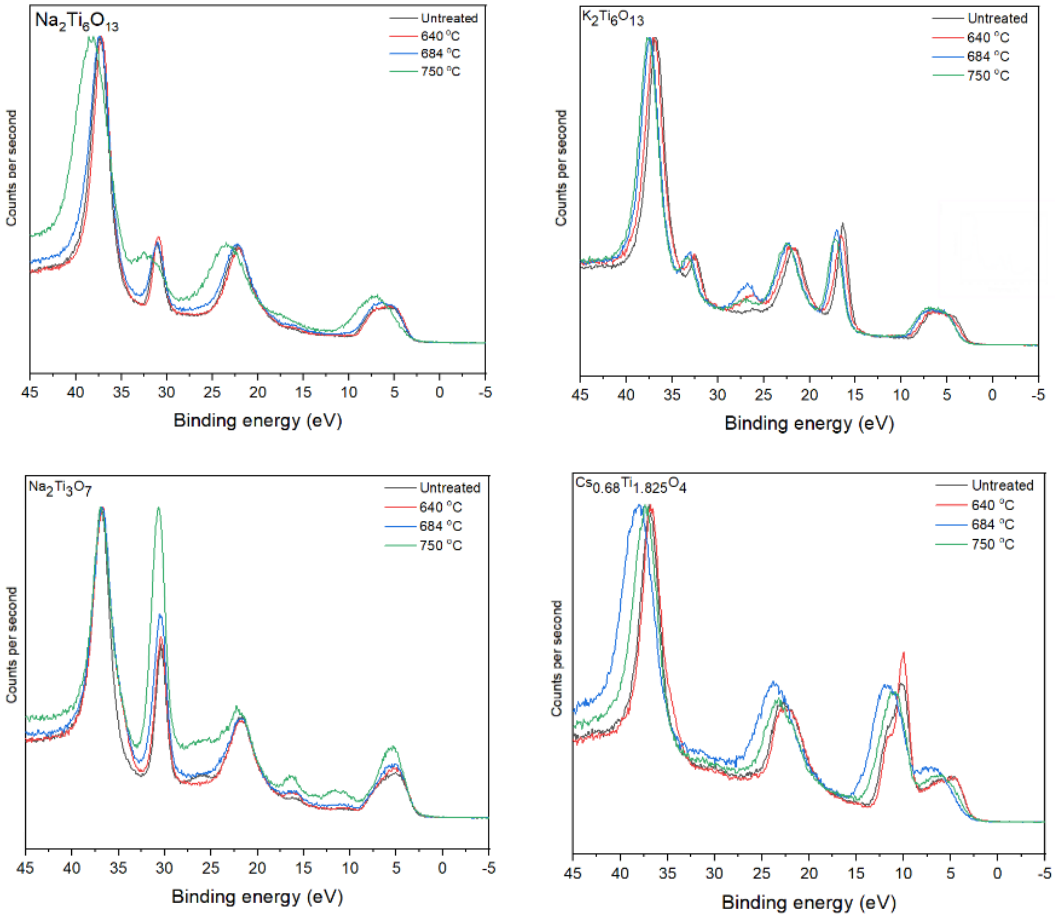

Figure 96 XPS valence band spectrum of the tunnelled (top) and open layered (bottom) titanates before and after nitrogen doping

In the XPS valence band spectrum, 0 eV corresponds to the fermi level, region > 0 eV corresponds to the valence band that is predominantly made of the O2p orbitals and the region < 0 eV makes up the conduction band that mainly consists of Ti3d, Ti4s and Ti4p orbitals. In all the titanates, the shape of the orbital contributions is different, while their binding energy is the same. The peaks located in the 10 eV to 3 eV range corresponds to the O 2p orbital contribution, which can be deconvoluted into

the O 2p σ and O 2p π contributions respectively. The peak at ~22 eV corresponds to the O 2s orbital, while the peak around 16 eV to 17 eV corresponds to K 3p. The peaks at 36 eV and 30 eV corresponds to the Ti 3p and Na 2p orbitals.

Nitrogen doping of the titanates have caused modifications to the orbital contributions of the XPS valence band spectrum (Figure 96). Upon nitrogen doping of $Na_2Ti_6O_{13}$, the orbital contributions remain the same at the doping temperatures 640 ^oC and 684 ^oC. With the doping temperature of 750 ^oC, the peak at 31 eV is observed to be broadened, potentially due to the mixing of the Na1s orbital with the new N1s state incorporated into the Na-O-Ti bonds, as per Raman data. Upon nitrogen doping of $K_2Ti_6O_{13}$, the orbital contributions remain the same except for 27 eV to 25 eV region of the O2s orbital contribution at all the three doping temperatures. The intensity of the peak in this region is observed to be increased. The highest intensity is seen at 684 ^oC and the lowest intensity at 750 ^oC. Upon nitrogen doping of $Na_2Ti_3O_7$, the orbital contributions remain the same at the doping temperatures 640 ^oC and 684 ^oC. With the doping temperature of 750 ^oC, the peak at 31 eV is observed to be broadened, potentially due to the new dopant state resulting from the incorporation of nitrogen into the Na-O-Ti bonds, as per Raman data. The peak at ~17 eV is seen to become more intense, potentially due to the mixing of the O2s state with the new N1s state arising from nitrogen incorporation into either the Na-O-Ti or Ti-O-Ti bonds, as per Raman data. The peak at ~13 eV also is seen to become more intense, suggesting the mixing of the O2p state new N1s state from nitrogen incorporation. Upon nitrogen doping of $Cs_{0.68}Ti_{1.825}O_4$, the orbital contributions remain the same only for the doping temperature of 640 ^oC. At 684 ^oC and 750 ^oC, the O2p peak centred around 10 eV is seen to be broadened. This is potentially due to the mixing of the O2s orbital with the new N1s state from nitrogen incorporation into the Cs-O-Ti and/ or Ti-O-Ti bonds, as per Raman data. Upon nitrogen doping of anatase-titania, the orbital contributions remained the same (Figure 97).

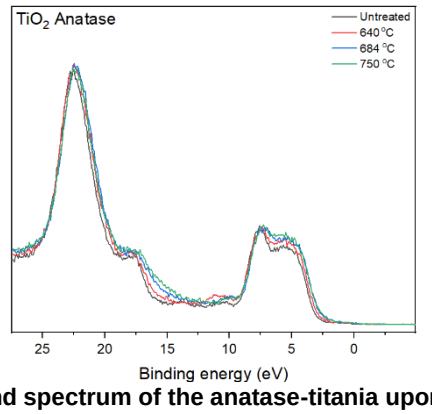

Figure 97 XPS valence band spectrum of the anatase-titania upon nitrogen doping at three different temperatures

8.4 Summary of Findings

The titanates investigated in this chapter can be classified into the tunnelled ($Na_2Ti_6O_{13}$ and $K_2Ti_6O_{13}$) or open layer ($Na_2Ti_3O_7$ and $Cs_{0.68}T_{1.825}O_4$) structured category. In addition, the sodium and potassium hexatitanates differ from each other by the size of their alkali metal ion (Table 36). Nitrogen was doped into the surface and the bulk structure of these titanates, as per XPS and CHN data. The bulk crystal structure of only the $Na_2Ti_3O_7$ remained the same as anatase, as their PXRD pattern stayed unchanged. However, changes to the cell volume was observed in all the titanates as well as anatase. The least volume change was observed in $K_2Ti_6O_{13}$ and $Cs_{0.68}T_{1.825}O_4$. This is potentially due to the non-preferential nitrogen incorporation into both the Ti-O-Ti bonds and the Cs-O-Ti / K-O-Ti bonds, as per Raman data. On the other hand, with $Na_2Ti_6O_{13}$ and $Na_2Ti_3O_7$, the nitrogen is preferentially doped into the Ti-O-Ti bonds, as per Raman data. This resulted in Ti^{3+} species formation in $Na_2Ti_6O_{13}$ and anatase, but not in $Na_2Ti_3O_7$, as per their optical absorption spectrum. The Ti^{3+} absence is potentially due to the relatively less amount of nitrogen incorporated into $Na_2Ti_3O_7$, as all three structures had nitrogen incorporated into both the substitutional and interstitial sites, as per XPS data. The formation of new Ti3d states associated with these Ti^{3+} species and new N1s states is potentially what caused the narrowing of the optical band gap. These new states have also caused the emergence of additional direct and indirect allowed transitions, as per the presence of the less intense absorption in the UV-vis spectrum. The changes in the electronic structure of the valence band is observed to be similar in the open layered structures, where the N1s state arising from the nitrogen incorporation into the Ti-O-Ti bonds mixes with the O2p orbitals in $Cs_{0.68}T_{1.825}O_4$ and O2s orbitals in $Na_2Ti_3O_7$ and in the tunnelled $K_2Ti_6O_{13}$. On the other hand, in the tunnelled $Na_2Ti_6O_{13}$, mixing of the Na1s orbital with the N1s state arising from nitrogen incorporation into the Na-O-Ti bonds is observed.

Table 36 Size of the ions in the interlayers of the titanate structures

Group 1 alkali metal	[183Reference] Ionic radius (Å)
Na^+	1.02
K^+	1.38
Cs^+	1.67

Chapter 9: Aluminium Doped Magnesium Silicon Nitrides

This chapter covers the synthesis and a comprehensive characterisation of aluminium doped magnesium silicon nitrides. **NB:** XX% doped aluminium refers to the percentage of aluminium added to the reaction. XX% Mg $MgSiN_2$ refers to the percentage of magnesium that is added in excess to the reaction.

9.1 Characterisation

Powder X-ray Diffraction (PXRD) was carried out on the Bruker STOE diffractometer with a monochromatic Mo K α λ = 0.7107 Å radiation to determine the crystal structure. The lattice parameters were extracted from the recorded XRD pattern using the UnitCell software. Thermoscientific Fisher K-alpha X-ray Photoelectron Spectrometer with a monochromatic Al K α source of 1486.6 eV energy was used to investigate the chemical nature and composition of the nitrogen doped titanate structures. The Renishaw inVia spectrometer with a laser wavelength of 785 nm set up with an Argon laser source was used for measuring the effect of nitrogen doping on the bond stretching and bending vibrations. An estimate of the nitrogen concentration in the bulk of the titanates were measured using the CHN analysis service at the UCL School of Pharmacy. Any shift in the optical absorption spectrum due to the doping was measured using the Perkin Elmer Lambda-950 UV/ VIS spectrometer.

9.2 Experimental

1. **$MgSiN_2$ synthesis**

Si_3N_4 powder, purchased from *Sigma-Aldrich* (>99.9% trace metal basis), was dried by heating it overnight at 80 ^oC, to remove any adsorbed water. Stoichiometric amounts of this dried Si_3N_4 (0.5816 g) and Mg powder, *Alfa Aesar*, -325 mesh, 99.8% (0.1008 g) was ground together using an agate pestle and mortar. This mixture was then thermally annealed under a dynamic flow of $N_{2\,(g)}$ at 1150 ^oC for 18 h (Equation 13).

$$Si_3N_{4\,(s)} + Mg_{\,(s)} \xrightarrow{1150\ ^oC,\ 18\ h,\ N_2\ (g)} 3\ SiMgN_2 \quad \textbf{Equation 13}$$

2. **Magnesium addition in excess**

The above $MgSiN_2$ synthesis was repeated exactly in the same manner with additional magnesium added to the reactant mixture (Equation 14). The aim was to

identify the percentage of magnesium powder that should be added in excess to make the $MgSiN_2$ powders as phase pure as possible.

$$Si_3N_{4\,(s)} + \text{excess } Mg_{\,(s)} \xrightarrow{1150\ ^oC,\ 18\ h,\ N_2\ (g)} SiMgN_2 \quad \textbf{Equation 14}$$

3. **Aluminium doping**

The as-received Si_3N_4 powder, Mg powder, Al fine powder (*BDH Lab supplies*, minimum assay 90%) were ground well using an agate pestle and mortar and thermally annealed using the same reaction conditions as above **(**Equation 15).

$$Si_3N_{4\,(s)} + \text{excess } Mg_{\,(s)} + Al_{\,(s)} \xrightarrow{1150\ ^oC,\ 18\ h,\ N_2\ (g)} SiMgN_2 \quad \textbf{Equation 15}$$

9.3 Results and Discussion

9.3.1 $MgSiN_2$ Synthesis

With the $MgSiN_2$ synthesised, the phase purity in the bulk is examined by studying the crystal structure and that of the surface is evaluated by investigating the chemical composition on the surface.

1. **Crystal structure**

The use of magnesium as a reactant, $N_{2\,(g)}$ for a reducing atmosphere and the high temperature for annealing makes the $MgSiN_2$ synthesis prone to magnesiothermic reduction[184]. The synthesised $MgSiN_2$ powder gave a PXRD pattern that matches well with that in the literature[185]. However, impurity peaks corresponding to silicon metal was also observed along with the presence of unreacted Si_3N_4 (Figure 98). The silicon impurity is a product of the undesirable magnesiothermic reduction, where the Si_3N_4 is reduced to give silicon, which is reported to be found in Si_3N_4/ Mg mixtures[186]. The evaporation of magnesium during the $MgSiN_2$ synthesis means that there comes a point during the 18 h annealing time where there is no enough magnesium to react with Si_3N_4. This explains the presence of the unreacted Si_3N_4 that is found along with the product.

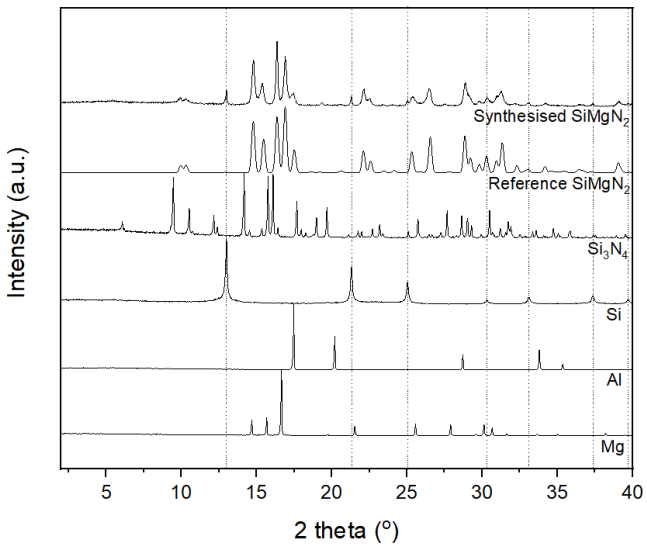

Figure 98 PXRD pattern of the synthesised $MgSiN_2$ powder in comparison with literature patterns of $MgSiN_2$ and the starting materials

2. **Chemical environment on the surface**

The chemical nature of the silicon, magnesium and nitrogen in the synthesised $MgSiN_2$ powders were studied using the XPS core line spectrum (Figure 99). The XPS Si2p spectrum is seen to consists of two peaks at 102.33 eV and 101.24 eV. The former peak corresponds to the Si-O environment usually found in oxidised silicon[187] (see Appendices Figure AB) that may potentially be present on the surface of the $MgSiN_2$ powder particles. The elemental Si impurity observed in the PXRD pattern is not found in this Si2p XPS spectrum. This suggests that Si is not present on the surface but only in the bulk since PXRD probes the bulk crystal structure. The presence of the Si-O environment is also confirmed by the presence of the XPS O1s peak at 532.78. The latter peak in the XPS Si2p spectrum corresponds to the Si environment in $MgSiN_2$. Although the presence of the unreacted Si_3N_4 environment (see Appendices Figure AC) is not observed in the XPS core line spectrum of $MgSiN_2$. This is not really the case as the presence of the unreacted Si_3N_4 environment is observed in the Si2p and N1s XPS core line spectra. This suggests that the unreacted Si_3N_4 environment is present on the surface (as per XPS) and in the bulk (as per the PXRD pattern). The XPS Mg 1s spectrum of the $MgSiN_2$ powder is seen to consist of two peaks at 1304.84 eV and 1306.49 eV. The former peak corresponds to the oxidised magnesium metal environment[188] (see Appendices Figure AD). The latter peak is not reported in the literature and so based on the PXRD pattern, this peak potentially corresponds to the $MgSiN_2$ chemical environment. The XPS N1s spectrum consists of two peaks at 397.34 eV and 398.5 eV. The former peak corresponds to

the unreacted Si_3N_4[189], which is also found in the PXRD pattern. The latter peak is not found in the literature and so based on the PXRD pattern, corresponds to the $MgSiN_2$ chemical environment.

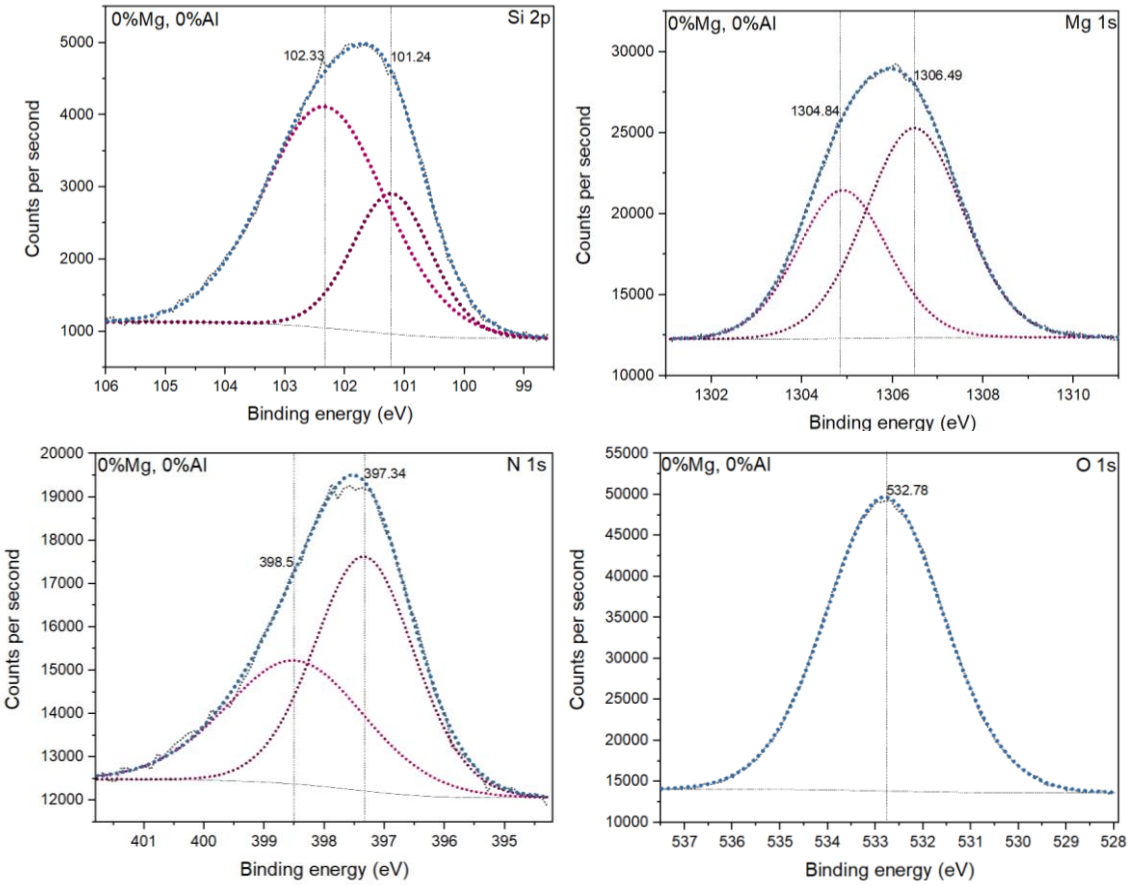

Figure 99 XPS Si2p, Mg1s, N1s and O1s principal core line spectrum of the synthesised $MgSiN_2$ powder

9.3.2 Magnesium Addition in Excess

To decrease the amount of unreacted Si_3N_4 in the synthesised $MgSiN_2$, the evaporated magnesium powder was attempted to be replaced by adding magnesium in excess to the reactant mixture. Since this chapter is on aluminium doped $MgSiN_2$, the effect of magnesium excess on the phase purity was investigated using 25% aluminium doped $MgSiN_2$ powders.

1. **Crystal structure**

The addition of magnesium in excess to the reactant mixture has been seen to reduce the amount of silicon and unreacted Si_3N_4 impurities, with the best phase purity observed with 100% magnesium excess (Figure 100). It is to be noted that potential

impurities such as aluminium, Al_2O_3 and SiO_2 are not seen to be present in any of the samples (see Appendices Figure AE). The FWHM of the PXRD peaks in the 25% aluminium doped $MgSiN_2$ powders are observed to be modified (Table 37) with the addition of varying amounts of magnesium reactant in excess. This suggests that the size of the particles is potentially increased with the addition of different amounts of magnesium in excess.

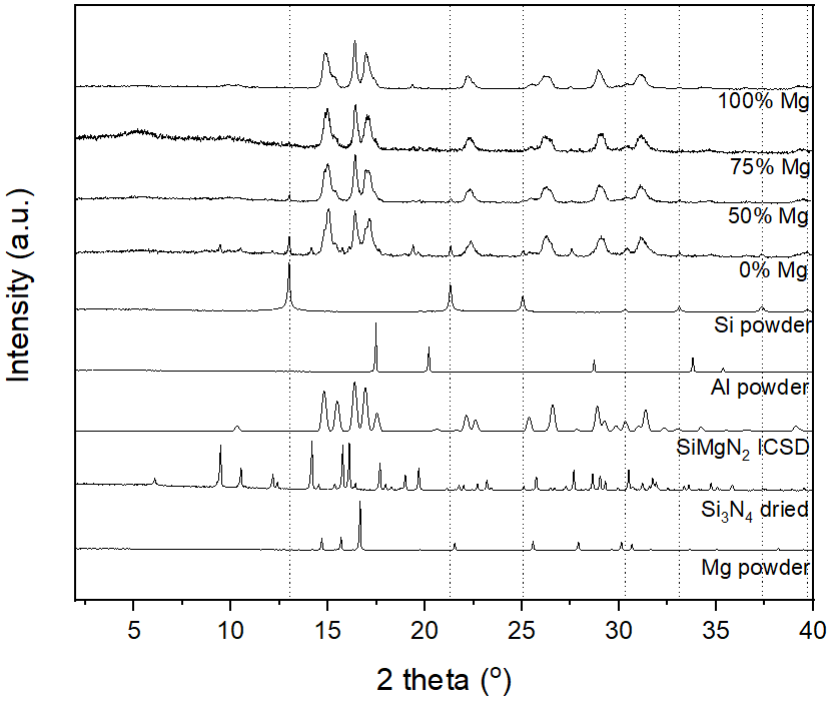

Figure 100 PXRD pattern of the synthesised 25% aluminium doped $MgSiN_2$ powder with different amounts of magnesium excess in comparison with literature patterns of $MgSiN_2$ and the starting materials

Table 37 The 2θ position and FWHM of the PXRD peaks that were seen to be modified upon the addition of varying amounts of magnesium reactant in excess for synthesising 25% aluminium doped $MgSiN_2$

2θ (°)	0% Mg	50% Mg	75% Mg	100% Mg
15.5	0.38	0.40	0.38	0.38
17.15	0.42	0.42	0.37	0.35
22.30	0.37	0.41	0.43	0.40
26.23	0.50	0.58	0.62	0.62
29.06	0.26	0.48	0.43	0.39
31.13	0.47	0.49	0.54	0.61

NB: the 2θ position was read off from the most intense point of the peaks

The structural changes that may have occurred upon magnesium addition was studied by analysing the unit cell parameters, which were calculated by assuming that

the structure of the synthesised $MgSiN_2$ is orthorhombic. To transform the AlN structure to the $MgSiN_2$ structure, two Al^{3+} ions can be replaced by a combination of Si^{4+} and Mg^{2+} ions[186]. This chapter discusses the doping of $MgSiN_2$ with aluminium, for it to get transformed into the AlN structure. The doping of $MgSiN_2$ with 25% aluminium has been seen to decrease the cell volume to 170 $Å^3$ (Table 40) from being 171 Å. This is potentially due to the substitution of the Mg^{2+} with Al^{3+}, as Al^{3+} has a higher ionic radius (Table 38) than Mg^{2+} ions in the host $MgSiN_2$ lattice.

The effect of the addition of different amounts of magnesium in excess, in the synthesis of 25% aluminium doped $MgSiN_2$, on the cell volume was being investigated. With 100% magnesium excess, the cell volume was observed to increase from 170 $Å^3$ to 171 $Å^3$, resulting from the contraction along the 'a' axis and expansion along the 'b' axis. This is potentially due to the substitution of the Mg^{2+} with Al^{3+}, as Al^{3+} has a higher ionic radius (Table 38) than Mg^{2+} ions in the host $MgSiN_2$ lattice. The unit cell volume of the undoped $MgSiN_2$ with 0% magnesium excess was also 171 $Å^3$. This suggests that although the 25% aluminium and 100% magnesium excess contract the unit cell along the 'a' axis and expands along the 'b' axis, the unit cell volume remains close to being unaffected. The greatest unit cell volume expansion by 5 $Å^3$ was observed with 75% aluminium, caused by expansion along the 'a' and 'b' axis while a contraction along the 'c' axis. This could potentially be because this sample had the highest amount of Al^{3+} ions which had replaced Mg^{2+} ions. On the other hand, the greatest unit cell contraction of ~10 Å was observed with 50% magnesium excess, caused by contraction along the 'a' and 'c' axis while expansion along the 'b' axis. Here, more Al^{3+} ions must have incorporated being substituted the Si^{4+} ions rather than the Mg^{2+} ions in the $MgSiN_2$ lattice where the Si^{4+} has a higher ionic radius than Al^{3+}, which has a higher ionic radius than Mg^{2+}. Although this is the case, the value of the cell volume upon the addition of different amounts of magnesium in excess is close to 170 $Å^3$ ± 10 $Å^3$, suggesting it to be closer to the $MgSiN_2$ structure than the AlN structure (Table 39). However, this does suggest the tendency for the structure to become more like AlN.

Table 38 Ionic radius of the elements present in AlN and $MgSiN_2$

Ion	[Reference [183]] Radius (Å)
Si^{4+}	0.26
Al^{3+}	0.39
Mg^{2+}	0.57
N^{3-}	1.46

Table 39 Calculated lattice parameters of 25% aluminium doped $MgSiN_2$ with different amounts of magnesium excess, undoped $MgSiN_2$ in comparison with the literature

Sample	Lattice parameter (Å)			Cell volume (Å^3)
	a	b	c	
25% Al doped $MgSiN_2$ with x% Mg				
0%Mg	5.320(2)	6.4069(10)	4.9874(6)	170.01(4)
50%Mg	4.896(5)	6.589(2)	4.9855(6)	160.87(10)
75%Mg	5.449(1)	6.469(1)	4.9736(7)	175.32(4)
100%Mg	5.2898(8)	6.479(1)	4.9871(6)	170.94(3)
Undoped $MgSiN_2$				
0%Mg	5.2974(9)	6.4654(6)	4.9957(5)	171.10(3)
Literature reference				
$MgSiN_2$ [ɱ]	5.2708	6.4692	4.9840	170.18
AlN (wurtzite-type) [β]	3.111	3.111	4.9878	41.71
AlN (NaCl-type) [β]	3.938	3.938	3.938	61.07

[ɱ] C. Fang, R. Groot, R. Bruls, H. Hintzen and G. With, Journal of Physics: Condensed Matter, 1999, 4833–4842.

[β] F. Litimein, B. Bouhafs, Z. Dridi and P. Ruterana, New Journal of Physics, 2002, 4, 64-64.

2. **Chemical environment on the surface**

A comparison of the chemical environments on the surface of the $MgSiN_2$ powders before (Figure 99) and after doping with 25% aluminium (Figure 101) is discussed below. With the untreated $SiMgN_2$, the presence of the SiO_2 and $SiMgN_2$ environments are observed by the XPS Si2p peaks at 102 eV and 101 eV respectively. The presence of magnesium impurity, which was not observed in the PXRD pattern, was observed. This surface-bound impurity was seen by the XPS Mg1s peak at ~1305 eV. The presence of unreacted Si_3N_4 and $SiMgN_2$ is observed by the peaks at ~398 eV and ~399 eV respectively. All these chemical environments are observed in the 25% aluminium doped $SiMgN_2$ powder. In addition, the presence of the Al-N chemical environment is observed by the XPS Al2p peak at ~74 eV[190]. The XPS O1s peak is observed before and after doping, suggesting the presence of oxygen on the surface of the synthesised $SiMgN_2$ powders.

It is important to see if the addition of varying amounts of magnesium in excess can affect the chemical environments in the $SiMgN_2$ host lattice as any such effect is undesirable. The XPS core line spectrum of 25% aluminium doped $SiMgN_2$ with varying amounts of magnesium added in excess is discussed below. With all the $MgSiN_2$ made using the different amounts of magnesium added in excess, the SiO_2 and $SiMgN_2$ environments was observed, indicated by the presence of the XPS Si2p

peaks at ~102 eV and ~101 eV respectively. This is confirmed by the presence of the XPS O1s peak at ~532.5 eV, which corresponds to the SiO_2 chemical environment in all the samples. The oxidised magnesium environment was also observed in all these samples, indicated by the presence of the XPS Mg 1s peak at ~1305 eV. This suggests that the magnesium oxide is surface bound and is sitting above the $MgSiN_2$, which constitutes the bulk as per PXRD data. The presence of unreacted Si_3N_4 reactant species is present with the $MgSiN_2$ synthesised using all the different amounts of magnesium excess. This is indicated by the XPS N1s peaks at ~397 eV and ~398 eV. With the 100% Mg excess, magnesium oxide formation is preferred over the reaction with Si_3N_4. The AlN chemical environment is observed in the $MgSiN_2$ samples synthesised using all the different amounts of magnesium added in excess. This is indicated by the XPS Al2p peak at ~74 eV. The presence of AlN is not observed in the PXRD data suggesting that the AlN observed is only surface-bound. The $MgSiN_2$ sample synthesised with 100% magnesium excess shows an additional peak at 69.15 eV, which is not reported in the literature.

Theoretically, $MgSiN_2$ has a chemical composition where the Mg: Si: N ratio should be 25%: 25%: 50%. This is not observed in the synthesised $MgSiN_2$ with 0% magnesium excess and 0% aluminium (Table 40). As per PXRD and XPS data, it is the magnesium and silicon environments that are affected the most from oxidation and magnesiothermic reduction while the nitrogen environment is the least affected. As per these findings, the silicon concentration is higher than the stoichiometric amount in the sample mentioned earlier. This is due to the silicon impurity, which is also seen in the PXRD data, formed from magnesiothermic reduction. Upon doping the $MgSiN_2$ with 25% aluminium, the fraction of silicon becomes roughly the same as the stoichiometric ratio as the concentration of nitrogen is also seen to be increased. This means that the presence of aluminium has decreased the rate of the magnesiothermic reduction, reducing the formation of the silicon impurity and thus allowing the reaction between Si_3N_4 and magnesium. The percentage of oxygen observed on the surface of the product particles is also seen to be reduced by 9 atomic%. However, the percentage of magnesium remains below the stoichiometric amounts and is caused by the formation of magnesium oxide, which is evident from the XPS data. Increasing the amount of magnesium excess used for the $MgSiN_2$ synthesis to 50%, 75% and 100% resulted in reducing the oxygen concentration by 10 atomic%, 12 atomic% and 7 atomic% respectively. Here too, the magnesium concentration remained the same.

Table 40 XPS elemental composition of $MgSiN_2$ powders

Elemental concentration (atomic%)				
	Mg1s	**Si2p**	**N1s**	**O1s**
0%Mg 0%Al	6	16	17	60
0%Mg 25%Al	6	15	27	51
50%Mg 25%Al	6	15	29	50
75%Mg 25%Al	5	15	32	48
100%Mg 25%Al	7	14	25	53

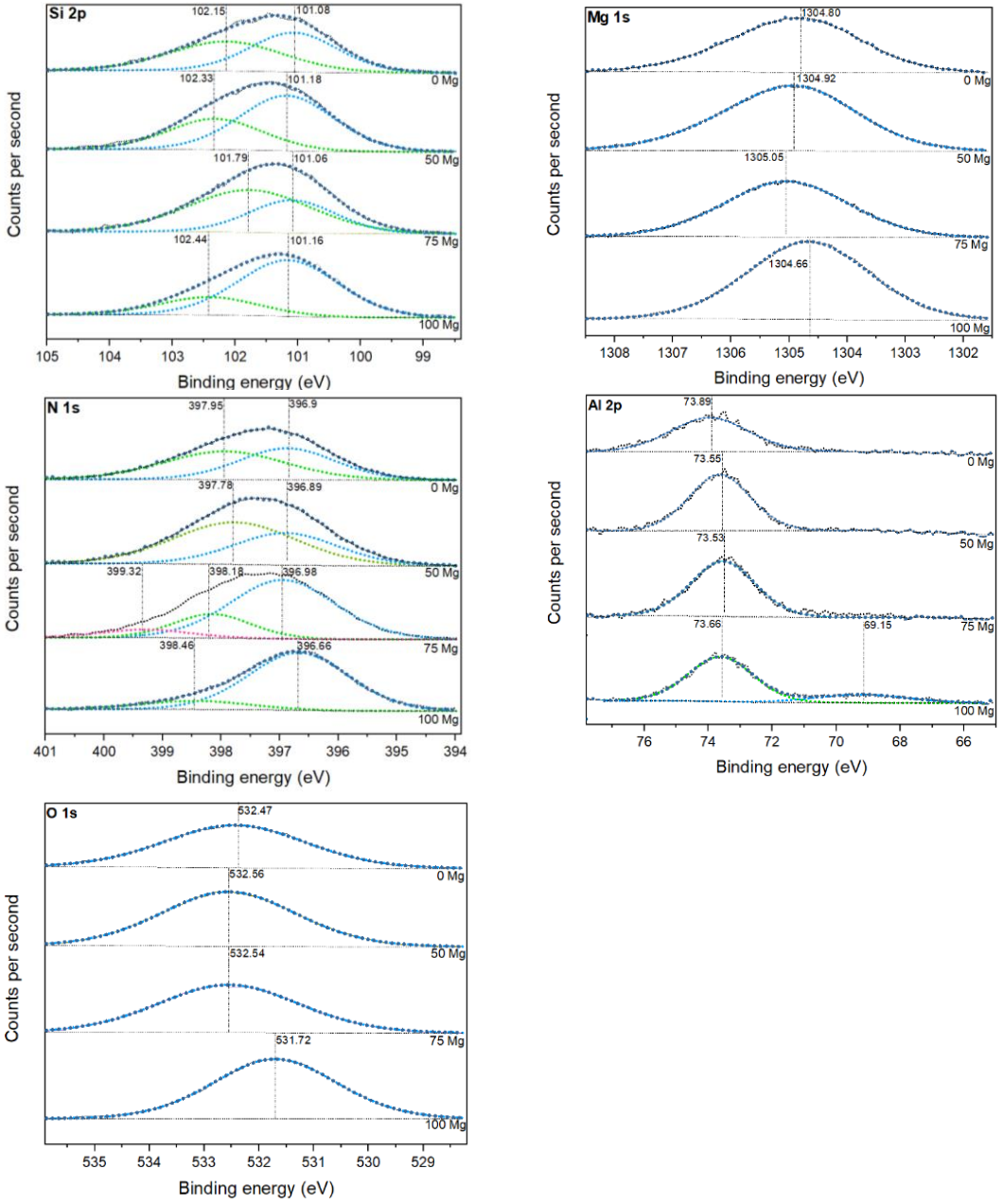

Figure 101 XPS Si2p, Mg1s, N1s, Al2p and O1s principal core line spectrum of 25% aluminium doped $MgSiN_2$ with 0%, 50%, 75% and 100% magnesium in excess. NB: the pink peak fitting in the N1s XPS spectrum is a mistake and should be ignored.

9.3.3 Effect of Low (25%) and High (75%) Aluminium Content

It is to note that the PXRD data showed phase pure $MgSiN_2$ in the bulk structure, with the addition of increasing amounts of magnesium in excess, which helped to remove the silicon metal impurity. However, it was also deduced earlier from the XPS data that the presence of aluminium has helped to bring silicon and nitrogen concentration on the surface of the $MgSiN_2$ to match theoretical stoichiometric ratios observed in $MgSiN_2$. The best phase purity was recorded to be with 100% magnesium excess, as already discussed earlier. To investigate this further, the effect of using different amounts of aluminium dopant on the phase purity of the $MgSiN_2$ synthesised with 100% magnesium excess was being studied. To do this, a new $MgSiN_2$ sample with 100% magnesium excess was synthesised with 75% aluminium. It was then compared with the already discussed $MgSiN_2$ sample with 100% magnesium excess and 25% aluminium.

1. **Crystal structure**

The crystal structures of the $MgSiN_2$ with 100% magnesium excess synthesised with 25% and 75% aluminium were found to be different (Figure 102). The PXRD pattern of the 75% aluminium doped sample has a smaller number of peaks compared to that of the 25% aluminium doped sample. This suggests that the latter sample has a relatively lower symmetry and the absence of several peaks expected to be at 15.46^o, 17.52^o, 22.58^o, 25.36^o and 29.18^o suggests a modification of the crystal structure. Also, peak shifts are seen to be greater with 75% Al compared to 25% Al. For example, a shift of +0.05^o is seen to be seen with the peak at 14.83^o and 22.11^o. While the 25% aluminium made the structure to look like the lower symmetry $MgSiN_2$, the use of 75% aluminium gave a structure that resembles AlN-wurtzite. So, with 75% aluminium, more Al^{3+} ions are occupied in the host lattice than the total number of Si^{4+} and Mg^{2+} ions. The vice-versa is true with the 25% aluminium. With 75% Al, an increase in crystallinity is observed as seen by the increase in sharpness of the peaks. With 25% Al, broadening of the peaks are seen to be observed, which could potentially be observed with increasing particle size.

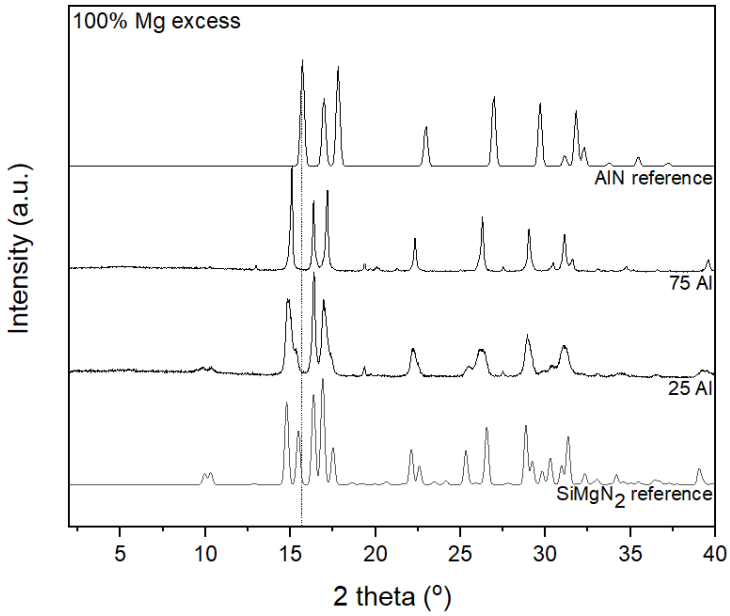

Figure 102 PXRD pattern of $MgSiN_2$ with 100% magnesium excess synthesised with 25% and 75% aluminium, in comparison with the literature patterns of AlN and $MgSiN_2$

2. **Chemical environment on the surface**

When the $MgSiN_2$ sample synthesised with 100% magnesium excess was doped with 25% aluminium (Figure 101), the chemical environments present on its surface were found to be same as when it was doped with 75% aluminium (Figure 103) instead. The presence of the SiO_2 and $MgSiN_2$ environments were evident from the XPS Si2p spectrum with peaks at ~102 eV and ~101 eV respectively. The presence of SiO_2 is also observed by the peak at ~532 eV in the XPS O1s spectrum. Magnesium oxide impurity was observed from the presence of the Mg1s peak at ~1305 eV. The presence of the $MgSiN_2$ as well as unreacted Si_3N_4 environments were confirmed from the XPS N1s peak at ~398 eV and ~399 eV respectively. The AlN chemical environment was observed in both the samples, as a peak at ~74 eV was seen in the XPS Al2p spectrum. It is to be noted that the AlN environment observed in the 25% aluminium doped sample is surface-bound and is the reason for it to be not seen in the PXRD pattern.

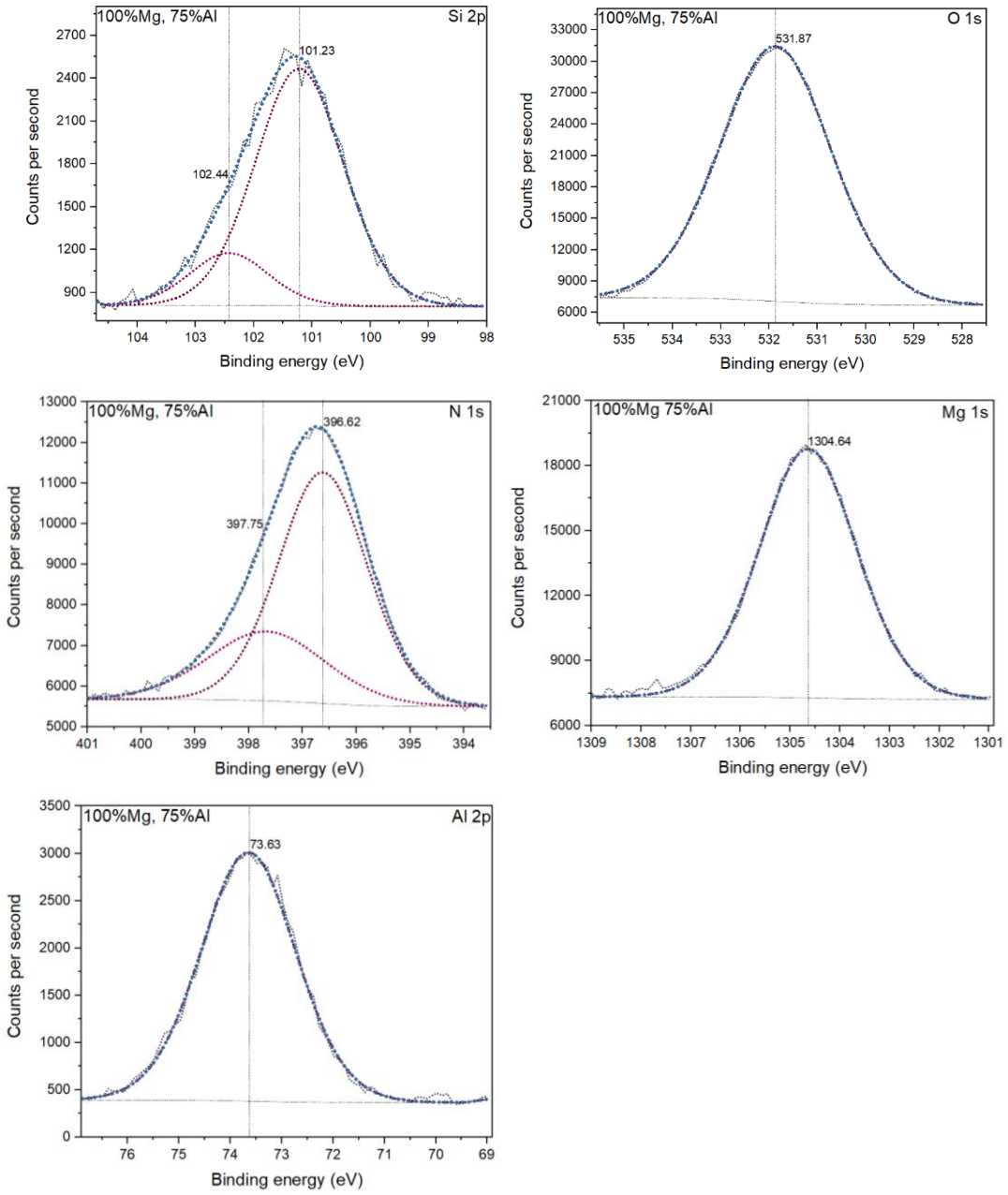

Figure 103: XPS Si2p, Mg1s, N1s, Al2p and O1s principal core line spectrum of $MgSiN_2$ with 100% magnesium excess doped with 75% aluminium

9.3.4 Crystal structure of $MgSiN_2$ and AlN Solid Solutions with Varying Amounts of Aluminium Content

The $MgSiN_2$ to AlN crystal structure transformation was observed earlier by increasing the aluminium content from 25% to 75%. To get a better idea of the percentage range of aluminium content where the transformation to AlN crystal structure occurs, the effect of 30% and 50% aluminium has been investigated using the $MgSiN_2$ with 100% magnesium excess.

1. **Crystal structure**

Increasing the aluminium content from 30% to 50% has made the PXRD peaks sharper (Figure 104), potentially suggesting an increase in crystallinity. It also results in less PXRD peaks, suggesting a transformation into a lower symmetry structure. The PXRD pattern in the 50% aluminium $MgSiN_2$ with 100% magnesium excess sample looks like that of the AlN-wurtzite PXRD pattern in the literature but shifted to lower angles. This potentially suggests that the host lattice has a $MgSiN_2$ crystal structure but with more Al^{3+} ions than a combination of Si^{4+} and Mg^{2+} ions. From these PXRD patterns, it can be suggested that the transformation to AlN occurs between the 30% aluminium and 50% aluminium introduction.

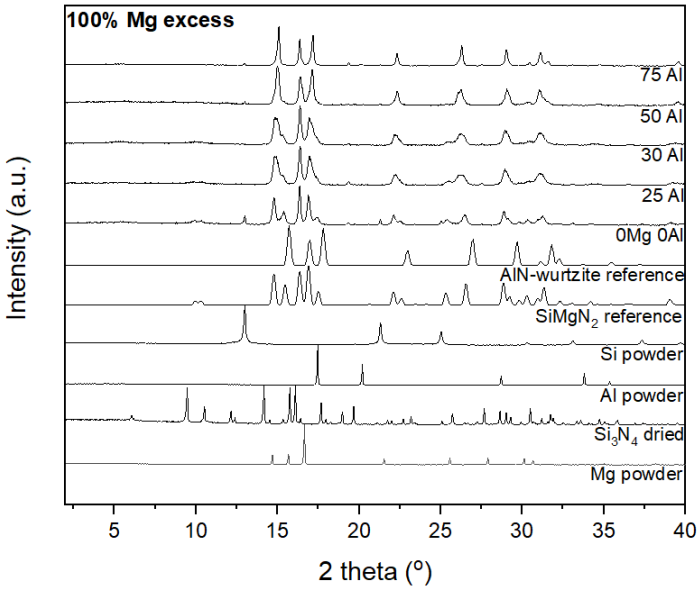

Figure 104 PXRD pattern of $MgSiN_2$ with 100% magnesium excess synthesised with different amounts of aluminium

Increasing the aluminium content, introduced into the $MgSiN_2$ with 100% magnesium excess, has resulted in the contraction of the unit cell volume (Table 41). Increasing the aluminium dopant from 25% to 30% has resulted in the contraction of the unit cell volume by 8 $Å^3$, caused by the contraction along the 'a' and 'b' axis and expansion along the 'b' axis. Increasing the aluminium content from 25% to 50%, results in the contraction of the cell volume by 12 $Å^3$. While increasing the aluminium content from 25% to 75%, contraction of the cell volume by only 2 $Å^3$ is observed. This also suggests that the transformation to AlN structure occurs between the aluminium content range of 30% to 50%.

Table 41 Calculated unit cell parameters of $MgSiN_2$ powders with 100% magnesium excess synthesised with different amounts of aluminium

Sample	Lattice parameter (Å)			Cell volume ($Å^3$)
	a	b	c	
0% Al 0%Mg	5.2974(9)	6.4654(6)	4.9957(5)	171.10(3)
25% Al	5.2898(8)	6.479(1)	4.987(6)	170.95(3)
30% Al	4.964(5)	6.605(2)	4.9721(6)	163.0(1)
50% Al	4.871(3)	6.521(1)	5.0038(5)	158.96(9)
75% Al	5.409(1)	6.263(2)	4.9879(7)	168.99(5)

2. **Chemical nature on the surface**

The introduction of 30% and 50% aluminium content into the $MgSiN_2$ with 100% excess has resulted in the formation of the same silicon, magnesium, nitrogen and oxygen chemical environments (Figure 105). The presence of SiO_2 and $MgSiN_2$ environments were indicated by the peaks observed at ~102 eV and ~101 eV respectively in the XPS Si2p spectrum. The presence of SiO_2 was also evident from the peak at ~532 eV in the XPS O1s spectrum. The magnesium oxide environment was also present as a peak at ~1305 eV was observed in the XPS Mg1s spectrum. Unreacted Si_3N_4 and $MgSiN_2$ environments corresponded to the peaks at ~396.5 eV and ~398 eV respectively in the XPS Si2p spectrum. While the 50% aluminium sample is seen to have the AlN chemical environment, the 30% aluminium sample is observed to only have an Al_2O_3 environment[191], indicated by the XPS Al2p peaks at ~74 eV and ~73 eV.

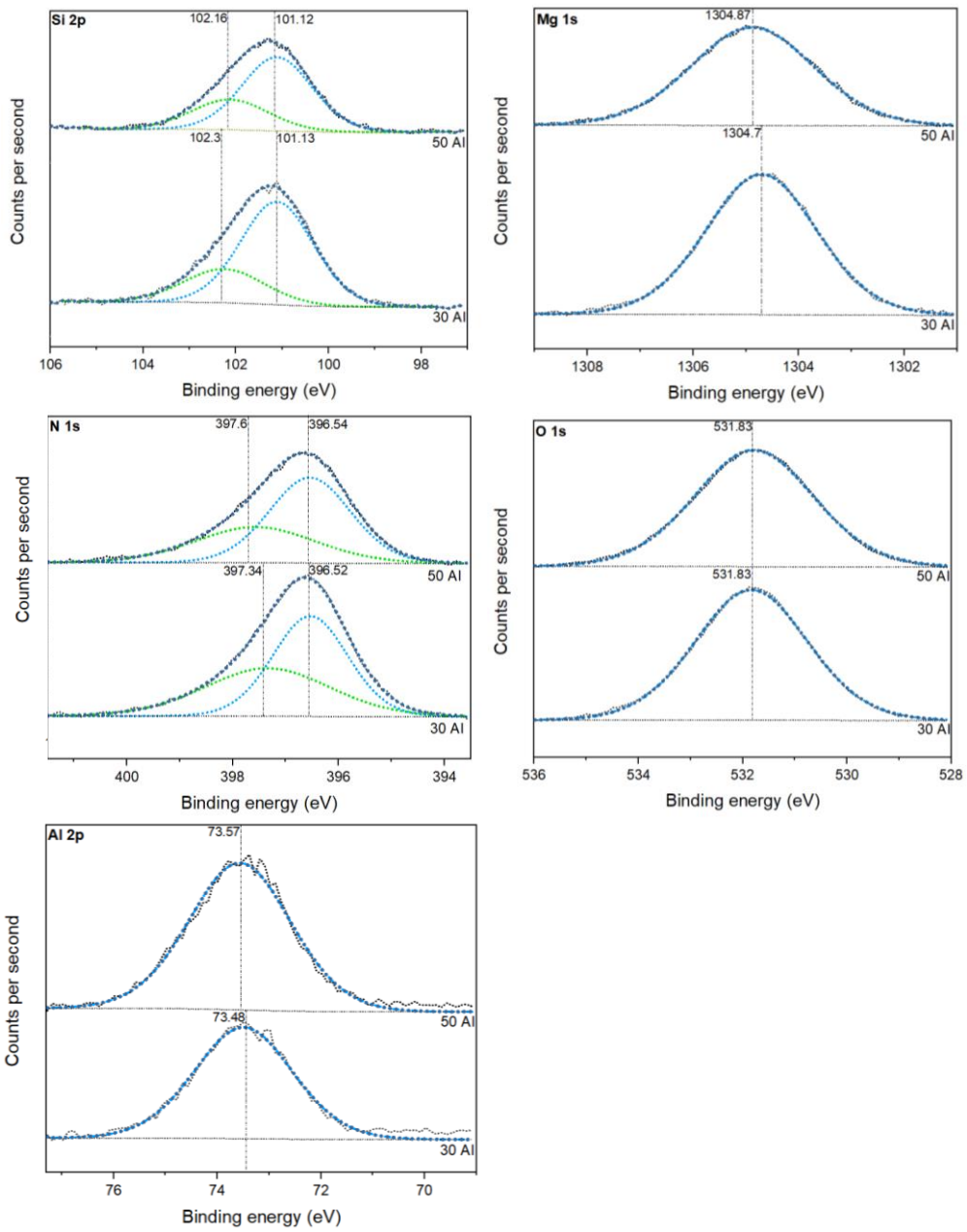

Figure 105 XPS Mg1s, Si2p, N1s, Al2p and O1s spectrum of $MgSiN_2$ with 100% magnesium excess synthesised with 30% and 50% aluminium

9.3.5 Magnesium Addition in Excess to $MgSiN_2$ with a Higher (75%) Aluminium Content

This section relates back to section 9.3.2 where the effect of the addition of various amounts of magnesium in excess on the 25% $MgSiN_2$ powder was investigated. In this section however, the same effect is investigated using $MgSiN_2$ with 75% aluminium.

1. **Crystal structure**

The silicon metal impurity observed, by the presence of the PXRD peak at ~13.5º, in 75% aluminium doped $MgSiN_2$ was found to decrease with increasing the magnesium reactant that was added in excess (Figure 106). Magnesium excess of 5%, 25% and 100% were experimented with and the best phase purity was observed with the sample made with 100% magnesium excess. The addition of 100% excess magnesium in the synthesis of 25% aluminium doped $MgSiN_2$ helped with the complete disappearance of the silicon metal impurity PXRD peak at ~13.5º. However, the addition of 100% excess magnesium in the synthesis of 75% aluminium doped $MgSiN_2$ still results in a small silicon impurity PXRD peak. This suggests that increasing the aluminium content increases the amount of magnesium reactant that needs to be added in excess to achieve the $MgSiN_2$ phase purity. This is because the presence of a higher aluminium content (75% versus 25%) potentially encourages Si_3N_4 reduction. With 75% aluminium, there are relatively less PXRD peaks in total, suggesting the formation of a higher symmetry structure. Additionally, the PXRD peaks of the 75% aluminium doped $MgSiN_2$ powders are observed to be more well-defined and not broadened compared to that of the 25% aluminium doped powders, where peak broadening was observed with increasing amounts of magnesium added in excess. The PXRD pattern of the 75% aluminium doped sample looks like to that of AlN-wurtzite.

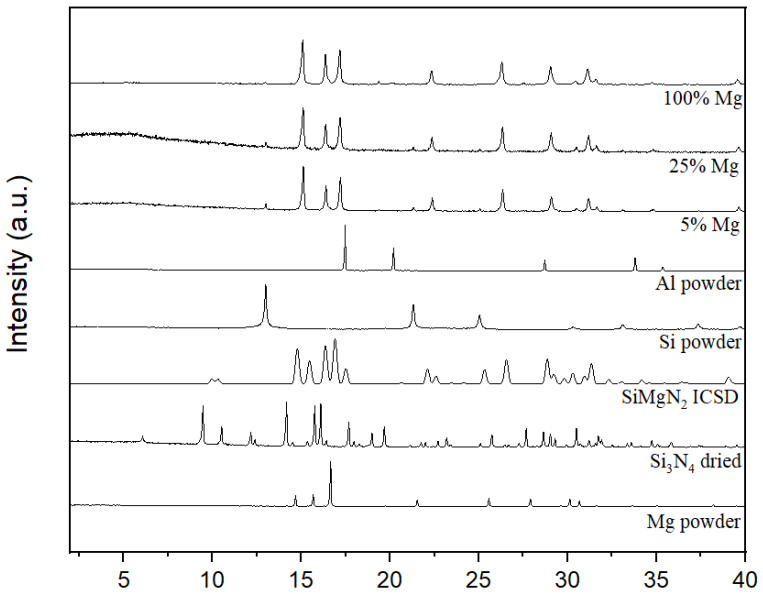

Figure 106 PXRD of 75% aluminium doped $MgSiN_2$ synthesised with varying amounts of magnesium added in excess

Increasing the amount of magnesium added in excess has been observed to decrease the crystallinity of the 75% aluminium doped $MgSiN_2$. This was evident from

the FWHM of the PXRD peaks that were seen to increase with increasing magnesium content (Table 42).

Table 41 FWHM of the PXRD peaks in the 75% aluminium doped $MgSiN_2$ synthesised with different amounts of magnesium excess

Peak position	Magnesium excess		
	5% Mg	25% Mg	100% Mg
15.05º	0.12	0.15	0.15
17.15º	0.12	0.15	0.15
22.30º	0.12	0.13	0.16
26.23º	0.14	0.14	0.17
29.06º	0.14	0.13	0.16
31.13º	0.15	0.17	0.16

Table 42 Lattice parameters (derived from experimental measurements) of 75% aluminium doped $MgSiN_2$ synthesised with different amounts of magnesium excess

Sample	Lattice parameter (Å)			Cell volume (Å^3)
	a	b	c	
75% Al doped $MgSiN_2$ with x% Mg				
5% Mg	5.403(1)	6.454(1)	4.9871(9)	173.94(5)
25% Mg	5.337(2)	6.3853(9)	4.9879(6)	169.99(4)
100% Mg	5.409(1)	6.263(2)	4.9879(7)	168.99(5)
Undoped $MgSiN_2$				
0%Mg 0% Al	5.2974(9)	6.4654(6)	4.9957(5)	171.10(3)
Literature reference				
$MgSiN_2$	5.27249(4)	6.47334(6)	4.98622(5)	170.18
AlN (wurtzite-type)	3.111	3.111	4.9878	41.71
AlN (NaCl-type)	3.938	3.938	3.938	61.07

The effect of the addition of different amounts of magnesium excess for the synthesis of $MgSiN_2$ is discussed in terms of the lattice parameters (Table 43). Increasing the magnesium excess from 5% to 25% has resulted in the reduction of the unit cell volume by 4 Å^3, caused by contraction along the ‘a’ and ‘b’ axis while expansion along the ‘c’ axis. Increasing the magnesium excess content from 25% to 100% has resulted in the contraction of the unit cell by 1 Å, caused by expansion along the ‘a’ axis and contraction along the ‘b’ axis. This is potentially because the presence of a high

aluminium content is encouraging the evaporation of magnesium, resulting in more aluminium taking up lattice sites than magnesium. This decreases the concentration of magnesium available for reacting with Si_3N_4 for $MgSiN_2$ formation. As a result, AlN formation is observed to predominantly occur, as supposed to $SiMgN_2$ formation.

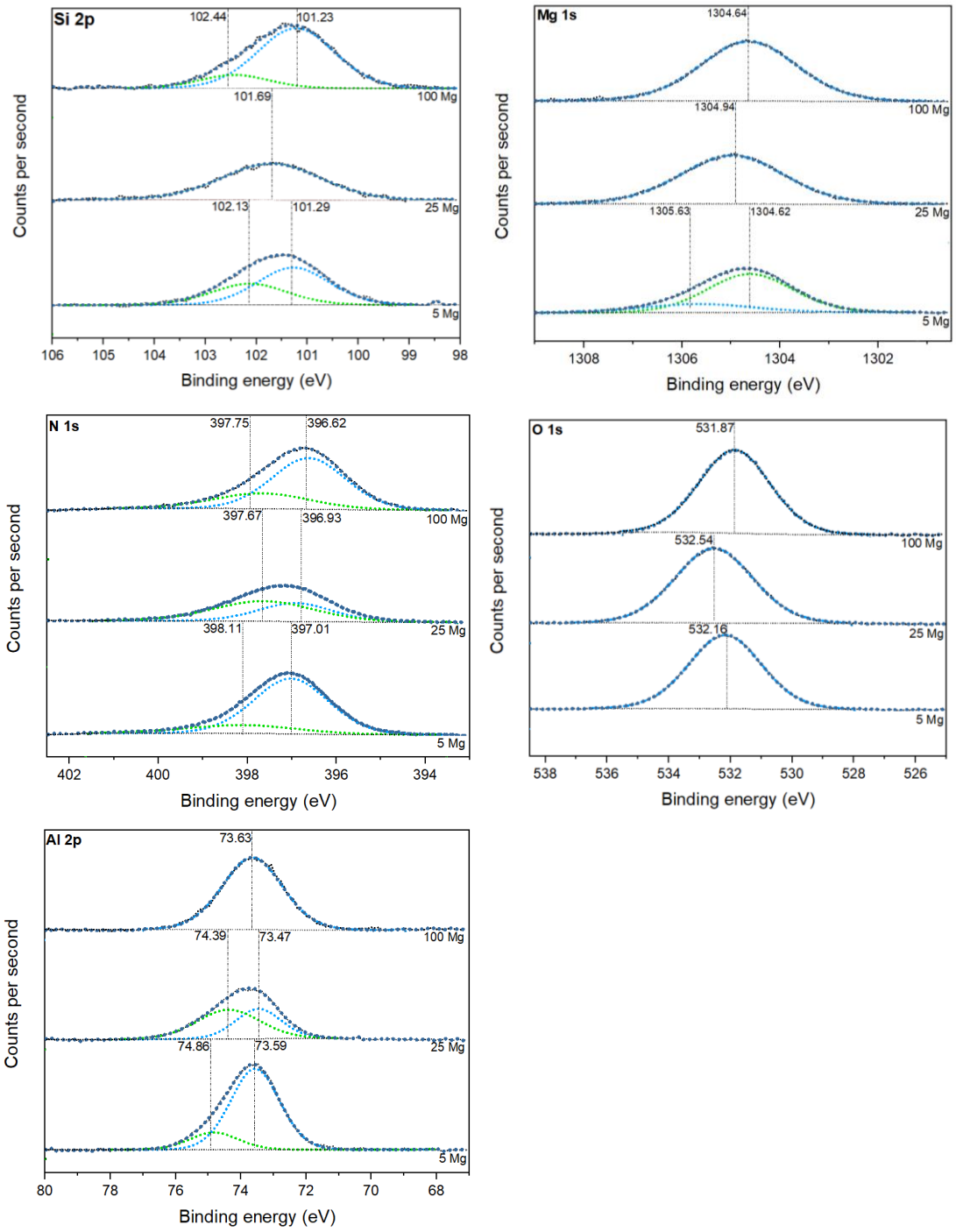

Figure 107 XPS Mg1s, Si2p, N1s, Al2p and O1s principal core line spectrum of 75% aluminium doped $MgSiN_2$ synthesised with varying amounts of magnesium excess

The chemical environments of the elements present in the 75% aluminium doped $MgSiN_2$ synthesised with varying amounts of magnesium is discussed below (Figure 107). The SiO_2 and $MgSiN_2$ environments, denoted by the XPS Si2p peaks at ~101 eV and ~102 eV respectively, were only observed on the surface of the samples made with 5% and 100% magnesium excess. On the other hand, only the $MgSiN_2$ environment was observed with the sample made with 25% magnesium excess. This is potentially because 25% magnesium is enough to replace the magnesium lost by evaporation, helping all the Si_3N_4 to react with the magnesium. The presence of the SiO2 environment in the sample with 5% and 100% magnesium excess is also indicated by the peak at ~532 eV in the XPS Si2p spectrum. On the other hand, a similar environment is observed to be present at ~533 eV in the sample with 25% magnesium excess. The samples prepared with 5%, 25% and 100% magnesium excess showed the presence of the oxidised magnesium indicated by the peak at ~1305 eV in the XPS Mg1s spectrum. On the other hand, with the 5% magnesium excess sample an additional peak at ~1306 eV is also observed, indicating the presence of the $MgSiN_2$ environment. The AlN environment is observed to be present in all the samples synthesised with 5%, 25% and 100% magnesium excess. This is indicated by the peak at ~74 eV in the XPS Al2p spectrum. An addition peak at ~75 eV, corresponding to Al_2O_3 is present in the sample synthesised with 5% and 25% magnesium excess. From this, it can be deduced that a high magnesium excess content potentially discourages Al_2O_3 formation and as per the XPS Si2p spectrum, the high magnesium excess content encourages SiO_2 formation.

9.3.6 Effect of Small Variation in the Aluminium Content on $MgSiN_2$ Synthesised with 25% Magnesium Excess

The effect of doping the $MgSiN_2$ with 25% magnesium excess with 67% and 75% aluminium content is being investigated.

1. **Crystal structure**

Increasing the aluminium content in the $MgSiN_2$ with 25% magnesium excess sample from 67% (Figure 108) to 75% (Figure 107) has helped to reduce the silicon metal impurity significantly. This is deduced from its PXRD pattern where the peak at ~13.5^o, which corresponds to the silicon impurity is seen to decrease in intensity in the sample with 75% aluminium. Both these samples have the same PXRD pattern, which is observed to be like the PXRD pattern of AlN-wurtzite found in the literature.

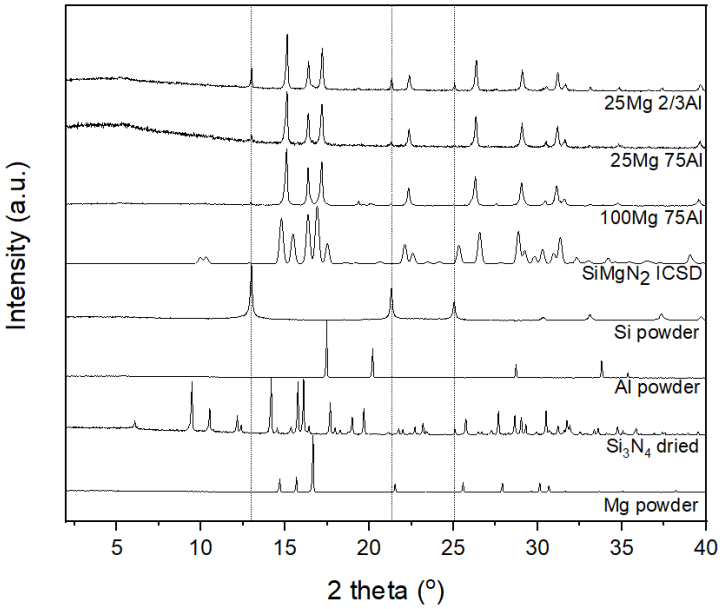

Figure 108 PXRD pattern of $MgSiN_2$ with 25% magnesium excess, synthesised using 67% and 75% aluminium content

Table 43 Calculated lattice parameters of $MgSiN_2$ with 25% magnesium excess, synthesised with 67% and 75% aluminium content

Sample	Lattice parameter (Å)			Cell volume (Å^3)
	a	b	c	
67% Al	5.324(2)	6.3639(10)	4.9880(6)	169.00(4)
75% Al	5.336(2)	6.3840(10)	4.9886(6)	169.94(4)

Increasing the aluminium content from 67% to 75% in the $MgSiN_2$ with 25% magnesium excess has resulted in the expansion of its unit cell volume by 1 Å^3 (Table 44). This is caused by the expansion along the 'a', 'b' and 'c' axis. This indicates the extent to which the increasing aluminium content has on the unit cell volume of the host lattice.

The effect of a small variation in the aluminium content from 67% to 75% on the surface chemical composition in $MgSiN_2$ with 25% magnesium is discussed below. The SiO_2 chemical environment is present in both these samples, indicated by the peak at ~102 eV in the XPS Si2p spectrum. The presence of SiO_2 is also observed by the XPS O1s peak at ~533 eV. The magnesium oxide environment is also present in both these samples, indicated by the presence of the peak at ~1305 eV in the XPS Mg1s spectrum. The presence of unreacted Si_3N_4 is also observed in both the samples, indicated by the XPS N1s peak at ~398 eV and ~397 eV. The AlN chemical environment is also present in both samples, indicated by the XPS Al2p peak at ~74

eV. An additional peak at ~73 eV, corresponding to Al_2O_3 is observed in the sample with 75% aluminium content, which is not present in the sample with 67% aluminium content. This is because increasing the aluminium content increases the probably of aluminium available to undergo oxidation along with reacting with Si_3N_4. Additional peaks at ~75 eV and ~77 eV is observed in the sample with 75% aluminium but is not observed in the sample with 67% aluminium content. The former peak corresponds to Al_2O_3 and the latter peak is not reported in the literature.

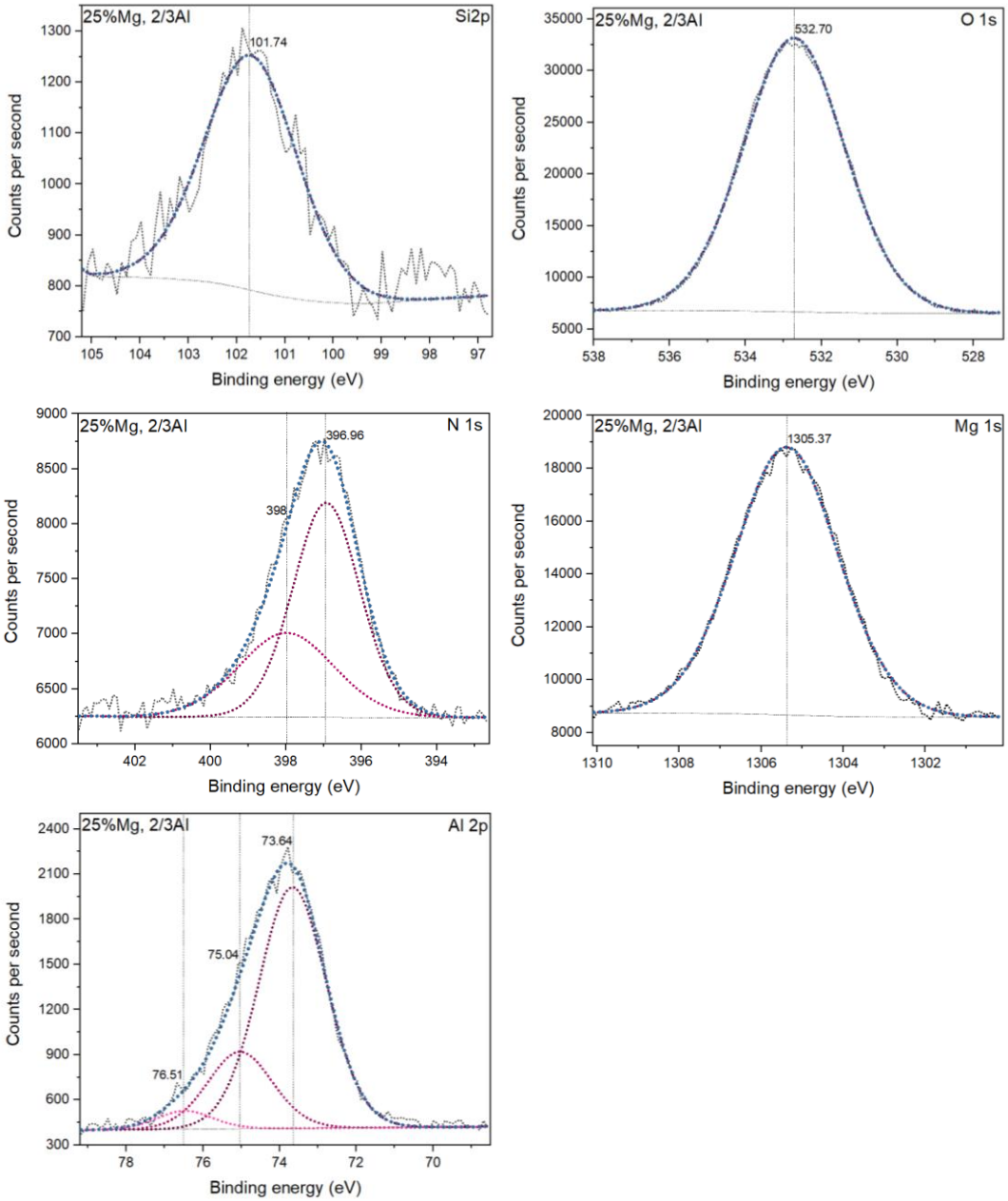

Figure 109 XPS Mg1s, Si2p, N1s, Al2p and O1s spectrum of 67% aluminium doped $MgSiN_2$ with 25% magnesium excess

The presence of oxygen is found to be predominantly on the surface of the synthesised $MgSiN_2$ powders. This was attempted to be removed by using XPS argon

etching process, which the literature suggests. However, as observed from the XPS survey scan before and after etching, the oxygen is not observed to be removed (Figure 110). This is due to the reasoning that powders do not have a well-defined surface or a bulk, therefore, etching the pelletised powder surface does not expose the bulk of the powder, but rather exposes the powder particles underneath it. Due to this reason, the unetched powders were used for the investigations in this chapter. Figure 110 also shows peaks at ~300 eV and ~350 eV which correspond to Ca 2p and K 2p respectively. A possible hypothesis to why this might be the case could be that these elements could be bulk impurities potentially present in the as-received single crystal substrates. During the high temperature solid-state doping process, these impurities could have potentially migrated onto the surface and therefore got detected by the XPS.

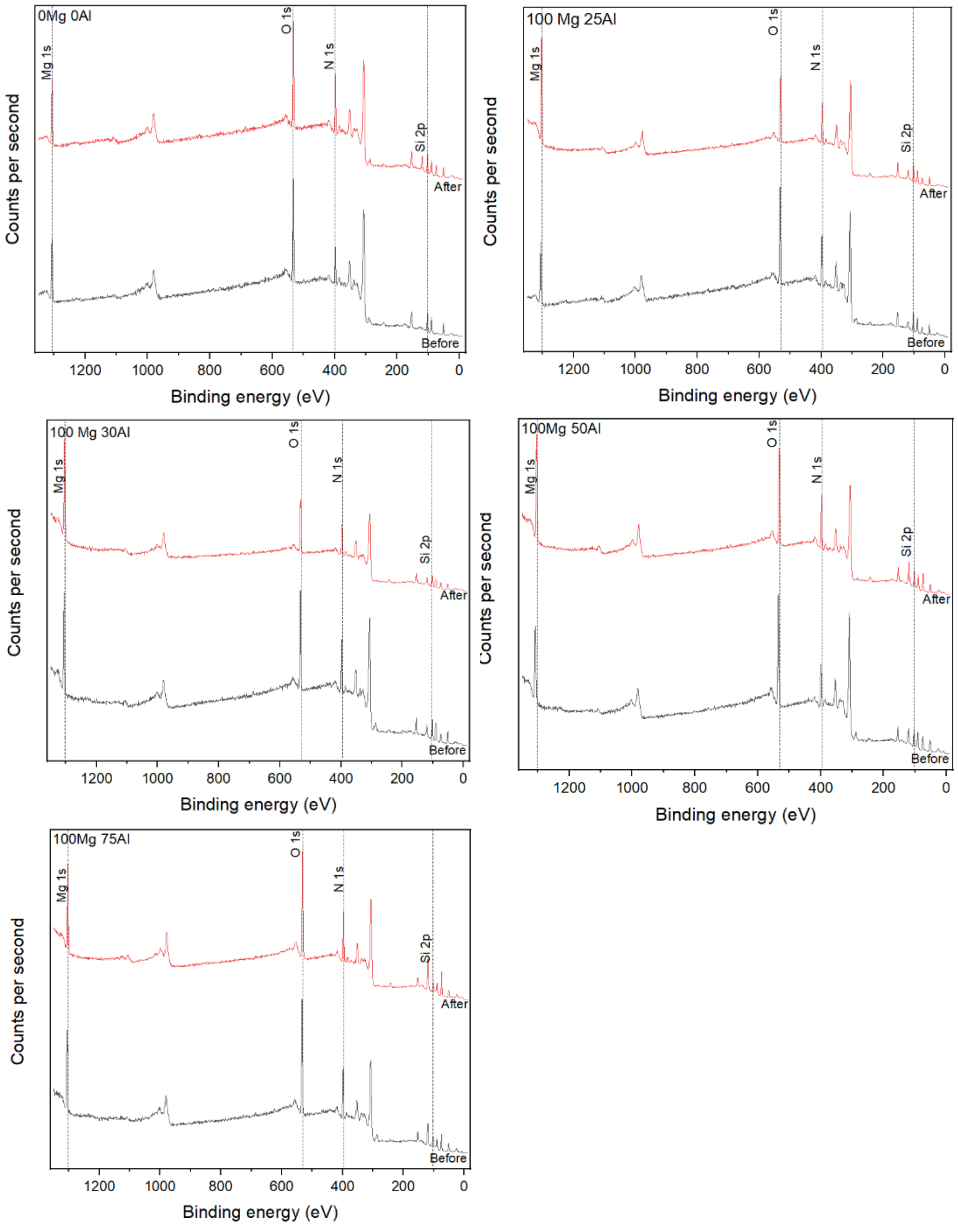

Figure 110 XPS survey scan of synthesised $MgSiN_2$ powders with different amounts of magnesium reactant added in excess and varying amounts of aluminium as a dopant

9.4 Summary of Findings

The $MgSiN_2$ powder synthesis is prone to magnesiothermic reduction due to the use of a reducing atmosphere such as N_2 (g) and a high annealing temperature. The synthesised $MgSiN_2$ crystal structure was not phase pure, as per PXRD data, as it was found to have unreacted Si_3N_4 reactant and silicon metal impurity. The high annealing temperature has led to the evaporation of the magnesium reactant, leaving a portion of the Si_3N_4 unreacted, which under the reducing N_2 (g) atmosphere resulted in the silicon metal impurity formation. The surface of the synthesised $MgSiN_2$ powders indicate the presence of oxidised silicon, oxidised magnesium, unreacted Si_3N_4 along with the $MgSiN_2$ composition. A modification to the experiment was devised specifically to replace the magnesium lost via evaporation. Since the aim of this chapter is to investigate aluminium doping in $MgSiN_2$ structure, the effect of the magnesium excess on the phase purity was studied using 25% aluminium doped $MgSiN_2$. Therefore, the modified 25% aluminium doped $MgSiN_2$ synthesis involved varying the amounts of the magnesium reactant to 50%, 75% and 100%. A completely phase pure $MgSiN_2$ crystal structure was obtained with a magnesium excess of 100%, although slight peak broadening was observed, as per PXRD data. The unit cell volume was observed to be contracted by ~9 $Å^3$ with 50% magnesium excess, while an expansion by 5 $Å^3$ and 1 $Å^3$ was observed with 100% and 75% of magnesium excess respectively. This is potentially not caused by the incorporation of magnesium ions into the host lattice, but rather these magnesium ions would have replaced the magnesium lost via evaporation, reducing the chances of magnesiothermic reduction. This reasoning is justified by the observation of the unit cell volume of the sample with 100% magnesium excess being close to the sample with 0% magnesium excess by ± 1 $Å^3$. Although, the concentration of oxygen on the surface is reduced the most with 75% magnesium excess, as per XPS data. The concentration of magnesium is still lower than the stoichiometric ratio theoretically found in $MgSiN_2$ and is potentially caused by the surface-bound magnesium oxide. The effect of a higher aluminium content of 75% on the crystal structure and surface composition was also investigated using $MgSiN_2$ synthesised with 100% magnesium excess. While 25% aluminium content gave a crystal structure close to that of $MgSiN_2$, an aluminium content of 75% gave a crystal structure that is close to AlN-wurtzite. The effect of varying the aluminium content in the $MgSiN_2$ synthesised with 100% magnesium excess was investigated. The unit cell volume was observed to be decreased with increasing the aluminium content to at least 50%, which is potentially caused by the replacement of the larger Si^{4+} and Mg^{2+} ions with smaller Al^{3+} ions. However, the 75% aluminium

content gave unit cell volume that is larger than that with 50% aluminium. This is potentially caused by a larger proportion of Al^{2+} being incorporated into the host lattice, increasing the overall size of the unit cell. The effect on phase purity with the addition of varying amounts of magnesium in excess in $MgSiN_2$ powders with a high aluminium content is also being investigated. It was found that even at 100% magnesium excess a small PXRD peak corresponding to the silicon metal impurity is still observed. This could potentially mean that the high aluminium content potentially encourages Si_3N_4 reduction. A small variation in the aluminium content from 67% to 75% was found to not cause any changes to the crystal structure, although an increase in the unit cell volume by approximately 1 $Å^3$ was observed.

Chapter 10: Conclusions

High photocatalytic activity or high electrical conductivity are examples of functionality in materials. Optimisation of this functionality in any material can be achieved from modification of their atomic level properties such as structural, optical and electronic properties. This is reason why these atomic level properties were comprehensively studied in this thesis: in titania (single crystal substrate), titanates (powder) and $MgSiN_2$ (powders).

The main novelty in chapters 3 to 8 is the fundamental approach that has been taken towards studying the well-studied anion doping in titania. In these chapters, anionic doping was comprehensively studied in single crystal forms of titania rather than in their powder forms. The well-defined surface and a bulk that single crystal substrates offer is exploited here to achieve stable dopant distributions and is comprehensively studied here, which is challenging to do with powdered forms.

In chapters 3 to 8, the diffusion coefficients of the anions such as carbon, nitrogen and sulphur in Rutile single crystal substrates were determined using the aid of a high temperature solid-state method. While boron incorporation into rutile was observed predominantly as a thick epitaxial film of $TiBO_3$ composition, the carbon anions were found to be predominantly surface bound in C-C, C-O-C and C=O-C chemical environments. Only the nitrogen anion was observed to have a distinct diffusion gradient indicating the presence of nitrogen doped rutile, while the sulphur incorporation was observed to have a $TiOSO_4$ composition. The effect of this anionic diffusion across the depths of the rutile substrates of the orientations (110), (100) and (001) were also investigated. The $TiBO_3$ composition was found to be predominantly present in the (110) oriented substrate, while the $TiOSO_4$ composition was predominantly observed in the (100) orientation. These findings which detail the doping behaviour of anions in single crystal substrates of titania serve as effective models to understand the same in powders, which is otherwise challenging to study at present. It is important to study powders as they offer high surface area which single crystals are not able to offer. This makes powders relatively more efficient at photocatalysis. This is the contribution and impact that these findings have towards the direction of future work in this research area which is around doping in photocatalytic materials. The insights gained from these results can be used to optimise the photocatalytic functionality in powdered titania, which has a higher photoactivity than single crystals forms. This is the reason why powders are more

widely used in photocatalysis than single crystals. This is important as photocatalysis is used for increasing the efficiency of water splitting process, used to produce hydrogen, which is a ‘clean’ energy fuel.

Chapter 9 has a slightly different approach towards achieving a comprehensive study of doping. This chapter looks at studying the challenge of doping in powders, where structural framework of the powdered material, in this case titanates, is used as a scaffold to control dopant distributions achieved. This is an important step to take towards achieving stable dopant distributions and associated comprehensive study in powdered materials. Any future advanced characterisation equipment that revolutionise and make it easier to probe dopant distribution in powders will be complemented nicely by the findings of this chapter. The main findings of this chapter are detailed as follows. The effect of nitrogen doping temperature in the open layered and tunnelled titanate structures (to include: sodium and potassium hexatitanates, sodium trititanate and caesium titanate) were explored using a modification to the ammonolysis technique, which ensures that the samples being compared were synthesised using the same gas flow rate. Nitrogen was observed to take up different sites within the $K_2Ti_6O_{13}$ and $Cs_{0.68}T_{1.825}O_4$ structures, either coordinated to the alkali metal ion or Ti ion. These structures were also seen to have the least change in cell volume upon nitrogen incorporation. On the other hand, in $Na_2Ti_6O_{13}$ and $Na_2Ti_3O_7$ structures, the nitrogen was seen to be predominantly occupied into sites with a Ti coordination. The emergence of the Ti^{3+} defect species is evident in the optical absorption spectrum in TiO_2, $Na_2Ti_6O_{13}$ and $K_2Ti_6O_{13}$ while not in the other titanates and is potentially due to the lower nitrogen concentrations in them. Nitrogen has been observed to be incorporated into either the substitutional, interstitial, or both sites in all the titanates.

The findings, reported in chapters 9, on the doping behaviour in layered titanate powders can also be used as effective models to understand the same in powders, which is otherwise challenging to study at present as mentioned earlier. This is particularly relevant when the material being investigated is in its powdered form, with no well-defined surface or a bulk. This is the contribution and impact that these findings have towards the direction of future work in this research area which is around doping in photocatalytic materials. The main insight gained from chapter 9 is about making use of the structure of titanate materials (e.g. in open layered and tunnelled titanates) as a scaffold, to control the spatial distribution of any given dopant. While these relationships are widely reported in the literature already, the challenge that this

study addresses are about carrying out nitrogen doping at three different temperatures in the same system to ensure the same ammonia flow rate, which is a parameter that is often very challenging to reproduce. This ensures reproducibility of results and therefore reliability in the conclusions. Also, this study is also more comprehensive than that reported in literature the and discusses samples that are fully characterised. These findings are important in driving future research towards a comprehensive understanding of doping behaviours and preferences of doping in atomic structures, which are important in understanding the main things that are underpinning the efficiency in functionality of materials in general.

The effect of the addition of aluminium into the one pot synthesis of $MgSiN_2$ was investigated in chapter 10. Phase purity was observed along with changes in the unit cell volume with the addition of different amounts of magnesium in excess. While 25% aluminium content gave a crystal structure close to that of $MgSiN_2$, an aluminium content of 75% gave a crystal structure that is close to AlN-wurtzite. The unit cell volume was observed to be decreased with increasing the aluminium content to at least 50%, which is potentially caused by the replacement of the larger Si^{4+} and Mg^{2+} ions with smaller Al^{3+} ions. However, the 75% aluminium content gave unit cell volume that is larger than that with 50% aluminium. This is potentially caused by a larger proportion of Al^{3+} being incorporated into the host lattice, increasing the overall size of the unit cell.

The main insight gained from chapter 10 is about exploring the alternative material that can replace the expensive aluminium nitride, which is known to be a promising substrate material with ideal thermal conductivity and minimal dissipation of heat. This was done by studying the change in structural properties including associated unit cell volume. The effect of the addition of varying amounts of aluminium as a dopant into the $MgSiN_2$ structure, helped to find that the phase transformation from $MgSiN_2$ to AlN-wurtzite structure is observed between 30% and 50% aluminium dopant introduction, as per XPS and XRD. While the doubling of the magnesium reactant mass led to a single phase $MgSiN_2$, it can potentially affect particle size properties, as hinted by the XRD peak broadening observed. Increasing the aluminium content to above 50% led to unit cell volume contraction as Al^{3+} ions are smaller than the lattice Mg^{2+} ions they are substituting. These findings can help gain an understanding of the fundamental chemistry underpinning the development of cheaper, alternative materials for any applications.

References

[1] A. Fujishima, K. Honda, *Nature*, 1972, 238, 5358, 37-38.

[2] A. Fujishima, K. Honda, S. Kikuchi, *Journal of the Chemical Society of Japan*, 1969, 72, 108-113.

[3] K. Hashimoto, H. Irie, A. Fujishima, *Japanese Journal of Applied Physics*, 2005, 44, 12, 8269-8285.

[4] K.I. Hadjiivanov, D.G. Klissurski, *Chemical Society Reviews*, 1996, 25, 61-69.

[5] A.J. Nozik, R. Memming, *Journal of Physical Chemistry B*, 1996, 100, 31, 13061-13078.

[6] A.L. Linsebigler, G. Lu, J.T. Yates, *Chemical Reviews*, 1995, 95, 3, 735-758.

[7] O. Ola and M. Maroto-Valer, *Journal of Photochemistry and Photobiology C: Photochemistry Reviews*, 2015, 24, 16-42.

[8] K. Fujihara, T. Ohno, M. Matsumura, *Journal of the Chemical Society, Faraday Transactions*, 1998, 94, 3705-3709.

[9] X. Chen, S.S. Mao, *Chemical Reviews*, 2007, 107, 7, 2891-2959.

[10] V. Dal Santo and A. Naldoni, *Catalysts*, 2018, 8, 591.

[11] K. Ozawa, M. Emori, S. Yamamoto, R. Yukawa, S. Yamamoto, R. Hobara, K. Fujikawa, H. Sakama and I. Matsuda, The Journal of Physical Chemistry Letters, 2014, 5, 1953-1957.

[12] M. Plank, *Annals of Physics*, 1901, 4, 553.

[13] D. O. Scanlon, C. W. Dunnill, J. Buckeridge, S. A. Shevlin, A. J. Logsdail, S. M. Woodley, C. A. Catlow, M. J. Powell, R. G. Palgrave, I. P. Parkin, G. W. Watson, T. W. Keal, P. Sherwood, A. Walsh and A. A. Sokol, *Nature Materials*, 2013, 12, 798–801.

[14] J.C. Yu, J. Yu, W. Ho, *Chemistry of Materials*, 2002, 14, 3808-3816.

[15] A.L. Linsebigler, G. Lu, J.T. Yates, *Chemical Reviews*, 1995, 95, 735-758.

[16] M. Batzill, E.H. Morales, U. Diebold, *Physical Review Letters*, 2006, 96, 26103.

[17] T. Jafari, E. Moharreri, A. Amin, R. Miao, W. Song and S. Suib, *Molecules*, 2016, 21, 900.

[18] R. Fagan, D. McCormack, D. Dionysiou and S. Pillai, *Materials Science in Semiconductor Processing*, 2016, 42, 2-14.

[19] D. Cromer and K. Herrington, *Journal of the American Chemical Society*, 1955, 77, 4708-4709.

[20] M. Landmann, E. Rauls and W. Schmidt, *Journal of Physics: Condensed Matter*, 2012, 24, 195503.

[21] H. Machida and T. Fukuda, *Journal of Crystal Growth*, 1991, 112, 835-837.

[22] D. Hanaor and C. Sorrell, *Journal of Materials Science*, 2010, 46, 855-874.

[23] A. Lotnyk, S. Senz and D. Hesse, *Thin Solid Films*, 2007, 515, 3439-3447.

[24] T. Luttrell, S. Halpegamage, E. Sutter and M. Batzill, *Thin Solid Films*, 2014, 564, 146-155.

[25] G. Colón, M. Hidalgo and J. Navío, *Catalysis Today*, 2002, 76, 91-101.

[26] A. Ahmed, T. Kandiel, T. Oekermann and D. Bahnemann, *The Journal of Physical Chemistry Letters*, 2011, 2, 2461-2465.

[27] U. Diebold, *Surface Science Reports*, 2003, 48, 53-229.

[28] H. Hussain, G. Tocci, T. Woolcot, X. Torrelles, C. Pang, D. Humphrey, C. Yim, D. Grinter, G. Cabailh, O. Bikondoa, R. Lindsay, J. Zegenhagen, A. Michaelides and G. Thornton, *Nature Materials*, 2016, 16, 461-466.
[29] M. Ramamoorthy, D. Vanderbilt and R. King-Smith, *Physical Review B: Condensed Matter*, 1994, 49, 16721-16727.
[30] M. Li, W. Hebenstreit, L. Gross, U. Diebold, M. Henderson, D. Jennison, P. Schultz and M. Sears, *Surface Science*, 1999, 437, 173-190.
[31] F. Labat, P. Baranek and C. Adamo, *Journal of Chemical Theory and Computation*, 2008, 4, 341-352.
[32] Y. Ikuma, S. Ogoe, Y. Watanabe, K. Niwa, H. Tajiri and O. Sakata, *Journal of the Ceramic Society of Japan*, 2013, 121, 254-257.
[33] J. Nowotny, M. Abdul Alim, T. Bak, M. Asri Idris, M. Ionescu, K. Prince, M. Zainizan Sahdan, K. Sopian, M. Asri Mat Teridi and W. Sigmund, *Chemical society reviews*, 2015, 44, 8424-8442.
[34] T. Bak, J. Nowotny and M. Nowotny, *The Journal of Physical Chemistry B*, 2006, 110, 21560-21567.
[35] M. Nowotny, L. Sheppard, T. Bak and J. Nowotny, *The Journal of Physical Chemistry C*, 2008, 112, 5275-5300.
[36] T. Koketsu, J. Ma, B. Morgan, M. Body, C. Legein, W. Dachraoui, M. Giannini, A. Demortière, M. Salanne, F. Dardoize, H. Groult, O. Borkiewicz, K. Chapman, P. Strasser and D. Dambournet, *Nature Materials*, 2017, 16, 1142-1148.
[37] G. Herman, R. Zehr and M. Henderson, *Surface Science*, 2013, 612, L5-L8.
[38] Á. Morales-García, O. Lamiel-García, R. Valero and F. Illas, *The Journal of Physical Chemistry C*, 2018, 122, 2413-2421.
[39] J. Pask and A. Evans, *Ceramic microstructures '86: Role of surfaces*, Plenum Press, New York, 1988, 519-530.
[40] A. Fick, *Journal of Membrane Science*, 1995, 100, 33-38.
[41] G. Li, L. Chen, N. Dimitrijevic and K. Gray, *Chemical Physics Letters*, 2008, 451, 75-79.
[42] M. Pelaez, N. Nolan, S. Pillai, M. Seery, P. Falaras, A. Kontos, P. Dunlop, J. Hamilton, J. Byrne, K. O'Shea, M. Entezari and D. Dionysiou, *Applied Catalysis B: Environmental*, 2012, 125, 331-349.
[43] M. Nasirian, Y. Lin, C. Bustillo-Lecompte and M. Mehrvar, *International Journal of Environmental Science and Technology*, 2017, 15, 2009-2032.
[44] N. Serpone, *Journal of Physical Chemistry B*, 2006, 110, 24287-24293.
[45] R. Bacsa, J. Kiwi, T. Ohno, *Journal of Physical Chemistry B*, 2005, 109, 5994-6003
[46] T. Morikawa, R. Asahi, T. Ohwaki, K. Aoki and Y. Taga, *Japanese Journal of Applied Physics*, 2001, 40, L561-L563.
[47] O. Diwald, T. Thompson, T. Zubkov, E. Goralski, S. Walck and J. Yates, *ChemInform*, 2004, 35, 219-221.

[48] K. Matsubara, M. Danno, M. Inoue, Y. Honda, N. Yoshida and T. Abe, *Physical Chemistry Chemical Physics*, 2013, 15, 5097.
[49] M. Kitano, K. Funatsu, M. Matsuoka, M. Ueshima and M. Anpo, *The Journal of Physical Chemistry B*, 2006, 110, 25266-25272.
[50] Y. Tang, X. Huang, H. Yu and L. Tang, *International Journal of Photoenergy*, 2012, 1-10.
[51] X. Zhou, J. Lu, J. Jiang, X. Li, M. Lu, G. Yuan, Z. Wang, M. Zheng and H. Seo, *Nanoscale Research Letters*, 2014, 9, 34.
[52] F. Peng, L. Cai, L. Huang, H. Yu and H. Wang, *Journal of Physics and Chemistry of Solids*, 2008, 69, 1657-1664.
[53] G. Yang, Z. Jiang, H. Shi, T. Xiao and Z. Yan, *Journal of Materials Chemistry*, 2010, 20, 5301.
[54] T. Umebayashi, T. Yamaki, H. Itoh and K. Asai, *Applied Physics Letters*, 2002, 81, 454-456.
[55] C. Dunnill, Z. Aiken, A. Kafizas, J. Pratten, M. Wilson, D. Morgan and I. Parkin, *Journal of Materials Chemistry*, 2009, 19, 8747.
[56] C. Han, M. Pelaez, V. Likodimos, A. Kontos, P. Falaras, K. O'Shea and D. Dionysiou, *Applied Catalysis B: Environmental*, 2011, 107, 77-87.
[57] H. Irie, Y. Watanabe and K. Hashimoto, *Chemistry Letters*, 2003, 32, 772-773.
[58] J. Park, S. Kim and A. Bard, *Nano Letters*, 2006, 6, 24-28.
[59] W. Ren, Z. AI, F. Jia, L. Zhang, X. Fan and Z. Zou, *Applied Catalysis B: Environmental*, 2007, 69, 138-144.
[60] N. Rao Neti, R. Misra, P. Kumar Bera, R. Dhodapkar, S. Bakardjieva and Z. Bastl, *Synthesis and Reactivity in Inorganic, Metal-Organic, and Nano-Metal Chemistry*, 2010, 40, 328-332.
[61] G. Wu, T. Nishikawa, B. Ohtani and A. Chen, *Chemistry of Materials*, 2007, 19, 4530-4537.
[62] S. Shen, T. Yang and M. Wong, *Surface and Coatings Technology*, 2016, 303, 184-190.
[63] D. Chen, D. Yang, Q. Wang and Z. Jiang, *Industrial & Engineering Chemistry Research*, 2006, 45, 4110-4116.
[64] C. Carlucci, B. Scremin, T. Sibillano, C. Giannini, E. Filippo, P. Perulli, A. Capodilupo, G. Corrente and G. Ciccarella, *Inorganics*, 2014, 2, 264-277.
[65] M. Quesada-González, K. Baba, C. Sotelo-Vázquez, P. Choquet, C. Carmalt, I. Parkin and N. Boscher, *Journal of Materials Chemistry A*, 2017, 5, 10836-10842.
[66] L. Li, Y. Yang, X. Liu, R. Fan, Y. Shi, S. Li, L. Zhang, X. Fan, P. Tang, R. Xu, W. Zhang, Y. Wang and L. Ma, *Applied Surface Science*, 2013, 265, 36-40.
[67] S. Ansari, M. Khan, M. Ansari and M. Cho, *ChemInform*, 2016, 47.
[68] M. Ceotto, L. Lo Presti, G. Cappelletti, D. Meroni, F. Spadavecchia, R. Zecca, M. Leoni, P. Scardi, C. L. Bianchi and S. Ardizzone, *The Journal of Physical Chemistry C*, 2012, 116, 1764–1771.
[69] H. Zhao, F. Pan and Y. Li, *Journal of Materiomics*, 2017, 3, 17-32.

[70] B. Viswanathan and K. Krishanmurthy, *International Journal of Photoenergy*, 2012, 1-10.
[71] C. Di Valentin, G. Pacchioni and A. Selloni, *The Journal of Physical Chemistry C*, 2009, 113, 20543-20552.
[72] A. Aronne, M. Fantauzzi, C. Imparato, D. Atzei, L. De Stefano, G. D'Errico, F. Sannino, I. Rea, D. Pirozzi, B. Elsener, P. Pernice and A. Rossi, *RSC Advances*, 2017, 7, 2373-2381.
[73] J. Alexander, Surface modifications and growth of titanium dioxide for photo-electrochemical water splitting, *Springer International Publishing*, Switzerland, 1, 2018.
[74] M. Batzill, E. Morales and U. Diebold, *Chemical Physics*, 2007, 339, 36-43.
[75] R. Asahi, *Science*, 2001, 293, 269-271.
[76] D. Shieh, Y. Lin, J. Yeh, S. Chen, B. Lin and J. Lin, *Chemical Communications*, 2012, 48, 2528.
[77] C. Di Valentin, G. Pacchioni, A. Selloni, S. Livraghi and E. Giamello, *The Journal of Physical Chemistry B*, 2005, 109, 11414-11419.
[78] J. Chai, M. Yang, Q. Chen, J. Pan, Z. Zhang, Y. Feng and S. Wang, *Journal of Applied Physics*, 2011, 109, 023707.
[79] R. Grau-Crespo and U. Schwingenschlögl, *Journal of Physics: Condensed Matter*, 2011, 23, 334216.
[80] G. Yang, Z. Jiang, H. Shi, T. Xiao and Z. Yan, *Journal of Materials Chemistry*, 2010, 20, 5301.
[81] J. Wang, K. Tapio, A. Habert, S. Sorgues, C. Colbeau-Justin, B. Ratier, M. Scarisoreanu, J. Toppari, N. Herlin-Boime and J. Bouclé, *Nanomaterials*, 2016, 6, 35.
[82] K. Yang, Y. Dai and B. Huang, *The Journal of Physical Chemistry C*, 2007, 111, 12086-12090.
[83] S. Livraghi, M. Paganini, E. Giamello, A. Selloni, C. Di Valentin and G. Pacchioni, *Journal of the American Chemical Society*, 2006, 128, 15666-15671.
[84] S. Cheung, P. Nachimuthu, A. Joly, M. Engelhard, M. Bowman and S. Chambers, *Surface Science*, 2007, 601, 1754-1762.
[85] J. Lynch, C. Giannini, J. Cooper, A. Loiudice, I. Sharp and R. Buonsanti, *The Journal of Physical Chemistry C*, 2015, 119, 7443-7452.
[86] S. Sato, *Chemical Physics Letters*, 1986, 123, 126-128.
[87] R. Asahi, T. Morikawa, H. Irie and T. Ohwaki, *Chemical Reviews*, 2014, 114, 9824-9852.
[88] M. Powell, R. Palgrave, C. Dunnill and I. Parkin, *Thin Solid Films*, 2014, 562, 223-228.
[89] R. Palgrave, D. Payne and R. Egdell, *Journal of Materials Chemistry*, 2009, 19, 8418.
[90] A. Breeson, G. Sankar, G. Goh and R. Palgrave, *Physical Chemistry Chemical Physics*, 2016, 18, 24722-24728.
[91] S. Cheung, P. Nachimuthu, M. Engelhard, C. Wang and S. Chambers, *Surface Science*, 2008, 602, 133-141.
[92] 12.I. Takahashi, D. Payne, R. Palgrave and R. Egdell, *Chemical Physics Letters*, 2008, 454, 314-317.
[93] L. Devi and R. Kavitha, *Materials Chemistry and Physics*, 2014, 143, 1300-1308.

[94] M. Smith, K. Setwong, R. Tongpool, D. Onkaw, S. Na-phattalung, S. Limpijumnong and S. Rujirawat, *Applied Physics Letters*, 2007, 91, 142107.
[95] L. Szatmáry, S. Bakardjieva, J. Šubrt, P. Bezdička, J. Jirkovský, Z. Bastl, V. Brezová and M. Korenko, *Catalysis Today*, 2011, 161, 23-28.
[96] T. Yamamoto, F. Yamashita, I. Tanaka, E. Matsubara and A. Muramatsu, *Materials Transactions*, 2004, 45, 1987-1990.
[97] T. Yamamoto, F. Yamashita, I. Tanaka, E. Matsubara and A. Muramatsu, *Materials Transactions*, 2004, 45, 1987-1990.
[98] R. Klaysri, M. Ratova, P. Praserthdam and P. Kelly, *Nanomaterials*, 2017, 7, 113.
[99] J. González-Torres, E. Poulain, V. Domínguez-Soria, R. García-Cruz and O. Olvera-Neria, *International Journal of Photoenergy*, 2018, 2018, 1-12.
[100] N. Patel, A. Dashora, R. Jaiswal, R. Fernandes, M. Yadav, D. Kothari, B. Ahuja and A. Miotello, *The Journal of Physical Chemistry C*, 2015, 119, 18581-18590.
[101] P. Carmichael, D. Hazafy, D. Bhachu, A. Mills, J. Darr and I. Parkin, *Physical Chemistry Chemical Physics*, 2013, 15, 16788.
[102] I. Grey, C. Li, C. MacRae and L. Bursill, *Journal of Solid-State Chemistry*, 1996, 127, 240-247.
[103] V. Gombac, L. De Rogatis, A. Gasparotto, G. Vicario, T. Montini, D. Barreca, G. Balducci, P. Fornasiero, E. Tondello and M. Graziani, *Chemical Physics*, 2007, 339, 111-123.
[104] S. In, A. Orlov, R. Berg, F. García, S. Pedrosa-Jimenez, M. S. Tikhov, D. S. Wright and R. M. Lambert, *Journal of the American Chemical Society*, 2007, 129, 13790–13791.
[105] R. Aziz, I. Misnon, K. Chong, M. Yusoff and R. Jose, *Electrochimica Acta*, 2013, 113, 141-148.
[106] L. Pauling and J. Sturdivant, *Zeitschrift für Kristallographie - Crystalline Materials*, 1928, 68.
[107] D. V. Bavykin and F. C. Walsh, *Materials Today*, 2010, 13, 66.
[108] B. Zhao, L. Lin and D. He, *Journal of Materials Chemistry A*, 2013, 1, 1659-1668.
[109] G. Liu, L. Wang, C. Sun, Z. Chen, X. Yan, L. Cheng, H. Cheng and G. Lu, *Chemical Communications*, 2009, 1383.
[110] H. Liu, D. Yang, Z. Zheng, X. Ke, E. Waclawik, H. Zhu and R. Frost, *Journal of Raman Spectroscopy*, 2010, 41, 1331-1337.
[111] T. Gao, H. Fjellvåg and P. Norby, *The Journal of Physical Chemistry B*, 2008, 112, 9400-9405
[112] A. Araújo-Filho, F. Silva, A. Righi, M. da Silva, B. Silva, E. Caetano and V. Freire, *Journal of Solid-State Chemistry*, 2017, 250, 68-74.
[113] K. Cao, L. Jiao, W. Pang, H. Liu, T. Zhou, Z. Guo, Y. Wang and H. Yuan, *Small*, 2016, 12, 2991-2997.
[114] S. Andersson and A. Wadsley, *Acta Crystallographica*, 1962, 15, 194-201.
[115] H. Cid-Dresdner and M. Buerger, *Zeitschrift für Kristallographie - Crystalline Materials*, 1962, 117, 411-430.

[116] H. He, W. Yao, C. Wang, X. Feng and X. Lu, *Industrial & Engineering Chemistry Research*, 2013, 52, 15034-15040.
[117] A. Sauvet, S. Baliteau, C. Lopez and P. Fabry, *Journal of Solid-State Chemistry*, 2004, 177, 4508-4515.
[118] 2.K. Sardar and R. Walton, *ChemInform*, 2012, 43, 32-37.
[119] Y. Nosaka, M. Matsushita, J. Nishino and A. Nosaka, *Science and Technology of Advanced Materials*, 2005, 6, 143-148.
[120] G. Liu, L. Wang, C. Sun, X. Yan, X. Wang, Z. Chen, S. Smith, H. Cheng and G. Lu, *Chemistry of Materials*, 2009, 21, 1266-1274.
[121] 4.R. Khanna, S. Yamaguchi, A. Valanezhad, T. Kokubo, T. Matsushita, Y. Naruta and H. Takadama, *Journal of Materials Chemistry A*, 2014, 2, 1809-1817.
[122] B. Buchholcz, K. Plank, M. Mohai, Á. Kukovecz, J. Kiss, I. Bertóti and Z. Kónya, *Topics in Catalysis*, 2018, 61, 1263-1273.
[123] G. Liu, P. Niu, L. Wang, G. Lu and H. Cheng, *Catalysis Science & Technology*, 2011, 1, 222.
[124] B. Buchholcz, E. Varga, T. Varga, K. Plank, J. Kiss and Z. Kónya, *Vacuum*, 2017, 138, 120-124.
[125] S. Nishioka and K. Maeda, *ChemInform*, 2016, 47, 100123-100128.
[126] R. J. Bruls, H. T. Hintzen and R. Metselaar, *Journal of Materials Science*, 1999, 34, 4519-4531.
[127] J. Yang, J. Qiu and J. Li, *Ceramics International*, 2011, 37, 673-677.
[128] Z. Lenčéš, K. Hirao, Y. Yamauchi and S. Kanzaki, *Journal of the American Ceramic Society*, 2003, 86, 1088-1093.
[129] J. Rivière and M. Sverre, *Handbook of Surface and Interface Analysis: Methods for Problem-Solving*, Taylor and Francis, CRC Press, 2nd edn., 2009.
[130] 4.D. Woodruff and T. Delchar, Modern techniques of surface science, *Cambridge University Press*, 2nd edn., 1986.
[131] T. Wang, B. Daiber, J. Frost, S. Mann, E. Garnett, A. Walsh and B. Ehrler, *Energy & Environmental Science*, 2017, 10, 509-515.
[132] M. Seah and T. Nunney, *Journal of Physics D: Applied Physics*, 2010, 43, 253001.
[133] J. Miller, S. Veeramasuneni, J. Drelich, M. Yalamanchili and G. Yamauchi, *Polymer Engineering & Science*, 1996, 36, 1849-1855.
[134] B. Comer and A. Medford, *ACS Sustainable Chemistry & Engineering*, 2018, 6, 4648-4660.
[135] V. Swamy, B. Muddle and Q. Dai, *Applied Physics Letters*, 2006, 89, 163118.
[136] Y. Zhang, C. Harris, P. Wallenmeyer, J. Murowchick and X. Chen, *The Journal of Physical Chemistry C*, 2013, 117, 24015-24022.
[137] H. Xu, S. Xu, H. Wang and H. Yan, *Journal of The Electrochemical Society*, 2005, 152, C803.
[138] U. Balachandran and N. G.Eror, *Journal of Solid State Chemistry*, 1982, 42, 276-282.

[139] J. Šebek, L. Pele, E. Potma and R. Benny Gerber, *Physical Chemistry Chemical Physics*, 2011, 13, 12724.
[140] A. Ryder, M. Przyjalgowski, M. Feely, B. Szczupak and T. Glynn, *Applied Spectroscopy*, 2004, 58, 1106-1115.
[141] I. Dreiling, C. Raisch, J. Glaser, D. Stiens and T. Chassé, *Wear*, 2012, 288, 62-71.
[142] A. Kumar Yadav and P. Singh, *RSC Advances*, 2015, 5, 67583-67609.
[143] F. Galeener, G. Lucovsky and J. Mikkelsen, *Physical Review B*, 1980, 22, 3983-3990.
[144] W. Baur and A. Khan, *Acta Crystallographica Section B Structural Crystallography and Crystal Chemistry*, 1971, 27, 2133-2139.
[145] M. Huber and H. Deiseroth, *Zeitschrift für Kristallographie - Crystalline Materials*, 1995, 210.
[146] M. Horn, C. Schwebdtfeger and E. Meagher, *Zeitschrift für Kristallographie - Crystalline Materials*, 1972, 136.
[147] C. Sanchez, H. Fonseca-Filho, M. Maia da Costa and F. Freire, *Thin Solid Films*, 2009, 517, 5683-5688.
[148] M. Quesada-González, N. Boscher, C. Carmalt and I. Parkin, *ACS Applied Materials & Interfaces*, 2016, 8, 25024-25029.
[149] C. Sanchez, B. Plata, M. da Costa and F. Freire, *Surface and Coatings Technology*, 2011, 205, 3698-3702.
[150] F. Huang, W. Liu, J. Sullivan, J. Barnard and M. Weaver, *Journal of Materials Research*, 2002, 17, 805-813.
[151] N. Feng, F. Liu, M. Huang, A. Zheng, Q. Wang, T. Chen, G. Cao, J. Xu, J. Fan and F. Deng, *Scientific Reports*, 2016, 6, 34765.
[152] G. Liu, J. Pan, L. Yin, J. Irvine, F. Li, J. Tan, P. Wormald and H. Cheng, *Advanced Functional Materials*, 2012, 22, 3233-3238.
[153] X. Li, Z. Guo and T. He, *Physical Chemistry Chemical Physics*, 2013, 15, 20037.
[154] F. Werfel and O. Brümmer, Physica Scripta, 1983, 28, 92-96.
[155] D. Zatsepin, D. Boukhvalov, E. Kurmaev, N. Gavrilov, S. Kim and I. Zhidkov, *Applied Surface Science*, 2016, 379, 223-229.
[156] G. Vásquez, D. Maestre, A. Cremades, J. Ramírez-Castellanos, E. Magnano, S. Nappini and S. Karazhanov, *Scientific Reports*, 2018, 8, 8740.
[157] G. Liu, W. Jaegermann, J. He, V. Sundström and L. Sun, *The Journal of Physical Chemistry B*, 2002, 106, 5814-5819.
[158] J. Surmacki, P. Wroński, M. Szadkowska-Nicze and H. Abramczyk, *Chemical Physics Letters*, 2013, 566, 54-59.
[159] E. Restrepo Parra, P. Jose Arango Arango and V. Javier Benavides Palacio, *Dyna-Colombia*, 2010, 77, 64-74.
[160] G. Greczynski and L. Hultman, *ChemPhysChem*, 2017, 18, 1507-1512.
[161] P. Lackner, Z. Zou, S. Mayr, U. Diebold and M. Schmid, *Physical Chemistry Chemical Physics*, 2019, 21, 17613-17620.

[162] F. Werfel and O. Brümmer, *Physica Scripta*, 1983, 28, 92-96.
[163] V. Allodi, S. Brutti, M. Giarola, M. Sgambetterra, M. Navarra, S. Panero and G. Mariotto, *Polymers*, 2016, 8, 68.
[164] K. Joseph Antony Raj, R. Shanmugam, R. Mahalakshmi and B. Viswanathan, *Indian Journal of Chemistry*, 2010, 49-A, 9-17.
[165] D. Gonbeau, C. Guimon, G. Pfister-Guillouzo, A. Levasseur, G. Meunier and R. Dormoy, *Surface Science Letters*, 1991, 254, A476.
[166] N. Moustakas, A. Kontos, V. Likodimos, F. Katsaros, N. Boukos, D. Tsoutsou, A. Dimoulas, G. Romanos, D. Dionysiou and P. Falaras, *Applied Catalysis B: Environmental*, 2013, 130-131, 14-24.
[167] X. Zhou, J. Lu, J. Jiang, X. Li, M. Lu, G. Yuan, Z. Wang, M. Zheng and H. Seo, *Nanoscale Research Letters*, 2014, 9, 34.
[168] B. Naik, K. Parida and C. Gopinath, *The Journal of Physical Chemistry C*, 2010, 114, 19473-19482.
[169] F. Peng, L. Cai, L. Huang, H. Yu and H. Wang, *Journal of Physics and Chemistry of Solids*, 2008, 69, 1657-1664.
[170] J. Pérez-Flores, F. García-Alvarado, M. Hoelzel, I. Sobrados, J. Sanz and A. Kuhn, Dalton Transactions, 2012, 41, 14633.
[171] O. Yakubovich and V. Kireev, Crystallography Reports, 2003, 48, 24-28.
[172] P. Ponce-Peña, M. González-Lozano, M. Escobedo-Bretado, P. de Lira-Gómez, E. García-Sánchez, E. Rivera and L. Alexandrova, *Ceramics International*, 2015, 41, 10051-10056.
[173] S. Andersson and A. Wadsley, *Acta Crystallographica*, 1961, 14, 1245-1249.
[174] I. E.Grey, C. Li, C. Madsen and J. A.Watts, *Journal of Solid-State Chemistry*, 1986, 66, 7-19.
[175] A. Weibel, R. Bouchet, F. Boulc' and P. Knauth, Chemistry of Materials, 2005, 17, 2378-2385.
[176] C. Bamberger and G. Begun, *Journal of the American Ceramic Society*, 1987, 70, C-48-C-51.
[177] W. Hou, Z. Shen, J. Miao, L. Li and W. Su, *Journal of Raman Spectroscopy*, 2000, 31, 391-394.
[178] C. Bamberger and G. Begun, *Journal of the American Ceramic Society*, 1987, 70, C-48-C-51.
[179] Z. Zhang, J. Goodall, S. Brown, L. Karlsson, R. Clark, J. Hutchison, I. Rehman and J. Darr, *Dalton Transactions*, 2010, 39, 711-714.
[180] G. Liu, P. Niu, L. Wang, G. Lu and H. Cheng, *Catalysis Science & Technology*, 2011, 1, 222.
[181] R. Gundeboina, N. Veldurthi, R. Velchuri, R. Guje, S. Pola, V. Muga and M. Nagegownivari R, *International Journal of Applied Ceramic Technology*, 2014, 12, 700-710.

[182] S. Valencia, J. Marín and G. Restrepo, *The Open Materials Science Journal*, 2010, 4, 9-14.

[183] Database of ionic radii, Atomic Simulation Group, Imperial College London, *https://www.chemguide.co.uk/atoms/properties/atradius.html*, Accessed on 23 November 2019

[184] K. Choi, H. Choi and I. Sohn, *Metallurgical and Materials Transactions B*, 2017, 48, 922-932.

[185] R. Bruls, H. Hintzen, R. Metselaar and C. Loong, *Journal of Physics and Chemistry of Solids*, 2000, 61, 1285-1293.

[186] R. Bruls, H. Hintzen and R. Metselaar, *Journal of Materials Science*, 1999, 34, 4519 – 4531.

[187] A. Guleria, S. Neogy, D. Maurya and S. Adhikari, *The Journal of Physical Chemistry C*, 2017, 121, 24302-24316.

[188] S. Aksoy, Y. Caglar, S. Ilican and M. Caglar*, Journal of Alloys and Compounds*, 2012, 512, 171-178

[189] H. Lu, Y. Huang, A. Lee and J. Huang, *Ceramics International*, 2014, 40, 14313-14317.

[190] J. Taylor and J. Rabalais, *The Journal of Chemical Physics*, 1981, 75, 1735-1745.

[191] Y. Kim, H. Park, J. Chun and W. Lee, *Thin Solid Films*, 1994, 237, 57-65.

Appendices

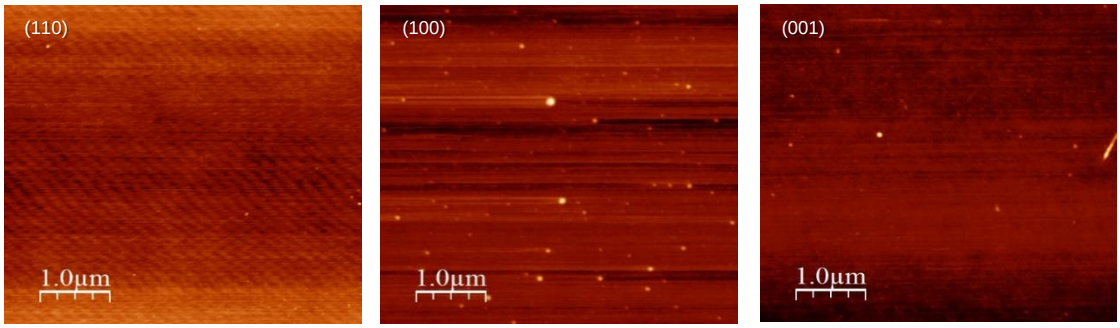

Figure A: AFM images showing the surfaces of the as-received rutile substrates (110), (100) and (001)

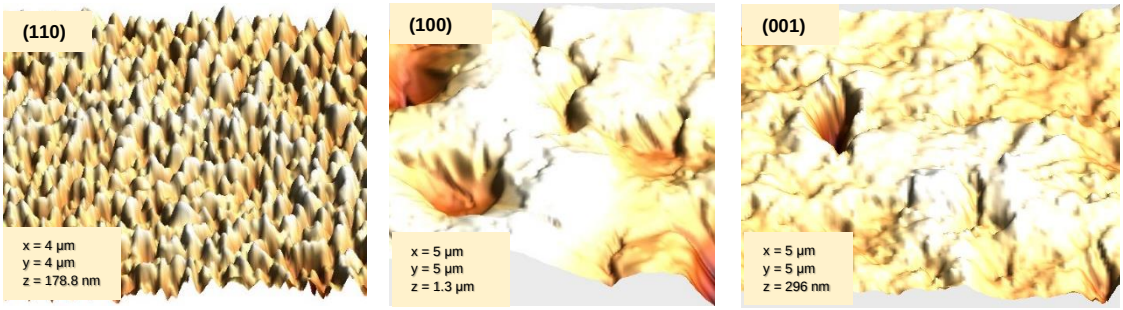

Figure B: AFM images in three-dimension, showing the roughening of the TiB_2 treated rutile substrates (110), (100) and (001)

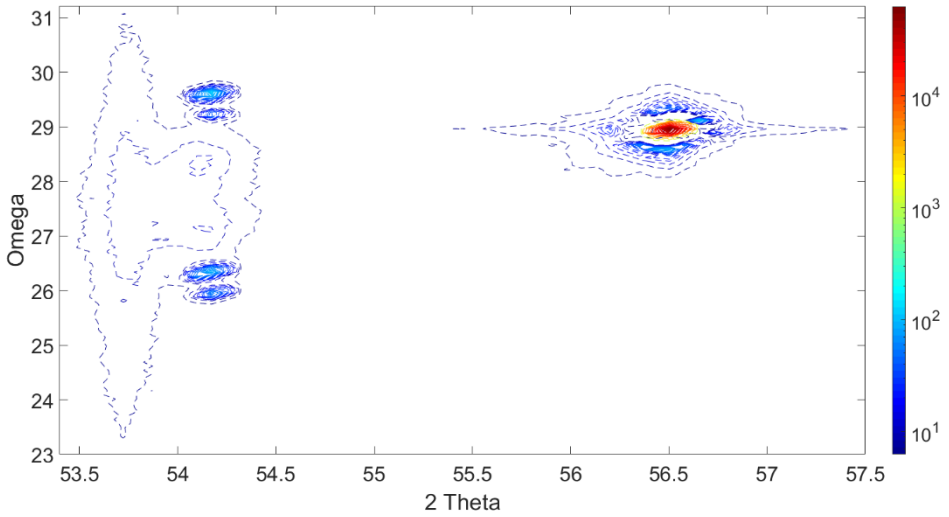

Figure C: Reciprocal space map of the TiB_2 treated rutile (110) substrate on an extended scale

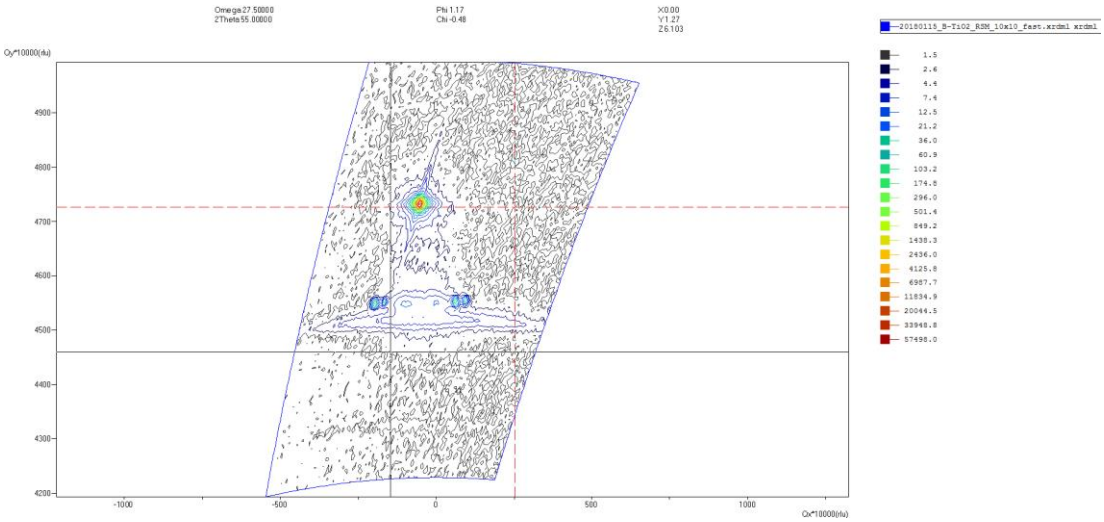

Figure D: Raw data collected of the reciprocal space map of the TiB_2 treated rutile (110) substrate

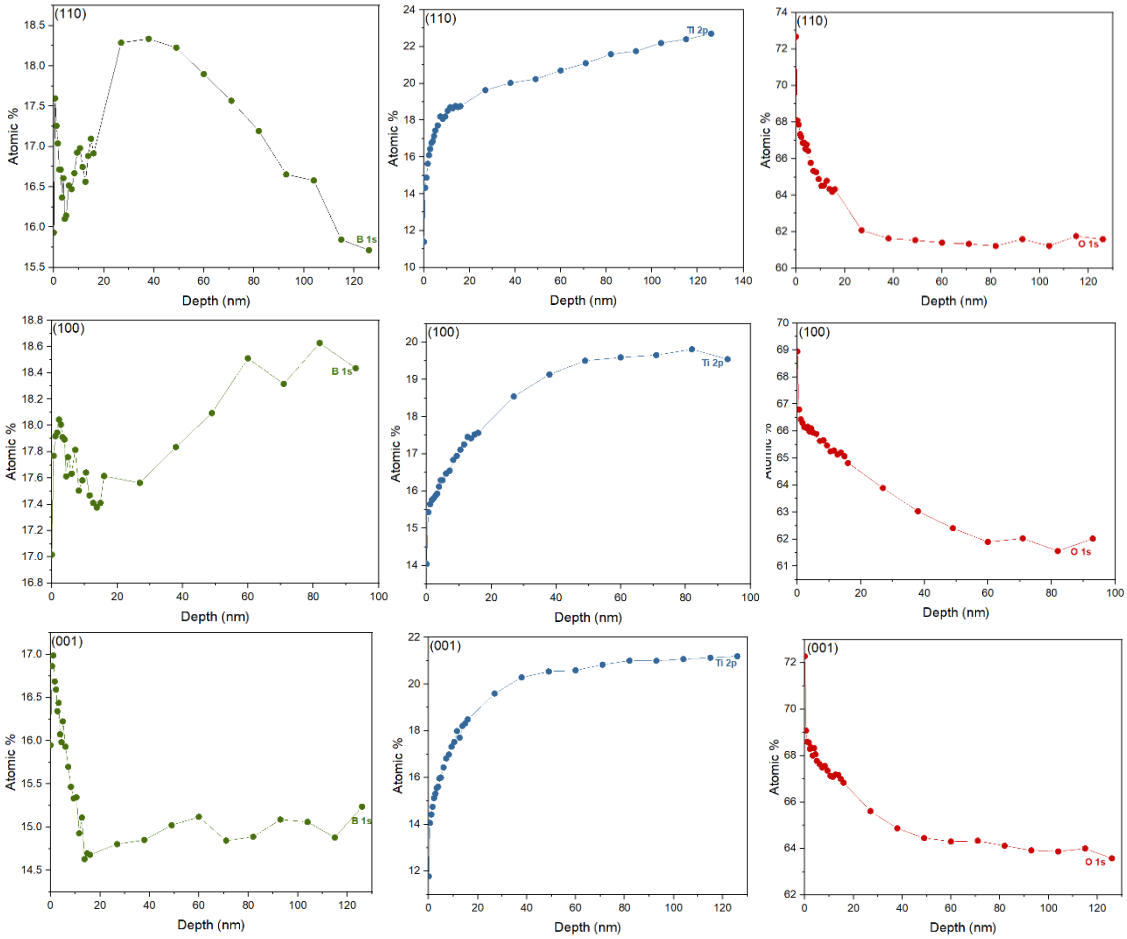

Figure E: XPS depth profiles of the principal core lines of (110), (100) and (001) single crystal substrates of rutile treated with TiB_2

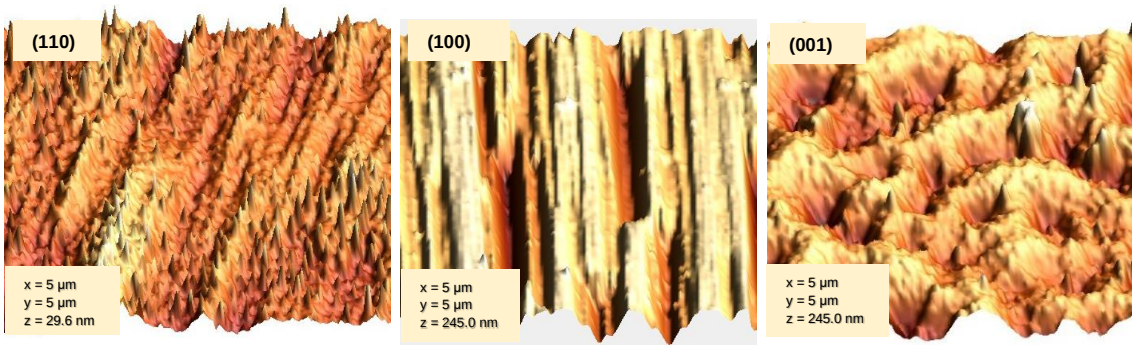

Figure F: AFM images in three-dimension, showing the roughening of the TiC treated rutile substrates (110), (100) and (001)

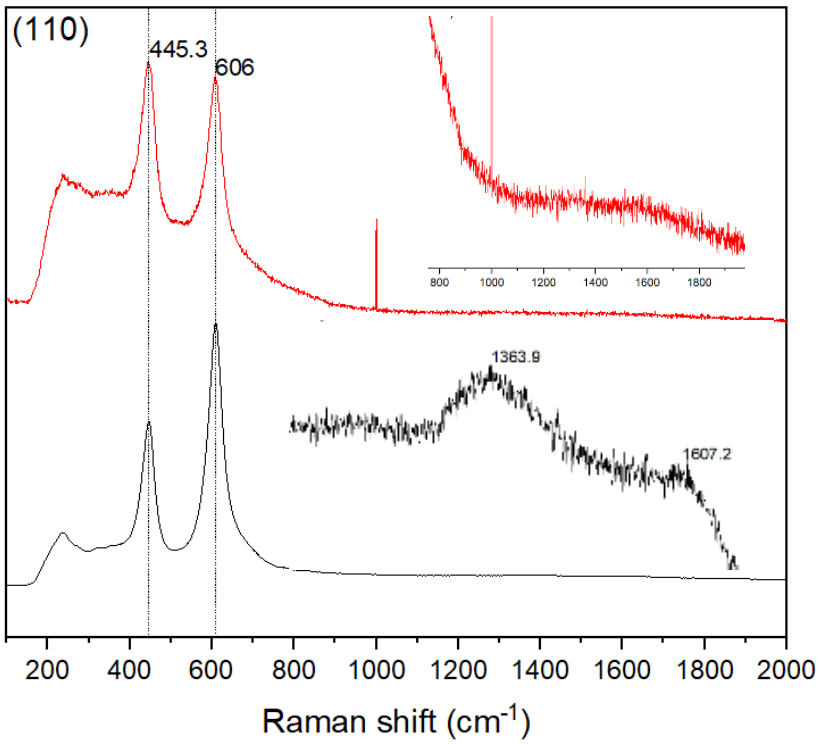

Figure G: Raman spectrum of the TiC treated rutile substrates of the orientation (110)

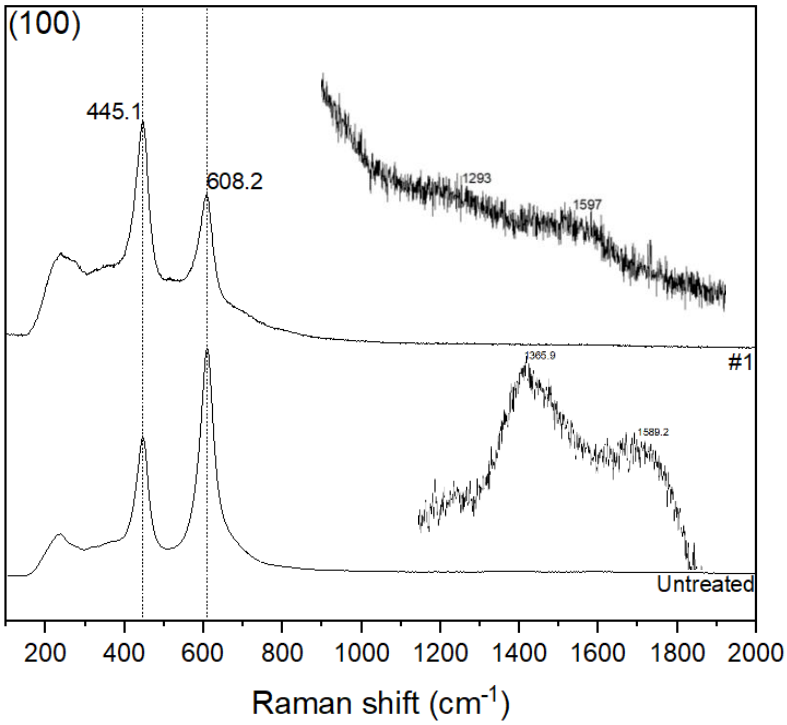

Figure H: Raman spectrum of the TiC treated rutile substrates of the orientation (100)

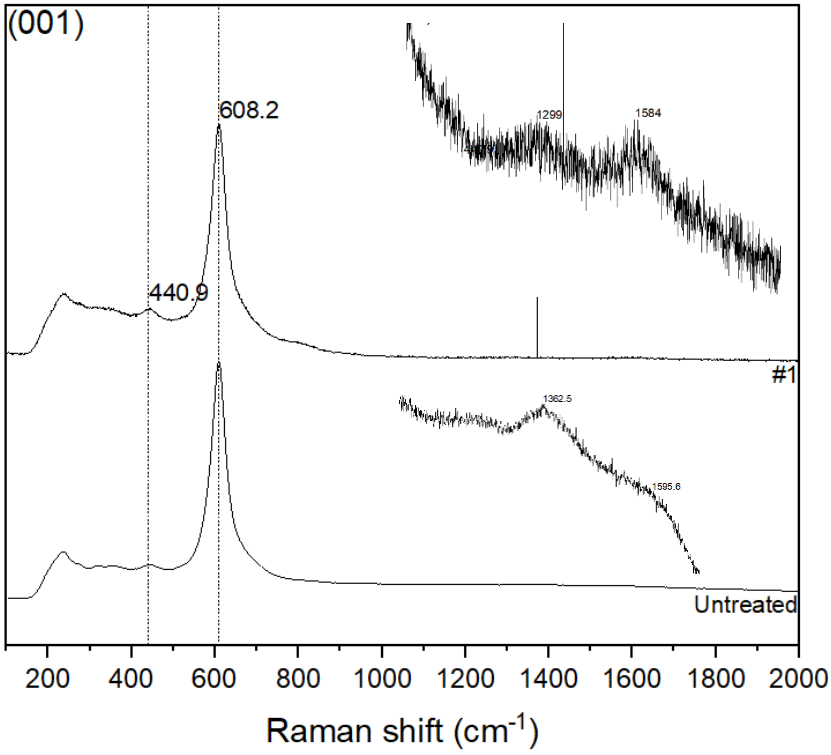

Figure I: Raman spectrum of the TiC treated rutile substrates of the orientation (001)

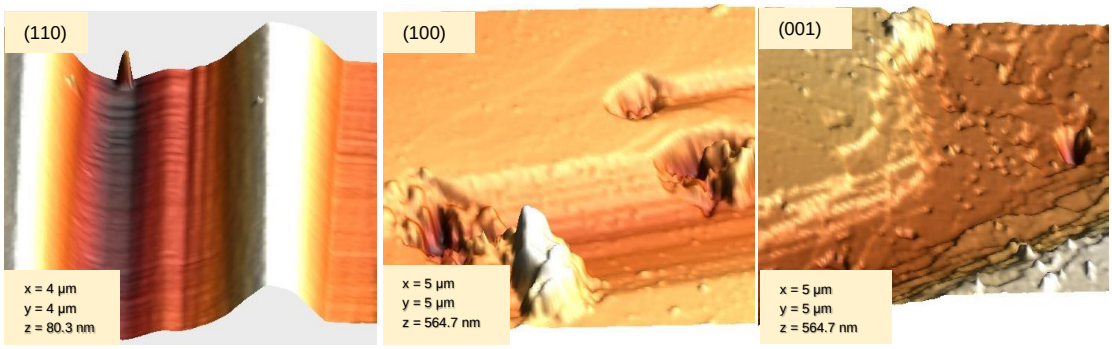

Figure J: AFM images in three-dimension, showing the roughening of the TiS_2 treated rutile substrates (110), (100) and (001)

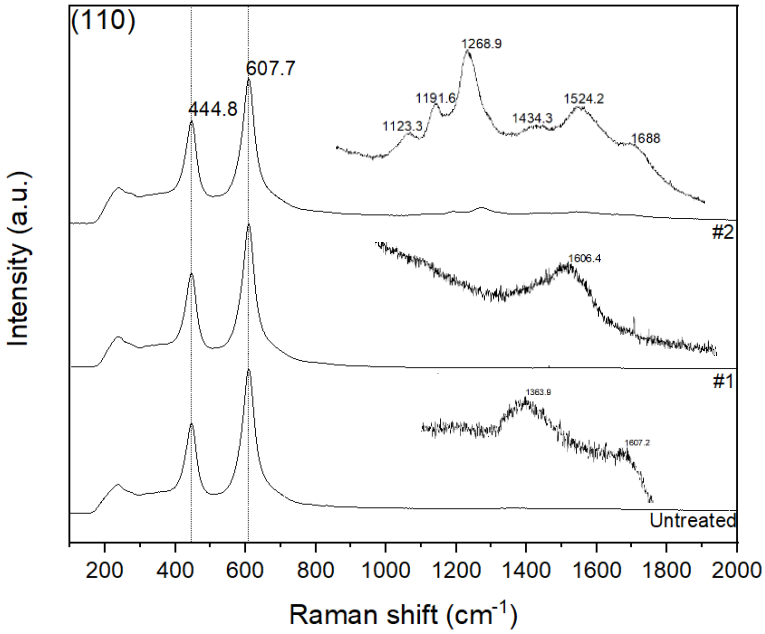

Figure K: Raman spectrum of the TiS_2 treated rutile (110) substrate, where #1 and #2 indicates different areas on the same substrate surface

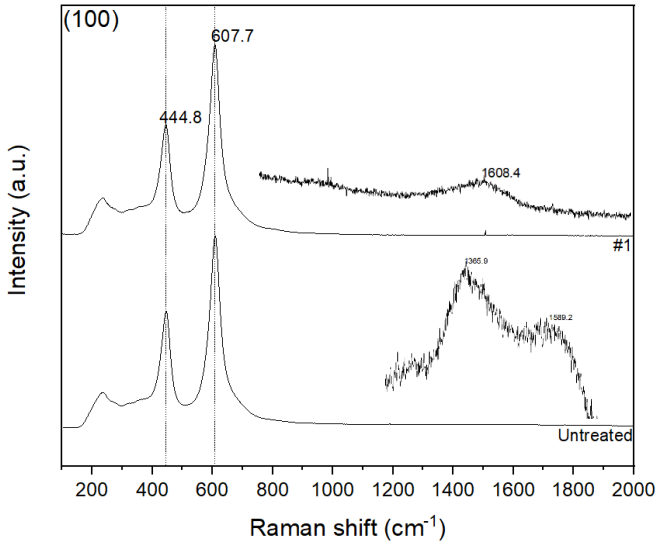

Figure L: Raman spectrum of the TiS_2 treated rutile (100) substrate

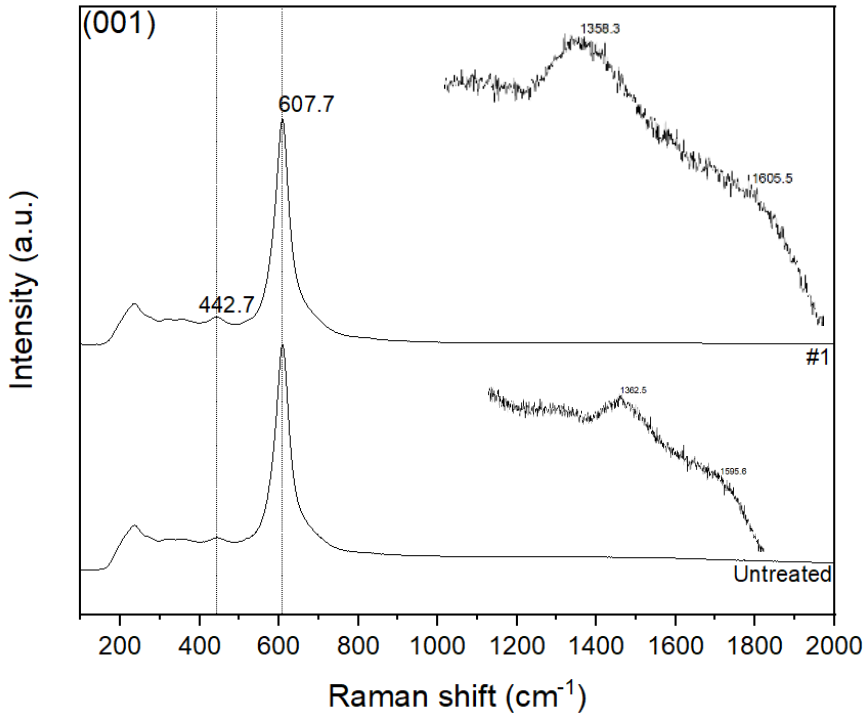

Figure M: Raman spectrum of the TiS_2 treated rutile (001) substrate

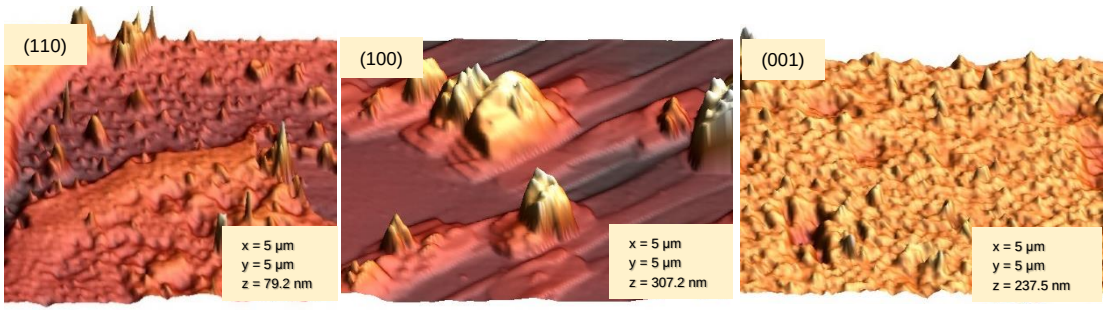

Figure N: AFM images in three-dimension, showing the roughening of the TiN treated rutile substrates (110), (100) and (001)

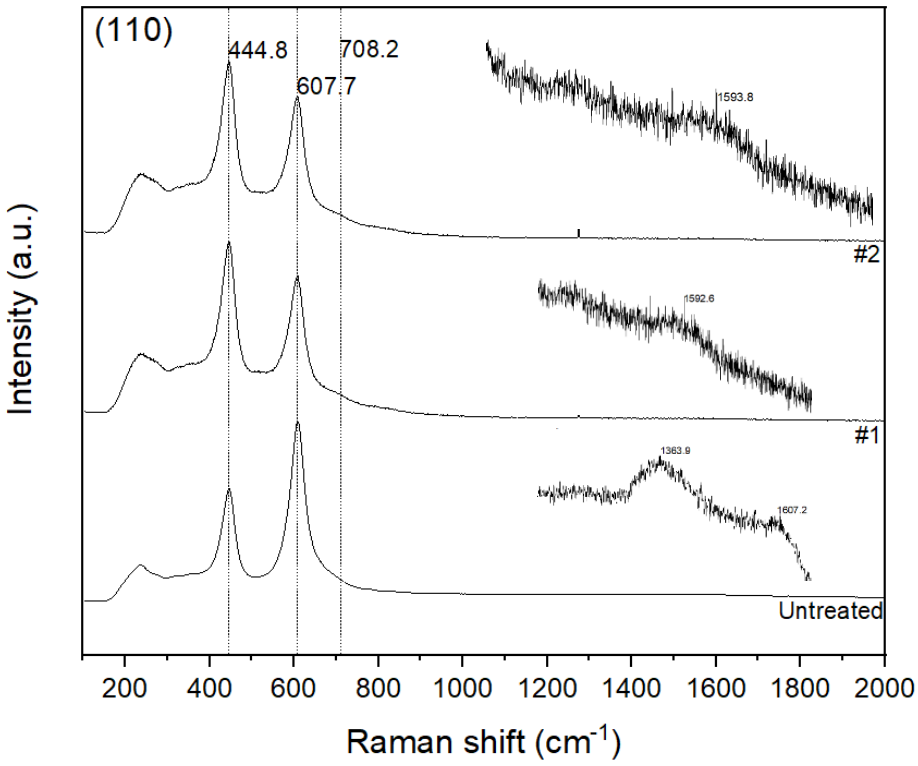

Figure O: Raman spectrum of the TiN treated rutile (110) substrate, where #1 and #2 indicates different areas on the same substrate surface

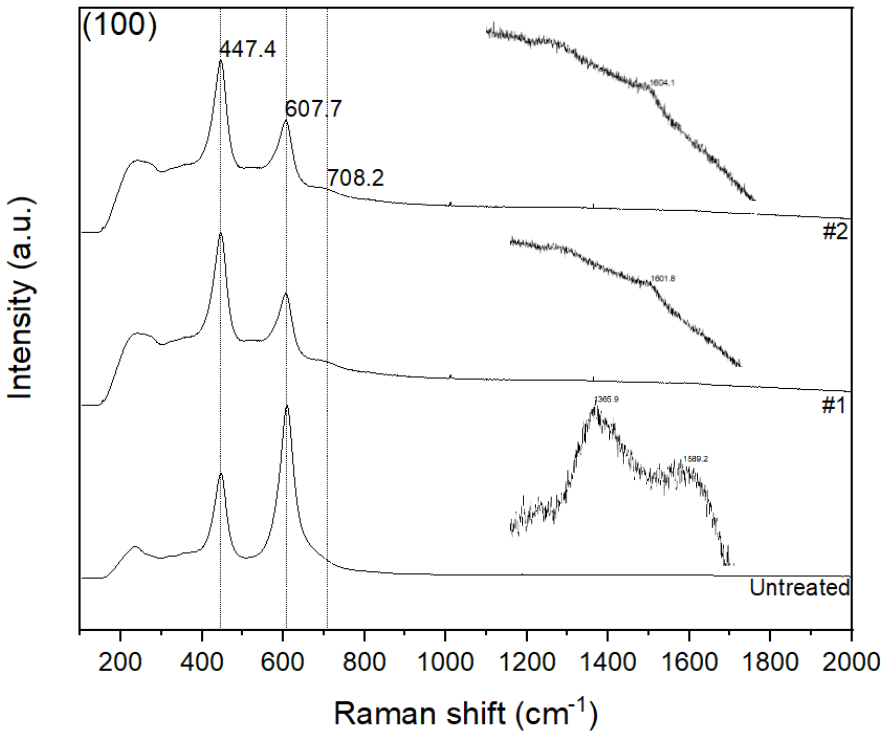

Figure P: Raman spectrum of the TiN treated rutile (100) substrate, where #1 and #2 indicates different areas on the same substrate surface

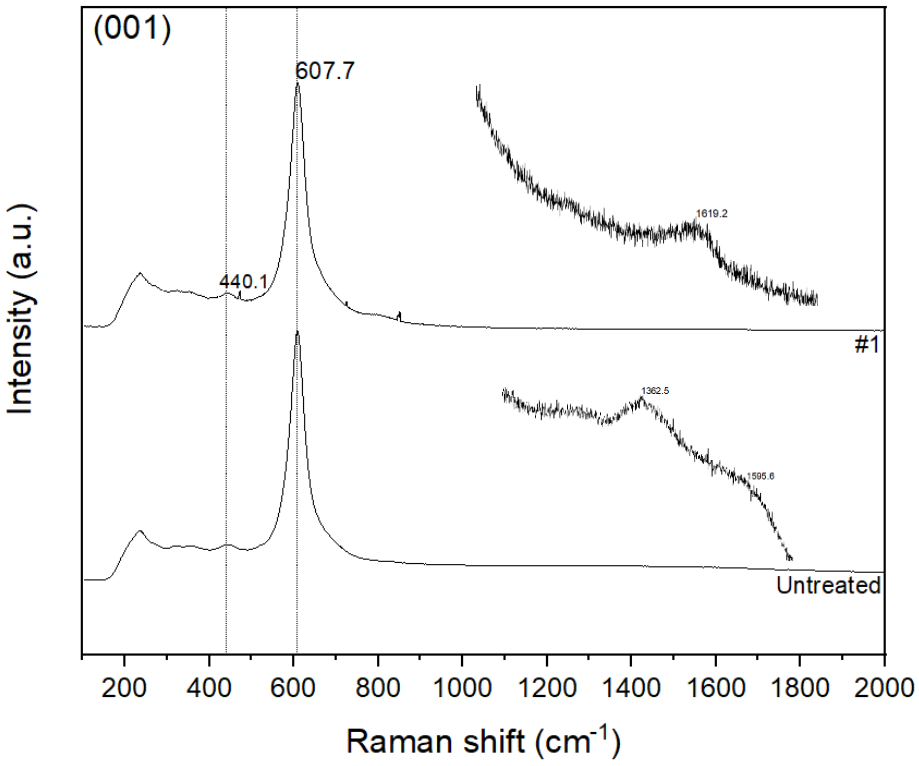

Figure Q: Raman spectrum of the TiN treated rutile (001) substrate, where #1 indicates an area on the substrate surface

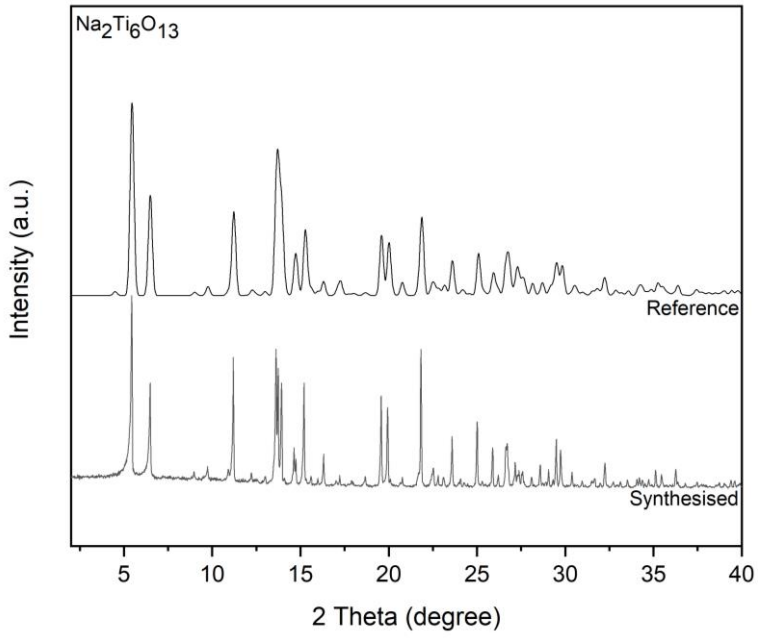

Figure R: PXRD pattern of the synthesised $Na_2Ti_6O_{13}$, compared to a reference spectrum obtained from the literature

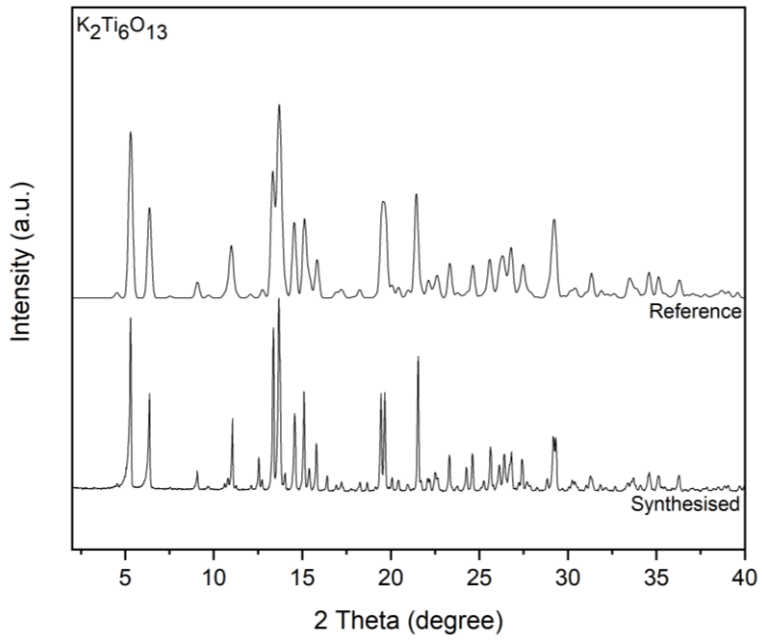

Figure S: PXRD pattern of the synthesised $K_2Ti_6O_{13}$, compared to a reference spectrum obtained from the literature

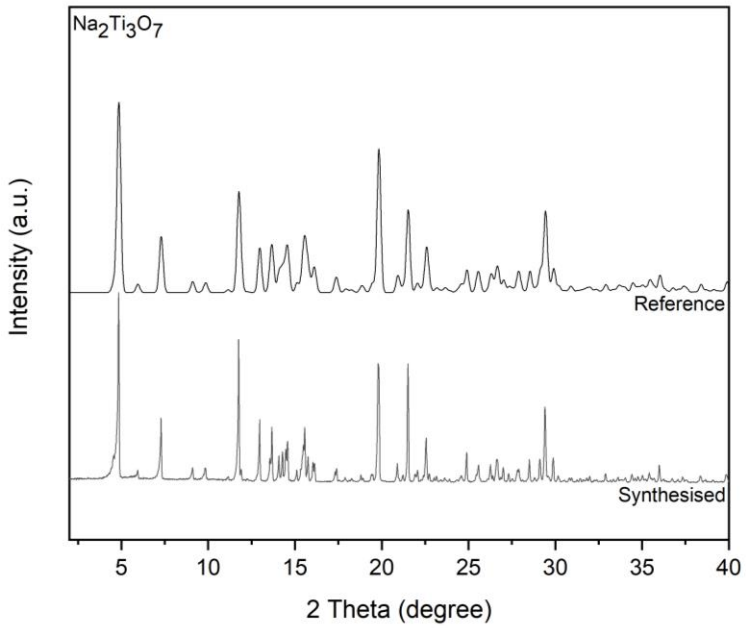

Figure T: PXRD pattern of the synthesised $Na_2Ti_3O_7$, compared to a reference spectrum obtained from the literature

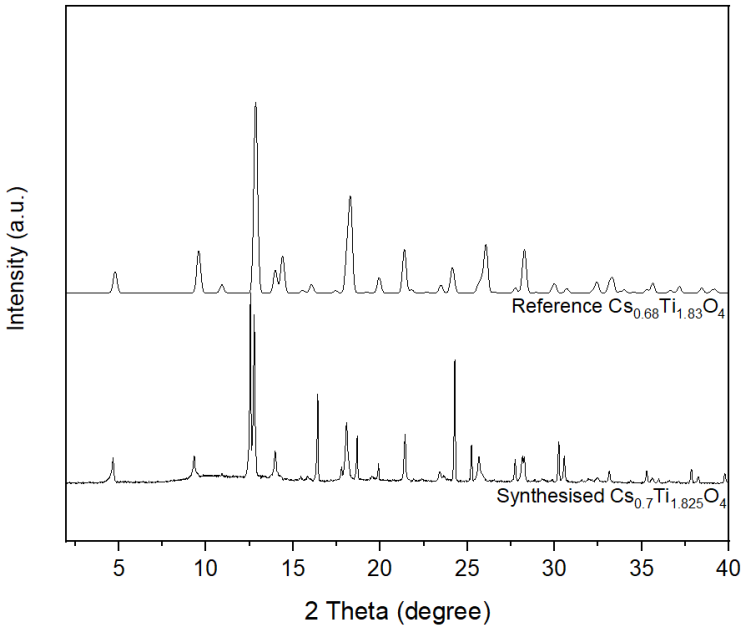

Figure U: PXRD pattern of the synthesised $Cs_{0.68}Ti_{1.825}O_4$, compared to a reference spectrum obtained from the literature

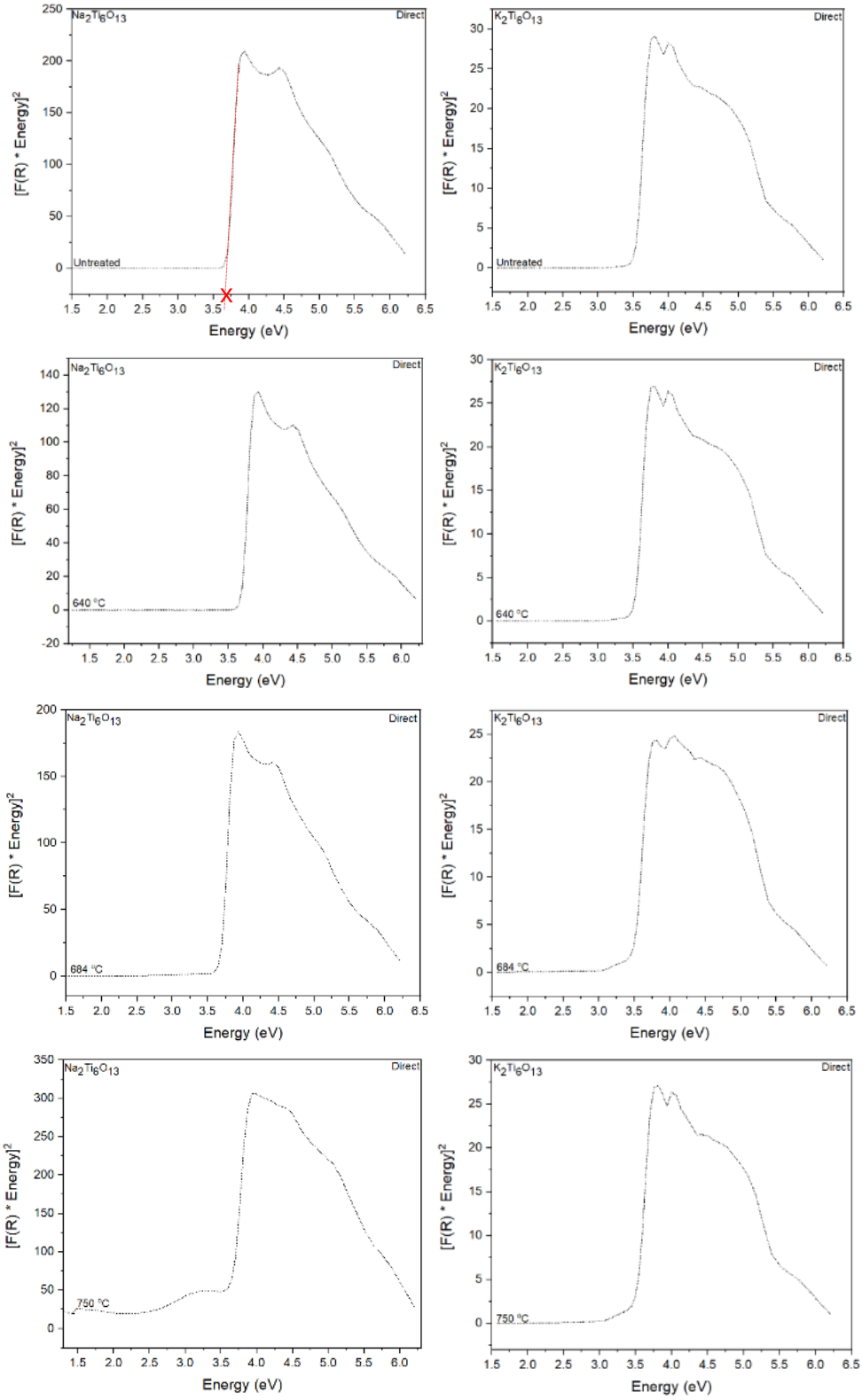

Figure V: Tauc plots (relating to the direct optical transitions) of the tunnelled titanates $Na_2Ti_6O_{13}$ and $K_2Ti_6O_{13}$ before and after nitrogen doping at three different temperatures

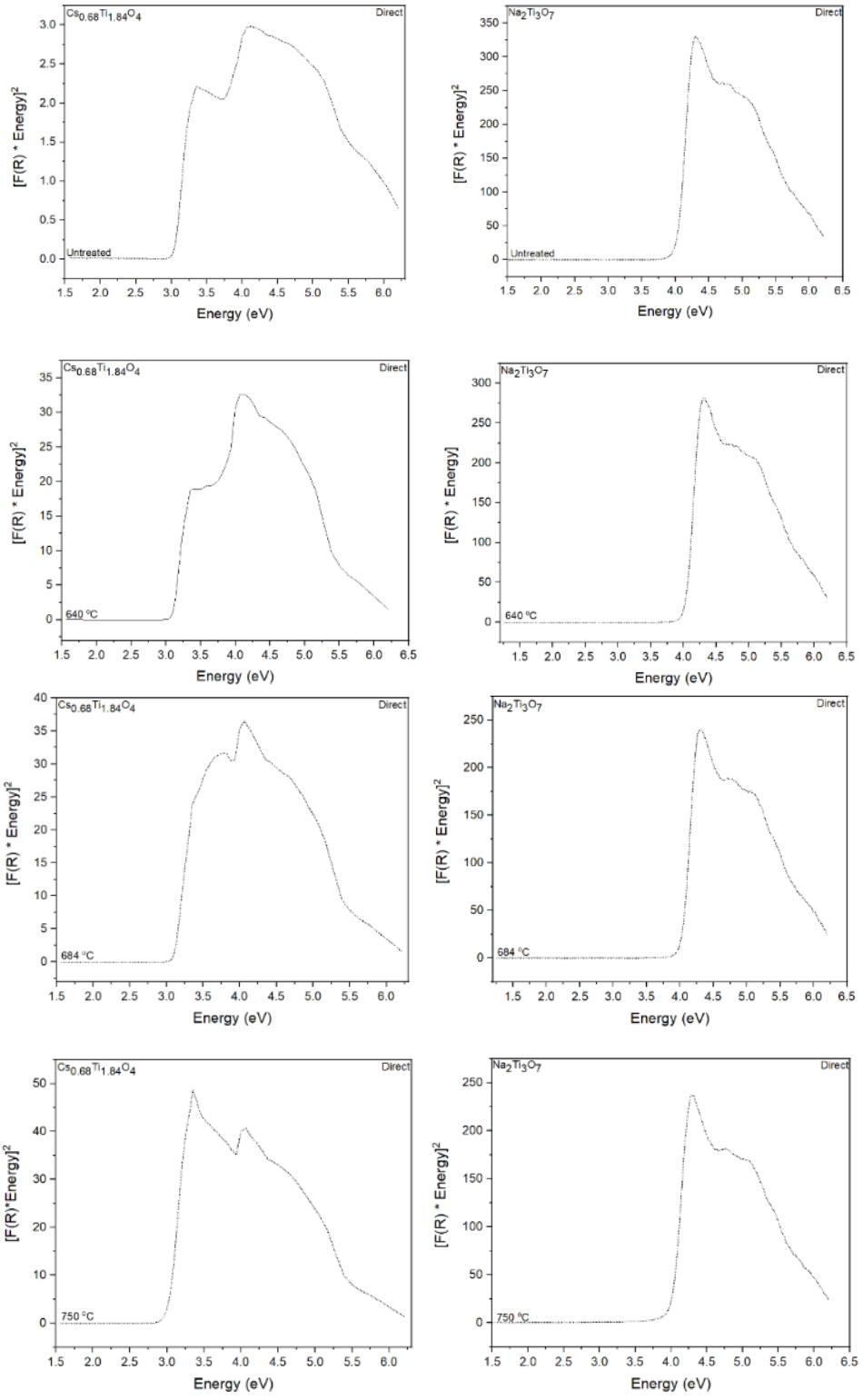

Figure W: Tauc plots (relating to the direct optical transitions) of the tunnelled titanates $Cs_{0.68}T_{1.825}O_4$ and $Na_2Ti_3O_7$ before and after nitrogen doping at three different temperatures

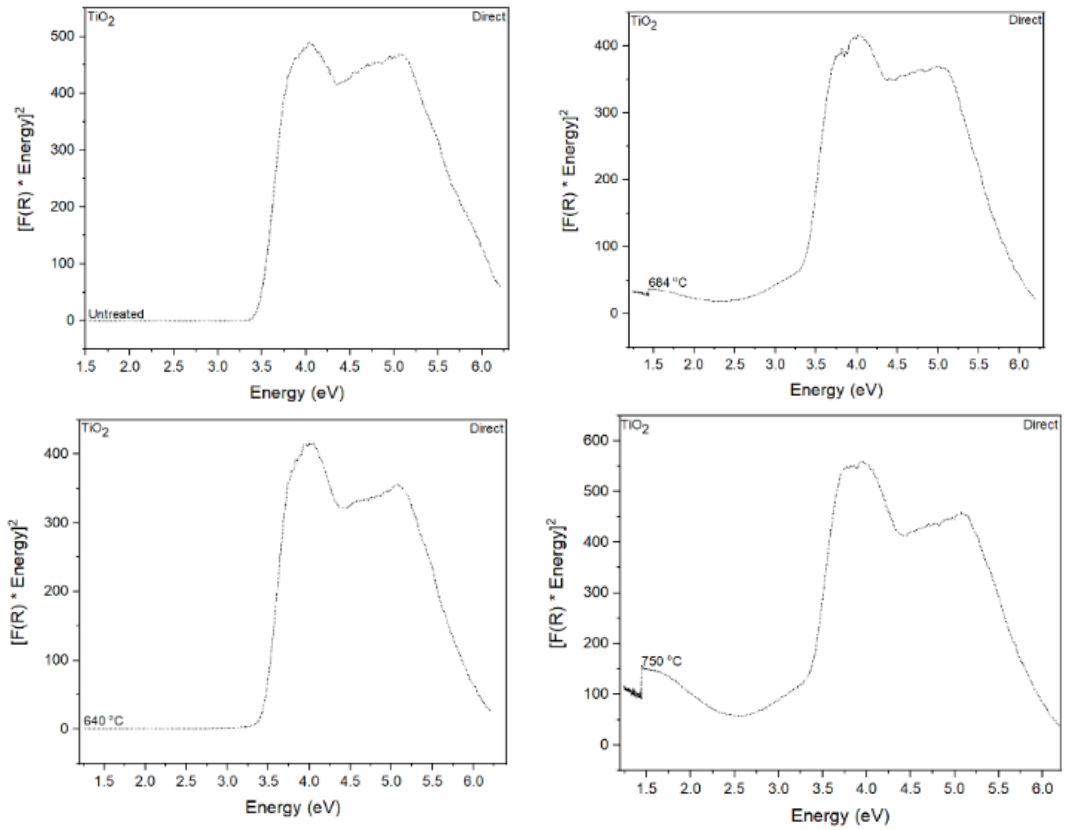

Figure X: Tauc plots (relating to the direct optical transitions) of the non-layered anatase-TiO_2 before and after nitrogen doping at three different temperatures

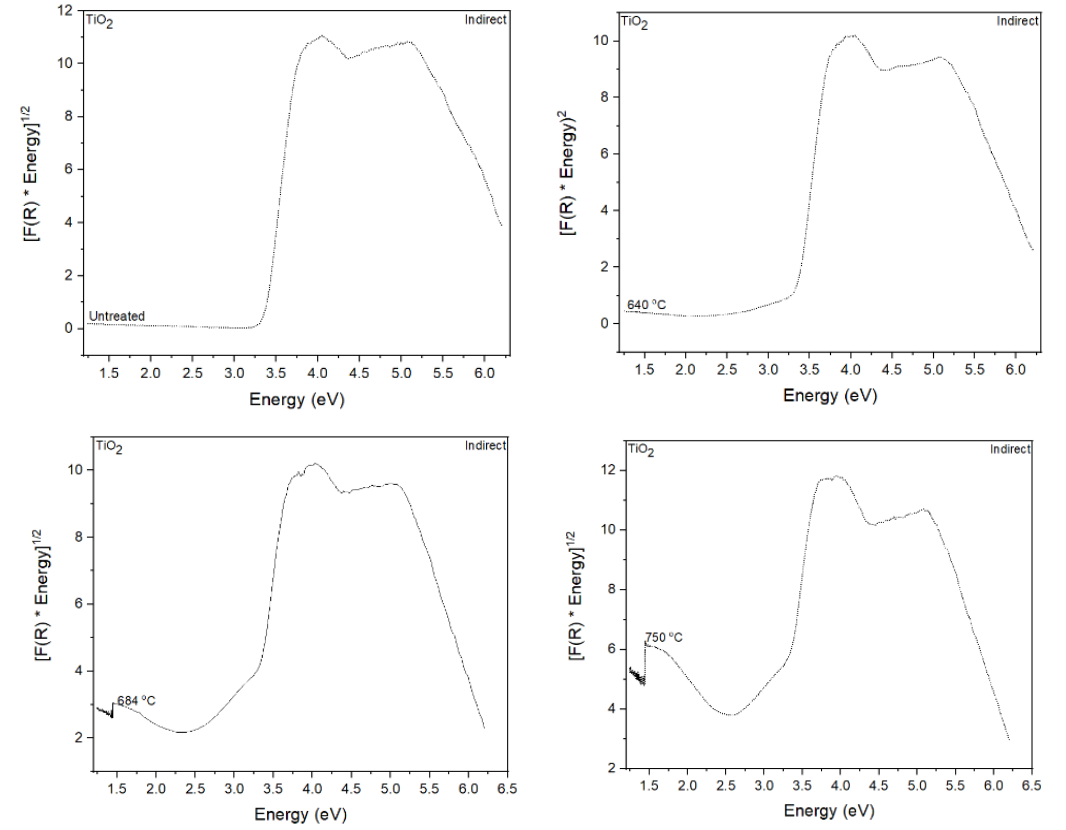

Figure Y: Tauc plots (relating to the indirect optical transitions) of the non-layered anatase-TiO_2 before and after nitrogen doping at three different temperatures

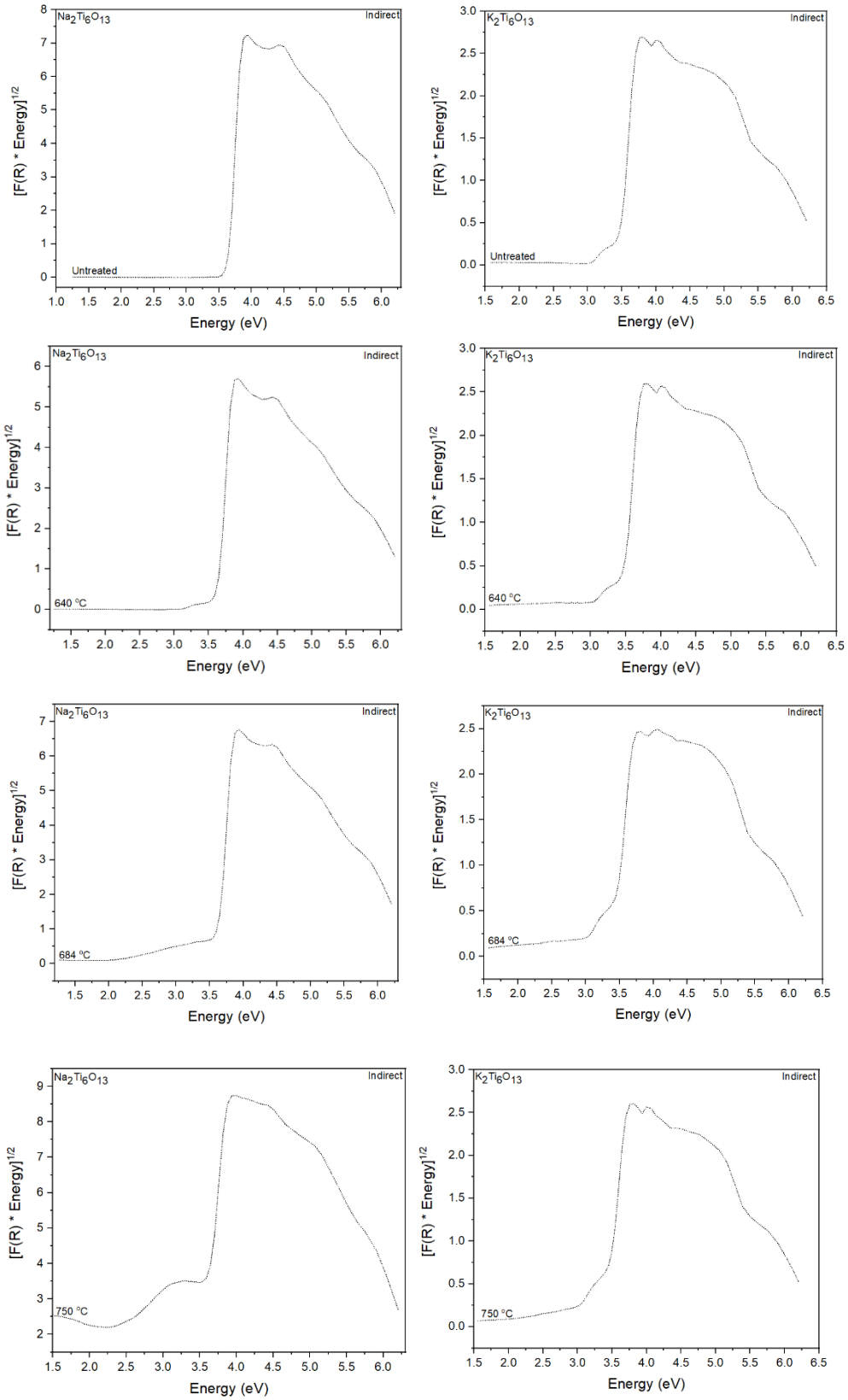

Figure Z: Tauc plots (relating to the indirect optical transitions) of the tunnelled titanates $Na_2Ti_6O_{13}$ and $K_2Ti_6O_{13}$ before and after nitrogen doping at three different temperatures

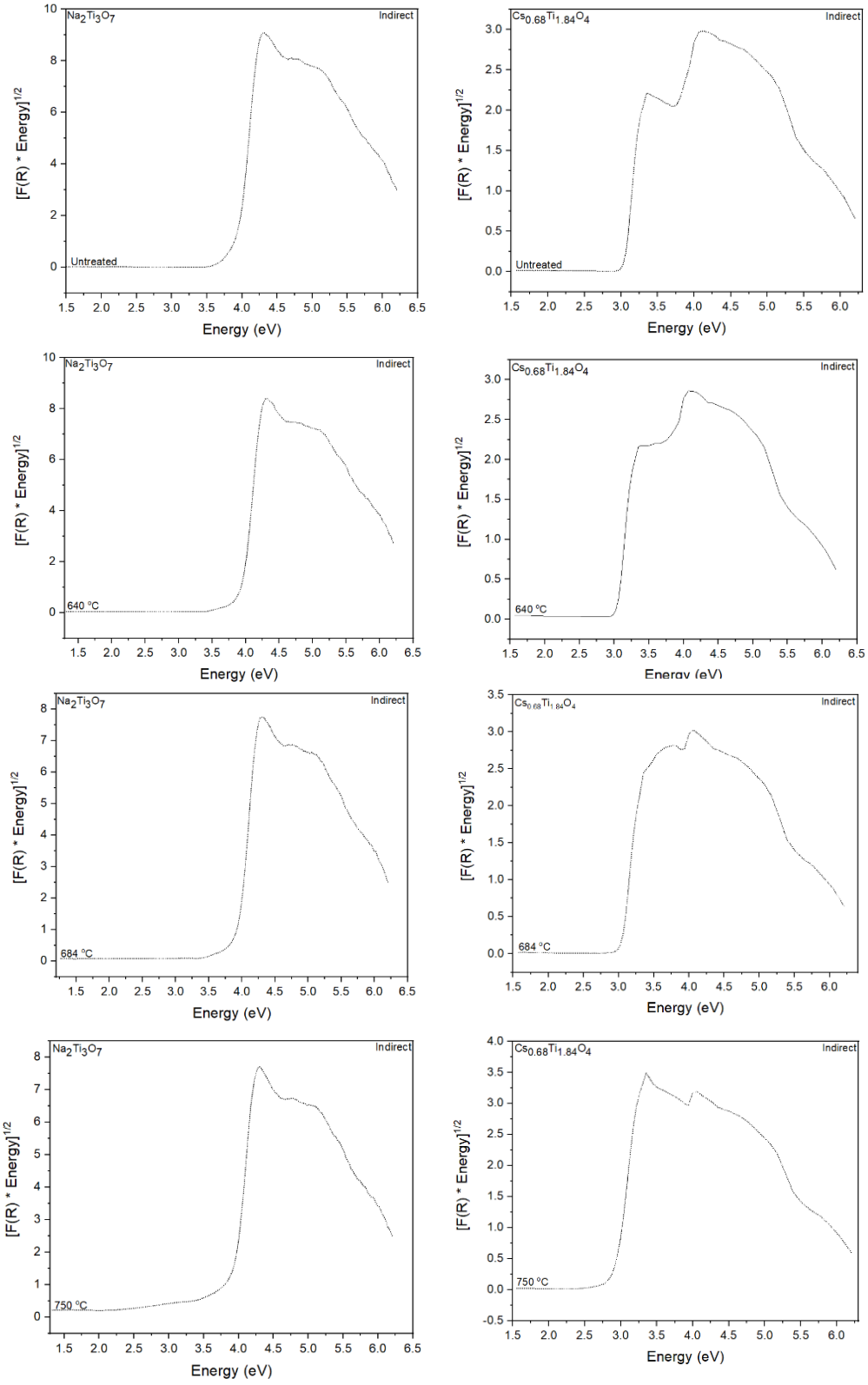

Figure AA: Tauc plots (relating to the indirect optical transitions) of the tunnelled titanates $Cs_{0.68}T_{1.825}O_4$ and $Na_2Ti_3O_7$ before and after nitrogen doping at three different temperatures

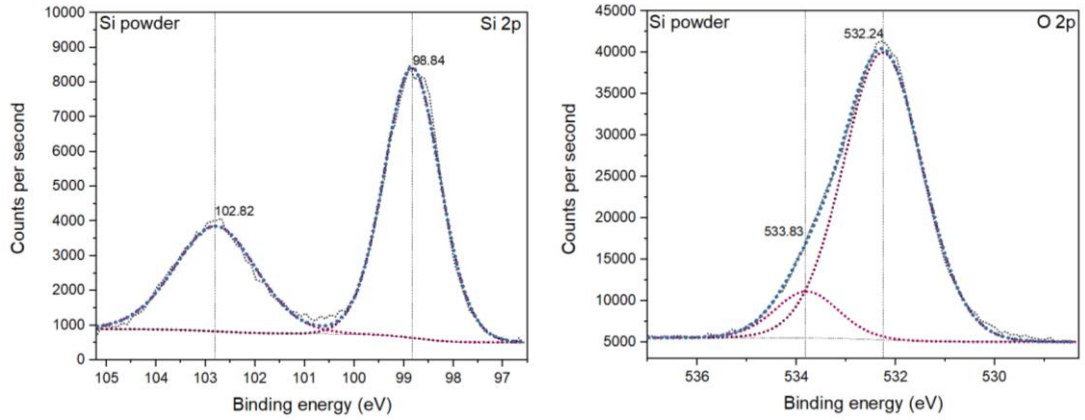

Figure AB: XPS core line spectrum of as-received silicon powder

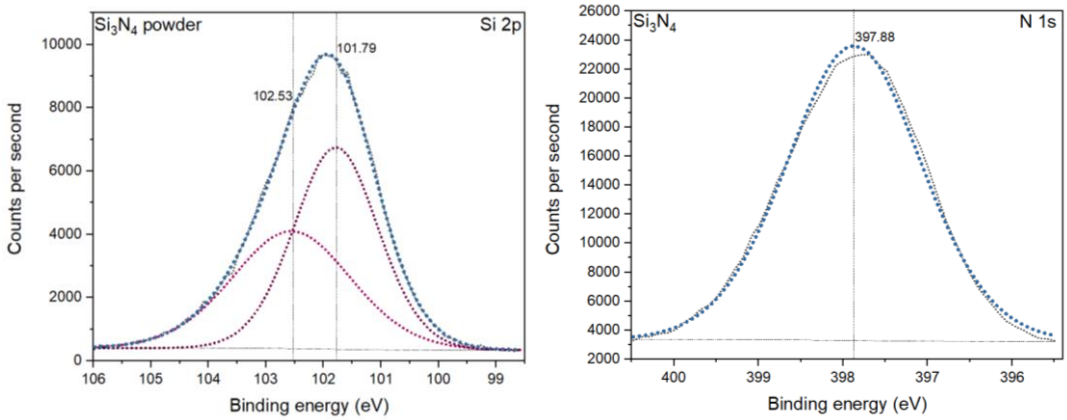

Figure AC: XPS core line spectrum of as-received Si_3N_4 powder

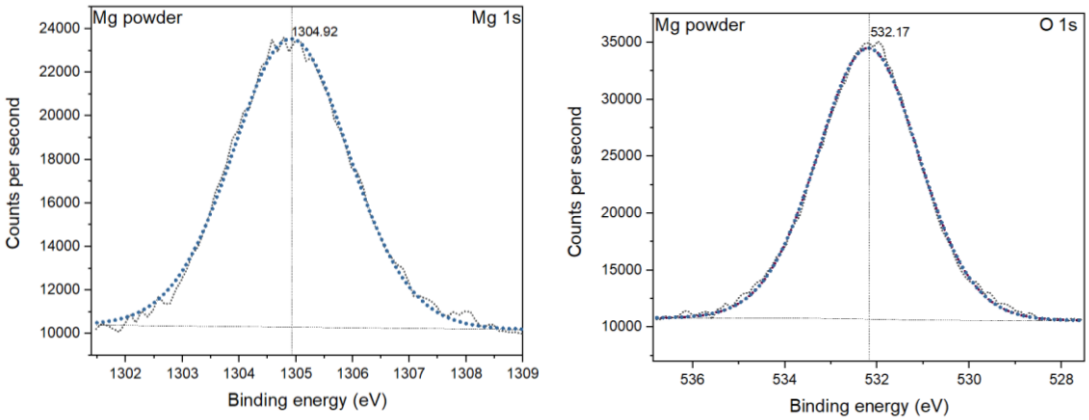

Figure AD: XPS core line spectrum of as-received magnesium powder

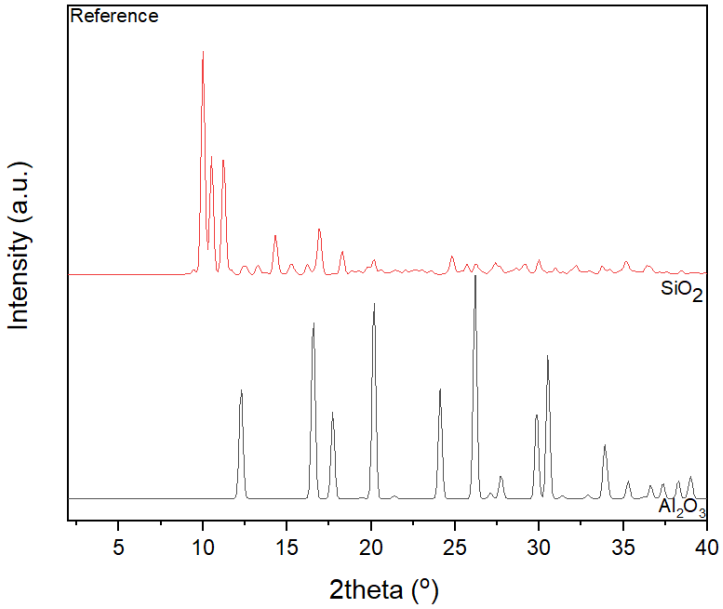

Figure AE: PXRD pattern of the SiO_2 and Al_2O_3 in the literature

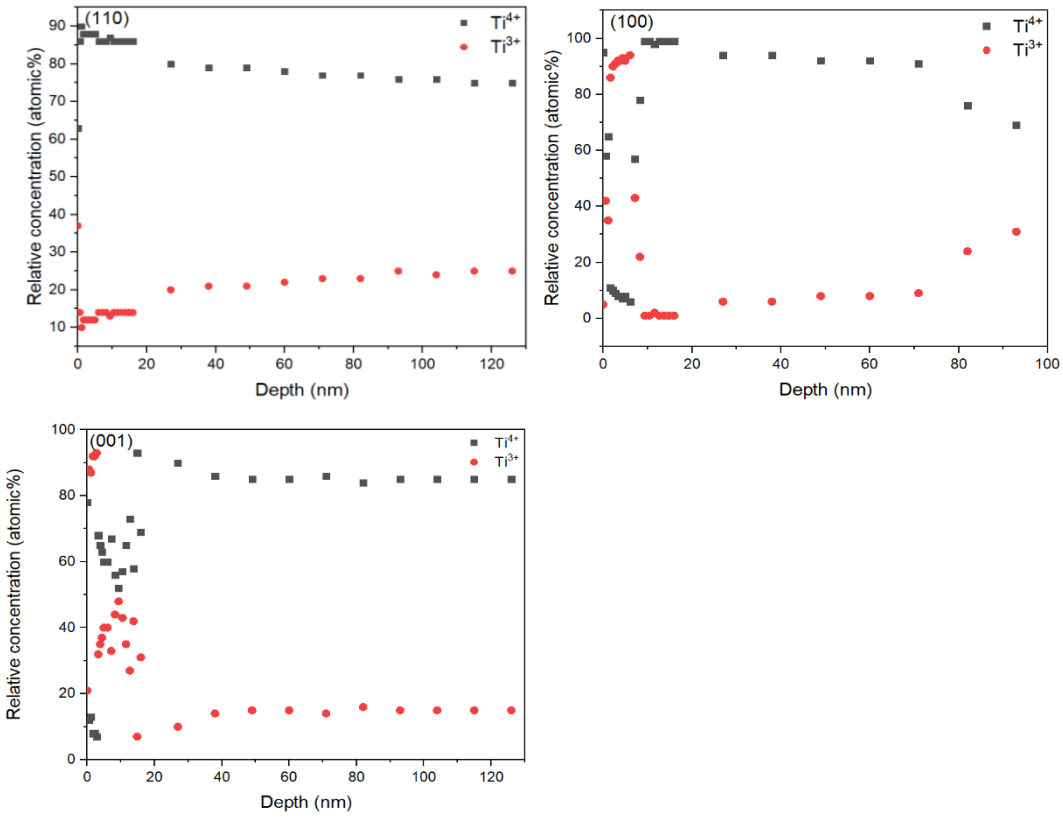

Figure AF: Relative concentrations of Ti^{4+} and Ti^{3+} in TiB_2 treated rutile single crystal substrates of the orientations (110), (100) and (001)